PROXY SIGNAL FORMATION IN PALAEOCLIMATE ARCHIVES

DISSERTATION

Alexandra M. Zuhr

ALFRED-WEGENER-INSTITUT
HELMHOLTZ-ZENTRUM FÜR POLAR- UND MEERESFORSCHUNG

Universität Potsdam

PROXY SIGNAL FORMATION IN PALAEOCLIMATE ARCHIVES

A characterisation of climate signal deposition and modification in marine sediments and polar ice

Publikationsbasierte Dissertation
zur Erlangung des akademischen Grades
"doctor rerum naturalium"
(Dr. rer. nat.)

in der Wissenschaftsdisziplin
Paläoklimatologie

eingereicht an der
Lehreinheit Geoökologie und Geowissenschaften der
Mathematisch-Naturwissenschaftlichen Fakultät an der
Universität Potsdam

angefertigt am
Alfred-Wegener-Institut
Helmholtz-Zentrum für Polar- und Meeresforschung

vorgelegt von
ALEXANDRA M. ZUHR

Potsdam, Mai 2022

Ort und Tag der Disputation:
Potsdam, 3. Februar 2023

REVIEWER

PROF. DR. THOMAS LAEPPLE
Alfred-Wegener-Institut Helmholtz
Zentrum für Polar- und Meeresforschung, Potsdam, Germany
and
University of Bremen, MARUM – Center for Marine Environmental
Sciences and Faculty of Geosciences, Bremen, Germany

ASSISTANT PROF. DR. SZE LING HO
Institute of Oceanography
National Taiwan University, Taipei, Taiwan

ASSISTANT PROF. DR. ANAÏS ORSI
Department of Earth Ocean and Atmospheric Sciences
University of British Columbia, Vancouver, Canada

Published online on the
Publication Server of the University of Potsdam:
https://doi.org/10.25932/publishup-58286
https://nbn-resolving.org/urn:nbn:de:kobv:517-opus4-582864

Alexandra M. Zuhr
Proxy signal formation in palaeoclimate archives:
A characterisation of climate signal deposition and modification in marine sediments and polar ice
Potsdam, Mai 2022

Document typeset using the LaTeX template `classicthesis` developed by André Miede with style inspirations by Robert Bringhurst's "*The Elements of Typographic Style*". Template is available at: https://bitbucket.org/amiede/classicthesis/

I believe firmly, deeply, that if we get the right information to people and show them the whole picture, that they will eventually make wise decisions.

– Richard B. Alley

Für meine Familie.

ABSTRACT

Throughout the last ~3 million years, the Earth's climate system was characterised by cycles of glacial and interglacial periods. The current warm period, the Holocene, is comparably stable and stands out from this long-term cyclicality. However, since the industrial revolution, the climate has been increasingly affected by a human-induced increase in greenhouse gas concentrations. While instrumental observations are used to describe changes over the past ~200 years, indirect observations via proxy data are the main source of information beyond this instrumental era. These data are indicators of past climatic conditions, stored in palaeoclimate archives around the Earth. The proxy signal is affected by processes independent of the prevailing climatic conditions. In particular, for sedimentary archives such as marine sediments and polar ice sheets, material may be redistributed during or after the initial deposition and subsequent formation of the archive. This leads to noise in the records challenging reliable reconstructions on local or short time scales. This dissertation characterises the initial deposition of the climatic signal and quantifies the resulting archive-internal heterogeneity and its influence on the observed proxy signal to improve the representativity and interpretation of climate reconstructions from marine sediments and ice cores.

To this end, the horizontal and vertical variation in radiocarbon content of a box-core from the South China Sea is investigated. The three-dimensional resolution is used to quantify the true uncertainty in radiocarbon age estimates from planktonic foraminifera with an extensive sampling scheme, including different sample volumes and replicated measurements of batches of small and large numbers of specimen. An assessment on the variability stemming from sediment mixing by benthic organisms reveals strong internal heterogeneity. Hence, sediment mixing leads to substantial time uncertainty of proxy-based reconstructions with error terms two to five times larger than previously assumed.

A second three-dimensional analysis of the upper snowpack provides insights into the heterogeneous signal deposition and imprint in snow and firn. A new study design which combines a structure-from-motion photogrammetry approach with two-dimensional isotopic data is performed at a study site in the accumulation zone of the Greenland Ice Sheet. The photogrammetry method reveals an intermittent character of snowfall, a layer-wise snow deposition with substantial contributions by wind-driven erosion and redistribution to the final spatially variable accumulation and illustrated the evolution of stratigraphic noise at the surface. The isotopic data show

the preservation of stratigraphic noise within the upper firn column, leading to a spatially variable climate signal imprint and heterogeneous layer thicknesses. Additional post-depositional modifications due to snow-air exchange are also investigated, but without a conclusive quantification of the contribution to the final isotopic signature.

Finally, this characterisation and quantification of the complex signal formation in marine sediments and polar ice contributes to a better understanding of the signal content in proxy data which is needed to assess the natural climate variability during the Holocene.

ZUSAMMENFASSUNG

Während der letzten ~3 Millionen Jahre war das Klimasystem der Erde durch Zyklen von Glazialen und Interglazialen gekennzeichnet. Die aktuelle Warmperiode, das Holozän, ist vergleichsweise stabil und hebt sich von dieser langen Zyklizität ab. Seit der industriellen Revolution wird das Klima jedoch zunehmend durch einen vom Menschen verursachten Anstieg der Treibhausgaskonzentrationen beeinflusst. Während instrumentelle Beobachtungen die Veränderungen der letzten ~200 Jahre beschreiben können, liefern Proxydaten die meisten klimatischen Informationen für den Zeitraum vor diesen Beobachtungen. Proxies zeichnen vergangene Klimabedingungen auf und sind in Paläoklimaarchiven rund um die Erde gespeichert. Das Proxysignal wird durch eine Vielzahl an Prozessen beeinflusst, die unabhängig von den vorherrschenden klimatischen Bedingungen sind. Insbesondere bei sedimentären Archiven wie Meeressedimenten und Eisschilden kann es während oder nach der Ablagerung zu einer Umverteilung des Materials und einer Änderung des Signals kommen. Dies führt zu nicht-klimatischen Unsicherheiten in den Daten, was zuverlässige Rekonstruktionen auf lokalen oder kurzen zeitlichen Skalen erschwert. Diese Dissertation charakterisiert die Ablagerung des Klimasignals und quantifiziert die daraus resultierende archiv-interne Heterogenität und ihren Einfluss auf das beobachtete Proxysignal, um die Repräsentativität und Interpretation von Klimarekonstruktionen aus marinen Sedimenten und Eiskernen zu verbessern.

Zu diesem Zweck wird die horizontale und vertikale Variabilität des Radiokarbongehalts in einem Sedimentkern aus dem Südchinesischen Meer untersucht. Die dreidimensionale Auflösung des Kastenbohrers wird genutzt, um die tatsächliche Unsicherheit in Alterabschätzung von planktonische Foraminiferen mittels der Radiokarbonmethode zu quantifizieren. Mit Hilfe von verschiedene Probenvolumina und wiederholten Messungen von kleinen und großen Anzahlen an Lebewesen wird eine Quantifizierung der Variabilität, die auf die Durchmischung des Sediments durch benthische Organismen zurückzuführen ist, durchgeführt. Die Durchmischung der Sedimente verursacht eine starke interne Heterogenität, was zu Fehlertermen, die zwei bis fünf Mal größer sind als bisher angenommen, und einer erheblichen zeitlichen Unsicherheit von Rekonstruktionen basierend auf Proxydaten führt.

Eine zweite dreidimensionale Analyse liefert Einblicke in die heterogene Signalablagerung in Schnee und Firn. Hierzu wird ein neues Studiendesign in der Akkumulationszone des grönländischen Eisschilds angewandt, wobei ein Structure-from-Motion Photogramme-

trie Ansatz mit zweidimensionalen Isotopendaten kombiniert wird. Die photogrammetrische Methode zeigt, dass die Akkumulation von Schnee sehr variable ist. Die Entwicklung der Schneeablagerung an der Oberfläche erfolgt primär schichtweise mit erheblichen Veränderungen durch eine windgestriebene Erosion und Umverteilung des Schnees. Diese Dynamik führt zu einer räumlich variablen Akkumulation und sratigraphischem Rauschens an der Oberfläche. Die heterogene Akkumulation bestimmt die räumliche Ablagerung der klimatischen Informationen, die in der Isotopenzusammensetzung des Schness enthalten ist. Stratigraphische Rauschen der Oberfläche bleibt in der oberen Firnsäule erhalten, was zu einem räumlich variablen Signaleindruck führt. Weiterhin werden zusätzliche Veränderungen nach der Ablagerung durch Austauschprozesse zwischen dem Schnee und der Atmosphäre untersucht, jedoch ohne eine schlüssige Quantifizierung dieses Beitrags zur endgültigen Isotopensignatur.

Die Charakterisierung und Quantifizierung der komplexen und heterogenen Signalbildung in marinen Sedimenten und Gletschereis verbessert letztlich das Verständnis des Signalgehalts in Proxydaten und trägt dazu bei, die natürliche Klimavariabilität des Holozäns besser abzuschätzen.

PUBLICATIONS OF THE AUTHOR

Peer-reviewed

Zuhr, A. M., T. Münch, H. C. Steen-Larsen, M. Hörhold, and T. Laepple (2021), Local-scale deposition of surface snow on the Greenland ice sheet, *The Cryosphere* 15 (10), 4873–4900, DOI: 10.5194/tc-15-4873-2021.

Zuhr, A. M., A. M. Dolman, S. L. Ho, J. Groeneveld, L. Loewemark, H. Grotheer, C.-C. Su, and T. Laepple (2022), Age-heterogeneity in marine sediments revealed by three-dimensional high-resolution radiocarbon measurements, *Frontiers in Earth Science - Marine Geoscience* 2022, DOI: 10.3389/feart.2022.871902.

Non peer-reviewed

Zuhr, A. M., S. Wahl, H. C. Steen-Larsen, M. Hörhold, H. Meyer, and T. Laepple (2022), A snapshot on the buildup of the stable water isotopic signal in the upper snowpack at EastGRIP, Greenland Ice Sheet, *submitted to Journal of Geophysical Research: Earth Surface*.

Articles not directly related to this dissertation submitted/published in peer-reviewed journals

Hughes, A. G., S. Wahl, T. R. Jones, A. Zuhr, M. Hörhold, J. W. C. White, and H. C. Steen-Larsen (2021), The role of sublimation as a driver of climate signals in the water isotope content of surface snow: laboratory and field experimental results, *The Cryosphere* 15 (10), 4949–4974, DOI: 10.5194/tc-15-4949-2021.

Wahl, S., H. C. Steen-Larsen, A. G. Hughes, L. J. Dietrich, A. M. Zuhr, M. Behrens, A.-K. Faber, and M. Hörhold (2022), Atmosphere-Snow Exchange Explains Surface Snow Isotope Variability, *submitted to Geophysical Research Letters*.

Zuhr, A., A. M. Dolman, S. L. Ho, J. Groeneveld, H. Grotheer, C.-C. Su, and T. Laepple (2022a), Radiocarbon age measurements on foraminifera from sediment core OR1-1218-C2-BC, data set, DOI: 10.1594/PANGAEA.942239, URL: https://doi.pangaea.de/10.1594/PANGAEA.942239.

Zuhr, A., T. Münch, H. C. Steen-Larsen, M. Hörhold, and T. Laepple (2020), Snow height data generated with a Structure-from-Motion photogrammetry approach at the EGRIP camp site in 2018, data set, DOI: 10.1594/PANGAEA.923418, URL: https://doi.org/10.1594/PANGAEA.923418.

Zuhr, A., T. Münch, H. C. Steen-Larsen, M. Hörhold, and T. Laepple (2021a), Day-to-day changes in the snow surface height derived from digital elevation models at the EGRIP camp site in 2018, data set, DOI: 10.1594/PANGAEA.936099, URL: https://doi.org/10.1594/PANGAEA.936099.

Zuhr, A., T. Münch, H. C. Steen-Larsen, M. Hörhold, and T. Laepple (2021b), Snow surface accumulation measured using manual stick measurements, EastGRIP camp Greenland, May 2018, data set, DOI: 10.1594/PANGAEA.931124, URL: https://doi.org/10.1594/PANGAEA.931124.

Zuhr, A., T. Münch, H.-C. Steen-Larsen, M. Hörhold, and T. Laepple (2021c), Digital elevation models generated with a Structure-from-Motion photogrammetry approach at the EGRIP camp site in 2018, data set, DOI: 10.1594/PANGAEA.936082, URL: https://doi.org/10.1594/PANGAEA.936082.

Zuhr, A., S. Wahl, H. C. Steen-Larsen, M. Hörhold, M. Behrens, H. Meyer, and T. Laepple (2022b), Stable water isotopic composition of the upper snow layer (0-30 cm) at the EastGRIP camp site in 2019, data set, to be submitted.

Zuhr, A., S. Wahl, H. C. Steen-Larsen, and T. Laepple (2022c), Snow height data generated with a Structure-from-Motion photogrammetry approach at the EGRIP camp site in 2019, data set, to be submitted.

CONTENTS

LIST OF FIGURES

LIST OF TABLES

LIST OF ABBREVIATIONS

CRDS Cavity Ring Down Spectrometer

GCP ground control point

DEM Digital Elevation Model

DOP Day of Observation Period

EAP East Antarctic Plateau

EGRIP East Greenland Ice-Core Project

GMWL Global Meteoric Water Line

GrIS Greenland Ice Sheet

IFA individual foraminifera analysis

IRIS Isotope Ratio Infrared Spectroscopy

IRMS Isotope Ratio Mass Spectrometer

PSM proxy system model

SCS South China Sea

SNR signal-to-noise ratio

SfM Structure-from-Motion

SLAP Standard Light Antarctic Precipitation

SST sea surface temperature

VSMOW Vienna Standard Mean Ocean Water

1 INTRODUCTION

The Earth's climate system is reliant on a complex interplay between the land surface, the vegetation, the oceans, the atmosphere and the cryosphere. External forcings affect these components at different spatial and temporal scales. An influencing factor is, for example, the solar radiation. The Earth's orbital cycles and volcanic eruptions determine the amount of insolation received at the Earth's surface by changing the amount of radiation going through the atmosphere. Such changes have extensive influence on the mean state of the climate system and its variability on different spatial and temporal scales, and is described as climate variability (Rohling et al., 2012). The last ~3 million years are, for example, characterised by a cyclicity of glacial and interglacial periods, as for instance revealed by a deep ice from Antarctica for the last ~800,000 years (EPICA community members, 2004). Since the last glacial maximum around 22,000 years ago, the climate transitioned to the current warm period, the Holocene. This period is comparably stable and characterised by a reduced climate variability (Rehfeld et al., 2018).

In recent decades, anthropogenic forcing has considerably affected the Earth's climate by increasing the concentration of greenhouse gases, including CO_2, in the atmosphere and thus causing the global average temperature to rise by about 1 °C compared to pre-industrial levels (IPCC, 2021). The knowledge of the rate and the magnitude of these changes can only partly be inferred from instrumental observations due to their temporal limitation to the last ~200 years (Parker et al., 2000). Yet, understanding past climatic changes is crucial to put human-induced perturbations into context, compared to the small variations during the Holocene, and to further distinguish the current changes from the long-term natural variability.

Beyond the instrumental era, palaeoclimate archives are the most important means to reconstruct the climatic history. The environmental information is recorded in *sensors*, such as calcite shells or ice crystals. They carry the signal of interest and are stored, for example, in marine sediments or ice cores, thus in *archives*, following the terminology of Evans et al. (2013). The actual *observation* made on these archives is called *proxy* and provides indirect information on the climate of the past. Besides the climatic information, each reconstructed signal requires an age estimate, e. g., the time of deposition. One of the first age estimates of a seashell was determined by Libby and Arnold around 1950 by measuring the radioactive carbon isotope ^{14}C (Arnold and Libby, 1949; Libby et al., 1949). At the same time and in

the same laboratory, Urey and Emiliani demonstrated the use of the ratio of heavy (^{18}O) to light oxygen isotopes (^{16}O) to reconstruct past temperatures from marine shells (Urey, 1948; Emiliani, 1955, 1958). At a similar time, Craig, Gordon and Dansgaard reported the relationship between the water isotopic composition and temperature, which has since been widely used for the reconstruction of climatic information from ice cores (Dansgaard, 1953; Craig, 1961a; Craig and Gordon, 1965; Dansgaard et al., 1973). These and other findings have laid the foundation for the use of proxy data and for today's knowledge of the climate history; and yet, in the context of climate change, it has become more important than ever before.

To reliably reconstruct the variability of the Earth's climate system before to the instrumental era, a profound understanding of the processes involved in the formation of the proxy signal is required. Depending on the archive, the imprint of the climatic information might be multivariate, non-linear and seasonal. Resulting time uncertainty and archive-internal heterogeneity can create random or systematic biases in proxy data and their interpretation (e. g., Schiffelbein and Hills, 1984; Werner et al., 2000). Recent developments and investigations tackled these issues with improved sampling schemes and dating methods for reliable chronologies (e. g., Blaauw and Christen, 2011; Lacourse and Gajewski, 2020; Münch et al., 2021), with spectral estimations of the signal and the uncertainties (Laepple and Huybers, 2013; Münch and Laepple, 2018), analytical error models and enhanced statistical analyses (e. g., Münch et al., 2016; Kunz et al., 2020; Dolman et al., 2021a,b) to improve the robustness of reconstructed time series. A further step towards refined interpretations of proxy data are forward models, such as proxy system models (PSMs), which generally help develop a clearer understanding of the proxy-climate relationship (e. g., Evans et al., 2013; Dee et al., 2017; Dolman and Laepple, 2018). All these efforts improve the mechanistic understanding of the climatic signal contained in the archives; however, detailed studies of the uncertainties introduced during the signal imprint to and preservation in the archive are elusive, but pivotal to ensure reliable reconstructions. This thesis, therefore, focuses on the uncertainties in reconstructions from sedimentary palaeoclimate archives by providing detailed insights into the processes and associated uncertainties during the proxy signal formation.

1.1 INTRODUCTION TO PROXY-BASED CLIMATE RECONSTRUCTIONS

Marine sediments and polar ice sheets, two examples of sedimentary archives, are key archives for climate reconstructions on short and long temporal scales and cover large parts of the Earth. In contrast to other archives, such as speleothems or tree rings, both ma-

rine sediments and polar ice sheets continuously record the climate history. Time series from regions with low accumulation rates are generally able to provide long-term climate information, but have the disadvantage of low temporal resolution. Vice versa, areas with high accumulation rates provide records with high temporal resolution, but limited in time. Reconstructions from the open ocean have, for instance, a much lower temporal resolution than ice cores from Greenland and Antarctica. The longest time series available from ice cores currently covers the last ~800,000 years (EPICA community members, 2004), while marine sediments can go back much further in time. With their different characteristics, both archives provide a wealth of information on different environmental parameters, such as the sea level height, the size of ice sheets, the salinity content in the oceans, atmospheric and sea surface temperature (SST), past accumulation rates as well as atmospheric CO_2 and other greenhouse gas concentrations, throughout glacial-interglacial periods (e. g., Pearson, 2012; Lea, 2014).

Sedimentary archives develop over time through successive deposition of particles from above, i. e., marine organisms or snow crystals (Fig. 1.1). The burial of these particles leads theoretically to a chronological sequence of climatic information. In fact, a multitude of processes before and during the accumulation as well as after the deposition within the archiving medium modify the layered information and add non-climatic noise. The most important principles of the imprint of the environmental signal into a signal carrier, i. e., a snow crystal or marine organisms, its deposition and preservation in marine sediments and polar ice sheets are introduced in the following section and provide the background for the studies in the Chapters 2, 3 and 4 and the additional Chapters in Appendix A and B. Further, similarities and differences between both archives are described and current challenges in the interpretation of proxy-based climate reconstructions are presented.

1.1.1 *Radiocarbon as a tracer of time*

The ocean covers more than 70 % of the Earth's surface. It is a vital component of the global climate and is in direct interaction with the biosphere, the atmosphere and the cryosphere. The oceans basins consist of sedimentary material of abiotic and biotic particles which store a wealth of environmental information. Part of the sediment consists of deceased organisms' calcite shells, for example planktonic foraminifera (Fig. 1.1a, in the following, foraminifera always refers to planktonic foraminifera). These organisms live in the upper water column and incorporate the prevailing environmental conditions of their habitat into their shells. This information can be reconstructed from the shells, for instance via the ratio of Magnesium to Calcium

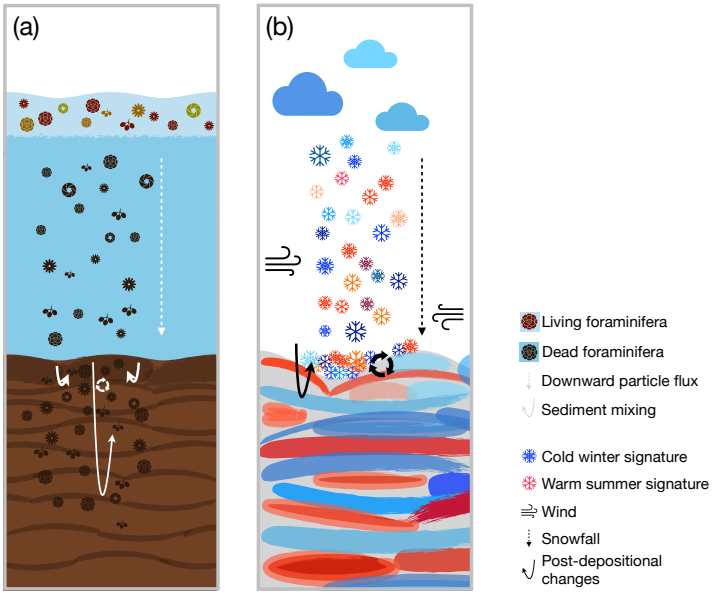

Figure 1.1: Schematic of marine sediments (a) and ice sheets (b). Both archives develop over time with successive deposition of sinking particles, containing the climatic information. Within each archive, a variety of processes interact with the environmental parameter and affect the linearity of the recorded information. Marine organisms, e. g., planktonic foraminifera, record the environmental information of their habitat in the upper water column, sink down and deposit on the seafloor (a). With time, they are advected downwards into the sedimentary column and affected by bioturbation. Similar processes occur above ice sheets (b). Snow crystals record the ambient conditions during their formation in clouds and carry this signal to the snow surface. During the incorporation into the firn column, they are affected by a number of depositional (e. g., snowdrift) and post-depositional (e. g., sublimation) modifications. Note, both illustrations are not to scale.

atoms or the ratio of heavy to light oxygen isotopes (e. g., Nürnberg et al., 1996; Lea, 2014). Further, the shell's radiocarbon content reflects the time passed since deposition, based on its radioactive decay, and is a commonly used dating method for material younger than 55,000 years (Libby et al., 1949; Blaauw and Heegaard, 2012).

The depth-age assignment via the ^{14}C content from marine sediments can be affected by many types of uncertainties, introduced during the variable deposition of the material or post-depositional within the sedimentary column. Bioturbation, for example, describes mixing in oxygenated sediments by burrowing and feeding organisms. This process significantly alters the stratigraphy of biological, physical and chemical properties of the sediment with variations in the intensity and the vertical extent for particles of different sizes and for different environmental conditions, either at other locations or

during different climatic periods (e. g., Peng et al., 1979; Schiffelbein and Hills, 1984; Trauth et al., 1997).

Mixing models with different complexities were developed to quantify this net displacement of material within the sedimentary column (e. g., Berger and Heath, 1968; Guinasso and Schink, 1975; Bard et al., 1987; Trauth, 2013). They generally assume uniform mixing of new deposited particles within an upper sedimentary layer, often referred to as the homogeneous layer (Fig. 1.1a). If the mixing is faster than the burial of particles, the initial signal gets dispersed, resulting in a uniform distribution of the proxy signal (e. g., derived $\delta^{18}O$ or ^{14}C from foraminifera). Statistically speaking, bioturbation acts as a low-pass filter smoothing the imprinted signal (Bard et al., 1987; Anderson, 2001).

In a number of studies since the 1970s, the radiocarbon content of calcite shells has been used to assess the mixing rate in marine sediments (Peng et al., 1979; Berger and Johnson, 1978; Broecker et al., 1991), showing that the simple but frequently used mixing model by Berger and Heath (1968) is too idealised. Linked to this is the interest in quantifying the horizontal age-heterogeneity, i. e., the spread in age in one depth layer. Recent developments towards ultra-small and high-precision radiocarbon techniques allowed measurements of few specimens and individual foraminifera analysis (IFA) (Wacker et al., 2010, 2013). This new method was applied to assess sediment characteristics and provide new insights into sediment mixing and the resulting horizontal age-heterogeneity (e. g., Lougheed et al., 2018; Fagault et al., 2019; Dolman et al., 2021a).

1.1.2 *Environmental information stored in snow, firn and ice*

The continuous deposition of snow leads to a geographically constrained recording of climatic information in ice (Fig. 1.1b) on the large ice sheets that cover Greenland and Antarctica. The use of ice cores as a palaeoclimate archive originated in the 1960s in the seminal work of Dansgaard, who documented a temperature-dependent change in the molecular structure of water. Water, water vapour, snow and ice share the same chemical structure of two hydrogen and one oxygen atom. In nature, atoms occur with different numbers of neutrons which are called isotopes. For hydrogen, the two stable isotopes ^{1}H (henceforth shortened to H) and ^{2}H (also referred to as Deuterium D) exist, whereas oxygen naturally has three stable isotopes, i. e., ^{16}O, ^{17}O and ^{18}O. Water molecules can therefore build combinations of different isotopes, resulting in the isotopologues $H_2{}^{16}O$, $HD^{16}O$, $H_2{}^{17}O$ and $H_2{}^{18}O$ with different natural abundances and molecular weights (Table 1.1). In parts of this thesis, stable water isotopologues are referred to as stable water isotopes, which is used as a synonym.

Table 1.1: The natural abundance and the molecular weight of stable water isotopologues (Nassar et al., 2007; Horita et al., 2008).

Isotopologue	Abundance	Weight [g mol^{-1}]
$H_2{}^{16}O$	0.997317	18.011
$HD^{16}O$	0.00031069	19.017
$H_2{}^{17}O$	0.000372	19.015
$H_2{}^{18}O$	0.00199983	20.015

The isotopic composition of water is commonly expressed in the δ-notation (in per mil, ‰)

$$\delta = \left(\frac{R_{sample}}{R_{reference}} - 1 \right) \tag{11}$$

following Craig (1961b) with R_{sample} being the abundance ratio of the rare (e. g., $H_2{}^{18}O$) to the common isotopologue $H_2{}^{16}O$ and $R_{reference}$ that of a reference water according to the international VSMOW/SLAP scale (Gonfiantini, 1978). By convention, the Vienna Standard Mean Ocean Water (VSMOW) has a reference value of 0 ‰ for both $\delta^{18}O$ ($^{18}O/^{16}O$) and δD (D/H), whereas the Standard Light Antarctic Precipitation (SLAP) reference has values of -55.5 ‰ and -427.5 ‰ for $\delta^{18}O$ and δD, respectively (IAEA, 2017).

The usage and interpretation of stable water isotopologues in palaeoclimate research is based on the fractionation between the light and the heavy components during phase changes, i. e., during the transition from water vapour to raindrops or snow crystals, due to differences in the volatility between light and heavy isotopologues. Fractionation during evaporation and condensation can be quantified with the fractionation factor α, which expresses the differences in the saturated vapour pressure between the light (p) and the heavy component (p'). This factor is temperature dependent and can be described with

$$\alpha = \frac{p}{p'} \tag{12}$$

in the case of equilibrium fractionation, i. e., when a slow rate of reaction allows for equilibrium conditions between the phases (Dansgaard, 1964). The temperature dependency of this process results in different isotopic ratios in snow crystals (Jouzel and Merlivat, 1984) and builds the foundation of ice core based climate reconstructions. The isotopic composition of firn and ice cores is, therefore, to a first order interpreted as a proxy for local air temperature variations (Jouzel et al., 2003).

An immediate removal of the condensate after formation is described by Rayleigh distillation and characterises the conditions during the formation of raindrops in clouds. Under kinetic conditions, this process shows higher fractionation rates than under equilibrium conditions. The isotopic composition of the remaining phase R is composed of the isotopic ratio of the original phase R_o and the remaining fraction of the initial phase f, following

$$R = R_0 \cdot f^{\alpha - 1} \tag{13}$$

(Dansgaard, 1964). Rayleigh distillation under equilibrium conditions results in a linear relation between the oxygen and the hydrogen isotopic ratios in the form of

$$\delta D \approx 8 \cdot \delta^{18}O + 10 \tag{14}$$

(Craig, 1961a) which was found in many natural waters from various places around the Earth. This ratio is defined as the Global Meteoric Water Line (GMWL) (Craig and Gordon, 1965).

In contrast to this co-variation, kinetic effects, i. e., non-equilibrium changes, are known to influence the isotopic composition during evaporation at the ocean surface and during the formation of snow crystals in the atmosphere (Dansgaard, 1964; Merlivat and Jouzel, 1979; Jouzel and Merlivat, 1984). While the slope of 8 between $\delta^{18}O$ and δD can be predicted from equilibrium fractionation, a deviation from this parallelism is expressed in the second-order parameter deuterium excess (d-excess), defined as

$$d - excess = \delta D - 8 \cdot \delta^{18}O \tag{15}$$

(Dansgaard, 1964). Besides an interpretation of oceanic source conditions (e. g., Jouzel et al., 1982; Stenni et al., 2010), this parameter additionally provides evidence of non-equilibrium processes after the initial deposition, including vapour-snow exchange processes such as sublimation as well as condensation at and beneath the snow surface (Fig. 1.1) (Ebner et al., 2017; Casado et al., 2021). Indeed, a clear assignment of the signal to the source conditions or to local changes after deposition can help to better understand the processes during and after deposition, but is still pending. In addition to the drivers of changes in the isotopic signature, accurate measurements and a detailed understanding of the signal deposition are essential for reliable climate reconstructions from ice cores.

Measuring stable water isotopologues

The abundance ratios of stable water isotopologues can be determined via the different weights using Isotope Ratio Mass Spectrometer (IRMS) or via the differences in the electromagnetic wave absorption at specific wavelengths using Isotope Ratio Infrared Spectroscopy (IRIS). The first method has been used for many decades and

provides reliable results. However, the analysis is time-consuming because the water has to be converted into gases which can be measured by the mass spectrometer. The second method is mostly applied by Cavity Ring Down Spectrometer (CRDS) instruments which measure all ratios simultaneously via specific absorption spectra in different wavenumber ranges (e. g., Kerstel et al., 1999; Kerstel and Gianfrani, 2008; Steig et al., 2014; Piarro Inc., 2022).

Despite the higher sample throughput, CRDSs, such as those from Picarro Inc. (2022), have two disadvantages. First, a carry-over of remaining material from the precursor to the successive sample within the instrument falsifies the measured value. This memory effect can be accounted for by repeated injections of the same sample which reduces the influence of the previous sample and reaches a stable value after certain injections, or by applying a mathematical correction. The second drawback is an instrumental drift which describes a gradual change in the measured isotopic ratios and is more pronounced during long measurement sequences. The drift has to be monitored and corrected with known reference values. Additionally, a normalisation to the VSMOW/SLAP scale is necessary (van Geldern and Barth, 2012). These three steps, memory- and drift-correction as well as normalisation, are usually referred to as the post-run correction.

Over the last decade, several calibration protocols have been developed using different measurement methods (e. g., different numbers of injections per sample) and post-run corrections (e. g., van Geldern and Barth, 2012; Gröning, 2018; Münch, 2021), highlighting the need for more accurate measurements. During the preparation of this thesis, different sample treatments and calibration protocols were tested and analysed regarding the number of injections per sample and different post-run corrections. The evaluation is partly presented in Braun (2019). Further description of the detailed results is beyond the scope of this thesis but shall be published in the future.

Measuring snow accumulation

The underlying principle for the use of stable water isotopologues from ice cores is the successive deposition of snow crystals on the surface of ice sheets (Fig. 1.1b). Hence, a detailed understanding of the accumulation history is necessary to account for potential biases during the signal imprint and preservation within the archive.

Current approaches to quantify snow accumulation on ice sheets cover a wide range of spatial and temporal scales. Remote sensing products and ground-penetrating radar surveys provide a large spatial coverage but lack the small-scale spatial resolution desired for local studies (van der Veen and Bolzan, 1999; Rignot and Thomas, 2002; Arthern et al., 2006; Herzfeld et al., 2021). Firn and ice cores provide long-term estimates of accumulation rates but are restricted to one sampling point. Similarly, sonic snow height sensors offer high

temporal resolutions but measure only a single point. Lines and grids of snow stakes allow a high temporal and spatial resolution and are easy to operate, but are limited to manual readings of personnel in the field (Kuhns et al., 1997; Mosley-Thompson et al., 1999; Schlosser et al., 2002). Laser scanner (e. g., Picard et al., 2016, 2019) and Structure-from-Motion (SfM) methods are used to obtain snow height data on scales from centimetres to kilometres. Both are nowadays often used methods for glaciological questions (e. g., Westoby et al., 2012; Nolan et al., 2015; Picard et al., 2016; Chakra et al., 2019).

1.2 CHALLENGES OF PROXY-BASED CLIMATE RECONSTRUCTIONS

The previous paragraphs introduced archive-specific characteristics of marine sediments and polar ice sheets. Combining proxies from both archives can complement each other by providing detailed insights into climatic relationships on various spatial and temporal scales (e. g., Charles et al., 1996; Maffezzoli et al., 2021). Both archives are influenced by a multitude of different processes, which add variations independent in time and possibly unrelated to climate, to the signal. This noise limits the spatial representativity of single records and the potential to reconstruct climatic variations on short temporal scales. The specific definitions of short and local depend on the particular archive and are described as required.

In recent years, major progress in the understanding of the Earth's climate system and its response to various external and anthropogenic forcings has been achieved by the acquisition of new palaeoclimate information via research on the inherent uncertainties in proxy data (e. g., Laepple et al., 2016; Münch et al., 2016) and the timescales which are meaningful to look at (e. g., Münch and Laepple, 2018; Casado et al., 2020). The question of the highest possible temporal resolution of isotope time series from firn and ice cores as well as marine sediment cores is increasingly coming to the fore and is tackled with improved sensor-models in PSMs (Evans et al., 2013; Dee et al., 2015). Many archive-related processes are, however, still missing in these models. In the following, a selection of these processes and relevant to this dissertation is presented.

1.2.1 *The particle flux*

The deposition of the signal carrier via vertical downward fluxes, i. e., sinking of foraminifera within the water column or falling snow crystals within the atmosphere (Fig. 1.1), varies in space and time. The flux of foraminifera depends on environmental parameters and water properties, including density horizons, chlorophyll concentration, light intensity, seawater temperature and food availability (Mortyn and Charles, 2003; Kuroyanagi and Kawahata, 2004; Jonkers

and Kučera, 2015). This vertical flux can be influenced by ocean currents that can carry foraminifera and, hence, cause a lateral and thus climatic shift between the living and sinking sites (van Sebille et al., 2015). Similar processes also prevail over ice sheets. The timing and the amount of snowfall is driven by synoptic weather regimes and prevailing winds that lead to an intermittent and potentially seasonally biased snow deposition (Steig et al., 1994; Schuenemann et al., 2009; Persson et al., 2011). This variability is particularly pronounced in very dry areas with low accumulation rates, such as the East Antarctic Plateau (EAP), where a few individual events account for most of the annual accumulation (Richardson-Näslund, 2004). The flux-weighted recording in both archives results, therefore, in an undersampling of the prevailing climatic conditions which can additionally depend on the climatic state, i. e., glacial or interglacial period (e. g., Kapsner et al., 1995; Cuffey and Clow, 1997).

1.2.2 *Modifications after the initial deposition*

After the initial particle settling, processes at the surface can erode and redistribute particles in both archives, i. e., marine organisms above the seafloor and snow crystals above ice sheets. While the transport of the particles above the respective surface is archive-specific and driven by different mechanisms, i. e., internal tides, deep-sea and turbidity currents at the seafloor (Heezen, 1959; Johnson, 1972; Young and Southard, 1978) vs. creep and saltation of snow (Filhol and Sturm, 2015), the processes themselves are similar; namely erosion and redistribution. This reshuffling of snow leads to the formation of surface features, which, in turn, influence the amount and location of subsequent snow deposition. This can lead to large differences in the amount of snow as well as the location between the initial and final accumulation, i. e., stratigraphic noise (e. g., Fisher et al., 1985; Pomeroy and Jones, 1996). These modifications lead to spatial heterogeneity in the local-scale accumulation history and the signal deposition, and add non-climatic noise to proxy time series in both archives (Münch et al., 2016, 2017).

The deposited and flux-weighted climatic signal experiences further modifications. Bioturbation within the sediment, for example, leads to a net displacement of material, as introduced in Section 1.1.1. Similar to the effects of bioturbation for marine sediments, the isotope signal within the firn column is influenced by firn diffusion. The transport of vapour within the pore space between snow grains attenuates the seasonal signals and smooths the isotopic gradients. However, firn diffusion is mainly restricted to the firn column above the pore close-off, spatially uniform and depending on the accumulation rate, the ambient temperature and the strain rate at the respective site on an ice sheet (Whillans and Grootes, 1985; Johnsen et al., 2000).

Hence, firn diffusion can be simulated with numerical models and corrected for before interpreting ice core isotopic data (e. g., Stevens et al., 2020; Gkinis et al., 2021). In contrast, bioturbation is more variable in space and time and less predictive because it is driven by the active mixing of benthic fauna. Deeper sediment layers can still be affected by bioturbation, in particular by deep-reaching burrows penetrating down to 1 m into the sedimentary column and falsifying the age estimate at a specific depth (Löwemark and Werner, 2001; Löwemark and Grootes, 2004). Since bioturbation is often characterised by variability in the strength and extent of mixing, the distortion of the chronological sequence manifests in temporal offsets (Bard et al., 1987), low signal-to-noise ratios (SNRs) in reconstructed time series, low correlations of nearby records (Reschke et al., 2019b, 2021) and a reduced amplitude of the climate variability (Schiffelbein, 1985; Anderson, 2001).

Besides firn diffusion, isotopic exchange between the snow and the atmosphere during sublimation, condensation, metamorphism and firn ventilation is increasingly observed to substantially modify the imprinted signal after the initial deposition, especially during precipitation-free summer periods (Town et al., 2008; Ebner et al., 2017; Wahl et al., 2021). However, this process is still subject of ongoing research and the contributions of snowfall, depositional (snowdrift) and post-depositional (vapour-snow exchange) modifications to the final signal are not quantified yet (Steen-Larsen et al., 2014; Casado et al., 2021). It could increase the signal content by continuously imprinting the prevailing temperature into the snow and firn column, or reduce the significance of the flux-weighted signal by adding a non-linear factor; however, due to their small magnitude, these processes are difficult to quantify.

1.2.3 *Sampling and measurement uncertainty*

Besides the presented uncertainties introduced during the signal formation, i. e., deposition and imprint, additional errors can stem from an unrepresentative physical sampling from an inherent heterogeneous archive or can be introduced during the measurement process.

The probability of a sample's age to represent the true mean age of the respective depth layer is affected by the archive-internal heterogeneity in oxygenated marine sediments. This is especially pronounced when age estimates are based on small numbers of individual signal carriers or from small sample volumes because they are more strongly affected by the net displacement of sedimentary material (Schiffelbein and Hills, 1984; Kunz et al., 2020; Dolman et al., 2021b). Besides the archive-internal heterogeneity, fewer individuals per sample also increase the measurement uncertainty, even though instrument developments have greatly improved the accuracy and

reduced the measurement errors (Wacker et al., 2010, 2013). The instrumental analytical error increases with a decreasing radiocarbon content; thus, older samples have larger uncertainties (Andree, 1987). Additionally, the raw ^{14}C values require a calibration to calendar age (Heaton et al., 2020) and potentially also a correction for the ocean's carbon reservoir age (Alves et al., 2018). Both corrections introduce an additional error to the final data point which has to be accounted for (Hajdas et al., 2021). It is important to know and consider these uncertainties for both, the analysis of reconstructed time series as well as modeling approaches.

The list of applications to measure the snow height is long, but they have only rarely been used to assess the characteristics of snow accumulation (e. g., Albert and Hawley, 2002; Picard et al., 2019). Combinations of snow height information with isotopic data sets can provide insights into the two-dimensional view of stable water isotopologues (Münch et al., 2016) and help to quantify potential post-depositional modifications. This further requires accurate isotope measurements to overcome the inherent heterogeneity in snow. IRMS and CRDS instruments have their individual advantages and drawbacks. A suitable measurement method and post-run correction might depend on the aim of a study, the required accuracy, financial possibilities and time constraints. The variety of available measurement protocols and post-run corrections presented in Section 1.1.2 hints to many potential parameters to reduce the measurement uncertainties which are, however, not fully explored yet. Comprehensive sampling designs that combine observations of snow deposition with isotopic data are rare, but would greatly improve the understanding of the processes acting during the signal formation at and beneath the snow surface.

1.3 OBJECTIVES AND OVERVIEW OF THE THESIS

Based on the presented challenges, the following scientific questions have evolved and are addressed in this thesis:

- How can we measure and characterise the heterogeneity in sedimentary palaeoclimate archives?
- How heterogeneous are sedimentary archives and at what spatial scale?
- What processes determine the signal formation and preservation as well as the spatial heterogeneity of the archive?
- How can the reliability of proxy-based climate reconstructions from sedimentary archives be improved?

Designed as a cumulative thesis, this dissertation comprises of three parts, presenting **(1)** a general introduction and theoretical

background (Chapter 1), **(2)** the main part which consists of three independent research articles from international peer-reviewed journals (Chapters 2 to 4) and two additional articles with co-author contributions (Appendix A and B), as well as **(3)** a general discussion answering the above-mentioned research questions (Chapter 5).

Chapter 2 analyses the three-dimensional age-heterogeneity in several sub-cores from a box-core from the South China Sea (SCS) based on radiocarbon data from foraminiferal tests. Three different sampling schemes are performed with different sample volumes and varying numbers of measured specimen. In addition, visual analyses of X-ray radiographs confirm the indicated strong sediment mixing without a clear separation between the mixed and historical layer, as assumed in simple mixing models. Besides a decreasing mixing intensity with depth and considerable contribution of deep-reaching burrows to the overall archive-internal heterogeneity, the study shows that previously assumed error terms underestimate the uncertainty by a factor between two and five on the depth and age scale, respectively. This Chapter is cited as Zuhr et al. (2022a) throughout the thesis.

Chapter 3 presents the application of a SfM photogrammetry approach that provides near-daily Digital Elevation Models (DEMs) of the snow surface at the East Greenland Ice-Core Project (EGRIP) campsite. Besides an evaluation of the method for applications in glacial environments, the SfM method gives insights into the snow surface evolution over a three-month period. DEM-derived snow height information reveal spatial and temporal precipitation intermittency associated with wind-driven erosion and redistribution of snow. The hereby created heterogeneity is illustrated with a two-dimensional view of the internal snowpack structure. Both the strong intermittency of snowfall and the internal varying layer thickness emphasise the event-based imprint of the climatic signal and the substantial modifications due to wind-driven post-depositional changes of the snow surface. Throughout the thesis, this Chapter is cited as Zuhr et al. (2021a).

Chapter 4 provides insights into the buildup of the stable water isotopic signal in the upper firn column for a two-month periods at the EGRIP campsite. The combination of near-daily snow height information, using the established SfM approach, with repeated snow sampling of the upper 30 cm of the snow column along a 40 m transect reveals that the observed isotopic signal is to a first order imprinted via snowfall. The unique data set additionally shows that the surface stratigraphic noise is transferred and preserved in deeper layers with spatial isotope variability persisting throughout the observation period. This Chapter is cited as Zuhr et al. (2022b) throughout the thesis.

Chapter A presents laboratory experiments and field measurements at EGRIP which investigate the role of sublimation on the isotopic signature in surface snow during precipitation-free periods. An increase in $\delta^{18}O$ and a decrease in d-excess is observed and related to sublimation and kinetic fractionation within the snow surface. In both setup, changes in the isotope signature are influenced by both sublimation and vapour deposition. The study, therefore, postulates that the snow surface isotopic signature does not only represent the condensation temperature in a cloud but also incorporates the atmospheric signature between precipitation events by moderate post-depositional modifications. Throughout the thesis, this Chapter is cited as Hughes et al. (2021).

Finally, Chapter B analyses the isotopic exchange between atmospheric water vapour and surface snow based on field observations at the EGRIP campsite and modelling approaches. Daily surface snow samples are jointly analysed with observations of the vapour isotopic composition for two consecutive summer seasons. During both periods, the latent heat flux suggests a positive net sublimation flux from the surface towards the atmosphere which is confirmed with a simple model. Throughout the thesis, this Chapter is cited as Wahl et al. (2022).

For consistency, the layout of some figures and tables has been adjusted. Additionally, the spelling has been changed from American to British English, but in none of the cases was the original content changed.

1.4 AUTHOR CONTRIBUTIONS TO THE MANUSCRIPTS

This section provides detailed information on the first-author research articles included in this thesis as well as the contributions as co-author to two additional publications in the Appendix.

First-author publications

Chapter 2: *Age-heterogeneity in marine sediments revealed by three-dimensional high-resolution radiocarbon measurements (Zuhr et al., 2022a)*: T. Laepple and S. L. Ho designed the study. C.-C. Su performed the fieldwork with the help of the crew of the research vessel OR1. A. M. Zuhr and S. L. Ho did the subsampling at the Institute of Oceanography, Taiwan, and J. Groeneveld and H. Grotheer carried out the picking of specimens and measuring of samples. C.-C. Su performed the X-ray measurements and L. Löwemark the analysis of the radiograph images. A. M. Zuhr performed the statistical analysis with help from A. M. Dolman and T. Laepple. All co-authors contributed with their specific expertise to the interpretation of the data. A. M.

Zuhr prepared the manuscript with contributions from all co-authors.

Chapter 3: *Local-scale deposition of surface snow on the Greenland ice sheet (Zuhr et al., 2021a)*: T. Laepple, T. Münch, M. Hörhold, and H.C . Steen-Larsen designed the study. A. M. Zuhr and H. C. Steen-Larsen carried it out. A. M. Zuhr generated the digital elevation models and performed the analyses. A. M. Zuhr prepared the manuscript with contributions from all co-authors.

Chapter 4: *A snapshot on the buildup of the stable water isotopic signal in the upper firn column (Zuhr et al., 2022b)*: T. Laepple, M. Hörhold, H. C. Steen-Larsen and A. M. Zuhr planned the study. H. C. Steen-Larsen, S. Wahl and A. M. Zuhr conducted the fieldwork. H. Meyer supervised the measurement of the isotopic data in the Stable Isotopes Facility at the Alfred Wegener Institute in Potsdam, Germany. A. M. Zuhr performed the data analysis with the help of T. Laepple. A. M. Zuhr wrote the original draft with contributions from T. Laepple. All authors reviewed and edited the final manuscript.

Publications with co-author contributions

Chapter A: *The role of sublimation as a driver of climate signals in the water isotope content of surface snow: laboratory and field experimental results (Hughes et al., 2021)*: A. G. Hughes and H. C. Steen-Larsen designed the laboratory and field setup and experiments. A. G. Hughes carried out the experiments with significant contributions from H. C. Steen-Larsen. S. Wahl and A. M. Zuhr assisted with field snow sampling, and M. Hörhold assisted with materials and production ideas of the laboratory experimental chamber. A. G. Hughes wrote the article with significant contributions from H. C. Steen-Larsen, T. R. Jones, and S. Wahl and edits from all authors.

Chapter B: *Atmosphere-Snow Exchange Explains Surface Snow Isotope Variability (Wahl et al., 2022)*: S. Wahl and H. C. Steen-Larsen conceputalised the study. Data curation was performed by M. Behrens, M. Hörhold, H. C. Steen-Larsen, S. Wahl and A. M. Zuhr. H. C. Steen-Larsen, S. Wahl and A.-K. Faber designed the methodology and S. Wahl, H. C. Steen-Larsen, L. J. Dietrich and A. G. Hughes carried out the data analysis. S. Wahl created the visualisations and wrote the original draft with contributions from H. C. Steen-Larsen. All authors contributed to the final draft.

2

AGE-HETEROGENEITY IN MARINE SEDIMENTS REVEALED BY THREE-DIMENSIONAL HIGH-RESOLUTION RADIOCARBON MEASUREMENTS

Alexandra M. Zuhr[1,2], Andrew M. Dolman[1], Sze Ling Ho[3], Jeroen Groeneveld[4], Ludvig Löwemark[5], Hendrik Grotheer[6], Chih-Chieh Su[3] and Thomas Laepple[1,7]

[1] Alfred-Wegener-Institut Helmholtz Zentrum für Polar- und Meeresforschung, Research Unit Potsdam, Potsdam, Germany
[2] Institute of Geosciences, University of Potsdam, Potsdam, Germany
[3] Institute of Oceanography, National Taiwan University, Taipei, Taiwan
[4] Institute for Geology, University of Hamburg, Hamburg, Germany
[5] Department of Geosciences, National Taiwan University, Taipei, Taiwan
[6] Alfred-Wegener-Institut Helmholtz Zentrum für Polar- und Meeresforschung, Research Unit Bremerhaven, Bremerhaven, Germany
[7] University of Bremen, MARUM – Center for Marine Environmental Sciences and Faculty of Geosciences, Bremen, Germany

This chapter is published in:
Frontiers in Earth Science - Marine Geoscience, DOI: 10.3389/feart.2022.871902, 2022.

Abstract. Marine sedimentary archives are routinely used to reconstruct past environmental changes. In many cases, bioturbation and sedimentary mixing affect the proxy time-series and the age-depth relationship. While idealized models of bioturbation exist, they usually assume homogeneous mixing, thus that a single sample is representative for the sediment layer it is sampled from. However, it is largely unknown to which extent this assumption holds for sediments used for palaeoclimate reconstructions.

To shed light on (1) the age-depth relationship and its full uncertainty, (2) the magnitude of mixing processes affecting the downcore proxy variations, and (3) the representativity of the discrete sample for the sediment layer, we designed and performed a case study on South China Sea sediment material which was collected using a box corer and which covers the last glacial cycle. Using the radiocarbon content of foraminiferal tests as a tracer of time, we characterise the spatial age-heterogeneity of sediments in a three-dimensional setup. In total, 118 radiocarbon measurements were performed on defined small- and large-volume bulk samples (~200 specimens each) to in-

vestigate the horizontal heterogeneity of the sediment. Additionally, replicated measurements on small numbers of specimens (10 x 5 specimens) were performed to assess the heterogeneity within a sample volume.

Visual assessment of X-ray images and a quantitative assessment of the mixing strength show typical mixing from bioturbation corresponding to around 10 cm mixing depth. Notably, our 3D radiocarbon distribution reveals that the horizontal heterogeneity (up to 1,250 years), contributing to the age uncertainty, is several times larger than the typically assumed radiocarbon based age-model error (single errors up to 250 years). Furthermore, the assumption of a perfectly bioturbated layer with no mixing underneath is not met. Our analysis further demonstrates that the age-heterogeneity might be a function of sample size; smaller samples might contain single features from the incomplete mixing and are thus less representative than larger samples. We provide suggestions for future studies, optimal sampling strategies for quantitative palaeoclimate reconstructions and realistic uncertainty in age models, as well as discuss possible implications for the interpretation of palaeoclimate records.

2.1 INTRODUCTION

Proxy data from climate archives have been used for decades to reconstruct climate beyond the instrumental period. The information of past temperatures is, for example, stored in the $\delta^{18}O$ and the Mg/Ca-ratio in calcite shells of organisms (e. g., foraminifera) embedded in marine sediments (e. g., Nürnberg et al., 1996; Lea, 2014). These shells are produced in the water column, rain down on the ocean seafloor, accumulate over time and build a continuous archive with deeper layers representing earlier times. For the interpretation of the recorded environmental parameters via palaeoclimate proxies, a reliable conversion from depth to age is necessary. For material from the past 55,000 years, the measured radiocarbon content can be interpreted as a tracer of time since deposition (Libby et al., 1949; Blaauw and Heegaard, 2012; Heaton et al., 2021). To this end, the ratio of $^{14}C/^{12}C$ (in the following, we only refer to ^{14}C) of carbon-containing sedimentary material, e. g., the calcite shell of foraminifera, is typically measured from several depth layers along a sediment core. These discrete age estimates are then interpolated by applying statistical methods to obtain a continuous depth-age scale for the entire sedimentary archive (Bard et al., 1987; Bronk Ramsey, 2008; Blaauw and Christen, 2011).

In oxygenated sediments that form the bulk of the marine sedimentary archives used for palaeoclimate reconstruction, the deposited material is mixed by burrowing and feeding activities of the benthic fauna in the upper layer of sediment (Berger et al., 1979; Savrda and Bottjer, 1991; Casanova-Arenillas et al., 2022). As the rate of biological

mixing, i. e., the bioturbation, is usually large compared to the sediment accumulation rate, the sediment becomes well mixed before it is eventually buried below the mixed layer (Figure 2.1A) (Berger and Heath, 1968). This mixing considerably modifies the sequence of recorded environmental properties and a down-core proxy time series represents only a smoothed version of the true climatic and temporal history (Goreau, 1980; Schiffelbein and Hills, 1984; Bard et al., 1987). Sediments from the same depth layer therefore contain a mixture of relocated younger and older material which complicates the interpretation of proxy variables, as well as the determination of the age of a sediment layer; the latter because measurements are performed on a finite number of specimens which may not be representative of the true mean age and proxy value of the layer (e. g., Lougheed et al., 2018; Dolman et al., 2021a).

Simple quantitative descriptions of the mixing (Berger and Heath, 1968; Berger and Killingley, 1982) assume a complete and instantaneous mixing of the sediment down to a fixed depth, and no further mixing below (Figure 21A). Under this assumption, the degree of smoothing affecting the archived climate record and the expected variations between age-determinations from different samples from the same sediment layer are well studied (e. g., Goreau, 1980; Dolman et al., 2021a).

In reality, the intensity of mixing might vary which would lead to non-uniform and incomplete mixing. Furthermore, secondary modifications by trace fossils of different sizes, such as *Chondrites*, *Planolites*, *Thalassinoides*, *Scolicia* and *Zoophycos*, result in vertical and horizontal variability as well (Figure 2.1B and C) (e. g., Dorador et al., 2020; Casanova-Arenillas et al., 2022). The impacts within the sediment are deep-reaching burrows and spreiten with fillings different from the surrounding sediment leading to considerable horizontal differences in age estimates on local (intra-sample, mm- to cm-scale) and regional (between different samples and cores, m- to km-scale) spatial scales (Anderson, 2001; Bard, 2001; Löwemark and Werner, 2001; Lougheed et al., 2020). These post-depositional modifications can be visualized and analysed with X-ray images highlighting the magnitude of sediment heterogeneity (e. g., Löwemark and Werner, 2001; Löwemark et al., 2008; Trauth, 2013).

For a quantitative use of palaeoclimate records, especially for large-scale compilations (e. g., Marcott et al., 2013), model-data comparisons (e. g., Laepple and Huybers, 2014) or data assimilation (e. g., Osman et al., 2021), the uncertainties and distortions in the proxy record and age-model have to be known. Here, proxy-system models (Evans et al., 2013; Dee et al., 2017; Dolman and Laepple, 2018) or analytical error models (Kunz et al., 2020; Dolman et al., 2021b) can be used if the processes contributing to the signal formation are known. Analysing global compilations of Holocene and Glacial ma-

rine records, Reschke et al. (2019a,b) showed that the correlation of nearby proxy records is very low compared to the expectations from climate models, and that this cannot be explained by the classical age model uncertainty estimates derived from radiocarbon measurement and calibration. One hypothesis for this low correlation is that the true uncertainty of the age model may be larger due to heterogeneity in the sediment. Such a strong effect of archive heterogeneity was previously found in other climate archive types, e. g., ice cores from polar ice-sheets (Münch and Laepple, 2018).

In the quest of a full characterization of sediment mixing and age uncertainty, recent developments of ultra-small sample radiocarbon dating techniques (e. g., $< 100\,\mu g\ CaCO_3$) provide an important tool. They allow the measurement of the age of individual or small numbers (< 10) of specimens (Wacker et al., 2010, 2013). This information can be used to quantify the within-sample variability, i.e. the spread between the youngest and the oldest material, at one depth (Lougheed et al., 2018; Fagault et al., 2019; Lougheed et al., 2020; Dolman et al., 2021a).

Here we characterise the heterogeneity and the factors contributing to the age uncertainty of sedimentary archives by generating radiocarbon data using nine replicate cores extracted from a single boxcore, thereby affording a 3-dimensional view on the ^{14}C variability within a 24 x 24 x 34 cm volume. This allows us to estimate the bioturbational mixing and the sediment heterogeneity and to infer the full age model uncertainty accounting for these effects. Finally, we discuss possible implications of the age-heterogeneity on palaeo reconstructions and provide suggestions for an optimal sampling scheme targeted to bioturbated sediments.

2.2 METHODS

2.2.1 *Study approach*

To quantify and characterise the sediment heterogeneity affecting palaeo-environmental reconstructions from marine archives, we study an oxygenated marine sediment core retrieved from the southern South China Sea using a box corer (Figure 2.2A, 10° 54.0262′ N, 115° 18.4611′ E, 2,208 m water depth), enabling the analysis of the three-dimensional (24 x 24 x 38 cm) spatial distribution of ages. The South China Sea core location was chosen because this region is characterised by sediments with medium to high carbonate concentrations (e. g., Broecker et al., 1988b; Broecker et al., 1988a; Sarnthein et al., 1994) and reported bioturbational activities (e. g., Wetzel, 2002; Löwemark and Grootes, 2004; Wetzel, 2008); both can be seen as representative for many deep sea sediment cores and are therefore suitable for a pilot study on age-heterogeneity. The sediment consists

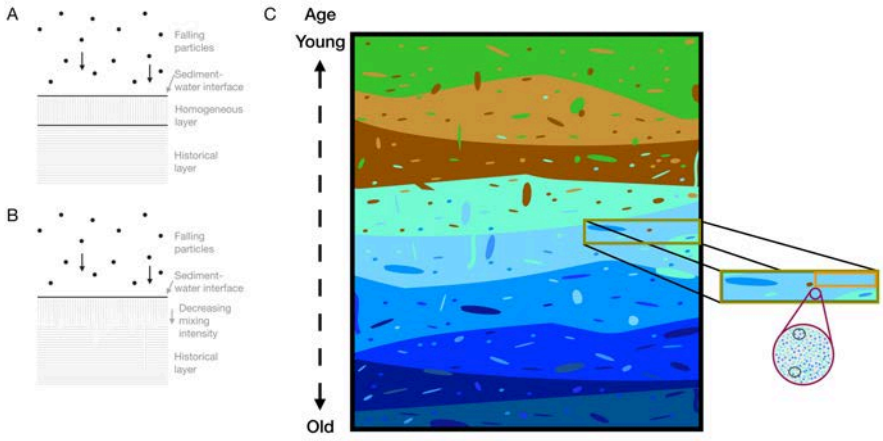

Figure 2.1: Conceptual sketches of mixing processes and sediment heterogeneity in a marine environment. Following the traditional terms of the mixed and the historical layer, **(A)** shows a well-defined boundary between both layers while **(B)** shows more dynamic mixing processes including deep reaching burrows. **(C)** illustrates a potential two-dimensional view of the heterogeneous distribution of consistently increasing ages with depth. The panels on the right hand side show a zoom into local age-heterogeneity. Coloured dots and areas indicate marks from mixing of fine materials, fossils and other detrital components.

of beige and light brown silty foraminiferal ooze which provides sufficient material for this extensive study with the need of many specimens in a finite volume.

We use the radiocarbon content in foraminiferal tests as a proxy of time since deposition. Following the different intensity and spatial extent of mixing and burrowing activities, the vertical and horizontal heterogeneity, which is a result of reworking by e. g., bottom currents and the displacement of foraminifera shells by benthic fauna (Figure 2.1B), might vary on different spatial dimensions from millimetres to decimetres. To guide our sampling strategy and interpretation, we posit that the overall age-heterogeneity can be described by the two terms defined below and illustrated in the idealized sketch of a two-dimensional sediment slice (Figure 2.1C).

1. The term **mixing** is used here as a description of the heterogeneity within a sample, i.e. the variations between individual specimens in a finite volume, which is the result of the uniform mixing over a certain depth interval. This in-sample heterogeneity can be overcome by measuring a large number of specimens.

2. The horizontal heterogeneity in the mean age can be thought of as a **net displacement** of the sediment. It describes the deviation of a sample from the mean age-depth relationship. In addition

to the process of mixing, this is also dependent on the sediment accumulation rate and the presence of trace fossils and resulting post-depositional modifications.

2.2.2 *Core setup and sampling*

The sediment core OR1-1218-C2-BC was taken in March 2019 onboard the research vessel Ocean Researcher 1 (OR1). The sediment consists of beige and light brown silty foraminiferal ooze. The core was directly divided into twelve sub-cores onboard the ship by pushing plastic tubes into the sediment (Figure 2.2B). Here, the sub-cores OR1-1218-C2-BC-1 to 9 (in the following we only refer to sub-cores 1 to 9) were analysed. The oxygen content of the core was not measured, but the number of fossil traces indicates oxygen-rich conditions (Savrda, 2007). The subsequent sampling was performed in the PaleoProxy Lab at the Institute of Oceanography, National Taiwan University, Taipei, Taiwan. From each sub-core, a thin slab with 1 cm thickness along the length of the core was taken for X-ray radiography before the sub-cores were split into smaller samples. The sub-cores 1 to 5 were vertically sampled in 2 cm thick slices and the sub-cores 6 to 9 in 1 cm slices. The sub-cores 7 to 9 were additionally horizontally split into two parts, A and B (Figure 2.2C). All samples were freeze-dried, wet-sieved through a 63 µ mesh and dried at 50 °C before foraminiferal tests were picked. All analyses were based on the most abundant planktonic foraminiferal species *Trilobatus sacculifer* (*T. sacculifer*, without sac-like final chamber, 315 - 355 µm size fraction).

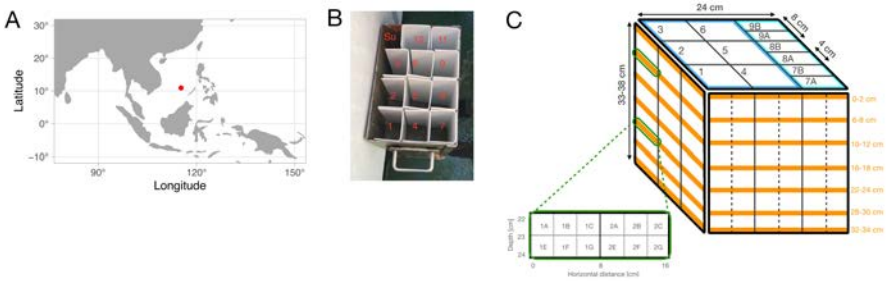

Figure 2.2: Location and setup of the boxcore OR1-1218-C2-BC. **(A)** Sampling location of the boxcore in the South China Sea. **(B)** Photo of the setup and the plastic tubes (courtesy of Yu-Huang Chen), the sub-cores 11 and 12 are not analysed. **(C)** Schematic overview of the individual samples analysed from the boxcore. Within each sub-core, seven depth layers were sampled for radiocarbon analyses (orange layers): 0 - 2, 6 - 8, 10 - 12, 16 - 18, 22 - 24, 28 - 30 and 32 - 34 cm. A detailed overview of the sample sizes is given in Table 2.1. Sub-core 1 was further used for small sample analyses, and together with sub-core 2 for small-volume bulk sample measurements (22 - 23 and 23 - 24 cm, green excerpt).

The sub-cores extracted from the box core were of different lengths, ranging between 33.5 and 38 cm (Table 2.1). We restricted the measurements to a maximum depth of 34 cm for all but sub-core 1, on which the first ^{14}C measurements were performed with 130 and 165 specimens for the depths from 0 - 1 and 36 - 37 cm, respectively, to estimate the age range covered by the core. Additionally, three replicates with 200 specimens from the depth of 36 - 37 cm from sub-core 1 were measured for a preliminary estimate of the sediment mixing intensity.

Table 2.1: Overview of different parameters from the sub-cores 1 to 9: lengths of the individual sub-cores, the measured horizontal and vertical sample size and the resulting volume for each large-volume bulk sample.

Sub-core	Length [cm]	Horizontal [cm]	Vertical [cm]	Volume [cm^3]
1	37	8x8	2	128
2	38	8x8	2	128
3	35	8x8	2	128
4	36.5	8x8	2	128
5	37	8x8	2	128
6	38	8x8	2	128
7A	33.5	4x8	2	64
7B	33.5	4x8	2	64
8A	33.5	4x8	2	64
8B	33.5	4x8	2	64
9A	35	4x8	2	64
9B	35	4x8	2	64

The sampling was divided into three types with the aim to investigate the afore-described processes which cause age-heterogeneity between individual specimens as well as among samples. The types differ in terms of the number of picked and measured specimens as well as the volume of the samples:

- **Large-volume bulk samples.** The age of the seven depth layers from each of the twelve sub-cores (indicated in orange in Figure 2.2C) was determined with samples based on volumes of 128 cm^3 (= 2 x 8 x 8 cm) for the sub-cores 1 to 6 and 64 cm^3 (= 2 x 4 x 8 cm) for the sub-cores 7A to 9B (Table 2.1). From each sample, 200 foraminiferal tests were picked, gently crushed and well mixed, so that each aliquot of the sample would contain

material from a large proportion of the individuals, and thus would reflect the mean age of the sample. The crushing and mixing is important as only about one-third of each sample (~800 µg $CaCO_3$) was used for each ^{14}C measurement in order to have remaining material for either a replicate measurement or a measurement of another proxy from the same batch of individuals (e.g. $\delta^{18}O$). These age estimates based on large-volume bulk samples are used to quantify spatial patterns of net vertical displacement of sediment leading to horizontal variation in the mean age.

- **Small-volume bulk samples.** From sub-core 1 and 2, small-volume samples with a volume of 1.8 cm^3 (= 1 x 1.8 x 1 cm) were taken from thin slabs for two depth layers (22 - 23 and 23 - 24 cm, indicated in green in Figure 2.2C zoom-in). As for the large-volume bulk samples, 200 specimens were picked, crushed and about one third of each sample (~800 µg CaCO3) was used for radiocarbon measurements. These data are used to test whether the net displacement depends on the spatial scale and thus the sample volume.

- **Small-n samples.** Ten replicates of five specimens were measured for the depth layers 6 - 8 and 36 - 37 cm from sub-core 1. In contrast to the 200 foraminifera samples, which are intended to average out the variation between individuals in a sample so that differences between distinct sediment volumes can be measured, these small-n samples are used to determine the within-sample age-heterogeneity and the vertical extent of the mixing. Samples from two different depths were used to test whether the mixing changed along the core and over time. However, the upper depth might be less reliable because it lies within the actively mixed layer.

All measurements were performed with an accelerator mass spectrometer Mini Carbon Dating System (MICADAS) equipt with a Carbonate Handling System (CHS) and Gas Interface System (GIS) at the Alfred Wegener Institute in Bremerhaven, Germany (Wacker et al., 2010; Mollenhauer et al., 2021). All samples were prepared and measured as gas targets following the standard operating procedures described by Mollenhauer et al. (2021). Briefly, all samples were weighed into 4.5 ml septum sealed vials, loaded into the CHS and flushed with ultra-pure helium for 5 minutes with 70 mL/min to remove all traces of atmospheric CO_2 using a two-way needle. After addition of 200 µL phosphoric acid (H_3PO_4, ⩾85 %, Fluka 30417) the hydrolyzation reaction took place over ~30 minutes at 70 °C. Following complete hydrolysis, sample CO_2 was flushed from the vial for 1 minute at 70 mL min^{-1} He flow and passed over a phosphorus pentoxide trap

to remove water vapor. CO_2 was subsequently concentrated on the zeolith trap of the GIS, quantified manometrically and fed into the ion source. Radiocarbon data were normalised against standard gas (CO_2 produced from NIST Oxalic Acid II, NIST SRM4990C) and blank corrected against sample size-matched blank foraminifera (pre-Eemian age) processed alongside the samples (Mollenhauer et al., 2021).

All radiocarbon data were calibrated and converted to calendar ages based on the Marine20 calibration (Heaton et al., 2020) using the R package Bchron (Haslett and Parnell, 2008; R version 4.0.3, R Core Team, 2020). We used the default reservoir age provided in Marine20 and did not adjust for local marine reservoir effects because we are only comparing relative, and not absolute ages.

Besides the processes affecting the signal prior to the core extraction, a number of steps during the sampling can also result in biases. A tilted incline of the corer at the seabed can result in skewed layers within the core and can lead to differences in derived parameters from different sides of the core especially when compared by sediment depth. Additional biases can arise from an imprecise manual sampling of single layers and from the preferential preservation of younger specimens due to their shorter residence time in the sediment compared to older counterparts. We carefully examined our data set with respect to the described errors by analyzing the difference in age between different sides of the core. We did not find any indication for biases in the core retrieval, the manual sampling or the preferential preservation of younger specimens.

2.2.3 *Estimation of the sediment accumulation rate*

The sediment accumulation rate is derived from a simulation with the depth-age model BACON (Blaauw and Christen, 2011) using a vertical resolution of 1 cm and the Marine20 calibration curve (Heaton et al., 2020) to convert raw ^{14}C data to calendar ages. We use all radiocarbon data for this approach, with the small-volume bulk samples and the small-n samples averaged for their respective depths.

2.2.4 *Estimation of the sediment mixing strength*

The variation in age between individual foraminifera from the same depth, σ_{ind}, can be used as a measure of the sediment mixing strength. As our current analytical capabilities do not allow us to measure the radiocarbon content of a single *T. sacculifer* test, we instead measure ^{14}C on samples of 5 individuals, and rescale the variance between them following Dolman et al. (2021a). To obtain σ_{ind} from σ_{rep} we first subtract the measurement error variance, σ_{meas}, before multiplying by the number of individual specimens, n_f, and taking the square root. σ_{meas} includes the reported measurement

error and the additional uncertainty from the calibration to calendar age.

$$\sigma_{ind} = \sqrt{n_f \left(\sigma^2_{rep} - \sigma^2_{meas}\right)} \tag{21}$$

If σ_{ind} is rescaled using the sediment accumulation rate, it represents the average distance that individual particles have been moved by mixing, and in a simple 1-box mixing model, it can be thought of as the mixing depth (e. g., Berger and Heath, 1968).

2.2.5 *Estimation of the net sediment displacement*

The variations in derived ^{14}C ages from the small- and large-volume bulk samples are used to describe the net sediment displacement, i. e., the effect of the spatially non-uniform mixing on the mean age of a sample. We evaluate this by analyzing the deviations of the individual age estimates to the respective mean of each depth layer corrected for the expected variations due to the large but still finite sample size. To only study the effect of the net displacement, we subtract the variations caused by the measurement error and the calibration as well as from the finite sample size.

2.2.6 *Visual assessment of mixing*

Radiograph images were taken from the thin slabs at the Institute of Oceanography at the National Taiwan University, Taipei, Taiwan, and are, together with optical photographs, used to qualitatively determine the mixing extent and intensity. Both types of images allow a visual inspection of the mixing conditions and a separation between homogeneously mixed material with a mottled appearance and the historical layer with potential deep reaching burrows (e. g., Löwemark and Werner, 2001; Löwemark, 2015).

2.3 RESULTS

In the following, we present the results of the individual ^{14}C measurements, grouped by sampling approach as described in section 2.2.2. We then derive the sediment accumulation rate (section 2.3.2) as well as the extent (section 2.3.3) and the spatial structure of the mixing (section 2.3.4) before describing different error terms affecting the reliability of derived age estimates (section 2.3.5).

2.3.1 *Radiocarbon measurements*

2.3.1.1 *Large-volume bulk samples*

The youngest calibrated ^{14}C age estimate from the large-volume bulk samples is 1,803 yrs (years) ($\pm$109 yrs 1 standard deviation (SD) measurement error), while the oldest sample has an age of 18,333 yrs ($\pm$226 yrs). The horizontal standard deviations (σ_{cores}) in each depth layer vary between 471 (22 - 24 cm) and 1,354 yrs (32 - 34 cm). Generally, the range of ages, the standard deviations within a depth layer and the measurement errors (σ_{meas}) increase with sediment depth and age (Figure 2.3, Table 2.2).

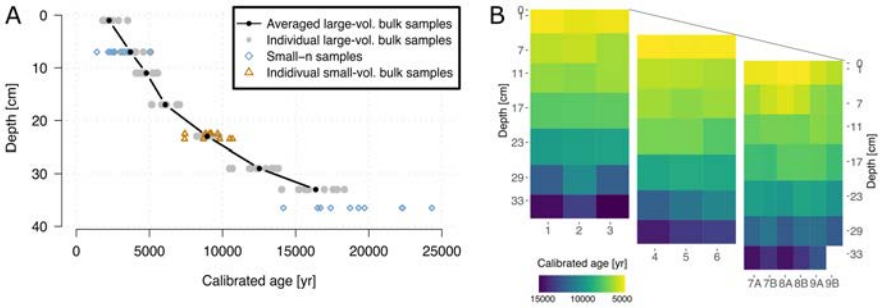

Figure 2.3: Depth-age illustrations for calibrated radiocarbon ages. **(A)** Calibrated ages for the large-volume bulk samples are shown with grey points and their respective mean per depth layer illustrated in black. Measurement errors for single data points are not displayed due to their small magnitude. The blue diamonds are age estimates based on small-n samples while the golden triangles show ages from the small-volume bulk samples. **(B)** Absolute calibrated calendar ages from the large-volume bulk samples are illustrated for each sub-core and arranged according to the subsampling of the core to illustrate the three dimensions (see Figure 2.2B).

2.3.1.2 *Small-volume bulk samples*

To investigate whether and how the net displacement varies in space, we analysed the horizontal variations in the small-volume bulk samples (1.8 cm^3). The mean ages of the small-volume samples are similar to those of the large-volume bulk samples from their respective depth and sub-core, and agree within the standard error. However, the small-volume samples show a significantly higher variance than the large-volume samples (golden triangles vs. grey points, Figure 2.3A, F-test with $p = 0.01$) with a SD of 1,089 yrs for the small-volume samples compared to 471 yrs for the large-volume samples, despite being based on measurements with the same number of foraminiferal tests.

Table 2.2: Overview of calibrated calendar ages derived from the ^{14}C measurements of the low- resolution bulk samples. For each depth interval (in cm), the mean age (μ_{lowres}), the standard deviation (σ_{cores}), the total range ($z = max_{age} - min_{age}$) as well as the mean measurement error (σ_{meas}) of all twelve subcores (see Table 2.1) are given in years. For the layer from 32 - 34 cm, the data point from sub-core 9B had to be removed due to reported problems during the measurement and is not included in the analyses.

Depth	μ_{low}	σ_{cores}	z	σ_{meas}
0 - 2	2,241	503	1,710	114
6 - 8	3,703	681	2,485	118
10 - 12	4,791	524	1,505	139
16 - 18	6,086	611	1,919	122
22 - 24	8,954	471	1,539	149
28 - 30	12,523	1,125	3,345	187
32 - 34	16,373	1,354	4,289	237

2.3.1.3 *Small-n samples and age heterogeneity*

To infer the age-heterogeneity within a sediment sample and thus the mixing, the replicated measurements of the small-n samples from 6 - 8 and 36 - 37 cm from sub-core 1 are used. The mean age for the upper layer is 2,849 yrs with σ_{rep} of 977 yrs, and 19,140 yrs with a SD of 3,126 yrs for the deeper layer (Table 2.3, individual data points in Figure 2.3A). The inferred SD between single foraminifera, σ_{ind} (equation 21), which can be seen as an estimate for the heterogeneity in ages within a sample, is 2,184 yrs for the upper layer and 6,990 yrs for the deeper layer. The mean of the small-n samples from 6 - 8 cm is younger than the large-volume samples mean (2,849 vs. 3,703 yrs, Table 2.2), but this difference is not statistically significant.

Table 2.3: Replicated ^{14}C measurements on small-n samples from sub-core 1. The number of measured specimens n_f as well as the number of replicate measurements n_{rep} is given. μ_{rep} is the mean of replicated age estimates per depth layer, σ_{rep} the standard deviation and σ_{meas} the mean measurement error. σ_{ind} is the inferred standard deviation in age between individual samples, following Dolman et al. (2021a). All estimates are given in years.

Depth	n_f	n_{rep}	μ_{rep}	σ_{rep}	σ_{meas}	σ_{ind}
6 - 8	5	10	2,849	977	139	2,184
36 - 37	5	10	19,140	3,126	299	6,990

2.3.2 *Sediment accumulation rate*

With an average age of 2,241 yrs for the top layer and 19,140 yrs for the lowest measured layer (36 - 37 cm), the sediment core covers the Holocene and the last glacial termination. The sediment accumulation rate was determined using the BACON model (Blaauw and Christen, 2011). To obtain estimates at a spatial scale comparable to the extent of mixing, we applied a running mean with a width of 10 cm to the derived accumulation rate model. For the upper part of the core (10 - 18 cm, disregarding the mixed layer), the model suggests an average sediment accumulation rate of 3.4 cm kyr^{-1} (Figure 2.4) while the deeper part of the core is characterised by a transition to lower sediment accumulation rates with a mean of 1.6 cm kyr^{-1} (> 18 cm).

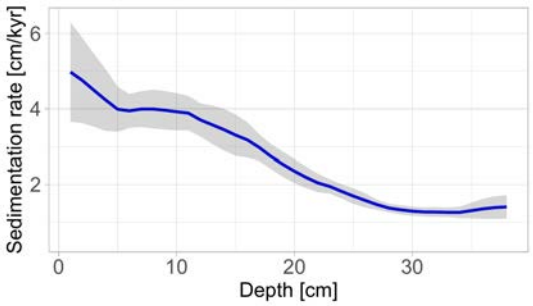

Figure 2.4: Derived sediment accumulation rates using the BACON model and all ^{14}C ages (averages of the small-volume bulk and the small-n samples). The rate decreases from the upper core part towards the bottom of the core. The confidence intervals are ± one standard deviation of all realizations from BACON.

2.3.3 *Sediment mixing and bioturbation depth estimates*

Visual analyses of optical images and radiographs are used to distinguish between a homogeneously mixed layer at the top of each sub-core, followed by increasingly distinct burrows which mark the transition to the historical layer with single deep reaching burrows, such as *Zoophycos* (Figure 2.5). The exemplarily shown sub-core 2 illustrates the vertical extent of sediment mixing which can be described with a homogeneous colour in the photograph and a mottled appearance in the radiograph. The homogeneously mixed layer extends to about 8 cm, followed by the transition from the increasingly distinct burrows to the historical layer between 12 and 13 cm. The historical layer is characterised by lighter and darker colours in the image, the occurrence of individual deep reaching burrows (Figure 2.5, marked in red) and loosely filled burrows (orange marks).

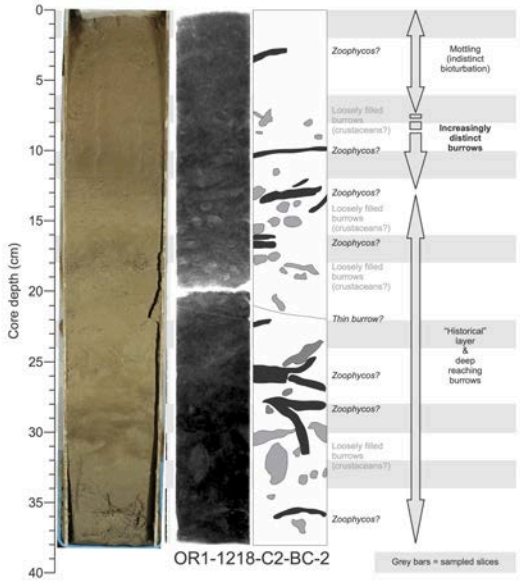

Figure 2.5: Assessment of the vertical extent of sediment mixing as well as the intensity by visually analyzing photograph and radiograph images from sub-core 2 exemplarily. All images are in the Supplementary Material Figure S1. The radiograph image was done on a thin slab (~1 cm thick sediment slice). Possible burrowing activities are indicated on the radiograph image for *Zoophycos* (black) and loosely filled burrows (grey). The characteristic depth intervals of bioturbated sediments are described as well. Horizontal grey bars indicate the sampled layers for ^{14}C analyses.

Similar structures are also found in all other cores (Supplementary Material Figure S1). The average extent of the mixed layer is 8.4 ± 1.2 cm (1 SD) and the transition to the historical layer occurs on average at 12.8 ± 0.9 cm. The visual assessment indicates horizontal variability for all analysed layers within the core. Individual depths for each sub-core are listed in the Supplementary Material Table S1.

In addition to the visual inspection of images, we used the derived age-heterogeneity from the small-n data together with the sediment accumulation rate (section 2.3.2) to derive a mixing depth. Depending on the considered depth interval and the accumulation rate, we derive a bioturbation depth between 7.5 and 11 cm, consistent with the independent visual estimates.

2.3.4 *Spatial structure of sediment mixing*

The individual age-depth profiles in Figure 2.3 indicate a continuous increase of age with depth for each sub-core. However, the horizontal structure shows spatial variability within single depth layers (Figure 2.6). Variations within a depth layer increase with depth, exceeding

± 2,000 yrs with large standard deviations for depths from 28 - 30 cm and 32 - 34 cm (see Table 2.2). The resulting heterogeneous spatial variability in the large-volume three-dimensional residuals (Figure 2.6) indicates spatial coherence: the right panel for the sub-cores 7A to 9B is often younger than its neighbouring panel for the sub-cores 4 to 6. Notably, the sub-cores 7A and 9B show consistently younger ages while sub-core 5 is consistently older than the average age. These patterns were tested for spatial autocorrelation with a 3D Moran's I (Moran, 1950) and are statistically significant ($p < 0.05$) which indicates more spatial clustering than expected from a random process.

The horizontal variability derived from the small-volume bulk samples (zoom-in panel in Figure 2.6) suggests that the spatial scale of mixing is smaller than the volume of the large samples which implies a dependency on the spatial scale of measurements.

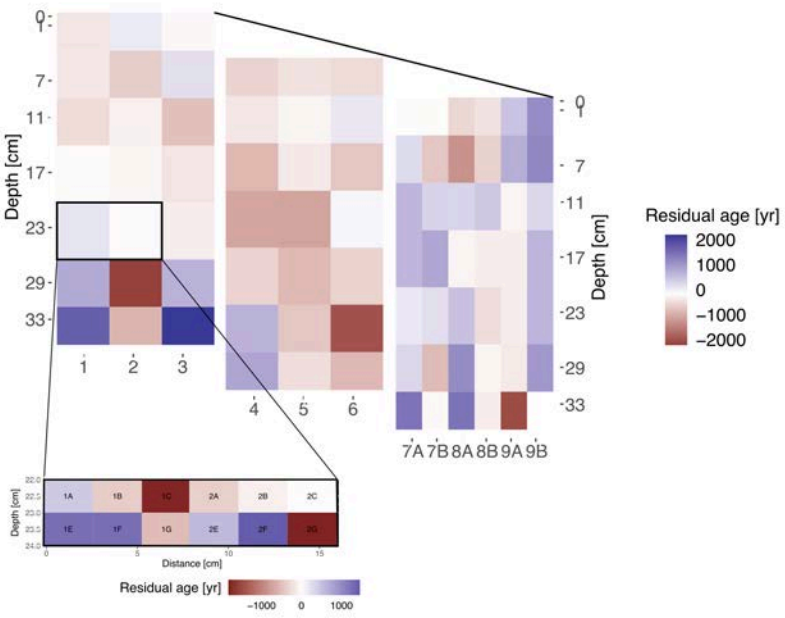

Figure 2.6: Three-dimensional view on age-heterogeneity within the core. Residuals to the respective mean of each depth layer are shown for all twelve sub-cores. They generally increase with depth and show the largest deviations towards the bottom of the core. Residuals from the small-volume bulk samples are compared to the overall mean of all twelve samples and are shown in the insert.

2.3.5 *Components of age uncertainty*

Uncertainties in age-depth profiles are usually based on analytical error terms, specifically the measurement error which is reported by

the laboratory and its conversion to calendar ages. However, additional uncertainties arise from both picking a finite number of specimens from a mixed sediment sample, and from horizontal variation in mean age. In order to account for these uncertainties, we assess the error terms from the measurement and calibration process, from the finite number of specimens as well as from the net displacement of sediment material (Figure 2.7). The first error term is the calibrated value of the reported uncertainty (derived from ^{14}C counting statistic) from the MICADAS laboratory and increases with depth due to the exponential decay of radiocarbon (mean of 152 yrs, individual estimates per depth layer are in Table 2.4). The error from picking and measuring a finite number of specimens can be expressed by σ_{ind} from the small-n samples divided by the square root of the number of picked specimens. This term shows a mean uncertainty of 325 yrs and increases with depth due to the decreasing sediment accumulation rate. We use this term as an approximation of the expected heterogeneity within the bulk-samples based on the derived age-heterogeneity in the small-n samples from 6 - 8 and 36 - 37 cm. The spatial age-heterogeneity σ_{cores} is the standard deviation of all large-volume bulk ^{14}C ages for each depth layer respectively. Due to the change in sediment accumulation rate with depth, the age uncertainty increases with depth from 291 to 1,253 yrs (mean 673 yrs) while the net vertical displacement in depth stays between 0.6 and 2.6 cm (mean 1.7 cm).

2.4 DISCUSSION

If sedimentation and mixing within the sediment is spatially uniform, neighbouring cores would be affected in the same way and thus, nearby records should demonstrate replicable profiles. In contrast, if mixing is incomplete, patchy or heterogeneous, the afore-mentioned simple assumption does not hold and proxy records from nearby cores will display differences due to their unique mixing history.

Following the simple assumption of a homogeneous mixed layer (Figure 2.1A), the transition to the historical layer is characterised by a kink in the depth-age-relation and this depth is interpreted as the mixing depth (Berger and Heath, 1968; Berger and Killingley, 1982; Trauth et al., 1997). This might be true if the mixing is intense and sediment accumulation rate low. However, even though both of these apply to the core shown here, we do not find a distinct kink in the ^{14}C record which suggests that mixing is incomplete, or spatially and temporally variable mixing describes the conditions more realistically (Figure 2.1B).

From previous studies, we recognise the importance of sediment mixing for proxy records and its influence on the representativity of such reconstructions. The mixing leads to additional uncertainty

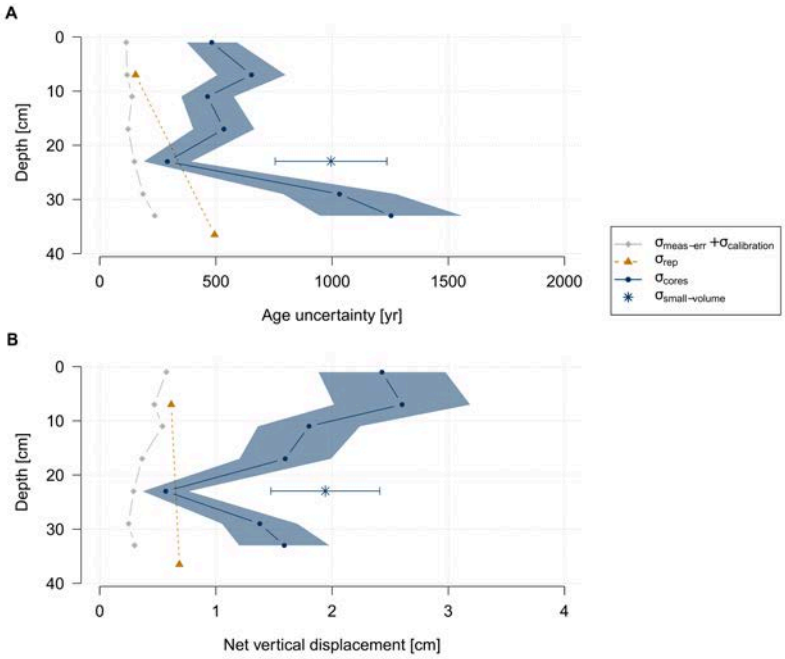

Figure 2.7: Different error terms affecting the reliability of ^{14}C ages derived from large-volume bulk (200 foraminifera) samples. The measurement error ($\sigma_{meas-err}$) is shown combined with the uncertainty from the calendar age calibration ($\sigma_{calibration}$, grey). Sampling only a finite number of specimens (σ_{rep}, orange) leads to an additional uncertainty term which increases with decreasing sediment accumulation rates. The largest contribution to the overall uncertainty stems from the horizontal age-heterogeneity which is represented as the standard deviation per depth layer between the large-volume bulk samples from all sub-cores (σ_{cores}, blue). The small-volume bulk samples ($\sigma_{small-volume}$, blue star) show an even larger uncertainty due to the smaller physical volume. The variations caused by the measurement error and the finite sample size are subtracted from both σ_{cores} and $\sigma_{small-volume}$ to show the true effect of the net displacement. The error terms are illustrated for **(A)** resulting age uncertainty and **(B)** the net vertical displacement by considering the change in sediment accumulation rate with depth (Figure 2.4). The confidence interval and the error bar are the standard deviation of the standard deviation of the bulk samples, but in (B) not accounting for the uncertainty in the sediment accumulation rate.

in the determination of the samples' age (e. g., Barker et al., 2007; Díaz-Asencio et al., 2020; Lougheed et al., 2020; Dolman et al., 2021a) and to a smoothing of the signal (Anderson, 2001). We can use simple models to estimate the additional noise as well as the magnitude of smoothing. However, these models assume homogeneous mixing which underestimates the afore-described spatial variability. Besides the active mixing, age-heterogeneity and age offsets can also arise

Table 2.4: Contributions to age and depth uncertainty from different error terms. The error terms are described and illustrated in section 2.3.5. The error from the standard deviation across all large-volume bulk samples (σ_{cores}) is the remaining uncertainty after accounting for $\sigma_{meas-err}$, $\sigma_{calibration}$ and an interpolated estimate of σ_{rep}. For the small-volume bulk samples, $\sigma_{small-volume}$ is mentioned in brackets at 23 cm depth. The depth estimates are derived by scaling the age estimates with the sediment accumulation rate output from the BACON model.

Depth	$\sigma_{meas-err}$ + $\sigma_{calibration}$ [yrs]	$\sigma_{meas-err}$ + $\sigma_{calibration}$ [cm]	σ_{rep} [yrs]	σ_{rep} [cm]	σ_{cores} [yrs]	σ_{cores} [cm]
1	114	0.6			482	2.4
7	118	0.5	154	0.6	653	2.6
11	139	0.5			464	1.8
17	122	0.4			534	1.6
23	149	0.3			291 [995]	0.6 [2.0]
29	187	0.3			1,032	1.4
33	237	0.3			1,253	1.6
36.5			494	0.7		

from changes in the foraminiferal flux (i. e., the number of specimens per cubic centimetre) which can amplify or reduce the variations caused by mixing. Changes in the flux are driven by variations in the surface productivity and/or the thermal structure of the upper water column (Bard et al., 1987; Jian et al., 2000); thus, also containing environmental information. However, the abundance of *T. sacculifer* does not change along our sediment core and is consequently not the factor causing the age-heterogeneity.

Likewise, selective bioturbation of different size-fractions can result in biassed age estimates (Peng et al., 1979; Broecker et al., 1984). Our study is based on the size fraction from 315 - 355 µm, thus our results might be invalid for the fine material and other size fractions which are differently affected by mixing (Wheatcroft, 1992; Díaz-Asencio et al., 2020). In addition, changing corrosivity of bottom water mass over time, oxygen-related changes in the benthic faunal community or preferential dissolution of older foraminifera shells due to their relatively longer residence time in the sediment can bias age estimates (Barker et al., 2007). However, we expect that dissolution at our study site is not important because the water depth at the core location lies above the typical depth of the lysocline in the South China Sea where the water is saturated with calcium carbonate (e. g., Regenberg et al., 2014; Wang et al., 2016). We also find no trend toward lower diversity

in trace fossils or a change in sediment colour from brown to grey, both of which would indicate changes in oxygen levels (e. g., Froelich et al., 1979; Savrda, 2007). We therefore interpret our observations as variability caused by mixing and discuss its spatial scale in the following.

2.4.1 *The spatial scale of mixing and sediment heterogeneity*

The conventionally considered error terms of the measurement and the calibration process underestimate the true uncertainty of the age-depth relationship that includes also spatial displacement (Figure 2.7), and disregard deep reaching bioturbation effects, e. g., the formation of spreiten, which can lead to significant deviations from the mean age and severe offsets in the horizontal age structure (Löwemark and Werner, 2001; Leuschner et al., 2002; Löwemark and Grootes, 2004). The magnitude of different error terms (section 2.3.5) is dependent on the sediment accumulation rate and can therefore be different in age and depth units.

Figures 2.8A and 2.8B illustrate in three dimensions the scale and pattern of variation in age that could be generated from the independent ^{14}C measurement error and the measurement of a finite number of specimens from a homogeneously mixed sediment, respectively. Figure 2.8C shows the pattern observed in the real data, which differs from that shown in the previous two figures, suggesting that it likely contains a component of incomplete and/or heterogeneous mixing leading to net displacement. The assumption that mixing is at least partly responsible for the clustering of spatial patterns from e. g., burrowing activities and resulting low reproducibility of nearby cores can be confirmed with a statistically significant spatial correlation within the presented core (Moran's I, $p < 0.05$).

The presented variability in Figure 2.8C is based on the large-volume bulk samples (200 specimens from volumes of 64 or 128 cm^3) which averages out small structures within the sediment, whereas age estimates from small-volume samples with 1.8 cm^3 are more likely to be influenced by small-scale mixing structures, have larger standard deviations and are less indicative for the mean age of a depth layer (Figures 2.3 and 2.6). As most proxy analyses are performed on sample volumes of 10 - 20 cm^3, the applicable net displacement and its uncertainties would be in between our estimates from the small- and large-volume samples and are likely contained but potentially not considered in conventional proxy analysis. Using fewer specimens increases the range of age estimates for a given depth layer which would rather be indicative of short-term local ^{14}C changes, such as upwelling and monsoonal activities for our study site in the South China Sea (e. g., Xie et al., 2003; Tan et al., 2020), instead of

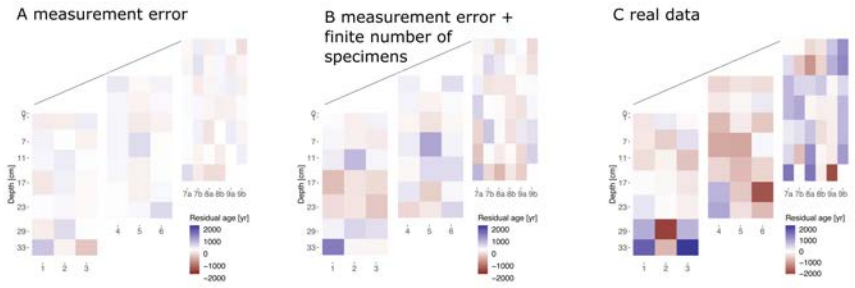

Figure 2.8: An illustration of the effect of different error terms on the three-dimensional variability of ^{14}C derived age estimates. The deviations from the mean age per depth layer are smallest considering **(A)** only a random measurement error (including the calendar age calibration error) and increase when **(B)** the finite number of randomly picked and measured specimens is taken into account. **(C)** The horizontal age-heterogeneity derived from all sub-cores (Figure 2.7, σ_{cores}) exceeds both deviations and shows the true age-heterogeneity caused by mixing.

the true mean age of the layer which is desired for reliable age-depth modeling.

The question remains to what extent our findings apply to other sediment sites used for palaeo-reconstructions. In most cases, age-models are not replicated. In the replicated down-core radiocarbon age estimates from different tubes from a multicore (SO213-84-2, Figure 7 in Dolman et al., 2021a), the difference between age models is one order of magnitude higher than expected from the uncertainty from the radiocarbon measurements which provides strong evidence for a significant net displacement. Furthermore, an indirect evidence for sediment mixing can be found in age-model reversals as seen in larger compilations of marine proxy records which regularly contain age-reversals in their chronologies (38 % of the age-models in the marine compilation in Marcott et al., 2013 contain an age reversal, 19 % have a reversal larger than twice the given uncertainty bounds). The true number might be even higher because cores or core-sections with difficult age-models may sometimes remain unpublished even though this might simply be the result of active sediment mixing. Thus, our findings are likely applicable beyond our study site but similar studies at other sites would be very useful to investigate the dependence of the sedimentation setting.

The magnitude of the errors associated with a ^{14}C age estimate influences the shape of a potential depth-age relationship. An example of a BACON realization for sub-core 8B (vertical resolution of 1 cm) with conventional error estimates based only on the uncertainty stemming from the measurement and calibration (as in Figure 2.8A) shows that most of the age estimates from the other sub-cores lie outside of

the suggested 95 % confidence interval (Supplementary Material Figure S2A). In contrast, when the observed variability in age estimates (Figure 2.8C) is used as an error estimate, the BACON model (not surprisingly) shows an overlap of the confidence intervals with most of the individual age estimates (Supplementary Material Figure S2B). Hence, it may be useful to include the effect of the net displacement, i. e., that a dated sample might not represent the correct age for the layer it was sampled from, into age-model strategies for marine sediments. A similar strategy was proposed for lake sediments already (Heegaard et al., 2005).

2.4.2 *Potential implications for palaeo-reconstructions*

While the classical uncertainty of radiocarbon dates (derived from ^{14}C counting statistic, $\sigma_{meas-err} + \sigma_{calibration}$) is independent of the sedimentation rate, the effect of measuring radiocarbon dates on a finite number of foraminifera in a mixed sediment (σ_{rep}) and the effect of the net displacement (σ_{cores}) are inversely proportional to the sedimentation rate and thus most important for low sedimentation conditions. For example, assuming a 10 cm sedimentation rate; a net displacement of 2 cm would lead to an additional 200 yrs (1 SD) uncertainty from the net displacement comparable to the typical radiocarbon uncertainty in the Holocene.

While for single records, such an age uncertainty might not affect the inferred conclusions, it does, however, affect the comparison between records from different sites, between reconstructed climate and independent forcing time-series as well as large scale stacks of records. For example, Marcott et al. (2013) (their SI Figure 17) estimated that in the global mean Holocene stack, variability at millennial scales (1/1000 yrs) is underestimated by a factor of two, mainly caused by the radiocarbon age-uncertainty. If we speculate that the true time uncertainty is 30 % times larger due to mixing and net displacement as shown here, this would imply that millennial scale variations might be damped by a factor of five in the reconstructions. Thus, the smooth reconstructed Holocene temperature evolution might be further away from the true temperature variations. Reschke et al. (2019b) used the correlation between nearby records to estimate the signal to noise ratio in marine sediment records. The study found that the results were strongly dependent on the age uncertainty estimates; if the true age uncertainty is considerably stronger than usually assumed, as proposed here, this would also imply that the signal to noise ratio and thus the quality of the sediment records is higher than suggested by Reschke et al. (2019b). Given the importance of knowing the accurate age-uncertainty, estimates of the mixing and the net displacement for other sedimentation conditions would be very valuable for quantitative palaeo-reconstructions.

2.4.3 *Suggested ^{14}C measurement strategy to determine mixing and net displacement and to enable a reliable dating*

A number of studies already compared different dating strategies (e. g., Andree, 1987; Blaauw et al., 2018; Lacourse and Gajewski, 2020) and we therefore do not want to propose an all-encompassing strategy, as this also depends on external conditions, such as financial and laboratory capacity, as well as the individual characteristics of each core. For studies which need reliable dating with a precise quantification of the age-model uncertainty and mixing, we suggest a sampling strategy based on our findings (Figure 2.9). It should be noted, however, that our suggestions focus on sampling strategies for optimal age modeling to derive from this information on the uncertainty inherent in the reconstructed proxy data that should be considered in the interpretation. Moreover, these results and recommendations apply to bioturbated sediments and would not apply to sediment cores which are clearly laminated or show other signs that they were deposited in dysoxic or anoxic conditions.

We recommend sampling in batches to adapt it to the accumulation characteristics of the core. Specific suggestions on the replications, the number of specimens and the sample volumes are mentioned in Figure 2.9. Samples for the age determination should have a similar sediment volume as those for the proxy, so that they are affected by the same sediment heterogeneity. Furthermore, if proxy and radiocarbon measurements are based on the same sedimentary material, e. g., calcite tests, they should be derived from the same sediment sample instead of two smaller sediment samples from the same depth. The minimal number of shells to measure in order to derive reliable age estimates can be approximated with the information on the sediment accumulation rate and the mixing depth as well as with calculations and reference charts (e. g., equation 5 and Figure 8 in Dolman et al., 2021a).

The ultimate aim of each dating approach is to establish a reliable depth-age scale. A first approximation of the covered temporal period of a core and a rough estimate of the sediment accumulation rate can be derived with age estimates ideally based on a large number of specimens from the top and the bottom of a core. An additional data point at an intermediate depth can provide information on the consistency of the sediment accumulation rate.

Replicated measurements of small numbers of foraminifera (10 x 5 specimens) from the same sample can be sampled from several depths to infer the mixing extent and intensity. Similar approaches were applied in previous studies and provided reliable estimates (e. g., Lougheed et al., 2018; Fagault et al., 2019; Dolman et al., 2021a). Additional information on the presence of bioturbational structures from trace fossils and their intensity (e. g., *Zoophycos*, Figure 2.5 and

Supplementary Material Figure S1) can be obtained from X-ray images. To further assess the small-scale heterogeneity among samples, we recommend the sampling of several horizontal samples, if possible. This might be restricted by the available core diametre and material, but will provide valuable insights.

As a last step, measurements with many specimens from large volumes for multiple, regularly spaced intervals can be performed. A high vertical density is desired but depends on the sedimentary conditions and might be limited by the availability of material and the financial resources. However, applying the strategy on a limited number of cores in different sedimentation conditions would allow an estimation the range of expected age displacements and thus allow for more realistic age-depth models including uncertainty estimates in the future.

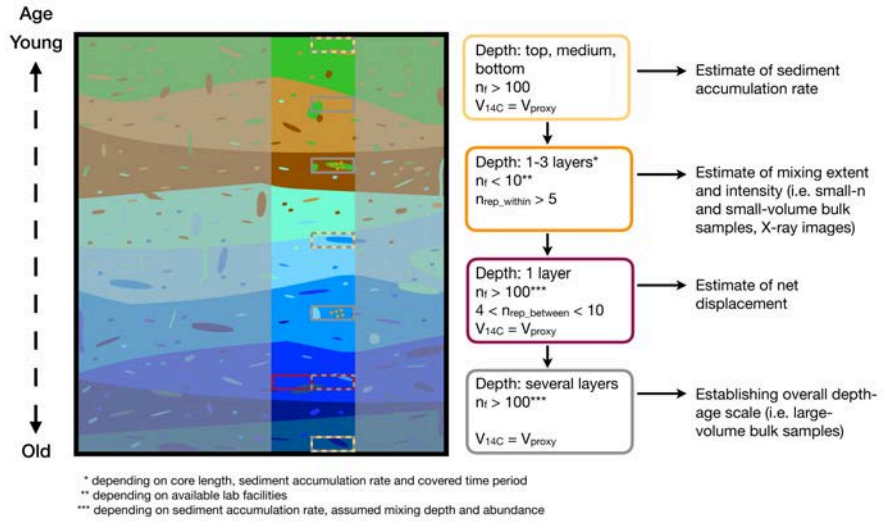

Figure 2.9: Overview and illustration suggested steps towards an improved sampling protocol for a single core. The boxes correspond to proposed samples in the 2D sketch and contain suggestions for different sample types with the depth and the number of layers to samples, the ideal number of specimens n_f, the number of replicates $n_{rep-within}$ from one sample or the number of replicated samples from one depth $n_{rep-between}$ as well as the physical volume of a sample V_{14C}. The sample volume should be similar or the same as the volume used for the proxy reconstruction (i.e. 10 - 20 cm^3). The second row indicates the information which can be derived from each individual sample type and it indicates to which of the samples from our study it can be compared.

2.5 CONCLUSIONS

The analysis of radiocarbon in foraminiferal tests as a tracer of time since deposition shows at a first sight that all sub-cores showed an

agreement on the temporal ^{14}C decrease from the early Holocene to the last glacial termination. However, the detailed investigation of the three-dimensional variability in ages pointed out a much larger uncertainty than what is usually accounted for in depth-age models. This is to some extent caused by the measurement of a finite number of specimens which leads to an uncertain estimate of the true age. An additional contribution to the increased uncertainty is the (vertical) displacement of sedimentary material which is more pronounced in small volume samples. Even if all of these parameters were taken into account, there is a lack of clear delineation or kink in the ^{14}C record between the mixed and the historical layer, which is often used in studies or simulations as a determination of the bioturbation depth (e. g., Berger and Heath, 1968; Berger and Killingley, 1982).

The new estimation of uncertainties implies that the traditionally considered errors related to ^{14}C derived ages are likely too optimistic. Both the mixing and the sediment displacement affect the representativity of a derived age estimate in a way which is not clearly quantified yet. We provide a data-based estimate of the vertical net displacement indicating that the depth of a specific age might vary by up to 3 cm from one core to another with an effective age uncertainty about five times larger than usually assumed. If resources and funding permit, we recommend replicated radiocarbon measurements of samples with small numbers of foraminifera, e. g., 10 x 5 specimens for one or two depths, and (replicated) measurements based on many specimens of large-volume samples, e. g., core halves, to quantify the full magnitude of uncertainty for the age-depth model. An examination of the spatial variability of age estimates under other sedimentary conditions, e.g. higher sediment accumulation rates or weaker/stronger mixing, would allow a more detailed description of the effects and a parameterisation of these in depth-age models.

2.6 SUPPLEMENTARY MATERIAL

2.6.1 *Supplementary figures and tables*

2.6.1.1 *Supplementary figures*

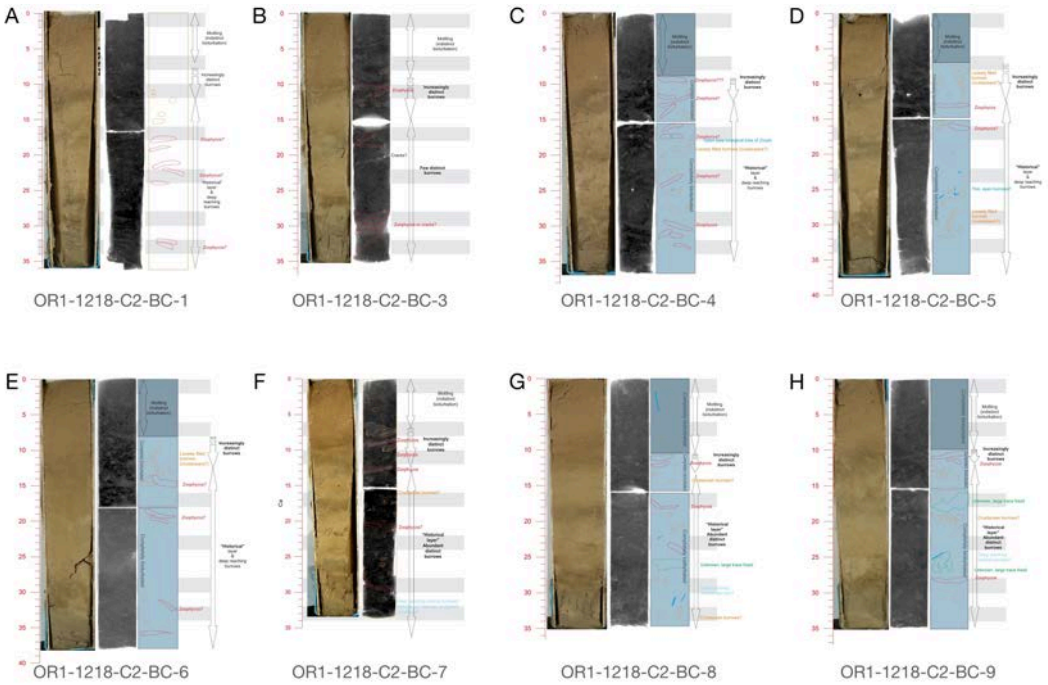

Figure 2.10: Visual assessment of the vertical extent of sediment mixing as well as the intensity derived from photographs and x-rays from all sub-cores except sub-core 2 (shown in Figure 5). Possible burrowing activities are indicated on the radiograph image for *Zoophycos* (red) and loosely filled burrows (orange). The characteristic depth intervals of bioturbated sediments are described as well. Horizontal grey bars indicate the sampled layers for 14C analyses. Each sub-core is shown in one panel: **(A)** sub-core 1, **(B)** sub-core 3, **(C)** sub-core 4, **(D)** sub-core 5, **(E)** sub-core 6, **(F)** sub-core 7, **(G)** sub-core 8 and **(H)** sub-core 9.

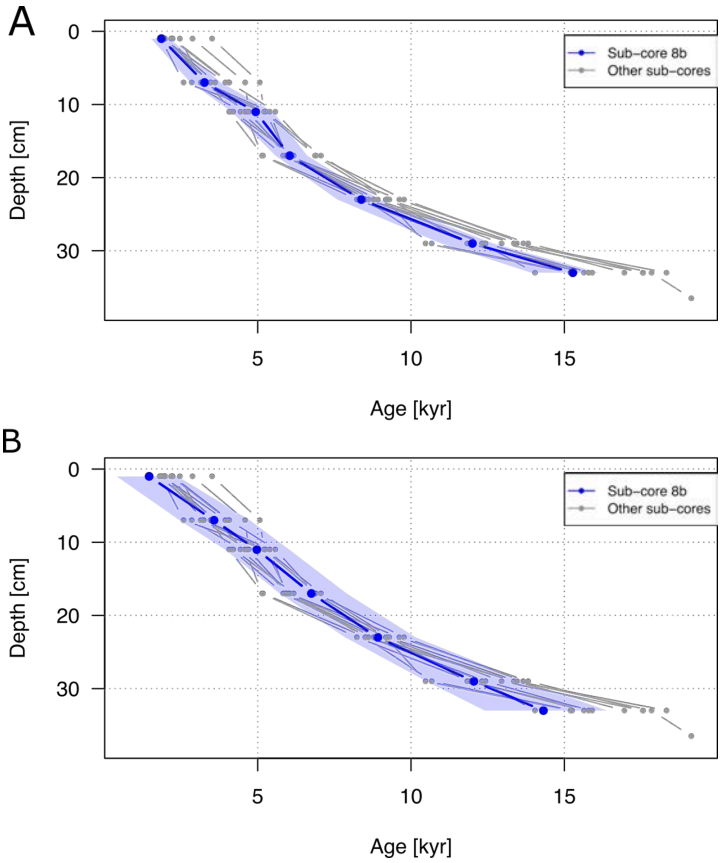

Figure 2.11: Depth-age models for sub-core 8B using BACON. The depth-age model is shown in blue (dots represent the sampled depth layers) and the shading indicates the 95 % confidence interval. Additionally, all individual age estimates from the large-volume bulk samples are included as well (black points). BACON was run with the large-volume bulk samples, the mean per sub-core from the small-volume bulk samples and the mean per depth layer from the small- n samples. For the uncertainty estimate required input by BACON, we used **(A)** the reported measurement error and **(B)** the increased uncertainty from Figure 7.

2.6.2 *Supplementary table*

Table 2.5: Estimates of the mixed layer depth and of the transition to the historical layer (both in centimetre) for each sub-core derived from visual analyses of the optical photographs and the radiographs as exemplarily illustrated in Figure 5. Averages ± one standard deviation are given as well.

Sub-core	Mixed layer [cm]	Historical layer [cm]
OR1-1218-C2-BC-1	7	12
OR1-1218-C2-BC-2	8.5	12
OR1-1218-C2-BC-3	9	15
OR1-1218-C2-BC-4	9	13
OR1-1218-C2-BC-5	7	13
OR1-1218-C2-BC-6	8	12.5
OR1-1218-C2-BC-7	7	12.5
OR1-1218-C2-BC-8	10	13
OR1-1218-C2-BC-9	10	12
Mean ± 1 σ	8.4 ± 1.2	12.8 ± 0.9

3

LOCAL-SCALE DEPOSITION OF SURFACE SNOW ON THE GREENLAND ICE SHEET

Alexandra M. Zuhr[1,2], Thomas Münch[1], Hans Christian Steen-Larsen[3], Maria Hörhold[4], and Thomas Laepple[1,5]

[1] Alfred-Wegener-Institut Helmholtz Zentrum für Polar- und Meeresforschung, Research Unit Potsdam, Telegrafenberg A45, 14473 Potsdam, Germany
[2] University of Potsdam, Institute of Geosciences, Karl-Liebknecht-Str. 24–25, 14476 Potsdam, Germany
[3] Geophysical Institute, University of Bergen and Bjerknes Centre for Climate Research, Bergen, Norway
[4] Alfred-Wegener-Institut Helmholtz Zentrum für Polar- und Meeresforschung, Research Unit Bremerhaven, 27568 Bremerhaven, Germany
[5] University of Bremen, MARUM – Center for Marine Environmental Sciences and Faculty of Geosciences, 28334 Bremen, Germany

This chapter is published in:
The Cryosphere, 15(10), 4873–4900, DOI: 10.5194/tc-15-4873-2021, 2021.

Abstract. Ice cores from polar ice sheets and glaciers are an important climate archive. Snow layers, consecutively deposited and buried, contain climatic information from the time of their formation. However, particularly low-accumulation areas are characterised by temporally intermittent precipitation, which can be further redistributed after initial deposition, depending on the local surface features at different spatial scales. Therefore, the accumulation conditions at an ice core site influence the quantity and quality of the recorded climate signal in proxy records. This study aims to characterise the local accumulation patterns and the evolution of the snow height to describe the contribution of the snow (re-)deposition to the overall noise level in climate records from ice cores. To this end, we applied a structure-from-motion photogrammetry approach to generate near-daily elevation models of the surface snow for a 195 m^2 area in the vicinity of the deep drilling site of the East Greenland Ice-core Project in northeast Greenland. Based on the snow height information we derive snow height changes on a day-to-day basis throughout our observation period from May to August 2018 and find an average snow height increase of ~ 11 cm. The spatial and temporal data set also allows an investigation of snow deposition versus depositional modifications. We observe irregular snow deposition and erosion causing uneven snow

accumulation patterns, a removal of more than 60 % of the deposited snow, and a negative relationship between the initial snow height and the amount of accumulated snow. Furthermore, the surface roughness decreased by approximately a factor of 2 throughout the spring and summer season at our study site. Finally, our study shows that structure from motion is a relatively simple method to demonstrate the potential influences of depositional processes on proxy signals in snow and ice.

3.1 INTRODUCTION

Ice cores from polar ice sheets and glaciers are one of the most important climate archives. Physical and chemical characteristics are preserved in the ice, store information on past climatic conditions, and are used as proxy data, for example, to reconstruct past temperatures (e. g., Dansgaard, 1964; Jouzel and Merlivat, 1984) or snow accumulation rates (e. g., Mosley-Thompson et al., 2001; Dethloff et al., 2002).

The accuracy and interpretability of reconstructed parameters depend on the understanding of the initial signal formation and the processes that potentially thereafter change the original signal imprinted in the deposited precipitation. Amongst these are local processes such as snow–air exchange processes; alteration of the isotopic composition (i. e., $\delta^{18}O$ or δD) by diffusion, sublimation, vapour deposition, or metamorphism (Steen-Larsen et al., 2014; Dadic et al., 2015; Ritter et al., 2016); depositional losses of chemical compounds (Weller et al., 2004), local-to-regional processes such as the spatial variability in snowfall and wind-driven redeposition leading with the local topography to stratigraphic noise (Fisher et al., 1985; Münch et al., 2016); and larger-scale processes such as precipitation intermittency (Persson et al., 2011).

One major obstacle is the apparent gap between precipitation – as determined from model approaches, reanalysis data, and remote sensing products – and the net snow accumulation at the local scale relevant for firn and ice core records. This gap is caused by processes such as snow erosion, drift, and redistribution, which depend on the wind speed, wind direction, and duration of wind events, as well as on the conditions of the surface snow (Li and Pomeroy, 1997b; Li and Pomeroy, 1997a; Sturm et al., 2001). While dunes and ripple marks are snow bedforms resulting from snow deposition by wind, sastrugi are the result of erosional processes at the snow surface and are very common at locations with high wind speeds (Filhol and Sturm, 2015; Kochanski et al., 2018). Furthermore, loose snow on top of consolidated features can easily be picked up, transported by wind, and redeposited at other locations, which results in spatially variable snow accumulation (Fisher et al., 1985; Libois et al., 2014; Naaim-Bouvet et al., 2016), rendering wind an important meteorological parameter

driving the changes in the observed snow surface (Albert and Hawley, 2002; Groot Zwaaftink et al., 2013). In order to understand the temporal and spatial variability of snow accumulation and to ascertain their contribution to accumulation intermittency and to the observed variability in proxy records (van der Veen and Bolzan, 1999; Ekaykin et al., 2016; Picard et al., 2019), quantification of the spatial and temporal snowfall events and of the changes in surface structure and surface roughness is therefore of crucial importance.

The acquisition of reliable snow height data is, however, still a challenge (Eisen et al., 2008; Chakra et al., 2019). Methods to measure the amount of snow accumulation include stake lines and farms, snow height sensors, remote sensing products (e. g., satellites, lidar and radar measurements, photogrammetry alone or in combination with Structure-from-Motion (SfM) approaches), as well as laser scanning approaches. Stake lines, grids, and farms are robust and low-cost ways to manually document snow height evolution (e. g., Kuhns et al., 1997; Mosley-Thompson et al., 1999; Schlosser et al., 2002); however, these methods require time and personnel in the field. Snow height sensors, often mounted next to an automatic weather station (AWS) (e. g., Steffen and Box, 2001; van de Wal et al., 2005), require less manual work, can provide measurements at high temporal resolution but are restricted to a single point. Remote sensing products provide large spatial coverage up to several hundreds of kilometres with spatial resolutions of, e. g., 0.7 m pixel size for laser altimeter systems (Herzfeld et al., 2021); however, their large spatial resolution is not suitable for small or local-scale studies (e. g., van der Veen and Bolzan, 1999; Rignot and Thomas, 2002; Arthern et al., 2006). To obtain snow height changes on the scale from centimetres to kilometres, various forms of SfM photogrammetry (Keutterling and Thomas, 2006; Westoby et al., 2012; Nolan et al., 2015; Basnet et al., 2016; Cimoli et al., 2017), laser scanners (Baltsavias et al., 2001; Picard et al., 2016, 2019), and large grids of snow stakes (Mosley-Thompson et al., 1999; Schlosser et al., 2002) are used. SfM is a widely used technique, also with applications in glaciology (e. g., Westoby et al., 2012; Chakra et al., 2019), and it can overcome some of the limitations of laser scanners, for example, the wind disturbance by the fixed scanning tower as well as the limited range of the laser scan (Picard et al., 2016, 2019).

In this study, we apply a custom-made SfM photogrammetry approach to explore the snow accumulation behaviour for a study site in northeast Greenland next to the deep drilling site of the East Greenland Ice-Core Project (EGRIP). The overall aims of this study are (1) to show that our method reliably characterises the temporal and spatial pattern of snow erosion and accumulation; (2) to provide insights into the temporal and spatial changes of the surface structures; and (3) to investigate the effect of wind, subsequent snow erosion, and trans-

port on the internal layering of the upper snowpack and the resulting implications for climate proxy analyses.

3.2 DATA AND METHODS

3.2.1 *Study site*

Our study site is located next to the EGRIP camp site in northeast Greenland (75° 38′ N, 36° W; 2708 m a.s.l.; Fig. 3.1a) (Dahl-Jensen et al., 2019). The location has a mean annual temperature of −29 °C and is characterised by prevailing westerly winds (Madsen et al., 2019) with a mean wind direction of 252° during our observation period (Appendix Figs. 3.15 and 3.16). Accumulation rates in the vicinity of EGRIP are 13.9 cm w.e. yr^{-1} as estimated over a period of ~5 years from 2011 to 2015 (using density data of the upper 2 m of the snowpack, Schaller et al., 2016), while shallow ice cores and geophysical surveys indicate between 10 and 12 cm w.e. yr^{-1} (Vallelonga et al., 2014; Karlsson et al., 2020). An AWS from the Programme for Monitoring of the Greenland Ice Sheet (PROMICE) (Fausto and van As, 2019) was installed in 2016 ~500 m southeast of the camp (Fig. 3.1b) and provides meteorological data with a 10 min resolution (Appendix Fig. 3.15).

3.2.2 *SfM photogrammetry and snow height reconstruction*

We apply a SfM photogrammetry approach to map the daily snow accumulation patterns by reconstructing the daily surface snow heights from digital images. To this end, we took images of the snow surface covering a 39 x 10 m rectangular area, with the long x-axis set up perpendicular to the main wind direction and the short y-axis pointing towards it (referred to as *Photogrammetry Area*; Fig. 3.1b). We set up 35 glass fiber sticks surrounding the area (30 sticks along the x-axis and five distributed on the surrounding edges, Fig. 3.1c) to provide absolute reference points for the snow height reconstructions. Furthermore, all sticks were levelled to the same relative height by using a theodolite.

Photos were taken almost daily from 16th of May to 1st of August, 2018 (77 days), mostly between 6 and 8 pm (local camp time, GMT-3) to ensure the best light contrast and similar light conditions on all photos (Nolan et al., 2015; Cimoli et al., 2017). No photos were taken on days with very cloudy or whiteout conditions, because these conditions do not allow a DEM generation from optical images. The photos were taken using a Sony α6000 camera with a fixed lens of 20 mm focal length and a focal ratio of f/16. The ISO value was set to 100. These parameters were chosen to get as much contrast in the images as possible. The camera was mounted at a height of ~1.6 m

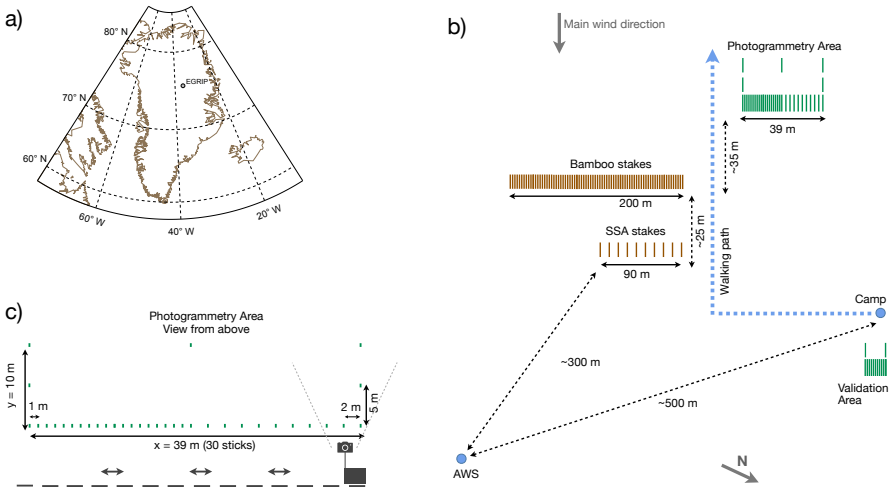

Figure 3.1: Overview maps for all relevant locations and transects in our study. a) Map of Greenland with the location of the EGRIP camp site in northeast Greenland. b) Schematic map of the EGRIP area including all relevant study sites. This area is approximately 200 m south of the deep drilling site at the EGRIP camp and about 300 m from the AWS. The map is not to scale. Data from the AWS, the Bamboo stakes, and the SSA transect (SSA = Specific Surface Area) are used for the comparison of snow height estimates. Data from the Validation Area are described in the Appendix 3.6.2. c) Schematic illustration of the Photogrammetry area with respective distances. 30 glass fiber sticks were set along the walking line (x-axis), four sticks were positioned on the edges towards the main wind direction (y-axis), and one in the back of the study area. The sledge with the camera is located as is shown in Fig. 3.2. The approximate field of view of the camera is illustrated with grey lines.

above ground on a setup consisting of a sledge, an ice core box, a plexiglass plate, and a metal pole (Fig. 3.2). During image acquisition, photos were taken every second using an automatic shutter control while the sledge was dragged on foot by a person along the downwind main side (Fig. 3.1, x-axis). This provided about 60 consecutive images with an overlap of ~70 %. If less than 50 photos were available, no DEM could be generated because of insufficient overlap between successive images. We obtained an effective data set of 37 out of 77 days (48 %, Table 3.3) due to overcast conditions affecting the light contrast, the inability to detect surface structures, failures in the image processing, or insufficient overlap of consecutive photos.

We used the software AgiSoft PhotoScan Professional (Version 1.4.3 Software, 2018, retrieved from http://www.agisoft.com/downloads/installer/) for the SfM workflow including the digital elevation model generation (hereafter referred to as DEM (digital elevation model), archived under https://doi.org/10.1594/PANGAEA.936082, Zuhr et al., 2020). The generated DEMs have a resolution of 1 x 1 cm.

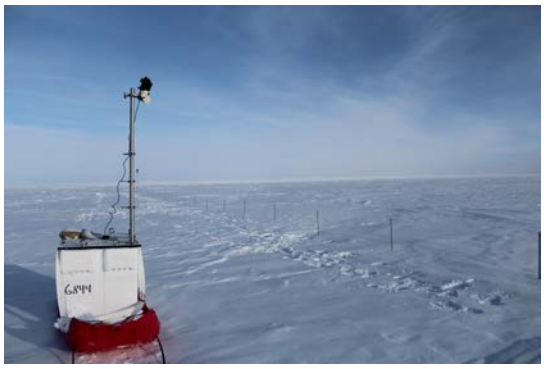

Figure 3.2: Camera setup for the image acquisition. The setup consists of a sledge, an ice core box, a plexiglass plate, a metal pole, and the camera used to take images of the Photogrammetry area. The sledge was dragged along the downwind main side of the study area, during which photos were taken using an automatic shutter control.

For reliable geo-referencing, we manually added ground control points (GCPs) with known coordinates using the top of the glass fiber sticks (Figs. 3.1c, 3.19b and c) within Agisoft PhotoScan. The sticks at $y = 10\,m$ were, however, not visible in every daily data set and could not always be used as GCPs. Therefore, all 35 sticks were used as GCPs if they were visible, otherwise the effective number of GCPs varied between 32 and 35. The absence of the GCPs at $y = 10\,m$ and the lower image quality might impair the height control in the back of the area. For further analyses, the study area was therefore restricted to $y \leqslant 5\,m$ and thus a DEM area of $195\,m^2$ (instead of $390\,m^2$) to ensure constant data availability.

We evaluated our DEMs by analysing the trueness of our DEM-derived snow height estimates compared to reference heights, i. e., manually measured snow heights. For this, we set up a validation area with independent validation points within the area, avoiding using the actual study area for the validation purposes to minimise the disturbances on the snow height evolution in the study area. The detailed validation analyses are presented in the Appendix 3.6.2 with the main findings summarised here:

1. Data quality: We assessed the data quality and uncertainty by comparing DEM-derived snow heights around the stick positions to manually measured snow heights at the stick locations (Appendix 3.6.2.1, Table 3.4, Fig. 3.18). We derived the temporal and spatial uncertainty across all stick positions and all measurement days with manual and DEM data and found a mean difference of 0.2 cm, a standard deviation of 1.2 cm, and a root mean square error (RMSE) of 1.3 cm. This uncertainty applies to single points in time and space and will reduce when averaging over the quantities.

2. Sensitivity test on the number of GCPs: We tested the dependency of the number of used GCPs on the DEM uncertainty by using additional sticks in the validation area as an independent measure of the accuracy of DEM-derived snow height estimates (Appendix 3.6.3, Table 3.6). Different numbers of GCPs have a very small effect on the overall accuracy with mean differences between -0.3 and 0.1 cm, standard deviations up to 1.5 cm and RMSEs up to 1.5 cm.

3. Sensitivity test on the alignment of GCPs: We evaluated the accuracy of our DEM-derived snow height estimates to the alignment of the sticks itself by using the detailed information from the validation sticks (Appendix 3.6.3, Table 3.7). The influence of misaligned sticks causes mean differences between -0.1 and 0.1 cm, standard deviations up to 1.0 cm and RMSEs up to 1.0 cm.

In summary, uncertainties from manually setting up the transect, distributing the GCP coordinates during the processing, as well as the uncertainty of the GCP alignment are small compared to the amplitude of snow height change throughout our observation period (11 cm on average). We therefore conclude that our elevation models provide reliable snow height estimates with a sufficient accuracy for the purpose of our study.

3.2.3 *Additional snow height and snowfall data*

Complementing the DEM-derived snow height data, four additional snow height evolution estimates are available with different temporal resolutions and spatial coverages (Table 3.1 and Fig. 3.1b): manual documentation of the relative snow heights from i) the glass fiber sticks in the photogrammetry area (*PT sticks*, archived under https://doi.pangaea.de/10.1594/PANGAEA.931124, Zuhr et al., 2021c), ii) a 200 m long transect with 200 wooden sticks with 1 m spacing (*Bamboo stakes*, archived under https://doi.pangaea.de/10.1594/PANGAEA.921855, Steen-Larsen, 2020a), iii) a 90 m long transect with 10 sticks and 10 m spacing (*SSA stakes*, SSA = specific surface area, archived under https://doi.pangaea.de/10.1594/PANGAEA.921853, Steen-Larsen, 2020b), and iv) automatic snow height measurements from the sonic snow height sensor at the nearby AWS (*AWS PROMICE*, http://www.promice.dk). The SSA stakes as well as the Bamboo stakes were aligned in the same orientation as our study area. The high-resolution data from the AWS PROMICE were averaged to daily values.

Both, snowfall and snowdrift can lead to an increase in snow height and a differentiation between these can be difficult in the DEMs. During the study period, snowfall was manually documented when visual snowfall was observed or physical snowfall was collected (Ap-

Table 3.1: Snow height estimates around the EGRIP camp site. The temporal resolution, the spatial extent, and the distance relative to the study area are given. The manual measurement of the 30 sticks at our study area refers to the sticks along the x-axis, because these were measured more frequently than the remainder of the 35 sticks. Estimates form the Bamboo stakes and the SSA stakes are averages across 200 or 10 sticks with 1 or 10 m spacing, respectively. The single point high-resolution data from the AWS PROMICE were averaged to daily values. Locations are illustrated in the overview map (Fig. 3.1b).

Name	Temporal resolution	Spatial extent	Distance (m)
DEMs	near-daily	39 x 5 m	0
PT sticks	3 days	30 sticks, 39 m	0
Bamboo stakes	3-5 days	200 sticks, 200 m	~ 50
SSA stakes	daily	10 sticks, 90 m	~ 70
AWS PROMICE	daily	single point	~ 370

pendix Table 3.3; snow collection setup described in Steen-Larsen et al., 2014). We use this simple, manual documentation of snowfall as well as the ERA5 snowfall product from the European Centre for Medium-Range Weather Forecasts (ECMWF, 2017; Hersbach et al., 2020) to obtain information about the time of snowfall events. ERA5 is increasingly used and provides reliable near-surface variables over the Greenland Ice Sheet (Delhasse et al., 2020). The data were downloaded with an hourly resolution from the Climate Data Store (`https://cds.climate.copernicus.eu`) and summed up to daily values. If the manual documentation indicates snowfall and the DEM data show an increase in surface heights, we consider this as snowfall. This does, however, not exclude the possibility that snowdrift (i. e., mobilised snow by wind) may have also contributed to the increase.

In addition to the SfM photogrammetry study, a snow sampling study was carried out every third day at the windward side of each stick position along the long x-axis of the PT area (resulting data is not part of this study). Even though the positions were filled up with snow after sampling to avoid artificial surface structures and drift, we manually removed these areas in the DEM generation to minimise biased snow height estimates.

3.2.4 *Estimation of surface roughness*

Surface roughness is often used to describe and analyse the size of landforms and features with respect to a specific scale, and it is therefore a useful tool to investigate the variability of the snow surface

in our study area (van der Veen et al., 2009; Grohmann et al., 2011; Veitinger et al., 2014). Here, we use the peak-to-peak amplitude of 2.5 m long, non-overlapping segments following the approach by Albert and Hawley (2002) and average the individual values to a representative surface roughness estimate R,

$$R = \frac{1}{n} \sum_{i=1}^{n} \left(h_{max_i} - h_{min_i} \right) \tag{31}$$

where h_{max_i} is the maximum and h_{min_i} the minimum snow height of an individual segment and where n is the number of considered segments. We analyse the surface roughness perpendicular (along the x-axis) and parallel (along the y-axis) to the main wind direction (schematic overview in Appendix in Fig. 3.23). Both estimates are averaged across n = ~3800 individual segments. This surface roughness estimate captures variations on spatial scales below 2.5 m. To account for the larger-scale undulations, we additionally compute the standard deviation of the entire DEM area after applying a spatial smoothing (using an isotropic Gaussian smoothing kernel with a standard deviation of 100 cm).

3.3 RESULTS

3.3.1 *Relative snow heights from digital elevation models*

Each of the 37 DEMs (Fig. 3.3, Appendix Table 3.3, Zuhr et al., 2020) represents a two dimensional map (39 x 5 m) of the relative snow height in the study area for the particular day. The zero-point was chosen arbitrarily to be at the bottom of the first GCP on the day of installation. All further snow heights are referenced to this zero-level.

On the first day of our observation period, 16th of May 2018 (hereafter we refer to the Day of Observation Period, *DOP*), the snow height varied from -10.5 cm to +11.3 cm, with a total amplitude of 21.8 cm (Fig. 3.3 top panel). Two pronounced features of elevated snow heights were elongated along the prevailing wind direction and located in x-direction from ~12 m to ~20 m and around 32 m. Considering the higher wind speeds during the winter (Appendix Fig. 3.17), these bedforms present in our study area are presumably dunes resulting from snow erosional processes (Filhol and Sturm, 2015). Until the middle of our observation period (20th of June 2018, DOP 36), the snow height has generally increased with a maximum increase of 12 cm while the surface structures flattened (Fig. 3.3 second panel). At the end of our observation period (1st of August 2018, DOP 78), snow heights ranged from +2.6 cm to +16.4 cm, thus showing a reduced amplitude of 13.8 cm compared to DOP 1 (Fig. 3.3 third panel). The bedform morphology is still dominated by undulations, although

they are no longer as dominant as in the beginning of the observation period.

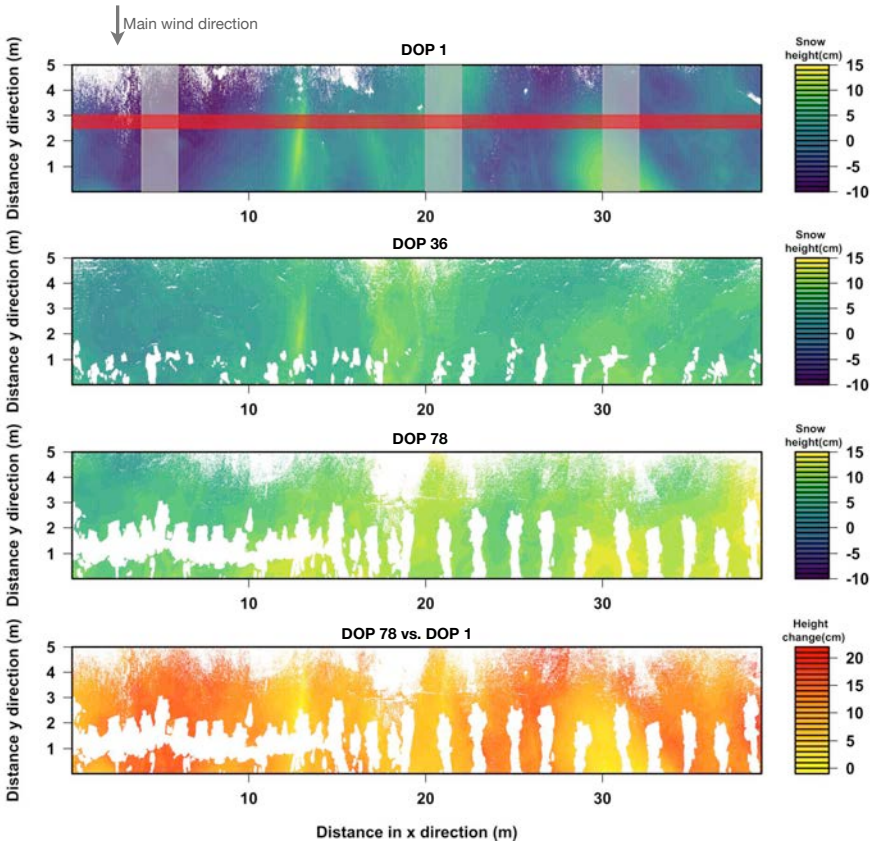

Figure 3.3: DEM-derived relative snow heights presented as two-dimensional maps (39 x 5 m). Shown are the snow heights for the Day of Observation Period 1 (16th of May 2018, DOP 1, upper panel), DOP 36 (20th of June 2018, second panel), and DOP 78 (1st of August 2018, third panel) as well as the change in snow height between DOP 1 and DOP 78 (fourth panel). Snow height estimates are given in cm relative to the snow height at x = 0 m and y = 0 m on the day of installation. The y-direction points towards the main wind direction. The red bar (in the top panel) indicates the band along the x-direction from y = 2.5 to y = 3 m (50 cm width), which is used to obtain average snow heights for each day for further analyses. The grey bars mark three subareas for the analyses in section 3.3.4 and Fig. 3.9. Missing data are shown as white areas and are caused either by a snow sampling performed in the same area (white spots close to the lower main line) or by insufficient image quality.

3.3.2 *Comparison of the mean temporal evolution of different snow height estimates*

Over the season, the area affected by the manual snow sampling and leading to missing DEM values is increasing. Thus, we focus our main

analyses on an averaged band from y = 2.5 to y = 3 m which remains largely unaffected by the disturbances from foot steps and snow sampling across the entire season, since it lies upwind of these activities (Fig. 3.3 red bar in the top panel). We refer to this band in the following as the *2.5 m-band*. By comparing the DEMs between the beginning and the end of our observation period, the change in snow height of the 2.5 m-band amounts to an overall but not homogeneous increase of ~11 cm (black vertical line in Fig. 3.4a; 10 and 90 % quantiles are 7.4 and 14.8 cm, respectively).

To investigate the consistency between snow height estimates obtained by different methods and from different locations, we compare our DEM-derived snow height data to the other, independently obtained estimates (Table 3.1, Fig. 3.4a and b). Compared to our DEM-derived increase in snow height of ~11 cm from DOP 1 to DOP 78 (top row in Table 3.2), the other measurements based on multiple sampling locations show increases from 8.5 to 10.9 cm, while the single snow height sensor mounted to the AWS PROMICE recorded an increase of only 5.8 cm. Part of the differences among the methods are due to the different time periods covered, since comparing the most common time interval yields a better agreement (lower row in Table 3.2). The remainder of the differences are expected due to the different spatial representativity of the measurement techniques. The individual pixel within our study site also show large spatial variability of snow height increase at the EGRIP site (see Appendix Fig. 3.20).

Table 3.2: Snow height changes (in cm) for the different snow height estimates (Table 3.1) throughout the observation period. Two different periods are considered to include first the entire observation period covered by the DEMs (i. e., DOP 1 to 78) and second to compare the most common time interval, especially for the PT sticks and the Bamboo stakes (temporal resolutions are mentioned in Table 3.1).

Name	DEM: 2.5 m-band	PT sticks	Bamboo stakes	SSA stakes	AWS PROMICE
DOP	1 - 78	5 - 78	10 - 75	2 - 78	1 - 78
Change (cm)	11	9.7	8.5	10.9	5.8
DOP	10 - 73	11 - 72	10 - 71	10 - 73	10 - 73
Change (cm)	10.3	10.7	8.5	10.9	7.6

Despite the differences in the average snow height increase between the individual estimates (Fig. 3.4a), they agree on the overall temporal evolution within their uncertainty ranges (Fig. 3.4b). The development over time is characterised by a few individual, large events, such as the event around DOP 21 that led to an increase of

~5 cm. Similar large snow height increases during single events have been reported in other studies (e. g., Libois et al., 2014).

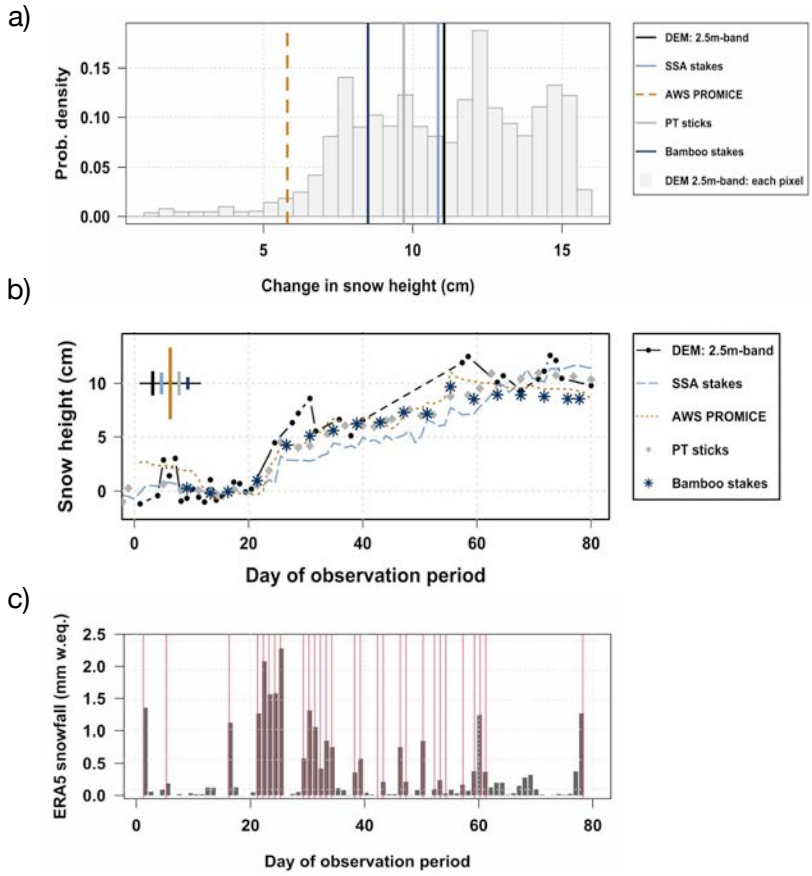

Figure 3.4: Evolution and changes of different snow height estimates throughout the observation period. a) Histogram of the DEM-derived change in snow height (grey bars) for every single pixel of the 2.5 m-band from DOP 1 to DOP 78 (Fig. 3.3 fourth panel) together with the mean snow height change (black vertical line) in the 2.5 m-band, as well as the mean snow height changes from other methods (vertical lines; Tables 3.1 and 3.2). Note that the latter estimates cover different spatial extents. b) Mean temporal evolution of snow height estimates throughout the observation period from the DEMs (2.5 m-band; black), the SSA stakes (light blue), the AWS PROMICE (gold), the PT Sticks (grey), and the Bamboo stakes (dark blue). For a direct comparison, each estimate is referred to its mean value from DOP 10 to DOP 20, which is defined as the zero level. Vertical bars include the uncertainty in cm ($\pm$ one standard error) due to the limited spatial resolution of each method assuming a spatial decorrelation length of 5 m for our study site. The AWS PROMICE has the largest uncertainty because it is a single point measurement. c) The ERA5 snowfall product (grey bars) and manually documented snowfall during the observation period (red lines, see Appendix Table 3.3).

Manual documentation of snowfall (Appendix Table 3.3) contains only the information when snowfall occurred, but no indication on the amount. By contrast, all snow height estimates show only the total snow accumulation including depositional and erosional changes such as snowdrift and redistribution, but not the net amount of snowfall during a single event. To close the gap, we compare these data sets to the ERA5 snowfall product (Fig. 3.4c). The ERA5 data and the manual documentation agree in general well on the timing of snowfall; however, ERA5 also indicates snowfall on some days without manual notes. This can have multiple reasons, e. g., no snowfall documentation during the night, snowfall which was directly blown away, or inaccuracies in ERA5. Comparing the ERA5 data with our snow height estimates, we find good agreement for all estimates concerning the strong event around DOP 21 (Fig. 3.4b). In addition, the many smaller events between DOP 30 and DOP 60 seem to constitute the gradual height increase in our observations.

3.3.3 *Day-to-day variations and the erosion of fresh snowfall*

To illustrate the nature of accumulation and erosion at the EGRIP site, we analyse the daily changes in the surface topography maps. Three examples are shown here (Fig. 3.5; the full maps are archived under https://doi.org/10.1594/PANGAEA.936099, Zuhr et al., 2021b).

The first example is an overall increase of the snow height; thus a full layer of fresh snow. The snow height increased by 2.9 ± 1.6 cm (one standard deviation) and, except for a small area in the bottom left corner, the entire area received snow (DOP 4 to DOP 5, Fig. 3.5a). The complementary behaviour, that we will later discuss in more detail, is an erosive event from DOP 7 to DOP 8, characterised by a snow height decrease of -2.9 ± 2.3 cm (Fig. 3.5b). A negative change in snow height can be caused by compaction or erosion. We consider erosion (i. e., physical depositional modifications) as the primary driver of negative snow height changes, neglecting compaction. Finally, some days show a patchy change in snow height as illustrated here for the evolution from DOP 35 to DOP 36 (net change of -1.1 ± 1.6 cm; Fig. 3.5c).

The spatial and temporal evolution can be investigated in a more continuous way by averaging across the y-direction (in the 2.5 m-band) to show the snow height evolution against time. For DOP 1 to DOP 12 (Fig. 3.6, for all DEMs see Appendix Fig. 3.21), large temporal changes in the snow height are visible. In detail, the mean snow height increased by 4.1 cm from the first to the fifth day, consistent with manually documented snowfall. The ERA5 snowfall product agrees in the timing of snowfall (Fig. 3.4c, Appendix Table 3.3), but not regarding the amount (0.6 cm when converting the ERA5 snowfall from mm w.eq. using a density of 290 kg m^{-3}). The DEM-derived

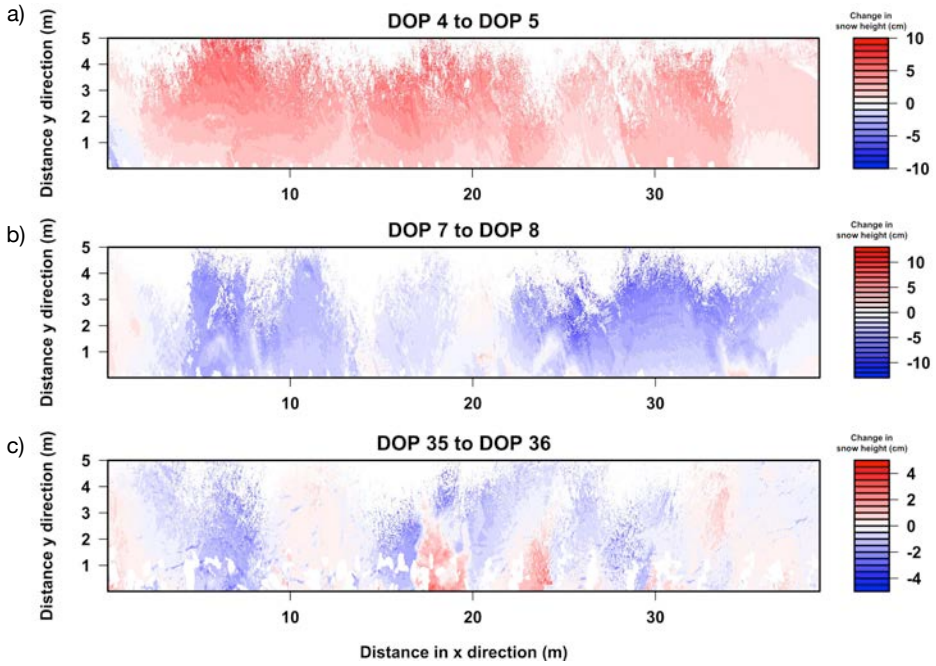

Figure 3.5: Day-to-day variations shown as the change in snow height (in cm) of the entire DEM-area for three periods: a) DOP 4 to DOP 5 shows an increase in the snow height for 78 % of all pixel, b) the change from DOP 7 to DOP 8 is dominated by snow erosion for 65 % of all pixel, and c) the snow height evolution from DOP 35 to DOP 36 is characterised by a spatially patchy pattern with positive and negative changes. For each panel, the zero-line indicates areas without changes in the snow height.

increase is evenly distributed across the troughs and dunes. The subsequent decrease in snow height from DOP 7 to DOP 8 (-3.6 cm) is similarly homogeneous and, remarkably, exposes the initial surface structure from DOP 1 again. After a few days with rather patchy snow height changes (DOP 9 to DOP 11), the snow surface shows again the initial structure on DOP 12.

To study how systematic these erosion events are, we analyse how the correlation between the surface structures changes over time (Fig. 3.7). For this, we provide for each day the correlation between the DEM on this day with all following DEMs, together with the evolution of the overall snow height. Erosive events can lead to an exposure of previous snow structures increasing the correlation between two DEMs while snowfall in combination with wind can cause inhomogeneous snow height increases which reduces the correlation. Indeed, the pattern of increasing and decreasing snow heights between DOP 4 and DOP 12 (Fig. 3.6) is reflected in varying correlations. Similar events occur between DOP 28 and DOP 31 as well as between DOP 70 and DOP 73, highlighting the contribution of snow erosion on the overall snowpack build-up.

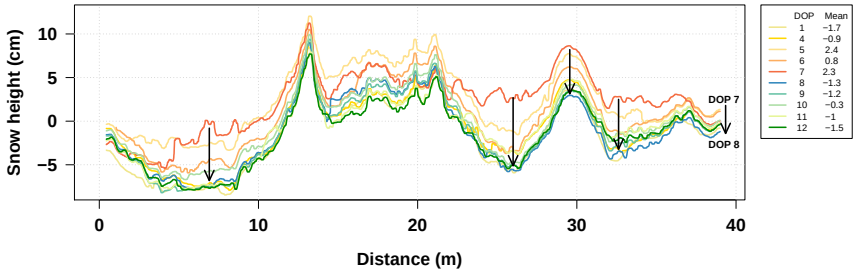

Figure 3.6: Temporal evolution of the relative horizontal snow height profiles from DOP 1 to DOP 12 (20-point running median, averaged 2.5 m-band). Different colours represent the different days as well as the respective mean snow heights in cm, both shown in the legend. Snowfall caused an overall snow height increase from DOP 1 to DOP 7, followed by an erosive event removing the new snow, and exposing the previous surface structure again. Arrows indicate the erosional decrease in the snow height from DOP 7 to DOP 8.

The study of Picard et al. (2019) compared the mean and standard deviation of the daily accumulation to snowfall and wind speed in order to investigate the influence of meteorological parameters on the snow accumulation for a study site on the East Antarctic Plateau, a region which receives only a quarter of the accumulation of the EGRIP site. Following their study, we derive the mean and standard deviation of the daily accumulation from our DEM data and compare these to the ERA5 snowfall and the wind speed from the AWS PROMICE to reproduce their Fig. 5. Surprisingly, we find patterns for our study site in northeast Greenland (Fig. 3.8) which are comparable to East Antarctica. Especially, we do not find significant relations between snowfall, wind speed, the mean daily accumulation and the standard deviation of the daily accumulation indicating that accumulation is not (solely) determined by snowfall or wind speed. Wind direction is not included in the analysis because the comparison did not indicate any relationship. The relation between the mean daily accumulation and the standard deviation of daily accumulation (bottom right plot) is also similar to the pattern observed on the East Antarctic Plateau; however, this funnel-type pattern is reproducible with random data and therefore only a statistical feature with no meaningful information on the physical processes determining the accumulation conditions. However, in contrast to the study by Picard et al. (2019), we find a statistically significant correlation of -0.55 ($p < 0.01$, not accounting for autocorrelation) between wind speed and the daily accumulation (middle plot on the left in Fig. 3.8) which suggests that snow drift and erosion are important processes determining the snow accumulation, with higher wind speeds increasing the potential for negative accumulation, i. e., snow erosion.

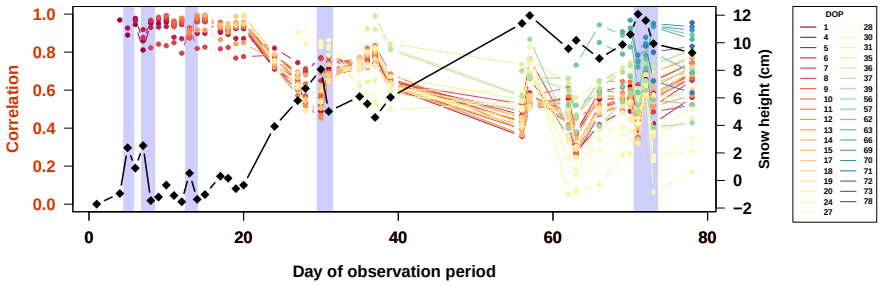

Figure 3.7: Correlation between the DEM-derived surface structures of a particular day and the surface structure on every following day (coloured points) as well as the overall snow height evolution (black diamonds). The colour-code indicates the DOP of the surface structure to which all subsequent structures are correlated to. The entire DEM area is considered for the correlation calculation. Vertical blue bars indicate an increase in the correlation and a decrease in the snow height. The second blue bar to the left shows the decrease in snow height from DOP 7 to DOP 8 which is illustrated in Fig. 3.6.

3.3.4 *Flattening of the surface and changes in surface roughness*

The surface snow becomes flatter towards the end of our observation period (Sect. 3.3.1, Fig. 3.3). This change from a heterogeneous to a homogeneous surface structure can be characterised in more detail by analysing the change in snow height between DOP 1 and DOP 78 relative to the initial snow height on DOP 1 for the 2.5 m-band (Fig. 3.9a) which shows a variable structure at the beginning and a rather flat snow surface at the end of the observation period. In addition, we investigate three selected subareas with different initial surface structures (grey areas in Fig. 3.3 upper panel) to account for snow height changes parallel to the main wind direction. On DOP 1, the snow structures in these subareas (Fig. 3.9b) were characterised by a trough (dotted grey line), the top of a dune (blue), and an undulating surface (gold). While the first and second subareas received a homogeneous snow accumulation of ~14 and ~6 cm, respectively, the third subarea suggests a spatially variable snow accumulation such that the partial dune undulation present at DOP 1 has nearly vanished at DOP 78. Thus, despite the differences at the beginning of the observation period, all three subareas developed to similar relative snow heights on DOP 78 (Fig. 3.9b solid lines). Combining all four subareas, we find a strong negative correlation of -0.9 between the change in snow height and the initial snow height (Fig. 3.9c) which indicates that areas which started with a relatively high snow height received less snow while areas with a comparably low initial snow height received more accumulation, a pattern that is also evident for the entire study area (see Appendix Fig. 3.22).

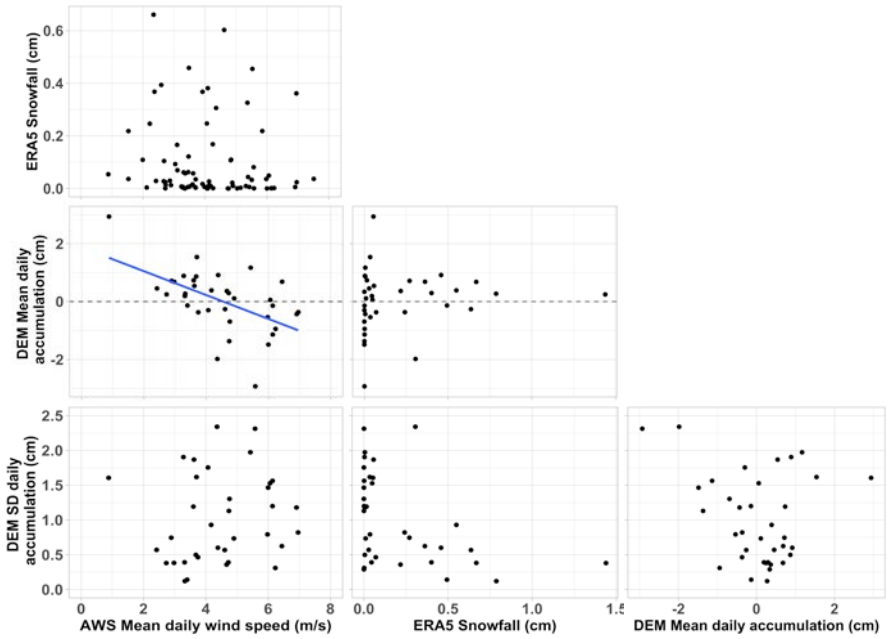

Figure 3.8: Following Fig. 5 in Picard et al. (2019), DEM-derived mean and standard deviation of the daily accumulation are compared to the daily wind speed from the AWS PROMICE and to the ERA5 snowfall product (converted to cm). During data gaps in the DEMs, the amount of snow accumulation was divided by the number of days to derive approximate daily accumulation. The accumulation conditions at the EGRIP site are largely remarkably similar to those on the East Antarctic Plateau, given the differences in accumulation rate, except for the relationship between mean daily wind speed and accumulation, which exhibits a negative correlation (r = -0.55; linear fit in blue) that is not apparent in Picard et al. (2019).

The change from a heterogeneous to a flatter surface structure is also reflected in a change of the surface roughness (Fig. 3.10). The temporal evolution of the roughness shows a consistent decrease from 4-5 cm to ~2 cm from DOP 1 to DOP 38 for both estimates parallel and perpendicular to the main wind direction (individual peak-to-peak amplitudes are in the Appendix Fig. 3.24). Interestingly, the same behaviour as found in the roughness (variations inside 2.5 m intervals) is also found for the large scale undulations. After the data gap of the DEM data between DOP 40 and DOP 56, the surface roughness estimates show an increase on DOP 56 followed by a successive decrease towards the end of the observation period. The surface roughness perpendicular to the main wind direction shows a larger amplitude than the surface roughness parallel to the main wind direction as well as the estimates from the entire study area. To investigate the evolution of the surface structure during the gap in the DEMs, we also include the standard deviation of the individual snow height readings from the PT sticks. This measure shows no changes in the strength

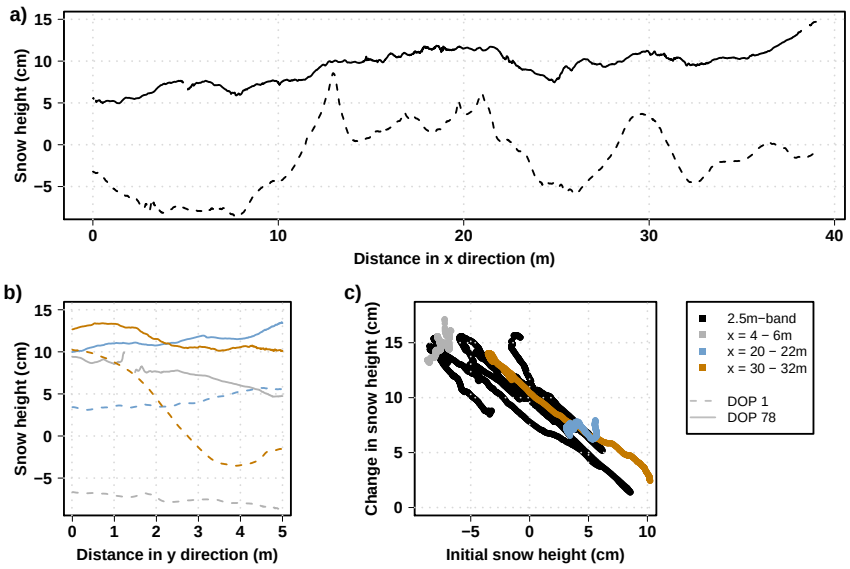

Figure 3.9: DEM-derived relative snow heights for 16th of May (DOP 1, dotted lines) and 1st of August, 2018 (DOP 78, solid lines) for four subareas of the study area: a) the 2.5 m-band perpendicular to the main wind direction; b) three subareas parallel to the main wind direction (grey: x = 4-6 m, blue: x = 20-22 m, and gold: x = 30-32 m) marked with grey bars in Fig. 3.3. c) Relationship between the initial snow height on DOP 1 and the change in snow height to DOP 78 for the subareas in a) and b). Note that the legend refers to all panels. The relation for each individual pixel in the study area is shown in the Appendix Fig. 3.22.

of surface undulations between DOP 40 and DOP 56. Similarly to the DEM-derived roughness estimates, the PT stick estimate records an increase in undulations around DOP 60 which indicates that the overall roughness increased at this point before decreasing again towards the end of the observation period.

3.3.5 *Implied internal structure of the snowpack*

The snow accumulation characteristics presented in the previous sections suggest spatial variability in the snow accumulation which might influence the internal structure of the snowpack. The DEM-derived snow height data can be used to extract the internal structure of the snowpack along the x-axis which we illustrate as a two-dimensional view of the upper snow layers for the last day of our observation period (Fig. 3.11). A snow height increase between two consecutive DEMs is considered as a positive contribution to the snowpack and adds a new layer to the internal structure. A decrease in the snow height removes previously deposited layers, neglecting snow compaction.

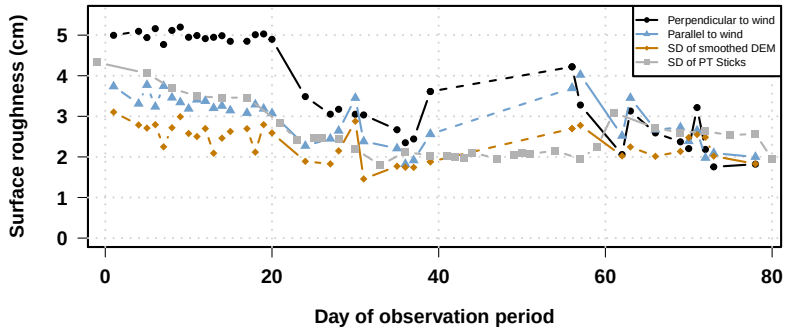

Figure 3.10: Temporal evolution of the surface roughness estimates throughout the observation period as described in section 3.2.4. The estimates parallel (blue) and perpendicular (black) to the main wind direction show an overall similar behaviour with the latter estimate suggesting higher roughness estimates at the beginning of the observation period. In addition, larger-scale undulations (gold) follow the overall pattern as well with an overall lower roughness estimate. The standard deviation across all PT stick measurements (grey) is used to fill the DEM data gap between DOP 40 and DOP 56 and follows the other estimates.

The internal structure is characterised by the fact that only a limited number of days with different layer thicknesses are finally preserved. The prominent snowfall event on DOP 4, for example, is not recorded due to its subsequent erosion (previously discussed in Fig. 3.6). Other strong events, such as the large increase in snow height at DOP 21, result in nearly continuous layers, albeit with varying thicknesses. Different layer thicknesses transfer the heterogeneity of the initially rough surface to the internal structure of the snowpack with considerable variations at different locations: at $x = 12$ m, no snowfall events were recorded prior to DOP 56, while at $x = 8$ or $x = 24$ m, for example, larger amounts of snow were accumulated during the first weeks of the observation period. Based on the small number (about five to six) of distinct days in Fig. 3.11, we conclude that only a small number of events is actually recorded in the internal structure even though we know that more snowfall events occurred, which suggests that physical and chemical properties might vary at different locations within our study area.

3.4 DISCUSSION

We presented a three dimensional data set of snow heights and their variations derived from elevation models. The data show the temporal and spatial changes of the snow surface for the summer season 2018 at the EGRIP location, provide insights into accumulation conditions and allow a comparison to similar studies from e. g., Antarctica (Picard et al., 2019). In this section, we discuss the changes of sur-

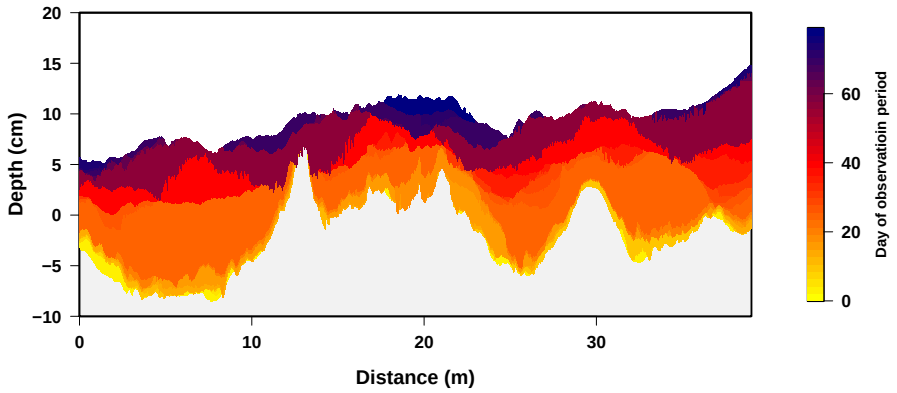

Figure 3.11: Two-dimensional view of the internal structure of our study area based on DEM-derived snow height variations along the 2.5 m-band for the last day of our observation period (DOP 78). Colours indicate the day of deposition during the season, namely when the DEM data recorded an increase in the snow height at the respective location. The grey background represents older snow and surface undulations prior to the first DEM on DOP 1. The long data gap between DOP 39 and DOP 56 does not cause an unrealistically thick snow layer which suggests that the temporal resolution of our data set does not affect the derived internal structure.

face structures, their implications for the interpretation of proxy data and the determination of accumulation estimates, and we assess the advantages and disadvantages of the SfM approach used.

3.4.1 *Temporal and spatial changes of surface structures*

The DEM-derived mean snow height increased by ~11 cm in the 2.5 m-band (Fig. 3.4b). The total amount of snow input into the area, however, was more than 30 cm, if we consider only the positive contributions from precipitated and drifted snow (Fig. 3.12). The cumulative ERA5 snowfall results in ~8 cm of net snowfall (Fig. 3.12). The DEM-derived net accumulation corresponds only to ~35 % of the total amount of temporarily deposited snow while the ERA5 snowfall is only ~24 %. Even though this could suggest that the ERA5 data might be biased towards drier conditions, we assume that both differences between the DEM-derived net accumulation and all positive contributions as well as between the DEM-derived estimate and the ERA5 snowfall are caused by substantial contributions of snowdrift and redistribution which emphasise their influence on the final snow accumulation during the observation period. Thus, the overall accumulation intermittency (Kuhns et al., 1997; Picard et al., 2019), presented here as the combination of snowfall and the intermittent depositional modifications, significantly influences the recording of climate proxies in the snow and firn and can either cause the removal of snow

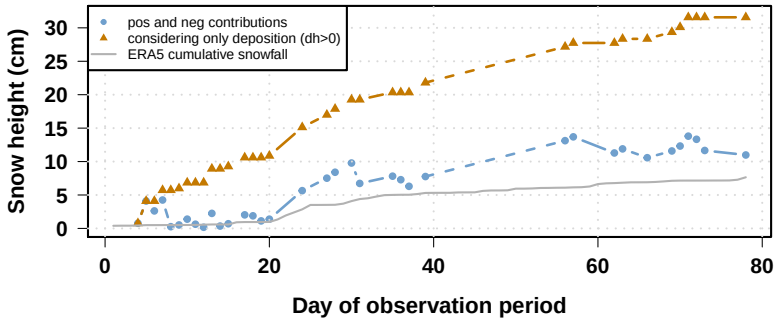

Figure 3.12: Cumulative snow height over the observation period from DEM-derived data and from the ERA5 reanalysis snowfall product. The DEM-derived snow height is shown for the two possibilities of i) counting both positive and negative contributions from one day to the next (blue), and ii) counting only the positive contributions (gold). The ERA5 snowfall (grey) is converted from mm w.eq. to cm assuming a mean snow density of 290 kg m^{-3} which was obtained from daily density measurements of the top 2.5 cm at the stick positions of the SSA transect. Considering only the positive changes in the DEM-derived data accounts for deposition by snowfall or drift, but not for snow removal (e. g., erosion). This indicates that more than half of the snow that arrived at the study site was eroded and redistributed, and was thus transported out of our study area.

from single spots and a transport to other locations, or, in turn, the deposition of snow from other locations at our study site.

Varying accumulation rates on a local scale can, especially in combination with wind, influence the surface structure. In our study area, two pronounced dunes were present at the beginning of the observation period which flattened towards the end of the summer season (Figs. 3.3, 3.9a and 3.9b). The process of building up and wearing down of surface undulations has been reported for different locations on ice sheets in Greenland (e. g., Albert and Hawley, 2002) and Antarctica (e. g., Gow, 1965; Groot Zwaaftink et al., 2013; Laepple et al., 2016). The observed flattening in our study is characterised by a negative correlation between the initial snow height and the local accumulation (Fig. 3.9c), which likely also holds in the long term, i. e., between the accumulation from one year to the next. This suggests that local deviations from the mean accumulation rate quickly average out over time as they cancel each other out (Fisher et al., 1985; Kuhns et al., 1997). Likewise, it explains why accumulation estimates from firn or ice cores that only sample one point in space but average across a large time-window, provide a good estimate of the regional accumulation rate, as already suggested by Kuhns et al., 1997 and van der Veen et al., 2009.

High wind speeds largely determine the growth or reduction of surface features and changes in the snow structure, in addition to smaller

contributions from e. g., temperature, humidity and metamorphism (e. g., Gow, 1965; Libois et al., 2014; Kochanski et al., 2018; Filhol and Sturm, 2019). Wind speed thresholds for drift and redistribution are 4 m s^{-1} on average for a 100 hour period, or higher for a shorter time period (Groot Zwaaftink et al., 2013). At our study site, the winter wind speed is generally higher than the summer wind speed (Appendix Fig. 3.17) which can lead to an enhanced formation of dunes. Even during our observation period, the wind speed exceeded the defined threshold values on some days (Appendix Fig. 3.16) which can possibly lead to snowdrift and might explain the observed erosion of entire snow layers and the exposure of previous surface structures (Figs. 3.6 and 3.7).

In the first half of our observation period, the surface roughness decreased from 4-5 to 2 cm (Fig. 3.10) followed by fluctuations around 2 cm. An increase of the surface roughness in winter, followed by a decrease in summer, is often attributed to seasonally changing wind speeds, with higher wind speeds in winter (e. g., Albert and Hawley, 2002). Our observed decrease in surface roughness towards the summer is comparable to studies from van der Veen et al., 2009 covering a large area of central and northern parts of the Greenland ice sheet, from van der Veen and Bolzan, 1999 for the location of the GRIP drilling site (close to Summit station, central Greenland), and to a study from Summit, Greenland, with a comparable spatial extent to our study (Albert and Hawley, 2002). van der Veen and Bolzan, 1999 and van der Veen et al., 2009 used different mathematical expressions to calculate the surface roughness and found no reduction in surface roughness during the summer season. However, Albert and Hawley, 2002 used similar spatial scales and found patterns comparable to our results. The spatial and temporal variations in surface roughness estimates highlight the natural complexity of this parameter and the lack of clear information. Even though the considered time period in our study is too short to characterise the seasonal behaviour of surface roughness, our data set contributes to an increasing understanding of this parameter by suggesting a smoothing of the surface and a flattening of surface features towards the summer.

Short-lived and rapidly changing snow structures resulting from wind-driven redistribution have been reported for sites on the East Antarctic Plateau and influence the snow accumulation (Libois et al., 2014; Picard et al., 2019). In contrast to the persistently "patchy" accumulation characteristics in Antarctica and to alpine settings with much higher accumulation rates, we characterise the studied accumulation at the EGRIP location as "layer by layer": we observe alternating and layer-wise increases and decreases of the snow surface between DOP 1 and DOP 20, a filling of troughs (Figs. 3.3 and 3.9) and a reduction of the surface roughness from DOP 20 to DOP 38 (Fig. 3.10) followed by accumulation in layers from DOP 56 to DOP 78 (Ap-

pendix 3.21). The ratio between the percentage of pixel with a positive and pixel with a negative DEM-derived day-to-day change in the snow height can be used to differentiate more quantitatively between "patchy" and "layer-by-layer" accumulation by defining an arbitrary threshold. In order to obtain a clearer result, we exclude changes between -0.5 and 0.5 cm. A ratio between 0.5 and 1.5 is considered to indicate "patchy" accumulation, i. e., about the same number of pixel show an increase as a decrease, whereas a ratio below 0.5 or above 1.5 is seen as indicative for "layer-by-layer" accumulation, i. e., an overall increase or decrease of the snow height from one day to the next. Indeed, 12 out of 36 day-to-day changes suggest a ratio below 0.5 and 18 above a ratio of 1.5. Thus, following our simple metric, 30 out of 36 days confirm the proposed "layer-by-layer" accumulation.

Picard et al. (2019) tried to link snow accumulation to meteorological conditions but did not find a robust relationship. In contrast, our DEM data show a significant negative correlation of -0.55 between the DEM-derived mean daily accumulation and the wind speed (Fig. 3.8), which suggests enhanced snow erosion during events with higher wind speeds, while lower wind speeds seem to be associated with more snow deposition, potentially leading to the deposition of redistributed snow during calmer conditions. Wind conditions are thus an important parameter for snow accumulation, which might also depend on the local accumulation rate and the amount of loose snow on top of a compacted snow surface. A key difference between the study by Picard et al. (2019) and our analyses is the considered time period: while their study covers a period of three years including several winter and summer seasons, our data only cover a timespan of three months. Meteorological conditions and their influence on the snow accumulation might depend on the respective season which would not be represented in our study. Repeating our study and extending it to cover a longer time period would be necessary to more thoroughly investigate the seasonal behaviour of the snow surface and the influence of the wind on the snow accumulation.

3.4.2 *Implications for the interpretation of proxy data*

The large heterogeneity in accumulation, the depositional modifications of the surface snow and their impact on the internal snow structure (Figs. 3.4a and 3.11) imply that at sites with similar environmental conditions, parameters measured in a single firn core will not be representative on a seasonal scale (e. g., Ekaykin et al., 2002; Ekaykin et al., 2016; Masson-Delmotte et al., 2015). This result is not only due to precipitation intermittency, a factor often considered in the interpretation of palaeoclimate records (Persson et al., 2011; Sime et al., 2011; Casado et al., 2018), but also due to the erosion of snow layers (Fig. 3.6). Erosion causes large differences between the total

snow input and the net accumulation (Fig. 3.12) and creates a strong noise level due to an under-sampling of the continuous environmental signal (Casado et al., 2019). In addition, a singular event, such as a singular deposition of a proxy signal from a volcano or a biomass burning peak, might be missed in a local record. Stable water isotopologues, density data and accumulation rates show large interannual variations on local (e. g., Münch et al., 2017) and also larger scales of e. g., 450 km in North Greenland (e. g., Schaller et al., 2016) which is likely the result of the accumulation heterogeneity.

Following studies on changes in the isotopic composition of surface snow (e. g., **hughes_sublimation_2021**; Casado et al., 2018), we use theoretical snow profiles based on the accumulation history from our DEM data set (Fig. 3.11) to demonstrate the variability of snow ages at one location for several days (Fig. 3.13a) and at different locations for a single point in time (Fig. 3.13b). On a single day, the derived mean snow age of a depth layer from 0 to 1 cm along our study area can vary by more than 20 days (Fig. 3.13b orange line). Even though we cannot distinguish between freshly precipitated and eroded or drifted snow in our data set, the variability within these theoretical snow profiles gives insight into the heterogeneous internal structure of the upper snowpack and shows the uneven snow accumulation at the EGRIP camp site and very likely also at other sites. Therefore, individual samples are not representative and should generally be avoided in favour of sampling multiple profiles.

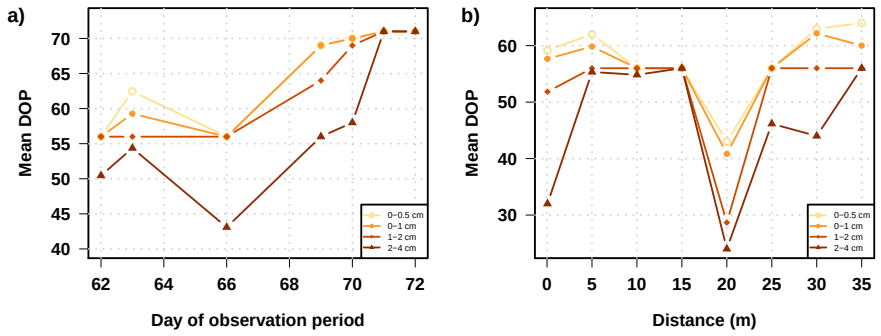

Figure 3.13: Theoretical temporal and spatial sampling of different depth intervals (0-0.5 cm, 0-1 cm, 1-2 cm and 2-4 cm) of the internal snow structure along the 2.5 m-band. a) Temporal sampling for ten consecutive days at x = 12 m. b) Spatial sampling at eight positions with 5 m spacing along the 2.5 m-band on DOP 69. The y-axes in a) and b) represent the average day of snow accumulation for the respective depth interval.

Further long-term observations of the precipitation vs. accumulation statistics (Picard et al., 2019) and spatial studies of the signal recorded in snow and firn (Münch et al., 2016, 2017) are needed to better constrain the effect of both precipitation and accumulation intermittency on the preserved climatic information and to allow for

a more reliable interpretation of proxy data from firn and ice cores. Compared to single point measurements, our spatial data set has the advantage of being better able to evaluate the redistribution and final settlement of snow. However, determining the origin and composition, e. g., the homogeneity, of drifted snow and associated imprinted climatic signals, is essential but still challenging. Measuring the proxy signal at different stages during the deposition process, i. e., freshly precipitated snow, surface snow during vapour exchange with the atmosphere, drifted snow, and buried snow (as exemplary shown in Fig. 3.13), and combining these data with DEM-derived snow height information, will help to close the gap between accumulation intermittency and the preserved climatic information.

3.4.3 *Implications for the measurement of snow accumulation*

Typically, a snow height sensor integrated in an AWS delivers high temporal resolution data for only a single point and measures the accumulation at one specific location on an ice sheet. Our results show that at least at our study site, such a single point measurement would not deliver spatially representative information on a seasonal timescale. If only a single point in our study area was chosen, it would result in a snow accumulation estimate that could range from 7.4 to 14.8 cm (10 and 90 % quantiles, Fig. 3.4a). The AWS PROMICE estimate is at the lower end of this range (5.8 or 7.6 cm depending on the selected time period, Table 3.2) and significantly deviates from the DEM-derived average snow height change of ~11 or 10.3 cm, respectively.

Accumulation estimates from snow stake farms and grids are averaged over multiple sites and are thus more representative (Kuhns et al., 1997; Eisen et al., 2008), but the remaining uncertainty is expected to depend on the number and the spacing of the stakes (Laepple et al., 2016; Münch et al., 2016). We can test this dependency based on our spatio-temporal data set. To this end, we use the DEM-derived snow height data at $y = 2.5$ m, identify each DEM pixel along this line with a possible snow stake position, and simulate different setups of snow stake samplings with varying stake numbers and spacings. For this, we chose different numbers of stakes between one and more than 200 sampling points with spacings between 10 cm and 10 m (Fig. 3.14). Depending on the chosen number of stakes and spacing, we determine all possibilities of positioning the stakes along the line at $y = 2.5$ m. Each possibility yields an accumulation estimate from averaging across the snow height changes at the stake positions, and we calculate the RMSE between the accumulation estimates from all possibilities and the reference accumulation estimate, i. e., the snow height change from averaging across all positions along the $y = 2.5$ m line.

The RMSE of the simulated snow stake accumulation estimates shows a clear dependency on the number of stakes and the choice of the distance between them (Fig. 3.14). Averaging ten snow stakes measurements with a one metre distance results in a similar error on the accumulation estimate as using only two stakes with a larger distance of 5 m, while an even larger spacing does not further reduce the estimation error. This effect can be explained by the typical size of the surface structures at our study site, which are on the scale of several metres. Sampling the same surface feature multiple times does not increase the representativeness of the accumulation estimate, whereas sampling points farther apart to avoid the same feature contain more independent information. Thus, for study sites similar to EGRIP, stake setups for reliable snow accumulation estimates (RMSE <1 cm) could for example consist either of 25 stakes with 1 m distance or of only seven stakes with 5 m distance, significantly reducing the workload.

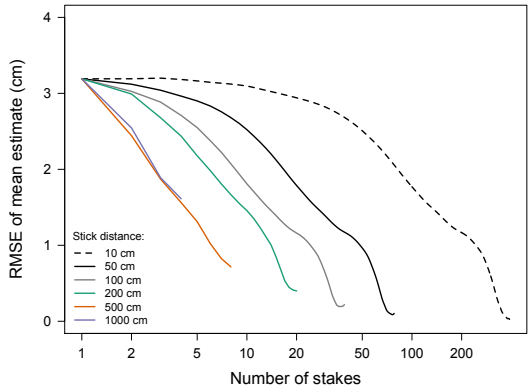

Figure 3.14: The uncertainty of the estimated mean snow height change as a function of the number of sampling points ("stakes") and the distance between them. The mean snow height change is calculated from the DEM data at y = 2.5 m for all possible sequences along the x-direction which consist of N sampling points with a given distance from one point to the next. The figure shows the RMSE between the DEM-derived mean snow height change of the respective sequences and the mean snow height change as calculated using all available sampling points.

3.4.4 *SfM photogrammetry as an efficient surface snow monitoring tool*

We showed that our SfM photogrammetry approach delivers reliable snow height information with an accuracy of ~1.3 cm. The method can be used to characterise the spatio-temporal snow evolution on a spatial decimetre to 100 m scale. Our setup has several advantages in contrast to alternative approaches. Compared to single point measurements, we benefit from spatial information encompassing an area of 195 m² which is easily scalable. Previous laser scanner studies cov-

ered areas of only 40 m² (Picard et al., 2016) and 110 m² (Picard et al., 2019) which can only be extended by placing the laser higher above the ground. However, a laser scanner itself is a high obstacle which can influence the snow redistribution and can thus affect the natural snow accumulation conditions. Our approach also offers the flexibility of repeatedly covering a spatial scale with specific desired dimensions (e. g., an area with a length of 100 m) and orientations. In contrast, this is not possible for a laser scanner that is fixed to one position with a specific radius, or for manual point measurements, sonic snow height sensors or ground penetrating radar (Basnet et al., 2016; Cimoli et al., 2017). In our specific study, we had to reduce the analysed area by removing parts influenced by a parallel snow sampling campaign, but this can be avoided if one is only interested in the DEM evolution.

Furthermore, our approach does not require expensive equipment, as all the necessary items for image acquisition are commercially available. The method can be easily operated in remote areas and the logistical effort is low. It does not require a permanent power supply, which can be a limiting factor for laser scanners and snow height sensors. No specific training for users is needed as is required for airborne studies with aircraft (e. g., Baltsavias et al., 2001), drones (e. g., Hawley and Millstein, 2019) or LiDAR operations (e. g., Deems et al., 2013). Even though our approach is limited by light availability and visual contrasts, which is also reported in many studies (e. g., Nolan et al., 2015; Harder et al., 2016; Cimoli et al., 2017), it has the advantage of being very easy to operate and that it can be used at other study sites without great effort. However, the approach requires a human operator which can possibly limit our method, especially if an application is planned for a longer time period or year-round, and it also needs a mobile base (here, a sledge) to take multiple images along the area of interest. Using less images or stationary cameras (e. g., two fixed cameras) would probably result in a very small surveyed area since the field of view of one image covers only 3-5 m width at the baseline of the study area. We also had to restrict our analysed area to 5 m towards the wind direction due to insufficient image quality and lack of data points.

Besides the field work, our method requires the use of a software with a graphical user interface, manual work of setting the GCPs during the post-processing and a computer with a strong GPU unit. All data, i. e., the photos and the DEMs, are less than 1 TB. The post-processing time and the effort to generate a DEM are less than four hours per DEM and are comparable or even less than reported by other studies (e. g., James and Robson, 2012).

Since the presented setup was used for the first time for this study, days with missing DEMs were the result of human errors, e. g., insufficient number of images or poor overlap between consecutive

photos. To improve future studies, we suggest to use an infrared filter to enhance the image quality and facilitate data acquisition even during cloudy and bad weather conditions (Bühler et al., 2015; Adams et al., 2018). Furthermore, placing the camera higher above the ground could enhance the spatial coverage (Picard et al., 2019). Finally, human errors can be reduced by providing a detailed manual for the data acquisition.

3.5 CONCLUSIONS

We presented high-resolution near-daily elevation models monitoring the surface snow evolution over a three-month period (May to August 2018) from the EGRIP campsite in northeast Greenland using a novel SfM photogrammetry approach. Comparing the DEM-derived snow height evolution to other snow height estimates from single or multi-point measurements showed an overall agreement on the general snow height increase of about 11 cm. The comparison emphasised the natural spatial variability of the snow accumulation on a local scale as well as its non-linear and event-driven character. Based on the observed spatial accumulation field, we recommend that a stake-setup to reliably derive snow height estimates should consist of either 25 sticks with 1 m distance or seven sticks with 5 m distance for locations similar to EGRIP.

Day-to-day changes in the observed snow height provided detailed insights on snowfall and erosion which are essential processes that shape the surface structure and contribute to the internal snowpack structure. The spatial information on wind-driven snow erosion allowed us to showcase the removal of entire snowfall layers which caused an exposure of previous surface structures. The inhomogeneous snow accumulation within our study area led to a flattening of the snow surface and a reduction in surface roughness from ~4-5 to 2 cm as a result of a negative correlation between the initial snow height and the amount of accumulated snow.

Based on the daily snow height information, we simulated the internal snowpack structure for our study area. Main features are the spatially and temporally varying layer thicknesses and the complete absence of snow layers for specific time periods. Extracting single profiles (in space or in time) from this internal layering illustrates the expected variability in proxy data. Averaging samples from several locations is therefore suggested to reduce the local noise and to receive a representative signal.

Proxy data from ice cores are typically interpreted as precipitation-weighted signals. However, we showed that there are significant differences between precipitation and accumulation and that depositional modifications considerably change the structure of the surface snow. Investigating the dependency of proxy signals on the surface

structures and on the general depositional processes leading to the signal imprint at different locations would therefore enhance the understanding and interpretability of proxy records. Combining snow height information, as provided by our study, with proxy data from the same area would be helpful to determine the influence of the internal snowpack heterogeneity on reconstructions from firn and ice cores.

3.6 APPENDIX

3.6.1 *Additional meteorological and photogrammetric information*

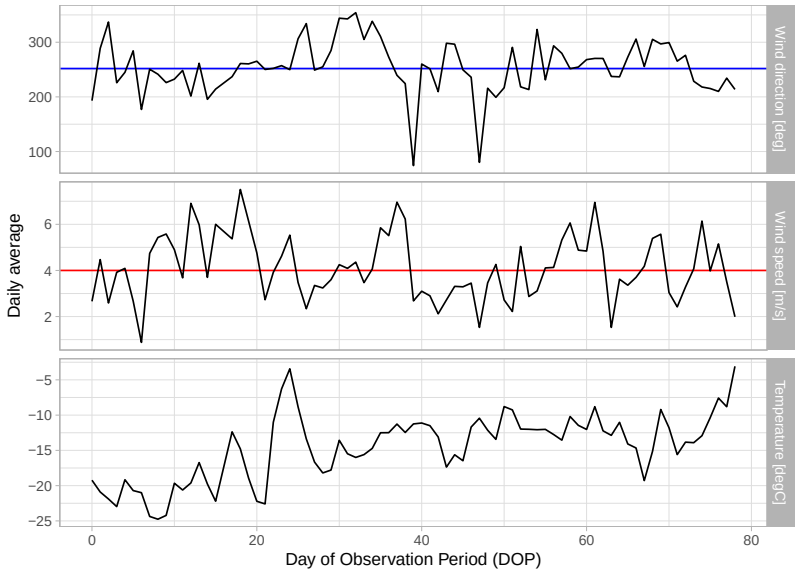

Figure 3.15: Daily averages of meteorological parameters, i. e., wind direction in degrees [°], wind speed in metres per second [$\mathrm{m\,s^{-1}}$], and air temperature in degrees Celsius [°C], measured at 2 m height at the AWS PROMICE for the observation period from 16 May (DOP 1) to 1 August 2018 (DOP 78). In the first panel, the horizontal blue line indicates the average wind direction of 252° during the observation period. The horizontal red line in the second panel marks the threshold wind speed of $4\,\mathrm{m\,s^{-1}}$. Snow transport is enabled when the threshold is exceeded for a 100 h average (Groot Zwaaftink et al., 2013).

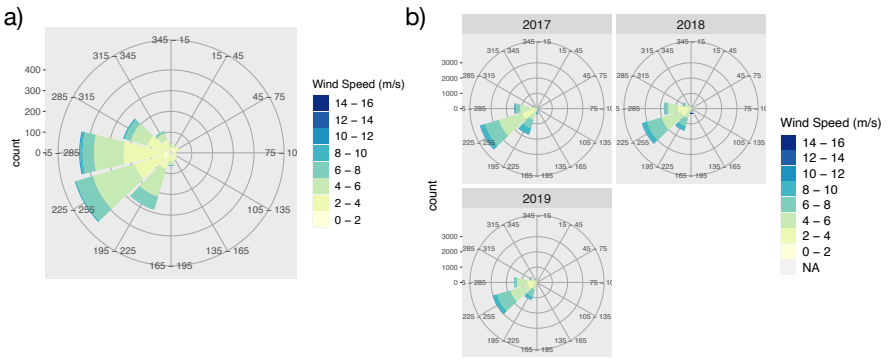

Figure 3.16: Wind characteristics (speed and direction) for the EGRIP camp site recorded by the PROMICE AWS for **(a)** the observation period (16 May to 1 August 2018) and **(b)** the years 2017, 2018, and 2019.

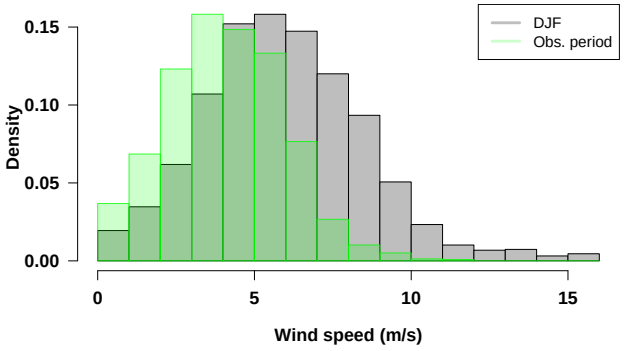

Figure 3.17: Hourly wind speed data from the PROMICE AWS for two different time periods. Wind speeds during the winter months of 2017 to 2019 (December, January, February; DJF; grey) are compared to wind speeds during our observation period (green). The winter months are characterised by higher wind speeds with a mean of $\sim 6\,\mathrm{m\,s^{-1}}$, while the average wind speed during our observation period was $4.1\,\mathrm{m\,s^{-1}}$.

Table 3.3: Detailed information on the fieldwork campaign, including day of observation period (DOP), day of year (DOY), the date, the availability of a DEM, manual snow height measurements at the PT sticks (PT), and manually documented snowfall. We refer to the DOP in the text, figures, and tables.

DOP	DOY	Date	DEM	PT	Snowfall	DOP	DOY	Date	DEM	PT	Snowfall
1	136	16/05/2018	x		x	40	175	24/06/2018			
2	137	17/05/2018				41	176	25/06/2018		x	
3	138	18/05/2018				42	177	26/06/2018		x	x
4	139	19/05/2018	x			43	178	27/06/2018		x	x
5	140	20/05/2018	x	x	x	44	179	28/06/2018		x	
6	141	21/05/2018	x			45	180	29/06/2018			
7	142	22/05/2018	x			46	181	30/06/2018			x
8	143	23/05/2018	x	x		47	182	01/07/2018		x	x
9	144	24/05/2018	x			48	183	02/07/2018			
10	145	25/05/2018	x			49	184	03/07/2018		x	
11	146	26/05/2018	x	x		50	185	04/07/2018		x	x
12	147	27/05/2018	x			51	186	05/07/2018			
13	148	28/05/2018	x			52	187	06/07/2018			x
14	149	29/05/2018	x	x		53	188	07/07/2018			x
15	150	30/05/2018	x			54	189	08/07/2018		x	x
16	151	31/05/2018			x	55	190	09/07/2018			
17	152	01/06/2018	x	x		56	191	10/07/2018	x		
18	153	02/06/2018	x			57	192	11/07/2018	x	x	x
19	154	03/06/2018	x			58	193	12/07/2018			
20	155	04/06/2018	x			59	194	13/07/2018		x	x
21	156	05/06/2018		x	x	60	195	14/07/2018			x
22	157	06/06/2018			x	61	196	15/07/2018		x	x
23	158	07/06/2018		x	x	62	197	16/07/2018	x		
24	159	08/06/2018	x		x	63	198	17/07/2018	x		
25	160	09/06/2018			x	64	199	18/07/2018			
26	161	10/06/2018		x		65	200	19/07/2018			
27	162	11/06/2018	x			66	201	20/07/2018	x	x	
28	163	12/06/2018	x	x		67	202	21/07/2018			
29	164	13/06/2018			x	68	203	22/07/2018			
30	165	14/06/2018	x	x	x	69	204	23/07/2018	x	x	
31	166	15/06/2018	x		x	70	205	24/07/2018	x		
32	167	16/06/2018			x	71	206	25/07/2018	x		
33	168	17/06/2018		x	x	72	207	26/07/2018	x	x	
34	169	18/06/2018			x	73	208	27/07/2018	x		
35	170	19/06/2018	x			74	209	28/07/2018			
36	171	20/06/2018	x	x		75	210	29/07/2018		x	
37	172	21/06/2018	x			76	211	30/07/2018			
38	173	22/06/2018			x	77	212	31/07/2018			
39	174	23/06/2018	x	x	x	78	213	01/08/2018	x	x	x

3.6.2 *Accuracy estimates and validation*

We evaluated our DEMs by analysing the trueness of our DEM-derived snow height estimates compared to reference heights, i. e., manually measured snow heights. For this, we first analysed the bias, i. e., the mean difference between DEM-derived estimates and manually measured reference data. We also investigated the variability and dispersion as well as the overall accuracy of our data by calculating the standard deviation and the root mean square error (RMSE) between DEM-derived and manually measured snow heights, respectively. Here, we report about two different evaluation schemes: (1) DEM-derived snow heights in the vicinity of the PT sticks are compared to manually measured snow heights at the PT sticks to assess the general data quality and uncertainty in the study area; and (2) a sensitivity test is performed on the number and dependency of GCPs by analysing DEM-derived and manually measured reference snow heights from a second, independent validation area.

3.6.2.1 *Data quality assessment via ground control analysis within the study area*

To assess the quality of DEM-derived snow height information, we compared manually measured data to DEM-derived snow heights at the PT stick locations ($\pm$ 10 cm in x and $+10$ cm in y direction) for all days for which both data are available (in total 14 d). We consider the manually measured data as reference values, i. e., as the true snow heights. We find a mean difference of 0.2 cm, a standard deviation of 1.2 cm, and a root mean square error (RMSE) of 1.3 cm. Single daily mean differences, standard deviations, and RMSEs are listed in Table 3.4 and illustrated in Fig. 3.18. Note that some estimates in Table 3.4 are based on less than 30 data points due to missing data caused by the snow sampling. Since manual data can be influenced by individual persons carrying out the measurement, for comparison we also analysed independent snow height estimates measured on the same day at the same locations by different people, which resulted in a mean difference of 0.2 cm, a standard deviation of 0.3 cm, and a RMSE of 0.4 cm, showing that the DEM RMSE of 1.3 cm is a conservative estimate.

Table 3.4: Accuracy estimates for the DEM-derived snow heights in our study area. Mean differences, standard deviations, and RMSEs between the DEM-derived snow heights in the vicinity of the PT stick locations (±10 cm in x and +10 cm in y direction) and the manual snow height measurements at the PT sticks are listed. Data are given for all days of the observation period (DOP) for which both DEM-derived and manually measured snow heights are available (Table 3.3).

DOP	5	8	11	14	17	28	30	36	39	57	66	69	72	78
Mean difference (cm)	0.35	−0.92	−0.02	−0.75	0.11	0.84	0.64	0.17	0.36	0.68	−0.15	0.37	0.93	0.23
Standard deviation (cm)	0.97	0.87	1.21	0.70	0.89	1.53	1.99	0.79	1.24	1.21	1.23	1.39	1.33	1.40
RMSE (cm)	1.01	1.25	1.19	1.00	0.88	1.73	2.06	0.79	1.27	1.37	1.22	1.42	1.60	1.39

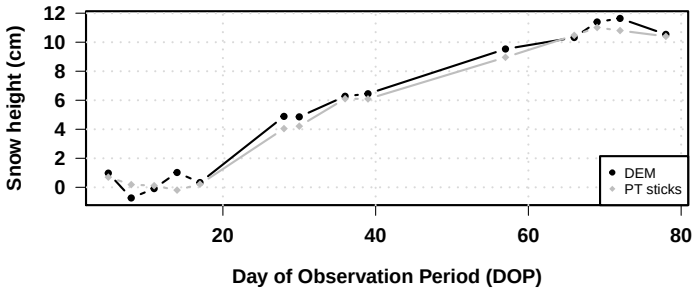

Figure 3.18: Temporal evolution of the DEM-derived snow heights in the vicinity of the PT stick locations (±10 cm in x and +10 cm in y direction, black) and of the manually measured snow heights at the PT sticks (grey). Presented are the data for all days during the observation period (DOP) for which both DEM-derived and manually measured snow heights are available (Table 3.3).

3.6.3 *Validation*

The quality of the DEMs can be affected by many aspects during the image acquisition, the GCP allocation, and the DEM processing. During the image acquisition, the camera resolution, the camera-to-object distance, and the angle of the camera towards the surface can influence the quality of the images (Basnet et al., 2016; Chakra et al., 2019). Moreover, the introduction of GCPs is necessary to generate geo-referenced DEMs. However, the models can be biased towards the fixed positions of the GCPs, i. e., the glass fibre sticks, due to a stronger contrast (Fig. 3.19b and c) (e. g., James and Robson, 2014; Cimoli et al., 2017). Since GCPs are only distributed around the study area, not inside, a detailed analysis on potential biases, such as doming effects inside the area, was performed. Furthermore, we investigate the influence of human mistakes during the aligning of the sticks as well as of potential misalignments of GCP marker points during the processing in Agisoft PhotoScan, which can introduce additional uncertainties.

Ground control analysis with a validation area

To assess possible biases by the distribution of GCPs, we set up a second, independent area with a size of 50 m^2 (10 m × 5 m, Fig. 3.19a). This area was set up with the same procedure as the study area and was surrounded by 13 glass fibre sticks which were used as GCPs. We chose a second area where we physically could walk into, which was not possible for the actual study area, in order to avoid snow height disturbances from the foot steps. Four additional sticks (hereafter called validation sticks) were distributed inside the validation area on different local snow structures and with different distances to the main line. Image acquisition of this area was performed on 3 d to account for varying uncertainties in time (Adams et al., 2018), with

Table 3.5: Accuracy measures for the validation area. Mean differences, standard deviations, and RMSEs between DEM-derived and manually measured snow heights are presented for the validation sticks in the validation area.

Date	16/06/2018	27/06/2018	9/07/2018
Mean difference (cm)	0.71	−1.73	0.04
Standard deviation (cm)	0.67	0.78	0.86
RMSE (cm)	0.92	1.86	0.74

photos taken on 16 June, 27 June, and 9 July 2018. In order not to disturb the DEM generation, the manual snow height measurements at the validation sticks were performed after the image acquisition. By comparing DEM-derived and manually measured snow height estimates at the validation sticks for all three dates, we obtained an overall mean difference of −0.3 cm, a standard deviation of 1.2 cm, and a RMSE of 1.3 cm (Table 3.5).

Camera-to-object distance and local snow height

The accuracy of the DEM-derived snow heights depends on all the steps involved in the SfM workflow. This includes the distance between the camera and the object, i. e., the snow surface in our case (Basnet et al., 2016). We therefore assessed the accuracy of the DEM-derived snow height data at the validation sticks for different camera-to-object distances (between 3.8 and 7 m) and found no dependency on the distance between camera and surface snow.

Since the validation points are distributed on different local surface structures, we also compared the accuracy between varying snow heights but did not find any dependence with respect to the relative snow height.

Dependency on number and alignment of GCPs

As a final step, we evaluated the accuracy of our DEM-derived snow height estimates depending on the number of used GCPs. It is recommended to use at least three GCPs; however, more GCPs provide a better geo-referencing and a reduced sensitivity to a single point (e. g., James and Robson, 2012; Tonkin et al., 2016). We generated DEMs with 5, 8, or 13 GCPs and used the detailed snow height information from the validation sticks as ground control analysis. The mean differences between the DEM-derived and the manually measured snow heights at the validation sticks for the different numbers of GCPs are 0.1, −0.2, and −0.3 cm, respectively, with the standard deviations and RMSEs listed in Table 3.6). The use of more than 10 GCPs leads to a decrease in the standard deviation and RMSE, while the mean difference remains comparable.

This analysis, however, assumes that all glass fibre sticks were vertically and horizontally precisely positioned, that all glass fibre sticks were aligned in a straight line, and that all GCP marker positions were accurately set during the data processing. However, inaccuracies in the GCPs can be caused either by misaligned glass fibre sticks or by misplaced GCP locations during the processing. We therefore investigated these effects by purposely misaligning GCP positions at the top of the glass fibre sticks. Deviations from the documented coordinates were independently drawn from a normal distribution with a mean of 0 cm and a standard deviation of 2 cm, and were added to the initial input marker coordinates in Agisoft PhotoScan leading to the scenarios (a) to (e) below. Furthermore, manual misalignment of GCP locations in Agisoft PhotoScan was simulated by deliberately misplacing the GCPs (scenario f).

a. Change in x coordinates (deviations along the main area).

b. Change in y coordinates (deviations from the arbitrary chosen zero line).

c. Change in z coordinates (deviations in the height of the stick top).

d. Change in x and y coordinates by combining the deviations from (a) and (b).

e. Change in x, y, and z coordinates by combining the deviations from (a), (b), and (c).

f. All 13 GCPs were manually set to the left and right margins of the sticks. The normal coordinates without changes were used.

The DEM-derived snow heights from each of these cases is referenced to a DEM assuming perfectly aligned sticks and correct GCP input marker coordinates. Mean deviations between changed and initial DEMs range from −0.1 to 0.1 cm, standard deviations range from 0.1 to 1.0 cm, and RMSEs range from 0.2 to 1.0 cm (Table 3.7). Based on this assessment, we conclude that inaccurate distributions of GCPs (e. g., tilted sticks and inaccuracies in the x, y, or z coordinates, scenarios a to e) result in an uncertainty of less than 1 cm. Changing the marker position (scenario f) has an even smaller effect on the overall accuracy of the final DEM.

Summary
Uncertainties from manually setting up the transect and distributing the GCP coordinates during the processing, as well as the uncertainty of the GCP alignment, are small, especially compared to the amplitude of snow height change throughout our observation period (11 cm on average). We therefore conclude that our elevation models provide

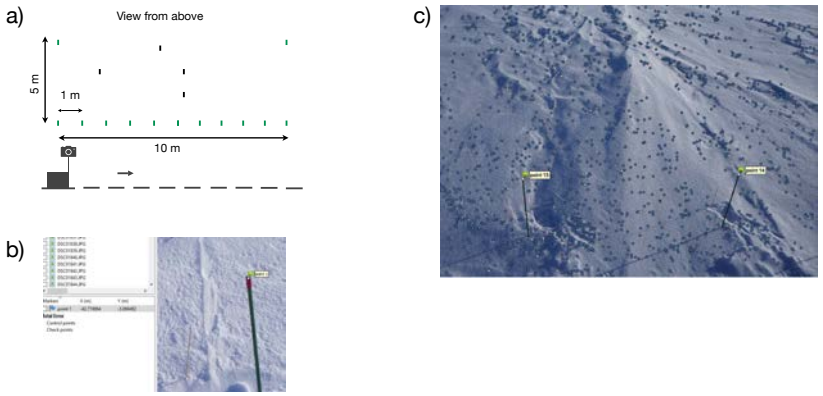

Figure 3.19: Validation area and possible error sources during the processing workflow. **(a)** Schematic illustration of the validation area which was set up according to the same procedure as the main study area. A total of 13 glass fibre sticks were distributed around the validation area (green): 11 sticks were aligned at the downwind side in a straight line with 1 m spacing and 2 sticks at the upwind corners at 5 m distance from the main line. Four additional sticks (validation sticks, black) were distributed inside the area. **(b)** Allocation of GCPs (ground control points) during the process of DEM (digital elevation model) generation. The tops of the glass fibre sticks were used as GCPs and manually checked for correct alignment **(c)**.

reliable snow height estimates with a sufficient accuracy (RMSE of 1.3 cm) for the purpose of our study.

3.6.4 *Overall snow height evolution*

The mean snow height evolution derived from the 2.5 m band shown in Fig. 3.4b consists of ~195 000 individual estimates based on the DEM resolution of 1×1 cm. The snow height evolution for each individual pixel within this band is illustrated in Fig. 3.20, and the relation between the snow height on DOP 1 and the change in snow height from DOP 1 to DOP 78 are illustrated in Fig. 3.22.

The relative horizontal snow height profiles along the 39 m long x axis (Fig. 3.21) show the overall increase in snow height in our study area.

3.6.5 *Surface roughness*

The surface roughness is calculated on 2.5 m long segments along and perpendicular to the main wind direction as illustrated in Fig. 3.23.

Table 3.6: Accuracy measures for varying numbers of GCPs used in the DEM generation. Mean differences, standard deviations, and RMSEs between DEM-derived and manually measured snow heights using 5, 8, or 13 GCPs are shown here. Values are averaged for all three dates for which DEMs are available for the validation area (i. e., 16 June, 27 June, and 9 July 2018).

Number GCPs	5	8	13
Mean difference (cm)	0.09	−0.21	−0.32
Standard deviation (cm)	1.54	1.52	1.23
RMSE (cm)	1.48	1.46	1.27

Table 3.7: Accuracy measures for inaccurate GCP coordinates and positions. Mean differences, standard deviations, and RMSEs between normal DEM-derived snow heights and DEM-derived snow heights with altered input marker coordinates or GCP positions. Scenarios (a) to (f) are explained in the text.

Scenario	(a)	(b)	(c)	(d)	(e)	(f)
Mean difference (cm)	0.04	−0.09	−0.09	0.06	0.08	0.09
Standard deviation (cm)	0.12	0.17	0.92	0.14	0.98	0.10
RMSE (cm)	0.13	0.2	0.92	0.15	0.99	0.14

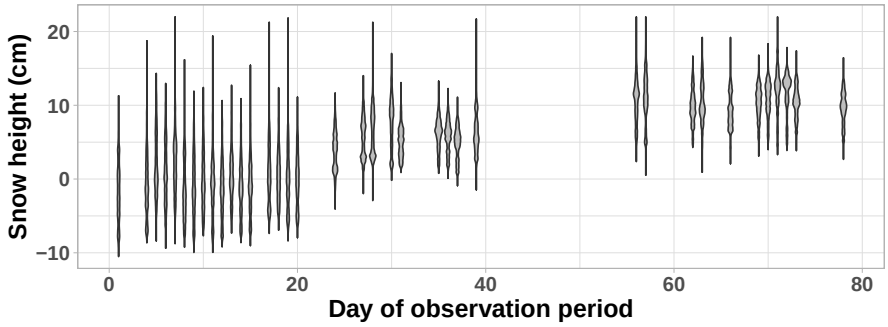

Figure 3.20: Daily variability in snow height throughout the observation period. Each density represents the daily snow height distribution across all individual pixel in the study area. The spatial resolution of the DEM is 1 × 1 cm. Due to increasingly missing data in the area (footsteps and snow sampling positions), the number of available points per day decreases to about 70 % of the initial number of data points towards the end of the observation period (1 885 506 with 64 494 missing data points due to bad image quality on DOP 1 to 1 319 095 on DOP 78 due to foot steps).

Individual peak-to-peak amplitudes of the 2.5 m long segments are shown in Fig. 3.24 and indicate the spread of the individual roughness estimates perpendicular and parallel to the main wind direction as illustrated in the schematic (Fig. 3.23).

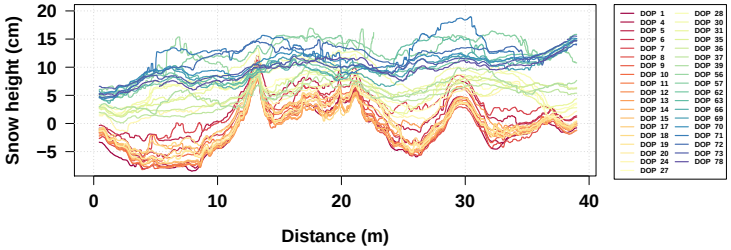

Figure 3.21: Relative horizontal snow height profiles throughout the entire observation period (20-point running median, averaged in the y direction across the 2.5 m band). Different colours represent the different days from DOP 1 to DOP 78, as shown in the legend. Overall, snowfall caused an increase in the snow height at each point in the study area. The first 12 d are shown in more detail in Fig. 3.6.

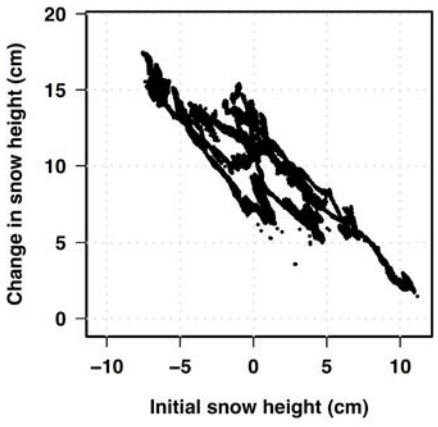

Figure 3.22: Relationship between the initial snow height on DOP 1 and the change in snow height on DOP 78 relative to DOP 1 for each pixel in the study area.

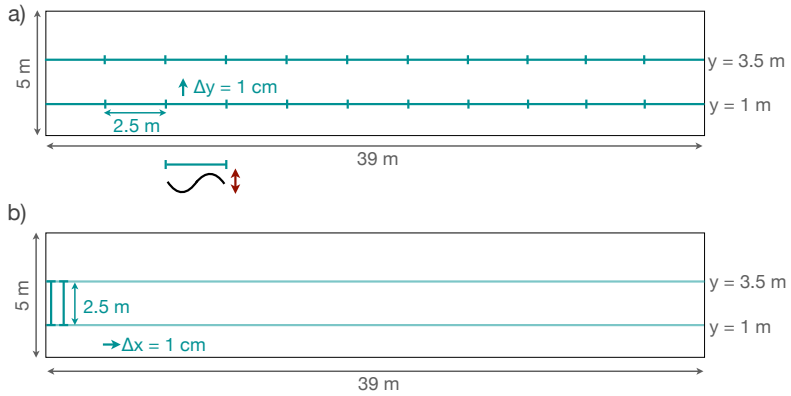

Figure 3.23: Schematic overview of the surface roughness estimates based on Eq. (31). The peak-to-peak amplitude of 2.5 m long non-overlapping segments is calculated **(a)** perpendicular and **(b)** parallel to the main wind direction. Individual estimates are averaged in each case to obtain a representative surface roughness value. Both estimates cover the same area from $x = 0$ to $x = 39$ m and $y = 1$ to $y = 3.5$ m.

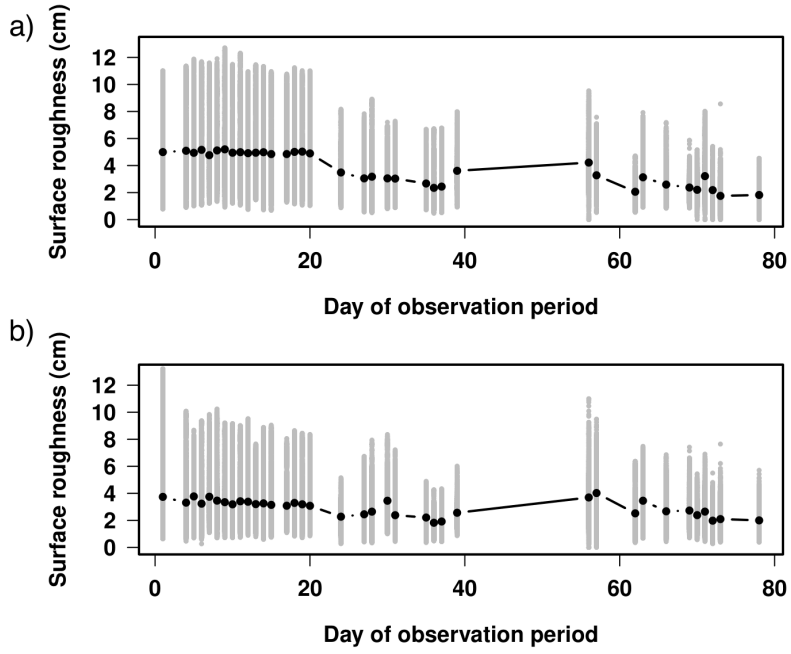

Figure 3.24: Surface roughness estimates throughout the observation period following Eq. (31) **(a)** perpendicular (Fig. 3.23a) and **(b)** parallel to the main wind direction (Fig. 3.23b). Single peak-to-peak amplitudes from the 2.5 m segments are given in grey with the daily average surface roughness in black (Fig. 3.10).

4

A SNAPSHOT ON THE BUILDUP OF THE STABLE WATER ISOTOPIC SIGNAL IN THE UPPER SNOWPACK AT EASTGRIP, GREENLAND ICE SHEET

Alexandra M. Zuhr[1,2], Sonja Wahl[3,4], Hans Christian Steen-Larsen[3], Maria Hörhold[4], Hanno Meyer[1], and Thomas Laepple[1,5]

[1] Alfred-Wegener-Institut Helmholtz Zentrum für Polar- und Meeresforschung, Research Unit Potsdam, Telegrafenberg A45, 14473 Potsdam, Germany

[2] University of Potsdam, Institute of Geosciences, Karl-Liebknecht-Str. 24–25, 14476 Potsdam, Germany

[3] Geophysical Institute, University of Bergen and Bjerknes Centre for Climate Research, Bergen, Norway

[4] Alfred-Wegener-Institut Helmholtz Zentrum für Polar- und Meeresforschung, Research Unit Bremerhaven, 27568 Bremerhaven, Germany

[5] University of Bremen, MARUM – Center for Marine Environmental Sciences and Faculty of Geosciences, 28334 Bremen, Germany

This chapter is submitted to:
Journal of Geophysical Research: Earth Surface, 2022.

Abstract. The stable water isotopic composition in firn and ice cores provides valuable information on past climatic conditions. Because of uneven accumulation and post-depositional modifications, time series derived from adjacent cores differ significantly and do not directly reflect the temporal evolution of the precipitated snow isotopic signal. Hence, a characterization of how the isotopic profile in the snow develops is needed to reliably interpret the isotopic variability in firn and ice cores. By combining digital elevation models of the snow surface and repeated high-resolution snow sampling of a transect at the EastGRIP campsite on the Greenland Ice Sheet, we are able to visualise the buildup and post-depositional changes of the snow column across one summer season. To this end, 30 cm deep snow profiles were sampled on six dates at 20 adjacent locations along a 40 m transect. Near-daily photogrammetry provided snow height information for the same transect. By combining both methods, this unique data set demonstrates the buildup of the strong horizontal heterogeneity with some locations showing winter snow (low delta values) and others summer snow (high delta values) at the same depth. The spatial variability can be attributed to the observed strong influence of the prevailing surface features on the location and the amount of

new snow accumulation. Our data set suggests that this uneven accumulation has a major impact on the imprint of the atmospheric climate signal in the upper snowpack, and also provides the basis for quantification of how post-depositional modifications influence the snow column after deposition.

4.1 INTRODUCTION

Glaciers and ice sheets are a key component of the Earth's climate system. They are formed by deposition of snow through time which also builds up a chronology of climatic information. The stored information within stable water isotope records (e. g., $\delta^{18}O$) from ice cores is commonly used as a palaeo-thermometer to infer past temperature variations (e. g., Dansgaard, 1964; Jouzel and Merlivat, 1984; Jouzel et al., 2003).

While water isotopes are a proven proxy for temperature on long timescales and have been used to reconstruct continuous temperature series dating back ~800,000 years (EPICA community members, 2004), isotope profiles from Antarctica and Greenland depict a low signal-to-noise ratio (SNR) on annual to decadal temporal scales (Fisher et al., 1985; Graf et al., 2002; Münch and Laepple, 2018) and single records only show a poor correlation among each other (Karlöf et al., 2006; Münch et al., 2016).

On local scales from several metres to hundred metres, snow is spatially unevenly deposited and the final accumulation is primarily driven by depositional modifications of the initial snowfall. Driving processes are wind scouring, snow drift and redistribution, potentially building up characteristic surface features that influence the local accumulation (Fisher et al., 1985; Kuhns et al., 1997). This creates substantial heterogeneity between individual firn profiles (i. e., stratigraphic noise) (Fisher et al., 1985), and causes low correlations between adjacent firn or ice core records (Karlöf et al., 2006). The characteristics of this stratigraphic noise have recently been visualised and analysed using density (Laepple et al., 2016; Weinhart et al., 2020) and isotopic data (Münch et al., 2016, 2017) from two-dimensional trenches in Antarctica.

The classical interpretation of the $\delta^{18}O$ signal in firn and ice cores assumes that the isotope signal reflects the signal of the deposited snow (e. g., Lorius et al., 1969). It is further assumed that this signal is primarily affected by downward advection due to new deposited snow (Münch et al., 2017) and modified by densification and isotopic diffusion until the depth of firn-ice transition (Johnsen, 1977; Johnsen et al., 2000). However, in recent years, the basic principle of this palaeo-thermometer has been questioned (e. g., Town et al., 2008; Steen-Larsen et al., 2014; Casado et al., 2021). Studies show that the original isotopic composition of snow is considerably altered after the

initial deposition by molecular exchange processes at the snow-air interface at and beneath the surface, including wind-driven ventilation, sublimation, vapour deposition and snow metamorphism (Town et al., 2008; Harris Stuart et al., 2021; Wahl et al., 2021). Such modifications have been reported from laboratory experiments (e. g., Sokratov and Golubev, 2009; Ebner et al., 2017; Hughes et al., 2021) and observations from locations in Greenland (Steen-Larsen et al., 2014) and Antarctica (Ritter et al., 2016; Casado et al., 2021) with different accumulation rates.

To estimate the uncertainty introduced by stratigraphic noise and vapour-snow exchanges, to correct for the noise in climate variability estimates (Münch and Laepple, 2018), or to even use the heterogeneity as a proxy for past surface roughness (Wolff et al., 2005; Barnes et al., 2006), there is a need to characterise the driving processes accurately to parametrise and model them.

Here, we designed and performed a study to analyse for the first time the buildup of the isotopic signal in the upper snowpack over a summer season for a study site next to the deep drilling site of the East Greenland Ice-core Project (EastGRIP) in the accumulation zone of the Greenland Ice Sheet (GrIS). Based on previous studies and findings, we designed and performed an extensive two-dimensional snow sampling scheme making use of the liner technique (Schaller et al., 2016). Throughout the two-months observation period, we sampled six 30 cm deep transects, sub-sampled them with 2 cm resolution and analysed the samples for their stable water isotopic composition. Additionally, near-daily digital elevation models (DEMs) for the same area were generated applying an established Structure-from-Motion (SfM) photogrammetry technique (Zuhr et al., 2021a) to quantify the changes in the snow surface height. The combination of both methods results in a unique data set that provides important information on the temporal evolution of the heterogeneity of the isotopic signal in firn and ice cores.

4.2 METHODS AND DATA

4.2.1 *Study site*

A 40 m long transect was studied next to the EastGRIP campsite in northeast Greenland (75° 38′ N, 36° 00′ W, ~2,700 m altitude, Fig. 4.1a). The site is characterised by an annual mean temperature of −29 °C and prevailing westerly winds (Madsen et al., 2019). The studied transect was oriented perpendicular to the main wind direction with the walking area on the downwind side of the transect, following a similar setup as Zuhr et al. (2021a). Annual accumulation rate estimates vary between 10 and 14 cm w.eq. yr^{-1} (Vallelonga et al., 2014; Schaller et al., 2016; Karlsson et al., 2020). The influence of post-depositional

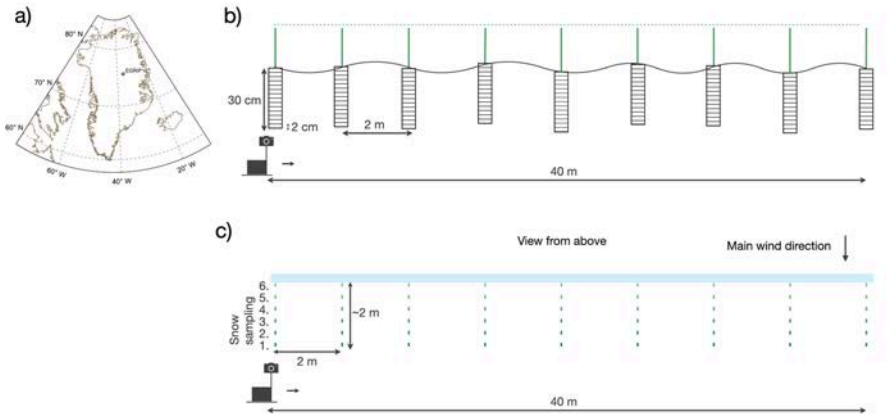

Figure 4.1: Location of the study site (abbreviated with EGRIP, a), and illustration of the used setup for DEM generation (b) and snow sampling (c). Along the 40 m transect, glass fiber sticks with 2 m spacing mark the snow sampling positions and were used as ground control points during the DEM generation (b). The dashed line indicates that all sticks were levelled to the same height. (c) At each stick position, snow profiles were sampled which had to move by about 30 to 40 cm with every sampling day. The blue area provides a representative snow height along the transect which was used to analyse the temporal evolution of the snow height and to simulate the signal content within the snow surface. For a better overview, the number of profiles and sticks is reduced and does not represent the original setup.

influences of vapour-snow exchange on the snow isotopic composition have been studied at the same location for the same observation period in (Wahl et al., 2021).

A nearby automatic weather station (AWS) from the Programme for Monitoring of the Greenland Ice Sheet (PROMICE) has been measuring meteorological data since 2015 (Fausto et al., 2021). During the observation period from 27 May to 27 July 2019, a mean temperature of -10.3 °C and an average wind speed of 4.5 m s^{-1} mainly from the west (~240 °, standard deviation of 46 °) were observed (Fig. 4.2, yellow area marks the study period).

4.2.2 *DEM generation*

Two-dimensional maps of the snow surface (i. e., DEMs) were generated for each day with suitable weather conditions to obtain detailed information on the snow height and its evolution throughout the observation period. For this, we carried out a SfM photogrammetry approach following the method established in Zuhr et al. (2021a). Relative to their study, we used a Sony α7R camera with a fixed lens of 35 mm focal length, mounted at a height of ~2 m (instead of ~1.5 m). Our DEMs have the same resolution of 1 x 1 cm while the im-

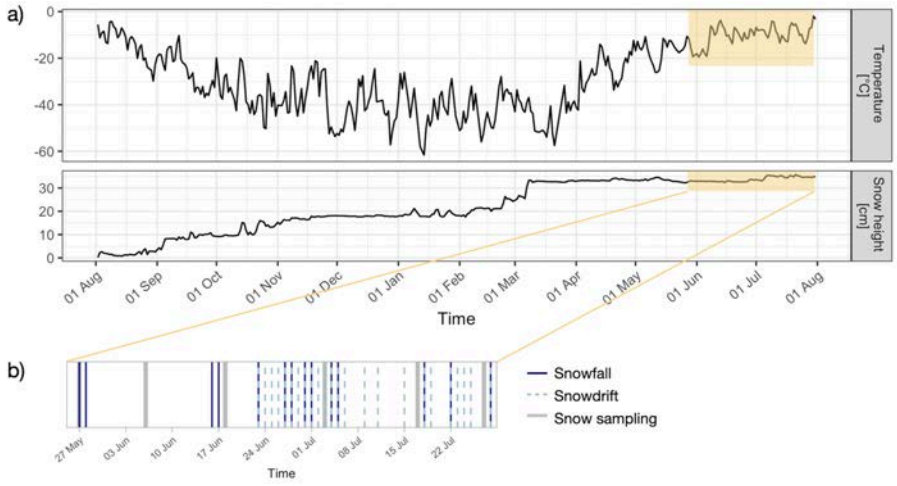

Figure 4.2: Meteorological observations showing in a) daily mean temperature and relative snow height from 1 August 2018 to 1 August 2019 measured at the PROMICE AWS, and b). The yellow area denotes the summer period covered in this study and for which manual observations of snowfall (in total 13 x, dark blue) and snowdrift (in total 23 x, light blue) are illustrated in b). In addition, the snow sampling dates are shown as well (grey).

proved setup enabled a larger coverage of 400 m² (= 40 x 10 m) than the 195 m² in Zuhr et al. (2021a).

At the beginning of the season, glass fiber sticks with 2 m spacing were distributed along the transect and used as ground control points for an absolute georeferencing (Fig. 4.1b) (e. g., James and Robson, 2012). The DEM generation was carried out with the software Agisoft Metashape and the snow height at the first sticks on 27 May 2019 was defined as an arbitrary zero level to which all further DEMs were referenced. Due to the improvements of the setup, the accuracy of the DEMs should be equal (1.3 cm) or better than in Zuhr et al. (2021a).

DEMs are available for 30 out of 62 days of the observation period providing an effective data coverage of 48 %. Missing days are caused by cloudy and overcast conditions which impede the alignment of the photos. The largest gap between consecutive DEMs is three days, but mostly less. In case a DEM was not available for a day of snow sampling, a DEM from the day before or after was used instead.

4.2.3 *Isotope measurements*

To investigate the spatial and temporal evolution of the stable water isotopic composition of the upper firn layer, vertical snow profiles were collected at 20 positions with 2 m spacing along the 40 m transect on six days during the 2019 summer season (27 May, 6 June, 18 June, 3 July, 17 July and 27 July 2019). The sampling distance is small enough to resolve the scale of spatial variations in accumulation (Zuhr et al.,

2021a) and the length is a trade-off to capture some representative dune features while still being feasible to sample in a single day.

Carbon fiber tubes of 30 cm length and 10 cm diameter were used to collect mini-cores at each position (Fig. 4.1c), following the liner technique described in Schaller et al. (2016). The sampling positions were filled with snow and flattened after each sampling to avoid disturbing surface features. Each position was moved by about 30 to 40 cm towards the main wind direction between successive samplings to avoid contamination from the previous sampling.

The mini-cores were sampled immediately after the collection with a 2 cm vertical resolution which is enough to resolve the isotopic variations as faster scales are damped by the isotopic diffusion. Depending on the recovered length of the snow cores (26 to 30 cm), the number of samples of single profiles varied between 13 and 15. The maximum sampled depth for single locations alternates between 26 and 30 cm; thus, covering at least half a year of accumulation.

All snow samples were airtightly stored in Whirl-Paks® and transported to Germany in a frozen state. Stable water isotope measurements were performed in the Stable Isotope Facility at the Alfred-Wegener-Institute in Potsdam, Germany, using a cavity ring-down spectrometer from Picarro Inc. (model L2140-*i*). Isotopic ratios are reported in the standard δ-notation given in per mil (‰) following

$$\delta = \frac{R_{sample}}{R_{reference}} - 1 \tag{41}$$

Craig (1961b) with R_{sample} as the isotopic ratio of the sample and $R_{reference}$ the ratio of an in-house reference water calibrated against the international VSMOW/SLAP scale (Gonfiantini, 1978). All data were corrected for memory and instrumental drift as suggested in van Geldern and Barth (2012) using the calibration algorithm described in Münch et al. (2016). Only $\delta^{18}O$ will be analysed in this study. The mean measurement uncertainty for $\delta^{18}O$ derived from an independent quality control standard was 0.13 ‰ and 0.09 ‰ for all used reference waters.

4.2.4 *Simulation of the snowpack layering*

To interpret the buildup of the internal signal content and the imprinted temperature information, we simulate the expected layering using the near-daily snow height information from the DEM's and the temperature data from the nearby AWS. Using the daily temperature as a proxy for the signal in the new accumulated snow, this model provides the expected internal structure of the snow column.

We extract the DEM-derived snow height for a 20 cm wide field behind the sampling locations (Fig. 4.1c, blue area) and use it as a representation for the evolution of the mean snow height along the

40 m transect. This area is chosen because it is well-covered by the DEMs, close to the sampling positions (within 2 m) and, hence, representative of the snow height evolution at the sampling spots while not disturbed by the sampling itself. Using this snow height information, we simulate the expected internal structure of the upper snowpack, similar to Fig. 11 in Zuhr et al. (2021a), by assigning the daily mean temperature to the respective day-to-day change in the snow height. We also account for snow erosion by considering negative changes in the snow height.

We perform this simulation for each day with available DEMs, starting on the day after the first sampling, i. e., 28 May 2019, and show the results for the same five following days at which the snow sampling was performed. To qualitatively compare the simulated two-dimensional structure, which is still in temperature units, to our observed isotope profiles, we manually adjust the colour-scales. We do not transfer the temperature to isotopic values since the temporal slope cannot be determined with the temporally limited data set. The comparison is not affected by this, because it would not change the correlation due to the linear character of the calibration.

4.2.5 *Expected uncertainty due to changes in the sampling position*

To study the temporal evolution of a snowpack, it would be desirable to sample the same place and exactly the same snow at each time step. This is, however, not possible due to the destructiveness of snow sampling. Thus, sampling positions were moved each time by 30 to 40 cm towards the main wind direction, i.e. perpendicular to the transect, to avoid disturbances (Fig. 4.1c). As we move the sampling positions with time, we have to consider the heterogeneous character of surface snow (Münch et al., 2016, 2017). At the end, the first and last sampling locations are ~2 m apart, similar as the spacing between two adjacent sampling positions. As a measure of the expected $\delta^{18}O$ variability, we calculate the standard deviation of the differences (in sampling depth) from the same sampling day between adjacent profiles. The mean of all standard deviations accounts to 2.9 ‰. Hence, we cannot detect any significant change in the $\delta^{18}O$ data smaller than 2.9 ‰.

4.3 RESULTS

4.3.1 *Snow height evolution*

The snow height along the transect is illustrated for each day (Fig. 4.3) and shows an overall increase of ~6 cm from the end of May to the end of July 2019. This increase is, however, not spatially uniform and influenced by precipitation intermittency and snow redistribu-

tion as indicated by manual observations of snowfall and snowdrift (Fig. 4.2b). While the (net) snow accumulation exceeded 10 cm snow depth change at few locations (e. g., at the transect positions 2, 38 and 40 m), other spots received no or only very little new snow (e. g., the positions at 12 and 36 m). Comparing the first (Fig. 4.3, blue line) and the last (yellow line) day of the sampling period shows a flattening of the surface topography over time as troughs (between 0 and 10 m, 18 and ~32 m and between 37 and 40 m) receive more snow than the local elevation maxima at ~13 and 36 m. Further, we also observe decreases in the snow height between consecutive days, indicating snow erosion. The dune between 11 and 14 m in the beginning of the observation period is eroded/sublimated with time. Similarly, the second dune between 32 and 38 m first becomes more pronounced before erosion/sublimation flattens this feature towards the end of July.

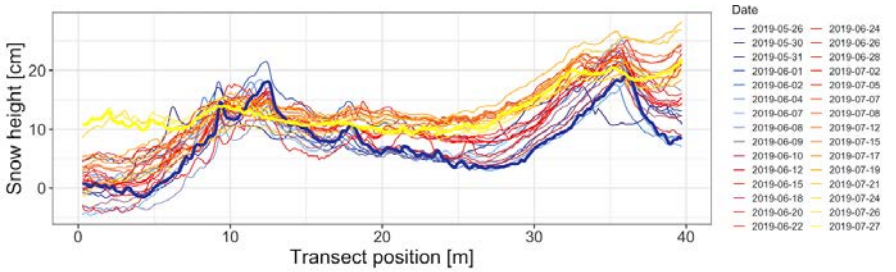

Figure 4.3: Temporal evolution of the DEM-derived snow height (20-point running mean) along the 40 m transect. The colour code indicates the day throughout the observation period from blue representing end of May via red to yellow indicating end of July. The bold lines in blue and yellow denote the first (27 May 2019) and last sampling day (27 July 2019), respectively.

4.3.2 *Mean isotopic records*

Mean $\delta^{18}O$ values across all profiles increase from -38.3 ‰ on 27 May to -35.8 ‰ on 3 July, followed by a decrease to -36.3 ‰ towards the end of July 2019 (Fig. 4.4, vertical lines) with $\delta^{18}O$ values of individual samples ranging between -57.0 and -21.9 ‰ across all sampling days. The mean $\delta^{18}O$ profile on 27 May 2019 is characterised by a local isotopic minimum at ~9 cm sampling depth (Fig. 4.4). Towards the end of July, this layer is found at 17 cm depth with almost no change in the $\delta^{18}O$ value. Throughout June and July, the lowest mean value changed from -42.5 to -41.4 ‰. We assign this part of low $\delta^{18}O$ values to the winter period (Fig. 4.2). On each sampling day, the highest $\delta^{18}O$ value is always found at the surface and increases with time due to the deposition of new, isotopically enriched snow throughout the summer period and/or due to sublimation induced enrichment of surface snow (Fig. 4.4). The mean $\delta^{18}O$ surface values across all 20 sampling locations rose from -30 ‰ in May to -23.4 ‰ in July.

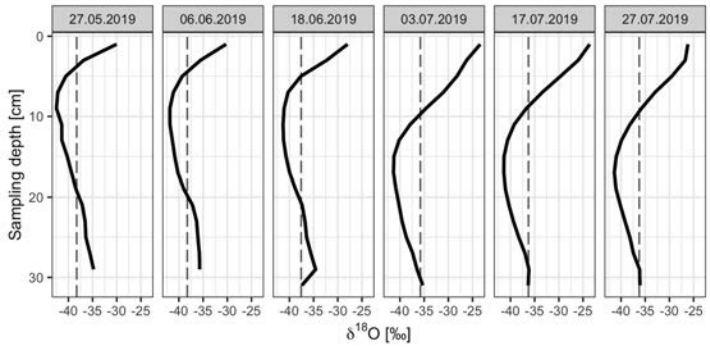

Figure 4.4: Mean $\delta^{18}O$ profiles vs. sampling depth for each of the six sampled days. No correction for downward advection due to new snow accumulation is performed. The dashed vertical line shows the mean $\delta^{18}O$ value for each day.

4.3.3 *Combining isotopic data with snow height information*

Analysing the two-dimensional temporal sampling in combination with snow height information (Fig. 4.5) offers insights into the spatial and temporal $\delta^{18}O$ variability. On 27 May, the transect was characterised by a layer with depleted $\delta^{18}O$ values between -47 and -42 ‰ with a local minimum in the profile at 10 m (Fig. 4.5, dark blue). The vertical extent of this depleted layer varies between 5 and 10 cm within most profiles. However, the profile at 36 m has an exceptionally large vertical extent of ~24 cm, while the nearby profiles at 28 and 30 m do not show this layer at all. The depleted layers were mostly surrounded by isotopically more enriched layers.

The relative depth of the depleted $\delta^{18}O$ values changes over time due to a downward advection from new snow accumulation whereas the layers themselves, such as the depleted area between 10 and 25 m, change only slightly. The low $\delta^{18}O$ values between 30 and 40 m are noteworthy because they remain quasi constant and only show slight changes with on average 1.1 ‰ with time for the lowest $\delta^{18}O$ values (Fig. 4.5).

The amount of the successively deposited snow in the upper layers corresponds to the thickness of the difference in snow height as observed in the DEMs (Fig. 4.5, grey line indicates the first sampling day). The change in snow height between the first and the third sampling, i. e., from 27 May to 18 June, indicates a gradual filling of the trough between 15 and 27 m with the deposition of snow with slightly enriched $\delta^{18}O$ values with on average -30.2 ‰. In contrast, the new layers on 3 and 17 July, defined via changes in the snow height, indicate a deposition of strongly enriched mean isotopic ratios of -25.1 and -23.6 ‰, respectively, and a continued flattening of surface undulations. This snow stayed until the end of July. The last sampling day

showed a locally constrained accumulation in a corner between 2 and 4 m with a more negative $\delta^{18}O$ value than the previous depositions.

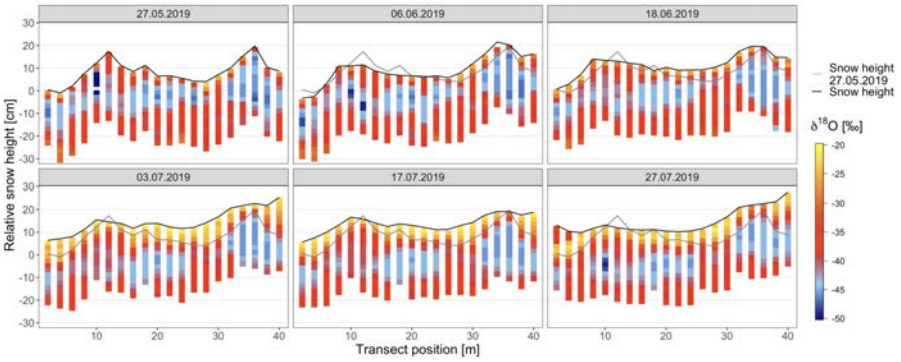

Figure 4.5: Two-dimensional view on the $\delta^{18}O$ variability of each profile on a respective sampling day aligned with DEM-derived snow height information. The black line indicates the relative snow height for each individual sampling day and the grey line the snow height of the first sampling day, i. e., 27 May 2019. Transect position corresponds to the distance along the transect (Fig. 4.1c).

4.3.4 *Observed vs. simulated composition*

A better understanding of the buildup of the upper snowpack can be achieved by visually comparing the observed isotopic composition (Fig. 4.6a) with the expected precipitation-weighted temperature content (Fig. 4.6b) within the two-dimensional transects. This comparison will enable us to distinguish between changes due to depositional processes (redistribution, erosion or new deposition) and post-depositional modifications of the snow (air-snow exchange).

The $\delta^{18}O$ data suggests that the accumulated snow throughout the observation period represents several snowfall events with spatially heterogeneous layer thicknesses (Fig. 4.6a). In the beginning of July, for example, most of the surface snow is characterised by layers of strongly enriched snow up to -21.9 ‰. This layer persists for several weeks, especially at the positions between 0 and 30 m. Similar features are found in the expected temperature content as shown by the simulations (Fig. 4.6b). On 27 July, however, the area between 0 and 6 m indicates differences between the observed isotope ratios and the simulated internal layers from DEM-derived snow height changes.

4.3.5 *Changes in the isotope signal over time*

The presented analysis suggests that the main changes of the isotope signal through time is the addition of snow with a distinct isotope signature at the surface or a retrieval of material, i.e. wind-driven uptake and redeposition. To test whether the isotope signal is also changing

over time in the depth range not directly affected by accumulation or erosion, we analyse the isotope anomaly maps in the zones that were not eroded at any point during the two months (Fig. 4.7, dotted line) after removing the time-mean two-dimensional isotope profile (Fig. 4.7).

Even if no change in the isotopic composition in a given snow parcel would have occurred, we would expect some variations due to the horizontal changes in the sampling position and, thus, sampling a new snow column every day. As the changes in the horizontal sampling position relative to the mean position is less than 1 m (i. e., half of the 2 m spatial range), we use 2.9 ‰ (two times the expected standard deviation for a 1 m horizontal shift) as a heuristic threshold for local significance.

In general, more than 86 % of the anomalies are within ±2 SD, i. e., 2.9 ‰ (Fig. 4.7) suggesting that only some locations show changes not explainable with spatial heterogeneity. Stronger changes are observed close to the surface while changes further down in the snowpack are weaker. Whereas the sign of change seems systematic near the surface from negative anomalies in the beginning of the season to positive anomalies at the last sampling, the sign of the changes further down in the snow column is varying.

4.4 DISCUSSION

We present a new approach to study the buildup of the isotopic signal in the snow column, combining elevation models from SfM photogrammetry and a transect of snow profiles sampled throughout a two-months field season.

4.4.1 *Evolution of the snow surface*

Our new DEM data confirms the results found in a similar transect in the previous year (Zuhr et al., 2021a), i. e., the snow deposition is irregular in space, ranging from a net negative change (erosion) up to an increase of 14 cm (Fig. 4.3) throughout the season. Similar to 2018, the snow surface became generally flatter during the season in 2019, as troughs were filled up and peaks eroded, also visible in the negative correlation between the initial snow height and the amount of accumulated snow (not shown here). This supports that the observed pattern was not a specific feature of the season in 2018 but is a systematic behaviour for this area in northeast Greenland, similar to findings from other locations with comparable accumulation characteristics in central Greenland (Kuhns et al., 1997; Albert and Hawley, 2002).

4.4.2 *Two-dimensional view of water isotopes in the snow*

Our two-dimensional profiles (40 m wide and 30 cm deep) of the isotopic variations (Fig. 4.5) provide the first visualization of the $\delta^{18}O$ signal and stratigraphic noise in snow from the Greenland ice sheet, similar to the findings from snow trenches in Antarctica (Münch et al., 2016, 2017). We find a pattern of enriched-depleted-enriched isotopic composition, presumably indicative for seasonal layering in addition to horizontal isotopic variability which is caused by local stratigraphic noise. While our profiles are too short to quantify the stratigraphic noise, a very rough estimation of the signal-to-noise variance ratio (SNR = (σ_v^2 - σ_h^2) / σ_h^2), comparing the horizontal (σ_h^2) and vertical (σ_v^2) variance (Münch et al., 2016), results in a SNR of 1.8. This is consistent with typical SNR values documented for Greenlandic sites that range from 1 to 3 (Fisher et al., 1985) and considerably higher than the SNR of 0.6 found in the trench studies in Antarctica from an area with approximately half of the annual accumulation than our study site. The lower stratigraphic noise (thus higher SNR) at our site compared to Antarctica is expected as it is mainly determined by the ration of the annual layer thickness (about twice as high at this study site) relative to the thickness of snow surface undulations (similar at both sites) (Fisher et al., 1985).

The two-dimensional profiles also demonstrate that single vertical profiles, such as firn cores, can miss individual seasons, as observed in this study by a missing winter layer at transect position 32 m as well as reported from single ion records (Gfeller et al., 2014). On the contrary, seasons can be strongly overrepresented in other close-by profiles, e. g., in the profile at 36 m (Fig. 4.5).

4.4.3 *Buildup of the snowpack isotopic signal*

The isotopic signature in snow and firn profiles has previously been interpreted to reflect the temporal development of the isotopic signature of snowfall. However, the signal at a specific depth is influenced by the interplay between spatially variable processes, such as snow accumulation, redistribution (Ekaykin et al., 2004; Picard et al., 2019) as well as post-depositional modifications at the surface (Steen-Larsen et al., 2014; Hughes et al., 2021) and within the upper snowpack (Johnsen, 1977; Town et al., 2008). To shed light on these processes at and beneath the surface, we make use of the two-dimensional isotopic data set and investigate the signal deposition and its subsequent development through time.

The first order pattern, that is visible when averaging across all $\delta^{18}O$ profiles to minimize the stratigraphic noise (Fig. 4.4) is in agreement with the traditional perception of a downward movement ('advection') of the depleted winter layer throughout the season as more

isotopically enriched summer snow is deposited at the top. Taking into account the respective snow height of each of the spatially distributed profiles (Fig. 4.5) confirms, that the downward advection of the winter layer is caused by the snow accumulation as the isotope profiles, accounting for the elevation changes, remains largely constant through time below the layer affected by accumulation and erosion.

To test for systematic changes in the isotopic composition of the snow column through time, for example by forced ventilation (Town et al., 2008; Ebner et al., 2017), we analysed the temporal $\delta^{18}O$ anomalies in the two-dimensional snow transect (Fig. 4.7). This comparison is limited by the magnitude of expected variations caused by the spatial change of the sampling locations between consecutive samplings. We were, thus, only able to separate temporal changes larger than 2.9 ‰ from this spatial sampling effect. Given this limitation, our study did not indicate significant alterations below 10 cm depth throughout the two-months period. However, we found few changes closer to the surface that might be related to isotopic diffusion. For future studies, the noise from the spatial shift of sampling locations should be reduced in order to allow testing for potential post-depositional alterations. This could be achieved with optimized sampling schemes that enable shorter distances between successive sampling positions.

During the summer season, the changes at the surface were characterised by a spatially unequal deposition of warmer, i. e., isotopically enriched snow (Fig. 4.6). To see which signal we would expect in the simplest case without post-deposition or snowdrift, we constructed a model in which we piled up layers according to the topographical changes with a signal representing the respective daily air temperature. The visual comparison to the observed isotope signature in the surface snow shows that, while the general characteristics of higher $\delta^{18}O$ values corresponding to higher temperatures are captured (described in chapter 3.4), there are also some differences. A thin layer of isotopically depleted snow between 30 and 40 m along the transect was deposited between the first and the second sampling and persisted throughout the summer season (Fig. 4.6a). This layer is also represented in the simulation by cold temperatures (Fig. 4.6b). In contrast, the alternating sequence of high and low isotopic values between 0 and 6 m is, however, not shown in the simulation.

This mismatch can have several reasons. One reason could be the quality and temporal gaps in the DEMs as for some days the low visual contrast of the flat surface did not allow a faithful reconstruction of the snow height. However, the largest gap between consecutive DEMs is three days. Moreover, Zuhr et al. (2021a) investigated in detail the uncertainties of the photogrammetry method and concluded that the observed magnitude of snow height changes is larger than

the uncertainty of 1.3 cm. For future studies, improvements in the DEM recovery rate, for example by using infrared filters (Bühler et al., 2017), or the use of other DEM generating methods, such as laser scanners (Picard et al., 2019), could reduce these uncertainties.

Another aspect might be the patchy deposition of drifting snow at the surface which can substantially contribute to accumulation at one site and might lead to the deposition of snow at another site containing an environmental fingerprint from another location (Ekaykin et al., 2002; Picard et al., 2019). Zuhr et al. (2021a) showed a significant negative correlation between the mean daily wind speed and the mean daily snow height change and with the temporal snow height evolution in this study, it seems to be a persistent behaviour of the summer snow surface at EastGRIP. Summer wind conditions, thus, favour substantial snow drift that affects surface structures (Zuhr et al., 2021a) as well as the development of the isotopic layering.

Besides these rather mechanical contributions, additional modifications of the snow's isotopic signature might be caused by post-depositional processes at the very surface in the absence of snowfall or drift. In particular, sublimation is found to imprint a climate signal into the surface layer during precipitation-free periods in the summer (Casado et al., 2021; Hughes et al., 2021; Wahl et al., 2021). Hughes et al. (2021) performed sublimation experiments at the same study site and reported that the isotopic composition within the top few centimetres is affected by the atmospheric diurnal temperature cycle. (Harris Stuart et al., 2021) documented significant change in the isotopic composition of the surface snow following precipitation events, in effect masking the initial precipitation second order isotopic composition. However, high accumulation rates might dampen the magnitude of observed changes and bury the snow too quickly (Waddington et al., 2002), that the large spatial heterogeneity at our study site (Fig. 4.7) in combination with our setup cannot resolve the magnitude of these post-depositional modifications.

Repeating the study, ideally with a more frequent sampling interval than applied here (biweekly interval) to also cover snowfall-free periods, would allow for a better detection of post-depositional changes at and near the surface. In addition, combining our study approach with sampling and measurements of the isotopic composition of snowfall would allow us to perform more detailed simulations and to compare the skill of simulations to our measurements including or excluding processes, such as sublimation. Finally, making use of second-order parameters, such as d-excess and ^{17}O-excess, might provide additional constraints to evaluate the role of post-depositional processes on the preserved signal since these parameters are highly sensitive to non-equilibrium processes (Casado et al., 2021). The question of the driving processes that ultimately determine the isotopic signal remains, therefore, open but points to a combination of the pre-

cipitated isotope signal altered by post-depositional processes. Snowpack models, that consider exchanges with the vapour, could be used to estimate expected changes which could help to develop new study designs.

4.5 CONCLUSION

We investigated the temporal evolution of the snow surface in northeast Greenland based on snow height information and two-dimensional isotopic transects. We identified uneven snow deposition as the main driver for buildup and preservation of stratigraphic noise, confirming the conceptual model by Fisher et al. (1985). In addition, the isotopic data revealed that the climatic signal is mainly introduced at the surface by either snowfall or depositional and post-depositional modifications of the surface layer, such as snowdrift and snow-air exchange. Changes in the isotopic composition below ~10 cm were not significant and, therefore, cannot confirm wind pumping or other processes altering the properties of buried snow, confirming similar studies in Antarctic snow (Münch et al., 2016). However, the strong spatial variability limited the ability to detect significant changes smaller than 2.9 ‰ with the current setup during a two-months summer period.

We have shown that this study design, which combines snow height information with isotope records, allows to quantify the buildup of the snow column. In a next step, extending the gained knowledge through refined simulations of the expected isotopic composition of the snow column and comparisons with parameters such as d-excess, could allow an evaluation of the presented snowpack buildup. Ideally, these simulations should also include post-depositional changes, such as sublimation, as the influence of vapour-snow exchange processes has shown to have the potential to alter the snow isotopic composition.

Further optimizations of the study design with, for example, a higher temporal resolution to capture periods without snowfall or improved devices to reduce the spatial shift between consecutive sampling positions, should facilitate the investigation of the post-depositional changes. Additionally, improvements in the measurement of the isotopic composition in snowfall (Stenni et al., 2016), and a method to differentiate between snowdrift and fresh snow are needed to refine our understanding and simulations of the signal formation. Repeating this or improved study designs in regions with different environmental conditions, such as the low accumulation regions on the East Antarctic Plateau or other areas in Greenland with higher accumulation rates, should enhance our overall understanding of the climatic signal contained in stable water isotopes in polar firn and ice cores.

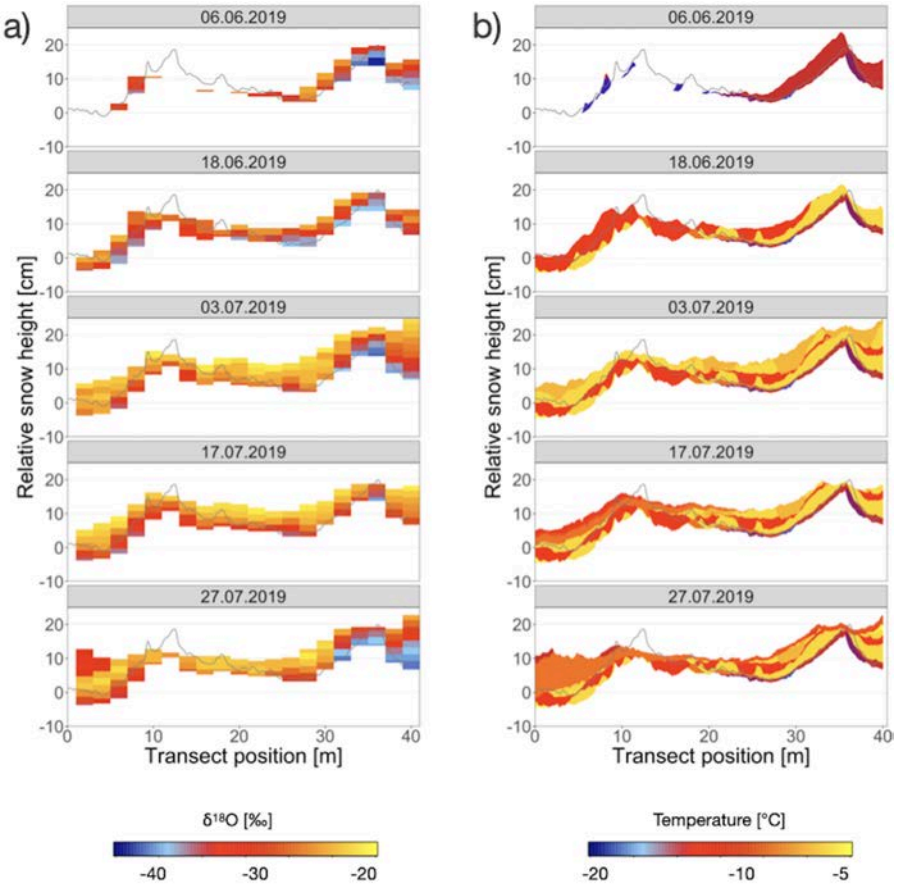

Figure 4.6: Two-dimensional view of the internal structure of the newly deposited snow from a) observations and b) simulations using DEM-derived snow height information and daily temperatures from the nearby AWS. The $\delta^{18}O$ observations in a) denote the newly accumulated snow during the observation period. The simulation in b) assigns the daily temperature to all positions which received accumulation on a given day. The thickness might be influenced by missing DEMs (largest gap is three days) which could lead to a slightly overestimated thickness of specific layers. The grey line indicates the snow height on the first day of sampling.

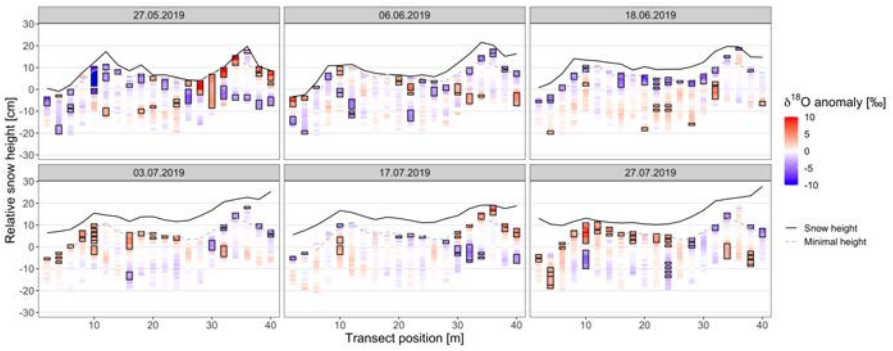

Figure 4.7: Anomalies of the mean isotopic composition for each sample. Only sample positions are considered which have a value on each sampling day. New snow accumulation is therefore not included. Black squares indicate significant anomalies, i. e., larger deviations than twice the local uncertainty of 1.45 ‰. The dashed grey line indicates the lowest snow height observed during the entire observation period and the black line the snow height for each sampling day, respectively.

5 GENERAL DISCUSSION AND CONCLUSIONS

This dissertation presents five research articles that investigate proxy signal formation in palaeoclimate archives. In particular, the articles cover the deposition and imprint of the signal as well as post-depositional modifications and the final preservation within sedimentary archives. To this end, novel sampling schemes were developed and applied to characterise and quantify the inherent heterogeneity in marine sediments and polar ice sheets. The results are primarily based on field observations and statistical analyses, accompanied by laboratory experiments and simulations. The following general discussion connects the presented studies and elucidates their contribution to an improved understanding of the proxy signal and related climate reconstructions.

5.1 HETEROGENEITY IN SEDIMENTARY ARCHIVES

5.1.1 *Quantifying archive-internal heterogeneity*

The radiocarbon content in planktonic foraminifera in marine sediments is traditionally used as a tracer of time since deposition (Arnold and Libby, 1949; Libby et al., 1949). This information can additionally be seen as a tracer of mixing by determining the heterogeneity of ^{14}C-derived age estimates (Peng et al., 1979). Chapter 2 uses this relation to quantify mixing extent and intensity via the horizontal heterogeneity in ^{14}C data at a study site in the South China Sea (SCS).

Indeed, a multitude of studies with X-ray radiographs (Bouma, 1964; Wetzel, 1991; Löwemark and Werner, 2001), high-resolution mass spectrometry imaging (Wörmer et al., 2014, 2019), radioactive tracers (Peng et al., 1979), novel instrument developments (Wacker et al., 2010, 2013) and modelling efforts (Goldberg and Koide, 1962; Berger and Heath, 1968; Guinasso and Schink, 1975; Trauth, 1998) indicated large spatial heterogeneity within marine sediments, but a data-based quantification of the dimensions of sediment mixing is missing so far. The presented evaluation of the horizontal age-heterogeneity is based on a grid of several sub-cores from a marine boxcore and is complemented by X-ray radiographs.

The heterogeneity is quantified by means of different sample types, i. e., small and large volume samples as well as small and large numbers of measured specimens. Several measurements of large volume samples from one depth layer reveal the spatial differences between

age estimates. Because these differ more than the measurement uncertainty, these estimates can be seen as a measure of the spatial heterogeneity (Fig. 2.3). The effect of different sample volumes (Fig. 2.6) suggests that the spatial dimension of a sample is, in this case, larger than the scale of sediment displacement. Replications of measurements within one sample reveal that a single estimate comprises a substantial spread of younger and older specimens, strongly deviating from the true mean age of the respective depth layer with decreasing numbers of measured specimen. The magnitude of the spread is indicative for the vertical extent of mixing leading to the observed heterogeneity. Hence, the heterogeneity within one sample can be determined by replications of measurements of small and large numbers of specimen and different sample volumes (Fig. 2.3).

X-ray radiographs confirm the estimation of the mixing extent by visualising the net displacement of sediment material (Fig. 2.5) and additionally indicate bioturbation below the so-called mixed layer depth (Fig. 2.1). Even though sampling multiple sub-cores and measuring more than 100 ^{14}C samples is very labour- and cost-intensive, the benefit of this unique data set is a remarkable visualisation of the inhomogeneous sedimentary structure (Fig. 2.6). Combining both three-dimensional data sets, the ^{14}C data and the X-ray images, reveals detailed insights into the archive-internal age-heterogeneity in marine sediments and the importance of post-depositional modifications on the apparent time uncertainty in past chronologies. However, this approach was only applied at this single location in the SCS and for this archive type. Local climate and sedimentation conditions might influence the heterogeneity; hence, analysing the archive-internal heterogeneity at other sites is therefore suggested.

As a second archive, the spatio-temporal heterogeneity of snow accumulation and isotopic composition within the upper snowpack is analysed because both influence the formation of the proxy signal in polar ice. A Structure-from-Motion (SfM) photogrammetry technique is used to generate near-daily two-dimensional maps of the snow surface (Fig. 3.3) for two consecutive summer seasons at the campsite of the East Greenland Ice-Core Project (EGRIP) on the Greenland Ice Sheet (GrIS) (Chapters 3 and 4). The application of this method was not new (e. g., Nolan et al., 2015; Cimoli et al., 2017). Its usage for a very flat white area without distinguished features challenges the generation of reliable Digital Elevation Models (DEMs) causing gaps in our records (Chapter 3). Nevertheless, the analysis of the DEMs reveals an event-based character and spatial variability of snowfall (Figs. 3.4a and Fig. 4.3). Besides this intermittency, the SfM method denotes the importance of snow erosion and redistribution to the overall snow accumulation (Figs. 3.5 and 3.6). The quantification of the redistribution is indicative of the heterogeneous character of snow accumulation in both studied summer seasons which is associated with a preferen-

tially deposition in troughs (Figs. 3.9, 3.11) and 4.3). Similar methods with a comparable precision have been used to quantify accumulation conditions at other locations on the GrIS (Kuhns et al., 1997; Albert and Hawley, 2002) and on the East Antarctic Plateau (EAP) (Picard et al., 2016, 2019). However, the SfM method is more flexible regarding the deployment, the surveyed location and the covered spatial dimensions and allows additional snow sampling relating the accumulation variability to the heterogeneity of stable water isotopes within the upper snowpack.

The combination of snow height information with two-dimensional isotopic transects enables a characterisation of the internal structure and reveals the heterogeneous buildup of the upper snowpack (Chapter 4, Figs. 4.5 and 4.7). Trench studies from the EAP revealed strong internal heterogeneity of the density of snow and its isotopic composition (Laepple et al., 2016; Münch et al., 2016, 2017; Weinhart et al., 2020). Compared to these studies, the advantage of the presented novel sampling design is the visualisation of the temporal evolution of the isotopic signature, its large internal heterogeneity and the buildup of stratigraphic noise at the surface throughout a two-month period (Fig. 4.5) based on the detailed snow height information and the repeated snow sampling. While this data set provides remarkable insights into vertical and horizontal isotopic variations and the preservation, i. e., downward shift, of these signals (Figs. 4.4 and 4.5), an ultimate quantification of the driving processes modifying the signal during (snow redistribution) and after the deposition (vapour-snow exchange) cannot be represented with this study design (Fig. 4.7.) Laboratory and field experiments as well as simulations are additional important tools to estimate the magnitude of change caused by particular processes (Appendix A and B). The observations as well as the experimental studies emphasise the heterogeneous imprint (Fig. 4.6) of the climatic signal at the surface and hint towards a potentially strong relation between the proxy signal formation and the archive-internal heterogeneity.

5.1.2 *Relationship between proxy signal formation and archive-internal heterogeneity*

Observed low correlations of palaeoclimate time series from cores close to each other suggest that the recording of climate signals might be subject to regional variations and/or superimposed by non-climatic noise in marine sediments (Reschke et al., 2019b, 2021) and polar ice sheets (Karlöf et al., 2006; Münch and Laepple, 2018). For instance, radiocarbon data from adjacent cores from a multicorer deployment showed an unexpected low reproducibility of age estimates. Their discrepancies exceeded the typically assumed uncertainties (Fig. 7 in Dolman et al., 2021a). This observation raises the

question, whether the internal heterogeneity on these local scales is real and how much this affects the depth-age assignment in climate reconstructions. To shed light on this relation between the proxy signal and heterogeneity, Chapter 2 quantifies and investigates the three-dimensional ^{14}C variability in several sub-cores from a marine boxcore on spatial scales below 30 cm.

Bioturbation is known to cause spatial and temporal variability in marine sediments. The extensive ^{14}C data set in Chapter 2 reveals a more realistic estimate of the inherent time uncertainty in proxy data which results from sediment net displacement. The mixing extent is quantitatively determined with a depth of ~8 cm. Hence, a homogeneous ^{14}C distribution from the surface down to this depth is expected (e. g., Peng et al., 1979; Berger and Killingley, 1982). However, this is not apparent in any of the analysed sub-cores (Fig. 2.3) and is further supported by X-ray radiographs revealing substantial bioturbation also at greater depths (Fig. 2.5). This indicates that post-depositional processes within the archive substantially modify the sedimentary structure and that the proxy-climatic relationship contains uncertainties larger than previously assumed (Fig. 2.7).

Post-depositional modifications within the marine sediments limit the proxy-climate relationship by adding substantial time uncertainty. BACON, an often-used depth-age model (Blaauw and Christen, 2011), considers only the reported measurement error by the laboratory for each individual ^{14}C data point. It neglects the constraints caused by bioturbation (Figs. 2.7 and 2.8). However, when accounting for the uncertainty, the spatial variability of marine sediments is actually covered by the depth-age model (Fig. 2.11). This calls for a consideration of uncertainties not only in the climatic signal, but also in the temporal information as both are affected by the archive-internal heterogeneity. These error terms support and explain the observation of increasing correlations of proxy records when accounting for time uncertainty (Reschke et al., 2021). They can further explain a number of observations, including the mentioned differences in age models from nearby records from a multi-corer (Fig. 7 in Dolman et al., 2021a) as well as observed age-model reversals in marine records within large proxy-compilations (such as the data compilation by Marcott et al., 2013).

Similarly investigations of the proxy signal content within polar ice sheets also benefit from two or three dimensions. Snow trench studies, performed in Dronning Maud Land on the EAP, offer a wealth of information on the heterogeneity of different parameters within the upper snowpack (Laepple et al., 2016; Münch et al., 2016, 2017; Weinhart et al., 2020). Münch et al. (2017) found a discrepancy between the isotopic signal in the upper firn and the observed temperature and concluded that processes prior to or during the snow deposition, and hence the signal deposition, are responsible for this difference.

This motivated a modification of their study design to repeated samplings of small trenches combined with a SfM method next to the EGRIP campsite (Chapters 3 and 4).

Following general assumptions of a precipitation-weighted signal imprint (Persson et al., 2011; Sime et al., 2011; Casado et al., 2020), the SfM method confirms an event-based character of the snowfall and the accumulation (Figs. 3.4a, 3.6 and 4.3) and with this an undersampling of the environmental conditions. However, the final snow accumulation corresponds to only ~35 % (Fig. 3.12) of the temporarily deposited snow which suggests that the $\delta^{18}O$ signal in the upper firn cannot purely represent a precipitation-weighted climatic signal, contradicting earlier assumptions (Steig et al., 1994; Persson et al., 2011). This local-scale redistribution is further complicated by the interplay between prevailing surface structures and drifting snow. We find a reduction of the surface roughness (Fig. 3.10) alongside a negative correlation between the snow height and the amount of accumulated snow (Fig. 3.9) during two consecutive summer seasons, visualising the development of stratigraphic noise (Fisher et al., 1985).

Based on the detailed snow height information and the repeated snow sampling, Fig. 3.11 and Fig. 4.5 remarkably illustrate the internal heterogeneity, expressed in varying layer thicknesses of the snow age and the isotopic composition, respectively. The visualised preservation of local stratigraphic noise (Fig. 4.5) and its influence on the horizontal isotopic variability within the upper snowpack confirm a strong influence of the surface spatial heterogeneity on the isotopic composition within the snowpack, referred to as stratigraphic noise, as it was suggested by Fisher et al. (1985). Compared to similar trench studies from the EAP (Münch et al., 2016, 2017), the extensive data set from the EGRIP location provides valuable insights into the signal preservation at a site with higher accumulation rates, but not the entire imprint of the isotopic signal might be precipitation-driven.

Vapour-snow exchange processes within the snow column but also with atmospheric vapour further influence the recorded isotopic signature (Johnsen, 1977; Town et al., 2008; Steen-Larsen et al., 2014; Casado et al., 2021). Field experiments conducted at the EGRIP camp site as well as laboratory experiments suggest modifications of the $\delta^{18}O$ signal in the upper few centimetre of the snow during precipitation-free periods (Appendix Chapters A and B). Analyses on the temporal change of the isotopic profiles, however, do not reveal any significant modifications within the upper 30 cm of the snow column throughout the studied summer period (Chapter 4). This might be due to the large inherent heterogeneity within the upper snowpack or the limited vertical extent of the mentioned processes. Further processes, in particular firn diffusion, are not considered in the presented studies but might alter the $\delta^{18}O$ signal as well.

The relationship between the signal of interest, i. e., the atmospheric temperature, and the proxy, i. e., $\delta^{18}O$, is affected by a multitude of processes within the archive. The presented studies provide a characterisation of the uncertainties introduced by precipitation intermittency, snowdrift, stratigraphic noise and post-depositional modifications for a study site on the GrIS. Future analyses with refined sampling designs, e. g., a higher temporal resolution, at the same study site as well as a characterisation of the discussed processes at other sites with different climatic conditions are needed to gain an overall estimate of the archive-internal heterogeneity and its relevance for the proxy-climate relation within firn and ice cores.

5.2 METHODS TO IMPROVE CLIMATE RECONSTRUCTIONS

Reassessing the generation of proxy data through refined sampling schemes and optimised measurement protocols can lead to an improvement in the reliability and reproducibility of palaeoclimate reconstructions. Depending on scientific objectives and available funding, current practice in, for instance, palaeoceanography can be optimised by adapting the sampling and measurement process for age estimates to more thoughtful study designs, as Chapter 2 suggests. This includes improvements regarding the sample volume, the number of measured specimen, the down-core density of data points and, in particular, replications of measurements with small and large numbers of specimen. These replications are needed to quantify the internal heterogeneity and to account for the influence on uncertainty in time or the climatic proxy variable (Fig. 2.7).

To this end, improvements in depth-age models by e. g., implementing an inflatable error term to account for the reconstructed net displacement as well as future instrument developments, are key to advance these efforts. For example, recent developments enabled measurements of small numbers of specimen and individual foraminifera analysis (IFA) (Wacker et al., 2010, 2013), i. e., providing information on the age distribution within a single sample. However, it is not recommended to routinely apply these measurements for dating purposes (Lacourse and Gajewski, 2020) or general climate reconstructions from sediments with low accumulation rates, due to the uncertainty associated with individual signal carriers (Thirumalai et al., 2013).

Proxy system models (PSMs) are a powerful tool to complement observational and proxy data (e. g., Evans et al., 2013; Dee et al., 2015; Dolman and Laepple, 2018). These models perform a forward simulation of a multitude of processes along the way from the climatic input to the observation from an archive. *PRYSM* is an example for oxygen-records (Dee et al., 2015) and *sedproxy* for marine-archive proxies (Dolman and Laepple, 2018). If basic parameters, such as the sedimenta-

tion rate and the mixing extent, are known, *sedproxy* can be used to simulate an expected proxy record from a marine sediment core as well as related uncertainties, depending on the number of measured specimen. Besides an improvement in the proxy understanding and the assessment of uncertainties, PSMs could be applied more frequently to also refine sampling setups.

The ice core palaeoclimate community is in general aware of the spatial heterogeneity in ice, but faces different challenges than the palaeoceanographic questions. Isotopic data from firn and ice cores are usually continuously sampled without gaps in the vertical dimension. The question of sampling density is, therefore, not as important as in marine sediment cores. However, the information contained in the signal is still not holistically understood and the need for more mature sampling schemes is great. This includes a precise estimation of the amount of initial snowfall with its spatial and temporal variations where the Chapters 3 and 4 present a step towards an improved understanding via refined study designs. Additionally, the analysis of parameters as d-excess can help to disentangle depositional from post-depositional modifications but requires a more profound understanding of the processes determining this factor and accurate measurements.

Modelling approaches with varying complexities have also been carried out to examine the isotopic signal in firn and ice cores for both ice sheets on Greenland and Antarctica (Sime et al., 2011; Sjolte et al., 2011; Dee et al., 2015; Laepple et al., 2018; Touzeau et al., 2018; Casado et al., 2020). These models have in common that they use temperature and an artificial representation of the particle flux, e. g., snowfall from global atmospheric reanalysis data sets. These snowfall estimates do not match the observed accumulation (Fig. 3.12) and disregard redistribution, which is an important factor (Chapter 3). Further important processes, such as intermittency and diffusion, are considered, for instance, in the forward model by Casado et al. (2020). A major caveat of their study, also stated by the authors, is the missing implementation of vapour-snow exchange processes which might in particular affect the surface snow isotopic composition during precipitation-free periods as shown in Appendix Chapters A. Yet, this process is missing in their model but also in *PRYSM* or other approaches. A simple simulation was performed in Appendix Chapter B, but did not provide a comprehensive quantification of the contribution of vapour-snow exchange processes. Hence, these attempts do not close the apparent gap between atmospheric temperature and observed $\delta^{18}O$ variability, but provide first steps towards an improved representation of the relevant processes within the upper snow and firn layer (Chapter 4); however, a more profound representation in e. g., archive-models, implemented in PSMs, is missing.

5.3 OUTLOOK: IMPLICATIONS FOR PROXY-BASED CLIMATE RECONSTRUCTIONS

In recent years, the question of the highest possible temporal resolution of isotope time series from firn and ice cores as well as marine sediment cores is increasingly coming to the fore and important for quantifying Holocene climate variability. The effective temporal scale at which isotope records can be meaningfully interpreted is limited by a variety of processes, among which precipitation intermittency, depositional and post-depositional modifications, stratigraphic noise and diffusion have a large share. In this dissertation, these processes are tackled for the EGRIP camp site with a modern accumulation rate of ~14 cm w.eq. yr^{-1} (Schaller et al., 2016). The presented results can be used to estimate the signal content in isotope records from the GrIS.

The overall noise level in isotope records is partly depending on precipitation intermittency (Helsen et al., 2005; Sime et al., 2009; Persson et al., 2011) and stratigraphic noise (Fisher et al., 1985; Laepple et al., 2016; Münch et al., 2016) which in turn, influence the signal content in the proxy data (Münch and Laepple, 2018; Casado et al., 2020). Fisher et al. (1985) estimated SNRs between 1.1 and 2.7 for isotopic records from different locations on the GrIS. Estimates from Antarctica, for example for Dronning Maud Land, increase from 0.1 on inter-annual time scale up to 1.5 on multi-centennial scales (Münch and Laepple, 2018). Due to the limited temporal coverage of less than one year, the isotope data from EGRIP provide a tentative SNR estimate which amounts to 1.8 (Chapter 4). Furthermore, the influence of vapour-snow exchange processes, especially diffusion, have not been taken into account so far. These processes would probably greatly reduce the SNR, as simulations show that the processes in combination with large noise terms determine the spectral structure of the observed signal (Laepple et al., 2018). However, the simulated diffusion was based on the diffusion model of Johnsen et al. (2000) which was reported to overestimate diffusion lengths in firn in Greenland (van der Wel et al., 2015). In an optimistic interpretation, the tentative SNR value for the EGRIP site argues that isotopic records from Greenland might have a larger climate-proxy signal share which might stem from a higher accumulation rate at EGRIP than at Dronning Maud Land with only half the accumulation rate than EGRIP (Fisher et al., 1985; EPICA community members, 2006; Münch and Laepple, 2018).

SNRs from marine sediments strongly depend on the time uncertainty of the proxy records. Chapter 2 shows that time uncertainty is usually underestimated. Therefore, the reported retrieval timescale of centennial to millennial scales (Reschke et al., 2019b) seems to be an optimistic estimate which might need a renewed evaluation considering a larger time uncertainty.

Overall, the presented isotope and ^{14}C data sets provide a step towards an improved understanding of the signal content in proxy data, which might allow reconstructions from Greenlandic isotope records on a higher temporal scale than the possible decadal to multi-decadal time scales from Antarctic records (Münch and Laepple, 2018; Casado et al., 2020). Additional statistical methods or stacking of several records can further improve the SNRs as well as improvements of forward models and PSMs with more realistic characterisations of previously neglected processes, e. g., vapour-snow exchange (Chapter B), and a better representation of the archive-internal heterogeneity can support the estimation of the noise level in proxy data and improve the signal retrieval timescales.

5.4 CONCLUDING REMARKS

One of the key challenges in closing the gap between the climatic signal and the archived proxy signal in firn and ice cores is the evaluation of the contribution of blowing snow to the statistical properties of $\delta^{18}O$. Although Robert Peary, in 1898, may not have been as aware as we are today of the wealth of the information contained in snow, he was similarly interested in the phenomenon shaping the apparent uncertainty to some extent, as his reflections show:

> *"There is one thing of special interest to the Glacialist - the transport of snow on the ice-cap by the wind"*

The ultimate motivation of palaeoclimate research is to learn about and constrain the climate prior to the instrumental era. This, however, ultimately depends on the reliability of proxy data that are stored in palaeoclimate archives and contain the long-term recording of environmental parameters. A fundamental understanding of the archive-internal heterogeneity and associated uncertainties is urgently needed to provide a holistic understanding of the embedded climatic information.

In recent years, major progress in the understanding of the Earth's climate system and its response to various external and anthropogenic forcings has been achieved by the acquisition of new palaeoclimate information as well as by fundamental research on the inherent uncertainties in proxy data on different temporal and spatial scales. The question of the highest possible temporal resolution of isotope time series from polar ice sheets as well as marine sediment cores is increasingly coming to the fore. With the presented steps towards improved uncertainty estimates and a characterisation of the climate signal deposition and modification, this dissertation greatly contributed to answering this question and revealed the need for further studies.

BIBLIOGRAPHY

Adams, M. S., Y. Bühler, and R. Fromm (2018), Multitemporal Accuracy and Precision Assessment of Unmanned Aerial System Photogrammetry for Slope-Scale Snow Depth Maps in Alpine Terrain, *Pure and Applied Geophysics* 175, 3303–3324, DOI: 10.1007/s00024-017-1748-y.

Albert, M. R. and R. L. Hawley (2002), Seasonal changes in snow surface roughness characteristics at Summit, Greenland: implications for snow and firn ventilation, *Annals of Glaciology* 35.

Alves, E. Q., K. Macario, P. Ascough, and C. Bronk Ramsey (2018), The Worldwide Marine Radiocarbon Reservoir Effect: Definitions, Mechanisms, and Prospects, *Reviews of Geophysics* 56 (1), Publisher: John Wiley & Sons, Ltd, 278–305, DOI: 10.1002/2017RG000588.

Anderson, D. M. (2001), Attenuation of millennial-scale events by bioturbation in marine sediments, *Paleoceanography* 16 (4), 352–357, DOI: 10.1029/2000PA000530.

Andree, M. (1987), The Impact of Bioturbation on AMS 14C Dates On Handpicked Foraminifera: A Statistical Model, *Radiocarbon* 29 (2), Publisher: Cambridge University Press, 169–175, DOI: 10.1017/S0033822200056927.

Arnold, J. R. and W. F. Libby (1949), Age Determinations by Radiocarbon Content: Checks with Samples of Known Age, *Science* 110 (2869), 678–680, DOI: 10.1126/science.110.2869.678.

Arthern, R. J., D. P. Winebrenner, and D. G. Vaughan (2006), Antarctic snow accumulation mapped using polarization of 4.3-cm wavelength microwave emission, *Journal of Geophysical Research: Atmospheres* 111 (D6), DOI: 10.1029/2004JD005667.

Baltsavias, E. P., E. Favey, A. Bauder, H. Bosch, and M. Pateraki (2001), Digital Surface Modelling by Airborne Laser Scanning and Digital Photogrammetry for Glacier Monitoring, *The Photogrammetric Record* 17 (98), 243–273, DOI: 10.1111/0031-868X.00182.

Bard, E., M. Arnold, J. Duprat, J. Moyes, and J.-C. Duplessy (1987), Reconstruction of the last deglaciation: deconvolved records of d18O profiles, micropaleontological variations and accelerator mass spectrometric14C dating, *Climate Dynamics* 1 (2), 101–112, DOI: 10.1007/BF01054479.

Bard, E. (2001), Paleoceanographic implications of the difference in deep-sea sediment mixing between large and fine particles, *Paleoceanography* 16 (3), PP. 235–239, DOI: 200110.1029/2000PA000537.

Barker, S., W. Broecker, E. Clark, and I. Hajdas (2007), Radiocarbon age offsets of foraminifera resulting from differential dissolution

and fragmentation within the sedimentary bioturbated zone, *Paleoceanography* 22 (2), PA2205, DOI: 10.1029/2006PA001354.

Barnes, P. R. F., E. W. Wolff, and R. Mulvaney (2006), A 44 kyr paleoroughness record of the Antarctic surface, *Journal of Geophysical Research* 111 (D3), DOI: 10.1029/2005JD006349.

Basnet, K., M. Muste, G. Constantinescu, H.-C. Ho, and H. Xu (2016), Close range photogrammetry for dynamically tracking drifted snow deposition, *Cold Regions Science and Technology* 121, 141–153, DOI: 10.1016/j.coldregions.2015.08.013.

Benson, L. V. and J. W. C. White (1994), Stable isotopes of oxygen and hydrogen in the Truckee River-Pyramid Lake surface-water system. 3. Source of water vapor overlying Pyramid Lake, *Limnology and Oceanography* 39 (8), 1945–1958, DOI: 10.4319/lo.1994.39.8.1945.

Berger, W. H. and G. R. Heath (1968), Vertical mixing in pelagic sediments, *Journal of Marine Research* 26 (2), 134–143.

Berger, W. H. and R. F. Johnson (1978), On the thickness and the14C age of the mixed layer in deep-sea carbonates, *Earth and Planetary Science Letters* 41 (2), 223–227, DOI: 10.1016/0012-821X(78)90012-2.

Berger, W. H. and J. S. Killingley (1982), Box cores from the equatorial Pacific: 14C sedimentation rates and benthic mixing, *Marine Geology* 45, 93–125.

Berger, W. H., A. A. Ekdale, and P. P. Bryant (1979), Selective preservation of burrows in deep-sea carbonates, *Marine Geology* 32 (3), 205–230, DOI: 10.1016/0025-3227(79)90065-3.

Blaauw, M. and J. A. Christen (2011), Flexible paleoclimate age-depth models using an autoregressive gamma process, *Bayesian Analysis* 6 (3), 457–474, DOI: 10.1214/ba/1339616472.

Blaauw, M., J. A. Christen, K. D. Bennett, and P. J. Reimer (2018), Double the dates and go for Bayes — Impacts of model choice, dating density and quality on chronologies, *Quaternary Science Reviews* 188, 58–66, DOI: 10.1016/j.quascirev.2018.03.032.

Blaauw, M. and E. Heegaard (2012), Estimation of Age-Depth Relationships, *Tracking Environmental Change Using Lake Sediments*, ed. by H. J. B. Birks, A. F. Lotter, S. Juggins, and J. P. Smol, Developments in Paleoenvironmental Research 5, 379–413, DOI: 10.1007/978-94-007-2745-8_12.

Bouma, A. H. (1964), Notes on X-ray interpretation of marine sediments, *Marine Geology* 2 (4), 278–309, DOI: 10.1016/0025-3227(64)90045-3.

Braun, V. (2019), Probenbehandlung und Messverfahren zur Optimierung der Messgenauigkeit für die stabilen Isotope von Wasser im Hinblick auf eine "Beyong EPICA - Oldest Ice Core"-Klimazeitreihe, MA thesis, Universität Bremen.

Broecker, W. S., M. Andree, M. Klas, G. Bonani, W. Wolfli, and H. Oeschger (1988a), New evidence from the South China Sea for an abrupt termination of the last glacial period, *Nature* 333 (6169), 156–158, DOI: 10.1038/333156a0.

Broecker, W., M. Andree, G. Bonani, W. Wolfli, M. Klas, A. Mix, and H. Oeschger (1988b), Comparison between radiocarbon ages obtained on coexisting planktonic foraminifera, *Paleoceanography* 3, 647–657, DOI: https://doi.org/10.1029/PA003i006p00647.

Broecker, W. S., M. Klas, E. Clark, G. Bonani, S. Ivy, and W. Wolfli (1991), The Influence of $CaCO_3$ Dissolution on Core Top Radiocarbon Ages for Deep-Sea Sediments, *Paleoceanography* 6 (5), 593–608, DOI: 10.1029/91PA01768.

Broecker, W., A. Mix, M. Andree, and H. Oeschger (1984), Radiocarbon measurements on coexisting benthic and planktic foraminifera shells: potential for reconstructing ocean ventilation times over the past 20 000 years, *Nuclear Instruments and Methods in Physics Research Section B: Beam Interactions with Materials and Atoms* 5 (2), 331–339, DOI: 10.1016/0168-583X(84)90538-X.

Bronk Ramsey, C. (2008), Deposition models for chronological records, *Quaternary Science Reviews* 27 (1-2), 42–60, DOI: 10.1016/j.quascirev.2007.01.019.

Bühler, Y., L. Meier, and C. Ginzler (2015), Potential of Operational High Spatial Resolution Near-Infrared Remote Sensing Instruments for Snow Surface Type Mapping, *IEEE Geoscience and Remote Sensing Letters* 12 (4), 821–825, DOI: 10.1109/LGRS.2014.2363237.

Bühler, Y., M. S. Adams, A. Stoffel, and R. Boesch (2017), Photogrammetric reconstruction of homogenous snow surfaces in alpine terrain applying near-infrared UAS imagery, *International Journal of Remote Sensing* 38 (8-10), 3135–3158, DOI: 10.1080/01431161.2016.1275060.

Casado, M., A. Landais, G. Picard, T. Münch, T. Laepple, B. Stenni, G. Dreossi, A. A. Ekaykin, L. Arnaud, C. Genthon, A. Touzeau, V. Masson-Delmotte, and J. Jouzel (2018), Archival processes of the water stable isotope signal in East Antarctic ice cores, *The Cryosphere* 12, 1745–1766, DOI: https://doi.org/10.5194/tc-12-1745-2018.

Casado, M., T. Münch, and T. Laepple (2019), Climatic information archived in ice cores: impact of intermittency and diffusion on the recorded isotopic signal in Antarctica, *Climate of the Past Discussions* 2019, 1–27, DOI: 10.5194/cp-2019-134.

Casado, M., A. Landais, G. Picard, L. Arnaud, G. Dreossi, B. Stenni, and F. Prié (2021), Water Isotopic Signature of Surface Snow Metamorphism in Antarctica, *Geophysical Research Letters* 48 (17), e2021GL093382, DOI: 10.1029/2021GL093382.

Casado, M., T. Münch, and T. Laepple (2020), Climatic information archived in ice cores: impact of intermittency and diffusion on the recorded isotopic signal in Antarctica, *Climate of the Past* 16 (4), 1581–1598, DOI: https://doi.org/10.5194/cp-16-1581-2020.

Casanova-Arenillas, S., F. J. Rodríguez-Tovar, and F. Martínez-Ruiz (2022), Ichnological evidence for bottom water oxygenation during organic rich layer deposition in the westernmost Mediterranean over the Last Glacial Cycle, *Marine Geology* 443, 106673, DOI: 10.1016/j.margeo.2021.106673.

Chakra, C. A., S. Gascoin, J. Somma, P. Fanise, and L. Drapeau (2019), Monitoring the Snowpack Volume in a Sinkhole on Mount Lebanon using Time Lapse Photogrammetry, *Sensors* 19 (18), DOI: 10.3390/s19183890.

Charles, C. D., J. Lynch-Stieglitz, U. S. Ninnemann, and R. G. Fairbanks (1996), Climate connections between the hemisphere revealed by deep sea sediment core/ice core correlations, *Earth and Planetary Science Letters* 142 (1), 19–27, DOI: 10.1016/0012-821X(96)00083-0.

Cimoli, E., M. Marcer, B. Vandecrux, C. E. Bøggild, G. Williams, and S. B. Simonsen (2017), Application of Low-Cost UASs and Digital Photogrammetry for High-Resolutiong Snow Depth Mapping in the Arctic, *Remote Sensing* 9 (1144), DOI: doi:10.3390/rs9111144.

Craig (1961a), Isotopic Variations in Meteoric Waters.

Craig, H. (1961b), Standard for Reporting Concentrations of Deuterium and Oxygen-18 in Natural Waters, *Science* 133 (3467), 1833–1834, DOI: 10.1126/science.133.3467.1833.

Craig, H. and L. I. Gordon (1965), Deuterium and Oxygen 18 variations in the ocean and the marine atmosphere, *V. Lischi e Figli, Pisa*, Stable isotopes in oceanographic studies and paleotemperatures 122, 9–130.

Cuffey, K. M. and G. D. Clow (1997), Temperature, accumulation, and ice sheet elevation in central Greenland through the last deglacial transition, *Journal of Geophysical Research: Oceans* 102 (C12), 26383–26396, DOI: 10.1029/96JC03981.

Cuffey, K. M. and E. J. Steig (1998), Isotopic diffusion in polar firn: implications for interpretation of seasonal climate parameters in ice-core records, with emphasis on central Greenland, *Journal of Glaciology* 44, 273–284.

Dadic, R., M. Schneebeli, N. A. Bertler, M. Schwikowski, and M. Matzl (2015), Extreme snow metamorphism in the Allan Hills, Antarctica, as an analogue for glacial conditions with implications for stable isotope composition, *Journal of Glaciology* 61 (230), 1171–1182, DOI: 10.3189/2015JoG15J027.

Dahl-Jensen, D., M. Kirk, I. Koldtoft, T. Popp, and J. P. Steffensen (2019), Field season 2019 East GReenland Ice core Project (EGRIP) 2015-2020: Third year of EGRIP deep drilling, URL: https://

eastgrip.nbi.ku.dk/documentation/2019/EGRIP2019FieldPlan_1stVersion.pdf.

Dansgaard, W. (1953), The Abundance of O18 in Atmospheric Water and Water Vapour, *Tellus* 5 (4), 461–469, DOI: 10.1111/j.2153-3490.1953.tb01076.x.

Dansgaard, W. (1964), Stable isotopes in precipitation, *Tellus* 16, 436–468, DOI: https://doi.org/10.3402/tellusa.v16i4.8993.

Dansgaard, W., S. F. Johnsen, H. B. Claussen, and N. Gundestrup (1973), Stable Isotope Glaciology, 3rd ed., vol. 197.

Dee, S. G., L. A. Parsons, G. R. Loope, J. T. Overpeck, T. R. Ault, and J. Emile-Geay (2017), Improved spectral comparisons of paleoclimate models and observations via proxy system modeling: Implications for multi-decadal variability, *Earth and Planetary Science Letters* 476, 34–46, DOI: 10.1016/j.epsl.2017.07.036.

Dee, S., J. Emile-Geay, M. N. Evans, A. Allam, E. J. Steig, and D. Thompson (2015), PRYSM: An open-source framework for PRoxY System Modeling, with applications to oxygen-isotope systems, *Journal of Advances in Modeling Earth Systems* 7 (3), 1220–1247, DOI: 10.1002/2015MS000447.

Deems, J. S., T. H. Painter, and D. C. Finnegan (2013), Lidar measurement of snow depth: a review, *Journal of Glaciology* 59 (215), 467–479, DOI: 10.3189/2013JoG12J154.

Delhasse, A., C. Kittel, C. Amory, S. Hofer, D. van As, R. S. Fausto, and X. Fettweis (2020), Brief communication: Evaluation of the near-surface climate in ERA5 over the Greenland Ice Sheet, *The Cryosphere* 14 (3), 957–965, DOI: 10.5194/tc-14-957-2020.

Dethloff, K., M. Schwager, J. H. Christensen, S. Kiilsholm, A. Rinke, W. Dorn, F. Jung-Rothenhäusler, H. Fischer, S. Kipfstuhl, and H. Miller (2002), Recent Greenland Accumulation Estimated from Regional Climate Model Simulations and Ice Core Analysis, *Journal of Climate* 15 (19), 2821–2832, DOI: 10.1175/1520-0442(2002)015<2821:RGAEFR>2.0.CO;2.

Díaz-Asencio, M., J. C. Herguera, P. T. Schwing, R. A. Larson, G. R. Brooks, J. Southon, and P. Rafter (2020), Sediment accumulation rates and vertical mixing of deep-sea sediments derived from14C and 210Pb in the southern Gulf of Mexico, *Marine Geology* 429, 106288, DOI: 10.1016/j.margeo.2020.106288.

Dolman, A. M. and T. Laepple (2018), Sedproxy: a forward model for sediment-archived climate proxies, *Climate of the Past* 14 (12), 1851–1868, DOI: 10.5194/cp-14-1851-2018, URL: https://cp.copernicus.org/articles/14/1851/2018/.

Dolman, A. M., J. Groeneveld, G. Mollenhauer, S. L. Ho, and T. Laepple (2021a), Estimating Bioturbation From Replicated Small-Sample Radiocarbon Ages, *Paleoceanography and Paleoclimatology* 36 (7), e2020PA004142, DOI: 10.1029/2020PA004142.

Dolman, A. M., T. Kunz, J. Groeneveld, and T. Laepple (2021b), A spectral approach to estimating the timescale-dependent uncertainty of paleoclimate records – Part 2: Application and interpretation, *Climate of the Past* 17 (2), Publisher: Copernicus GmbH, 825–841, DOI: 10.5194/cp-17-825-2021.

Dorador, J., F. J. Rodríguez-Tovar, and J. Titschack (2020), Exploring computed tomography in ichnological analysis of cores from modern marine sediments, *Scientific Reports* 10 (1), 201, DOI: 10.1038/s41598-019-57028-z.

Ebner, P. P., H. C. Steen-Larsen, B. Stenni, M. Schneebeli, and A. Steinfeld (2017), Experimental observation of transient $\delta^{18}O$ interaction between snow and advective airflow under various temperature gradient conditions, *The Cryosphere* 11 (4), Publisher: Copernicus GmbH, 1733–1743, DOI: 10.5194/tc-11-1733-2017.

ECMWF (2017), ERA5 data documentation. URL: https://software.ecmwf.int/wiki/display/CKB/ERA5+data+documentation.

Eisen, O., M. Frezzotti, C. Genthon, E. Isaksson, O. Magand, M. R. van den Broeke, D. A. Dixon, A. Ekaykin, P. Holmlund, T. Kameda, L. Karlöf, S. Kaspari, V. Y. Lipenkov, H. Oerter, S. Takahashi, and D. G. Vaughan (2008), Ground-based measurements of spatial and temporal variability of snow accumulation in East Antarctica, *Reviews of Geophysics* 46 (2), DOI: 10.1029/2006RG000218.

Ekaykin, A. A., T. Hondoh, V. Y. Lipenkov, and A. Miyamoto (2009), Post-depositional changes in snow isotope content: preliminary results of laboratory experiments, *Climate of the Past Discussions* 5 (5), Publisher: Copernicus GmbH, 2239–2267, DOI: 10.5194/cpd-5-2239-2009.

Ekaykin, A., L. Eberlein, V. Lipenkov, S. Popov, M. Scheinert, L. Schröder, and A. Turkeev (2016), Non-climatic signal in ice core records: lessons from Antarctic megadunes, *The Cryosphere* 10 (3), 1217–1227, DOI: 10.5194/tc-10-1217-2016.

Ekaykin, A. A., V. Y. Lipenkov, I. N. Kuzmina, J. R. Petit, V. MASSON-Delmotte, and S. J. Johnsen (2004), The changes in isotope composition and accumulation of snow at Vostok station, East Antarctica, over the past 200 years, *Annals of Glaciology* 39, 569–575, DOI: 10.3189/172756404781814348.

Ekaykin, A. A., V. Y. Lipenkov, N. I. Barkov, J. R. Petit, and V. Masson-Delmotte (2002), Spatial and temporal variability in isotope composition of recent snow in the vicinity of Vostok station, Antarctica: implications for ice-core record interpretation, *Annals of Glaciology* 35, 181–186, DOI: 10.3189/172756402781816726.

Emiliani, C. (1955), Pleistocene Temperatures, *The Journal of Geology* 63 (6), Publisher: The University of Chicago Press, 538–578.

Emiliani, C. (1958), Ancient Temperatures, *Scientific American* 198 (2), 54–63, DOI: 10.1038/scientificamerican0258-54.

EPICA community members (2004), Eight glacial cycles from an Antarctic ice core, *Nature* 429 (6992), 623–628, DOI: 10.1038/nature02599.

EPICA community members (2006), One-to-one coupling of glacial climate variability in Greenland and Antarctica, *Nature* 444, DOI: https://doi.org/10.1038/nature05301.

Evans, M. N., S. E. Tolwinski-Ward, D. M. Thompson, and K. J. Anchukaitis (2013), Applications of proxy system modeling in high resolution paleoclimatology, *Quaternary Science Reviews* 76, 16–28, DOI: 10.1016/j.quascirev.2013.05.024.

Fagault, Y., T. Tuna, F. Rostek, and E. Bard (2019), Radiocarbon dating small carbonate samples with the gas ion source of AixMICADAS, *Nuclear Instruments and Methods in Physics Research Section B: Beam Interactions with Materials and Atoms* 455, 276–283, DOI: 10.1016/j.nimb.2018.11.018.

Fausto, R. S., D. van As, K. D. Mankoff, B. Vandecrux, M. Citterio, A. P. Ahlstrøm, S. B. Andersen, W. Colgan, N. B. Karlsson, K. K. Kjeldsen, N. J. Korsgaard, S. H. Larsen, S. Nielsen, A. Pedersen, C. L. Shields, A. M. Solgaard, and J. E. Box (2021), Programme for Monitoring of the Greenland Ice Sheet (PROMICE) automatic weather station data, *Earth System Science Data* 13 (8), Publisher: Copernicus GmbH, 3819–3845, DOI: 10.5194/essd-13-3819-2021.

Fausto, R. and D. van As (2019), Programme for monitoring of the Greenland ice sheet (PROMICE): Automatic weather station data. Version: v03, Dataset published via Geological Survey of Denmark and Greenland, data set, DOI: https://doi.org/10.22008/promice/data/aws.

Filhol, S. and M. Sturm (2019), The smoothing of landscapes during snowfall with no wind, *Journal of Glaciology* 65 (250), 173–187, DOI: 10.1017/jog.2018.104.

Filhol, S. and M. Sturm (2015), Snow bedforms: A review, new data, and a formation model, *Journal of Geophysical Research: Earth Surface* 120 (9), 1645–1669, DOI: https://doi.org/10.1002/2015JF003529.

Fisher, D., N. Reeh, and H. Clausen (1985), Stratigraphic Noise in Time Series Derived from Ice Cores, *Annals of Glaciology* 7, 76–83, DOI: 10.3189/s0260305500005942.

Froelich, P. N., G. P. Klinkhammer, M. L. Bender, N. A. Luedtke, G. R. Heath, D. Cullen, P. Dauphin, D. Hammond, B. Hartman, and V. Maynard (1979), Early oxidation of organic matter in pelagic sediments of the eastern equatorial Atlantic: suboxic diagenesis, *Geochimica et Cosmochimica Acta* 43 (7), 1075–1090, DOI: https://doi.org/10.1016/0016-7037(79)90095-4.

Fudge, T. J., B. R. Markle, K. M. Cuffey, C. Buizert, K. C. Taylor, E. J. Steig, E. D. Waddington, H. Conway, and M. Koutnik (2016), Vari-

able relationship between accumulation and temperature in West Antarctica for the past 31,000 years, *Geophysical Research Letters* 43 (8), 3795–3803, DOI: 10.1002/2016GL068356.

Furukawa, R., R. Uemura, K. Fujita, J. Sjolte, K. Yoshimura, S. Matoba, and Y. Iizuka (2017), Seasonal-Scale Dating of a Shallow Ice Core From Greenland Using Oxygen Isotope Matching Between Data and Simulation, *Journal of Geophysical Research: Atmospheres* 122 (20), 10, 873–10, 887, DOI: 10.1002/2017JD026716.

Gfeller, G., H. Fischer, M. Bigler, S. Schüpbach, D. Leuenberger, and O. Mini (2014), Representativeness and seasonality of major ion records derived from NEEM firn cores, *The Cryosphere* 8 (5), 1855–1870, DOI: 10.5194/tc-8-1855-2014.

Gkinis, V., C. Holme, E. C. Kahle, M. C. Stevens, E. J. Steig, and B. M. Vinther (2021), Numerical experiments on firn isotope diffusion with the Community Firn Model, *Journal of Glaciology* 67 (263), Publisher: Cambridge University Press, 450–472, DOI: 10.1017/jog.2021.1.

Goldberg, E. and M. Koide (1962), Geochronological studies of deep sea sediments by the ionium/thorium method, *Geochimica et Cosmochimica Acta* 26, 417–450, DOI: 10.1016/0016-7037(62)90112-6.

Gonfiantini, R. (1978), Standards for stable isotope measurements in natural compounds, *Nature* 271 (5645), 534–536, DOI: 10.1038/271534a0.

Goreau, T. J. (1980), Frequency sensitivity of the deep-sea climatic record, *Nature* 287 (5783), 620, DOI: 10.1038/287620a0.

Gow, A. J. (1965), On the Accumulation and Seasonal Stratification Of Snow at the South Pole, *Journal of Glaciology* 5 (40), 467–477, DOI: 10.3189/S002214300001844X.

Graf, W., H. Oerter, O. Reinwarth, W. Stichler, F. Wilhelms, H. Miller, and R. Mulvaney (2002), Stable-isotope records from Dronning Maud Land, Antarctica, *Annals of Glaciology* 35 (1), 195–201, (visited on 07/17/2013).

Grohmann, C., M. Smith, and C. Riccomini (2011), Multiscale Analysis of Topographic Surface Roughness in the Midland Valley, Scotland, *IEEE Transactions on Geoscience and Remote Sensing* 49, 1200–1213.

Gröning, M. (2018), SICalib User Manual, Vienna, Austria, URL: https://nucleus.iaea.org/sites/ReferenceMaterials/Shared%20Documents/Publications/TechnicalNotes/TELTechNote01_SICalibUserManual.pdf.

Groot Zwaaftink, C. D., A. Cagnati, A. Crepaz, C. Fierz, G. Macelloni, M. Valt, and M. Lehning (2013), Event-driven deposition of snow on the Antarctic Plateau: analyzing field measurements with SNOWPACK, *The Cryosphere* 7 (1), 333–347, DOI: 10.5194/tc-7-333-2013.

Guinasso, N. L. G. and D. R. Schink (1975), Quantitative Estimates of Biological Mixing Rates in Abyssal Sediments, *Journal of Geophysical Research* 80 (21), PP. 3032–3043, DOI: 197510.1029/JC080i021p03032.

Hajdas, I., P. Ascough, M. H. Garnett, S. J. Fallon, C. L. Pearson, G. Quarta, K. L. Spalding, H. Yamaguchi, and M. Yoneda (2021), Radiocarbon dating, *Nature Reviews Methods Primers* 1 (1), 62, DOI: 10.1038/s43586-021-00058-7.

Harder, P., M. Schirmer, J. Pomeroy, and W. Helgason (2016), Accuracy of snow depth estimation in mountain and prairie environments by an unmanned aerial vehicle, *The Cryosphere* 10 (6), 2559–2571, DOI: 10.5194/tc-10-2559-2016.

Harris Stuart, R., A.-K. Faber, S. Wahl, M. Hörhold, S. Kipfstuhl, K. Vasskog, M. Behrens, A. Zuhr, and H. C. Steen-Larsen (2021), Exploring the role of snow metamorphism on the isotopic composition of the surface snow at EastGRIP, *The Cryosphere Discussions* 2021, 1–27, DOI: 10.5194/tc-2021-344.

Haslett, J. and A. Parnell (2008), A simple monotone process with application to radiocarbon-dated depth chronologies, *Journal of the Royal Statistical Society: Series C (Applied Statistics)* 57 (4), 399–418, DOI: 10.1111/j.1467-9876.2008.00623.x.

Hawley, R. L. and J. D. Millstein (2019), Quantifying snow drift on Arctic structures: A case study at Summit, Greenland, using UAV-based structure-from-motion photogrammetry, *Cold Regions Science and Technology* 157, 163–170, DOI: https://doi.org/10.1016/j.coldregions.2018.10.007.

Heaton, T. J., E. Bard, C. Bronk Ramsey, M. Butzin, P. Köhler, R. Muscheler, P. J. Reimer, and L. Wacker (2021), Radiocarbon: A key tracer for studying Earth's dynamo, climate system, carbon cycle, and Sun, *Science* 374 (6568), eabd7096, DOI: 10.1126/science.abd7096.

Heaton, T. J., P. Köhler, M. Butzin, E. Bard, R. W. Reimer, W. E. N. Austin, C. Bronk Ramsey, P. M. Grootes, K. A. Hughen, B. Kromer, P. J. Reimer, J. Adkins, A. Burke, M. S. Cook, J. Olsen, and L. C. Skinner (2020), Marine20—The Marine Radiocarbon Age Calibration Curve (0–55,000 cal BP), *Radiocarbon* 62 (4), Publisher: Cambridge University Press, 779–820, DOI: 10.1017/RDC.2020.68.

Heegaard, E., H. J. B. Birks, and R. J. Telford (2005), Relationships between calibrated ages and depth in stratigraphical sequences: an estimation procedure by mixed-effect regression, *The Holocene* 15 (4), 612–618, DOI: 10.1191/0959683605hl836rr.

Heezen, B. C. (1959), Dynamic Processes of Abyssal Sedimentation: Erosion, Transportation, and Redeposition on the Deep-sea floor, *Geophysical Journal International* 2 (2), 142–163, DOI: 10.1111/j.1365-246X.1959.tb05790.x.

Helsen, M. M., R. S. van de Wal, M. R. van Den Broeke, D. V. As, H. A. Meijer, and C. H. Reijmer (2005), Oxygen isotope variability in snow from western Dronning Maud Land, Antarctica and its relation to temperature, *Tellus B: Chemical and Physical Meteorology* 57 (5), 423–435, DOI: 10.3402/tellusb.v57i5.16563.

Hersbach, H., B. Bell, P. Berrisford, S. Hirahara, A. Horányi, J. Muñoz-Sabater, J. Nicolas, C. Peubey, R. Radu, D. Schepers, A. Simmons, C. Soci, S. Abdalla, X. Abellan, G. Balsamo, P. Bechtold, G. Biavati, J. Bidlot, M. Bonavita, G. De Chiara, P. Dahlgren, D. Dee, M. Diamantakis, R. Dragani, J. Flemming, R. Forbes, M. Fuentes, A. Geer, L. Haimberger, S. Healy, R. J. Hogan, E. Hólm, M. Janisková, S. Keeley, P. Laloyaux, P. Lopez, C. Lupu, G. Radnoti, P. de Rosnay, I. Rozum, F. Vamborg, S. Villaume, and J.-N. Thépaut (2020), The ERA5 global reanalysis, *Quarterly Journal of the Royal Meteorological Society* 146 (730), 1999–2049, DOI: https://doi.org/10.1002/qj.3803.

Herzfeld, U. C., T. Trantow, M. Lawson, J. Hans, and G. Medley (2021), Surface heights and crevasse morphologies of surging and fast-moving glaciers from ICESat-2 laser altimeter data - Application of the density-dimension algorithm (DDA-ice) and evaluation using airborne altimeter and Planet SkySat data, *Science of Remote Sensing* 3, 100013, DOI: https://doi.org/10.1016/j.srs.2020.100013.

Horita, J., K. Rozanski, and S. Cohen (2008), Isotope effects in the evaporation of water: a status report of the Craig–Gordon model, *Isotopes in Environmental and Health Studies* 44 (1), 23–49, DOI: 10.1080/10256010801887174.

Hughes, A. G., S. Wahl, T. R. Jones, A. Zuhr, M. Hörhold, J. W. C. White, and H. C. Steen-Larsen (2021), The role of sublimation as a driver of climate signals in the water isotope content of surface snow: laboratory and field experimental results, *The Cryosphere* 15 (10), 4949–4974, DOI: 10.5194/tc-15-4949-2021.

Hughes, A. G., T. R. Jones, B. M. Vinther, V. Gkinis, C. M. Stevens, V. Morris, B. H. Vaughn, C. Holme, B. R. Markle, and J. W. C. White (2020), High-frequency climate variability in the Holocene from a coastal-dome ice core in east-central Greenland, *Climate of the Past* 16 (4), Publisher: Copernicus GmbH, 1369–1386, DOI: 10.5194/cp-16-1369-2020.

IAEA (2017), Reference Sheet for VSMOW2 and SLAP2 International Measurement Standards, tech. rep., Vienna, Austria: International Atomic Energy Agency.

IPCC (2021), Climate Change 2021: The Physical Science Basis. Contribution of Working Group I to the Sixth Assessment Report of the Intergovernmental Panel on Climate Change, ed. by V. Masson-Delmotte, P. Zhai, A. Pirani, S. Connors, C. Péan, S. Berger, N. Caud, Y. Chen, L. Goldfarb, M. I. Gomis, M. Huang, K. Leitzell,

E. Lonnoy, J. B. R. Matthews, T. K. Maycock, T. Waterfield, O. Yelekçi, R. Yu, and B. Zhou, Cambridge, United Kingdom.

James, M. R. and S. Robson (2012), Straightforward reconstruction of 3D surfaces and topography with a camera: Accuracy and geoscience application, *Journal of Geophysial Research* 117, DOI: doi:10/1029/2011JF002289.

James, M. R. and S. Robson (2014), Mitigating systematic error in topographic models derived from UAV and ground-based image networks, *Earth Surface Processes and Landforms* 39 (10), 1413–1420, DOI: https://doi.org/10.1002/esp.3609.

Jian, Z., P. Wang, M.-P. Chen, B. Li, Q. Zhao, C. Bühring, C. Laj, H.-L. Lin, U. Pflaumann, Y. Bian, R. Wang, and X. Cheng (2000), Foraminiferal responses to major Pleistocene paleoceanographic changes in the southern South China Sea, *Paleoceanography* 15 (2), 229–243, DOI: https://doi.org/10.1029/1999PA000431.

Johnsen, S. J. (1977), Stable isotope homogenization of polar firn and ice, *Isotopes and Impurities in Snow and Ice, no. 118*, Proceedings of the Grenoble Symposium 1975, Grenoble, France, 210–219.

Johnsen, S. J., H. B. Clausen, K. M. Cuffey, G. Hoffmann, and T. T. Creyts (2000), Diffusion of stable isotopes in polar firn and ice: the isotope effect in firn diffusion, 121–140, DOI: 10.7916/D8KW5D4X.

Johnsen, S. J., D. Dahl-Jensen, N. Gundestrup, J. P. Steffensen, H. B. Clausen, H. Miller, V. Masson-Delmotte, A. E. Sveinbjörnsdottir, and J. White (2001), Oxygen isotope and palaeotemperature records from six Greenland ice-core stations: Camp Century, Dye-3, GRIP, GISP2, Renland and NorthGRIP, *Journal of Quaternary Science* 16 (4), 299–307, DOI: 10.1002/jqs.622.

Johnson, D. A. (1972), Ocean-Floor Erosion in the Equatorial Pacific, *GSA Bulletin* 83 (10), 3121–3144, DOI: 10.1130/0016-7606(1972)83[3121:OEITEP]2.0.CO;2.

Jones, T. R., K. M. Cuffey, J. W. C. White, E. J. Steig, C. Buizert, B. R. Markle, J. R. McConnell, and M. Sigl (2017a), Water isotope diffusion in the WAIS Divide ice core during the Holocene and last glacial, *Journal of Geophysical Research: Earth Surface* 122 (1), 290–309, DOI: 10.1002/2016JF003938.

Jones, T. R., J. W. C. White, E. J. Steig, B. H. Vaughn, V. Morris, V. Gkinis, B. R. Markle, and S. W. Schoenemann (2017b), Improved methodologies for continuous-flow analysis of stable water isotopes in ice cores, *Atmospheric Measurement Techniques* 10 (2), Publisher: Copernicus GmbH, 617–632, DOI: 10.5194/amt-10-617-2017.

Jonkers, L. and M. Kučera (2015), Global analysis of seasonality in the shell flux of extant planktonic Foraminifera, *Biogeosciences* 12 (7), 2207–2226, DOI: 10.5194/bg-12-2207-2015.

Jouzel, J., R. B. Alley, K. M. Cuffey, W. Dansgaard, P. Grootes, G. Hoffmann, S. J. Johnsen, R. D. Koster, D. Peel, C. A. Shuman,

M. Stievenard, M. Stuiver, and J. White (1997), Validity of the temperature reconstruction from water isotopes in ice cores, *Journal of Geophysical Research: Oceans* 102 (C12), 26471–26487, DOI: 10.1029/97JC01283.

Jouzel, J., F. Vimeux, N. Caillon, G. Delaygue, G. Hoffmann, V. Masson-Delmotte, and F. Parrenin (2003), Magnitude of isotope/temperature scaling for interpretation of central Antarctic ice cores, *Journal of Geophysical Research: Atmospheres* 108 (D12), DOI: 10.1029/2002JD002677.

Jouzel, J. and L. Merlivat (1984), Deuterium and oxygen 18 in precipitation: Modeling of the isotopic effects during snow formation, *Journal of Geophysical Research: Atmospheres* 89 (D7), 11749–11757, DOI: 10.1029/JD089iD07p11749.

Jouzel, J., L. Merlivat, and C. Lorius (1982), Deuterium excess in an East Antarctic ice core suggests higher relative humidity at the oceanic surface during the last glacial maximum, *Nature* 299 (5885), 688–691, DOI: 10.1038/299688a0.

Kapsner, W. R., R. B. Alley, C. A. Shuman, S. Anandakrishnan, and P. M. Grootes (1995), Dominant influence of atmospheric circulation on snow accumulation in Greenland over the past 18,000 years, *Nature* 373 (6509), 52–54, DOI: 10.1038/373052a0.

Karlöf, L., D. P. Winebrenner, and D. B. Percival (2006), How representative is a time series derived from a firn core? A study at a low-accumulation site on the Antarctic plateau, *Journal of Geophysical Research* 111 (F04001), DOI: 10.1029/2006JF000552, URL: http://doi.wiley.com/10.1029/2006JF000552 (visited on 08/13/2013).

Karlsson, N. B., S. Razik, M. Hörhold, A. Winter, D. Steinhage, T. Binder, and O. Eisen (2020), Surface accumulation in Northern Central Greenland during the last 300 years, *Annals of Glaciology* 61 (81), 214–224, DOI: 10.1017/aog.2020.30.

Kerstel, E. R. T., R. van Trigt, J. Reuss, and H. A. J. Meijer (1999), Simultaneous Determination of the ^{2}H/^{1}H, ^{17}O/^{16}O, and ^{18}O/^{16}O Isotope Abundance Ratios in Water by Means of Laser Spectrometry, *Analytical Chemistry* 71 (23), 5297–5303, DOI: 10.1021/ac990621e.

Kerstel, E. and L. Gianfrani (2008), Advances in laser-based isotope ratio measurements: selected applications, *Applied Physics B* 92 (3), 439–449, DOI: 10.1007/s00340-008-3128-x.

Keutterling, A. and A. Thomas (2006), Monitoring glacier elevation and volume changes with digital photogrammetry and GIS at Gepatschferner glacier, Austria, *International Journal of Remote Sensing* 27, 4371–4380, DOI: 10.1080/01431160600851819.

Kochanski, K., R. S. Anderson, and G. E. Tucker (2018), Statistical Classification of Self-Organized Snow Surfaces, *Geophysical Re-*

search Letters 45 (13), 6532–6541, DOI: https://doi.org/10.1029/2018GL077616.

Kuhns, H., C. Davidson, J. Dibb, C. Stearns, M. Bergin, and J.-L. Jaffrezo (1997), Temporal and spatial variability of snow accumulation in central Greenland, *Journal of Geophysical Research: Atmospheres* 102 (D25), 30059–30068, DOI: 10.1029/97JD02760.

Kunz, T., A. M. Dolman, and T. Laepple (2020), A spectral approach to estimating the timescale-dependent uncertainty of paleoclimate records – Part 1: Theoretical concept, *Climate of the Past* 16 (4), Publisher: Copernicus GmbH, 1469–1492, DOI: https://doi.org/10.5194/cp-16-1469-2020.

Kuroyanagi, A. and H. Kawahata (2004), Vertical distribution of living planktonic foraminifera in the seas around Japan, *Marine Micropaleontology* 53 (1), 173–196, DOI: 10.1016/j.marmicro.2004.06.001.

Lacourse, T. and K. Gajewski (2020), Current practices in building and reporting age-depth models, *Quaternary Research* 96, Publisher: Cambridge University Press, 28–38, DOI: 10.1017/qua.2020.47.

Laepple, T., M. Hörhold, T. Münch, J. Freitag, A. Wegner, and S. Kipfstuhl (2016), Layering of surface snow and firn at Kohnen Station, Antarctica: Noise or seasonal signal? *Journal of Geophysical Research: Earth Surface* 121 (10), 1849–1860, DOI: 10.1002/2016JF003919.

Laepple, T. and P. Huybers (2013), Reconciling discrepancies between Uk37 and Mg/Ca reconstructions of Holocene marine temperature variability, *Earth and Planetary Science Letters* 375, 418–429, DOI: 10.1016/j.epsl.2013.06.006.

Laepple, T. and P. Huybers (2014), Ocean surface temperature variability: Large model–data differences at decadal and longer periods, *Proceedings of the National Academy of Sciences* 111 (47), 16682–16687, DOI: 10.1073/pnas.1412077111.

Laepple, T., T. Münch, M. Casado, M. Hörhold, A. Landais, and S. Kipfstuhl (2018), On the similarity and apparent cycles of isotopic variations in East Antarctic snow pits, *The Cryosphere* 12 (1), Publisher: Copernicus GmbH, 169–187, DOI: 10.5194/tc-12-169-2018.

Lea, D. W. (2014), Elemental and Isotopic Proxies of Past Ocean Temperatures, *Treatise on Geochemistr*, 2nd ed., vol. 1-16, 373–397.

Leuschner, D. C., F. Sirocko, P. M. Grootes, and H. Erlenkeuser (2002), Possible influence of Zoophycos bioturbation on radiocarbon dating and environmental interpretation, *Marine Micropaleontology* 46 (1-2), 111–126.

Li, L. and J. W. Pomeroy (1997a), Estimates of threshold wind speeds for snow transport using meteorological data, *Journal of Applied Meteorology* 36, 205–213.

Li, L. and J. W. Pomeroy (1997b), Probability of occurrence of blowing snow, *Journal of Geophysical Research: Atmospheres* 102 (D18), 21955–21964, DOI: 10.1029/97JD01522.

Libby, W. F., E. C. Anderson, and J. R. Arnold (1949), Age Determination by Radiocarbon Content: World-Wide Assay of Natural Radiocarbon, *Science (New York, N.Y.)* 109 (2827), 227–228, DOI: 10.1126/science.109.2827.227.

Libois, Q., G. Picard, L. Arnaud, S. Morin, and E. Brun (2014), Modeling the impact of snow drift on the decameter-scale variability of snow properties on the Antarctic Plateau, *Journal of Geophysical Research: Atmospheres* 119 (20), 11, 662–11, 681, DOI: https://doi.org/10.1002/2014JD022361.

Lorius, C., L. Merlivat, and R. Hagemann (1969), Variation in the Mean Deuterium Content of Precipitations in Antarctica, *Journal of Geophysical Research* 74 (28), 7027–7031, DOI: 10.1029/JC074i028p07027.

Lougheed, B. C., P. Ascough, A. M. Dolman, L. Löwemark, and B. Metcalfe (2020), Re-evaluating ^{14}C dating accuracy in deep-sea sediment archives, *Geochronology* 2 (1), Publisher: Copernicus GmbH, 17–31, DOI: 10.5194/gchron-2-17-2020.

Lougheed, B. C., B. Metcalfe, U. S. Ninnemann, and L. Wacker (2018), Moving beyond the age–depth model paradigm in deep-sea palaeoclimate archives: dual radiocarbon and stable isotope analysis on single foraminifera, *Climate of the Past* 14 (4), 515–526, DOI: 10.5194/cp-14-515-2018.

Löwemark, L., K. Konstantinou, and S. Steinke (2008), Bias in foraminiferal multispecies reconstructions of paleohydrographic conditions caused by foraminiferal abundance variations and bioturbational mixing: A model approach, *Marine Geology* 256 (1-4), 101–106, DOI: 10.1016/j.margeo.2008.10.005.

Löwemark, L. (2015), Testing ethological hypotheses of the trace fossil Zoophycos based on Quaternary material from the Greenland and Norwegian Seas, *Paleoceanography, Palaeoclimatology, Palaeoecology* 425, 1–13, DOI: http://dx.doi.org/10.1016/j.palaeo.2015.02.025.

Löwemark, L. and P. M. Grootes (2004), Large age differences between planktic foraminifers caused by abundance variations and Zoophycos bioturbation, *Paleoceanography* 19 (2), PA2001, DOI: 10.1029/2003PA000949.

Löwemark, L. and F. Werner (2001), Dating errors in high-resolution stratigraphy: a detailed X-ray radiograph and AMS-14C study of Zoophycos burrows, *Marine Geology* 177 (3), 191–198, DOI: 10.1016/S0025-3227(01)00167-0.

Madsen, M. V., H. C. Steen-Larsen, M. Hörhold, J. Box, S. M. P. Berben, E. Capron, A.-K. Faber, A. Hubbard, M. F. Jensen, T. R. Jones, S. Kipfstuhl, I. Koldtoft, H. R. Pillar, B. H. Vaughn, D. Vladimirova,

and D. Dahl-Jensen (2019), Evidence of Isotopic Fractionation During Vapor Exchange Between the Atmosphere and the Snow Surface in Greenland, *Journal of Geophysical Research: Atmospheres* 124 (6), 2932–2945, DOI: 10.1029/2018JD029619.

Maffezzoli, N., B. Risebrobakken, M. W. Miles, P. Vallelonga, S. M. P. Berben, F. Scoto, R. Edwards, H. A. Kjær, H. Sadatzki, A. Saiz-Lopez, C. Turetta, C. Barbante, B. Vinther, and A. Spolaor (2021), Sea ice in the northern North Atlantic through the Holocene: Evidence from ice cores and marine sediment records, *Quaternary Science Reviews* 273, 107249, DOI: 10.1016/j.quascirev.2021.107249.

Marcott, S. A., J. D. Shakun, P. U. Clark, and A. C. Mix (2013), A Reconstruction of Regional and Global Temperature for the Past 11,300 Years, *Science* 339 (6124), 1198–1201, DOI: 10.1126/science.1228026.

Masson-Delmotte, V., H. C. Steen-Larsen, P. Ortega, D. Swingedouw, T. Popp, B. M. Vinther, H. Oerter, A. E. Sveinbjornsdottir, H. Gudlaugsdottir, J. E. Box, S. Falourd, X. Fettweis, H. Gallée, E. Garnier, V. Gkinis, J. Jouzel, A. Landais, B. Minster, N. Paradis, A. Orsi, C. Risi, M. Werner, and J. W. C. White (2015), Recent changes in north-west Greenland climate documented by NEEM shallow ice core data and simulations, and implications for past-temperature reconstructions, *The Cryosphere* 9 (4), 1481–1504, DOI: 10.5194/tc-9-1481-2015.

Merlivat, L. and J. Jouzel (1979), Global climatic interpretation of the deuterium-oxygen 18 relationship for precipitation, *Journal of Geophysical Research* 84 (C8), 5029, DOI: 10.1029/JC084iC08p05029.

Mollenhauer, G., H. Grotheer, T. Gentz, E. Bonk, and J. Hefter (2021), Standard operation procedures and performance of the MICADAS radiocarbon laboratory at Alfred Wegener Institute (AWI), Germany, *Nuclear Instruments and Methods in Physics Research Section B: Beam Interactions with Materials and Atoms* 496, 45–51, DOI: 10.1016/j.nimb.2021.03.016.

Moran, P. A. P. (1950), Notes on Continuous Stochastic Phenomena, *Biometrika* 37 (1/2), Publisher: [Oxford University Press, Biometrika Trust], 17–23, DOI: 10.2307/2332142.

Mortyn, P. G. and C. D. Charles (2003), Planktonic foraminiferal depth habitat and δ18O calibrations: Plankton tow results from the Atlantic sector of the Southern Ocean, *Paleoceanography* 18 (2), DOI: https://doi.org/10.1029/2001PA000637.

Mosley-Thompson, E., J. R. McConnell, R. C. Bales, Z. Li, P.-N. Lin, K. Steffen, L. G. Thompson, R. Edwards, and D. Bathke (2001), Local to regional-scale variability of annual net accumulation on the Greenland ice sheet from PARCA cores, *Journal of Geophysical Research: Atmospheres* 106 (D24), 33839–33851, DOI: 10.1029/2001JD900067.

Mosley-Thompson, E., J. F. Paskievitch, A. J. Gow, and L. G. Thompson (1999), Late 20th century increase in South Pole snow accumulation, *Journal of Geophysical Research* 104 (D4), 3877–3886, DOI: 10.3189/172756502781831692.

Münch (2021), piccr, version 1.2.1.9, URL: https://github.com/EarthSystemDiagnostics/piccr (visited on 03/30/2022).

Münch, T., S. Kipfstuhl, J. Freitag, H. Meyer, and T. Laepple (2016), Regional climate signal vs. local noise: a two-dimensional view of water isotopes in Antarctic firn at Kohnen Station, Dronning Maud Land, *Climate of the Past* 12 (7), 1565–1581, DOI: 10.5194/cp-12-1565-2016.

Münch, T., S. Kipfstuhl, J. Freitag, H. Meyer, and T. Laepple (2017), Constraints on post-depositional isotope modifications in East Antarctic firn from analysing temporal changes of isotope profiles, *The Cryosphere* 11 (5), 2175–2188, DOI: 10.5194/tc-11-2175-2017.

Münch, T. and T. Laepple (2018), What climate signal is contained in decadal- to centennial-scale isotope variations from Antarctic ice cores? *Climate of the Past* 14 (12), 2053–2070, DOI: 10.5194/cp-14-2053-2018.

Münch, T., M. Werner, and T. Laepple (2021), How precipitation intermittency sets an optimal sampling distance for temperature reconstructions from Antarctic ice cores, *Climate of the Past* 17 (4), Publisher: Copernicus GmbH, 1587–1605, DOI: 10.5194/cp-17-1587-2021.

Naaim-Bouvet, F., G. Picard, H. Bellot, L. Arnaud, and V. Vionnet (2016), Snow Surface Roughness Monitoring Using Time-Lapse Terrestrial Laserscan, *Proceedings, International Snow Science Workshop, Breckenridge, Colorado*, 649–654.

Nassar, R., P. F. Bernath, C. D. Boone, A. Gettelman, S. D. McLeod, and C. P. Rinsland (2007), Variability in HDO/H2O abundance ratios in the tropical tropopause layer, *Journal of Geophysical Research: Atmospheres* 112 (D21), DOI: 10.1029/2007JD008417.

Nolan, M., C. Larsen, and M. Sturm (2015), Mapping snow depth from manned aircraft on landscape scales at centimeter resolution using structure-from-motion photogrammetry, *The Cryosphere* 9 (4), 1445–1463, DOI: 10.5194/tc-9-1445-2015.

Nürnberg, D., J. Bijma, and C. Hemleben (1996), Assessing the reliability of magnesium in foraminiferal calcite as a proxy for water mass temperatures, *Geochimica et Cosmochimica Acta* 60 (5), 803–814, DOI: 10.1016/0016-7037(95)00446-7.

Osman, M. B., J. E. Tierney, J. Zhu, R. Tardif, G. J. Hakim, J. King, and C. J. Poulsen (2021), Globally resolved surface temperatures since the Last Glacial Maximum, *Nature* 599 (7884), Number: 7884, 239–244, DOI: 10.1038/s41586-021-03984-4.

Parker, D. E., T. A. Basnett, S. J. Brown, M. Gordon, E. B. Horton, and N. A. Rayner (2000), Climate Observations - The Instrumental Record, *Space Science Reviews* 94 (1), 309–320, DOI: 10.1023/A:1026787727530.

Pearson, P. N. (2012), Oxygen isotopes in foraminifera: Overview and historical review, *Paleontological Society Papers* 18, 1–38.

Peng, T. .-.-H., W. S. Broecker, and W. H. Berger (1979), Rates of benthic mixing in deep-sea sediment as determined by radioactive tracers, *Quaternary Research* 11 (1), 141–149, DOI: 10.1016/0033-5894(79)90074-7.

Persson, A., P. L. Langen, P. Ditlevsen, and B. M. Vinther (2011), The influence of precipitation weighting on interannual variability of stable water isotopes in Greenland, *Journal of Geophysical Research: Atmospheres* 116 (D20), DOI: https://doi.org/10.1029/2010JD015517.

Piarro Inc. (2022), PICARRO: Cavity Ring-Down Spectroscopy (CRDS), URL: https://www.picarro.com/company/technology/crds (visited on 03/30/2022).

Picard, G., L. Arnaud, R. Caneill, E. Lefebvre, and M. Lamare (2019), Observation of the process of snow accumulation on the Antarctic Plateau by time lapse laser scanning, *The Cryosphere* 13, 1983–1999, DOI: https://doi.org/10.5194/tc-13-1983-2019.

Picard, G., L. Arnaud, J.-M. Panel, and S. Morin (2016), Design of a scanning laser meter for monitoring the spatio-temporal evolution of snow dpeth and its application in the Alps and in Antarctica, *The Cryosphere* 10, 1495–1511, DOI: doi:10.5194/tc-10-1495-2016.

Picarro Inc. (2022), PICARRO: L2140-*i* Isotope and Gas Concentration Analyzer, URL: https://www.picarro.com/products_solutions/peripherals/for_h2o/ih2o_solids_liquids_and_vapor (visited on 03/30/2022).

Pomeroy, J. W. and H. G. Jones (1996), Wind-Blown Snow: Sublimation, Transport and Changes to Polar Snow, *Chemical Exchange Between the Atmosphere and Polar Snow*, ed. by E. W. Wolff and R. C. Bales, Berlin, Heidelberg, 453–489, DOI: 10.1007/978-3-642-61171-1_19.

R Core Team (2020), R: A language and environment for statistical computing, manual, tex.organization: R Foundation for Statistical Computing, Vienna, Austria, URL: https://www.R-project.org/.

Regenberg, M., A. Regenberg, D. Garbe-Schönberg, and D. W. Lea (2014), Global dissolution effects on planktonic foraminiferal Mg/Ca ratios controlled by the calcite-saturation state of bottom waters, *Paleoceanography* 29 (3), 127–142, DOI: 10.1002/2013PA002492.

Rehfeld, K., T. Münch, S. L. Ho, and T. Laepple (2018), Global patterns of declining temperature variability from the Last Glacial

Maximum to the Holocene, *Nature* 554 (7692), 356–359, DOI: 10.1038/nature25454.

Reschke, M., I. Kröner, and T. Laepple (2021), Testing the consistency of Holocene and Last Glacial Maximum spatial correlations in temperature proxy records, *Journal of Quaternary Science* 36 (1), 20–28, DOI: 10.1002/jqs.3245.

Reschke, M., T. Kunz, and T. Laepple (2019a), Comparing methods for analysing time scale dependent correlations in irregularly sampled time series data, *Computers & Geosciences* 123, 65–72, DOI: 10.1016/j.cageo.2018.11.009.

Reschke, M., K. Rehfeld, and T. Laepple (2019b), Empirical estimate of the signal content of Holocene temperature proxy records, *Climate of the Past* 15 (2), 521–537, DOI: 10.5194/cp-15-521-2019.

Richardson-Näslund, C. (2004), Spatial characteristics of snow accumulation in Dronning Maud Land, Antarctica, *Global and Planetary Change* 42, 31–43, DOI: 10.1016/j.gloplacha.2003.11.009.

Rignot, E. and R. H. Thomas (2002), Mass Balance of Polar Ice Sheets, *Science* 297 (5586), 1502–1506, DOI: 10.1126/science.1073888.

Ritter, F., H. C. Steen-Larsen, M. Werner, V. Masson-Delmotte, A. Orsi, M. Behrens, G. Birnbaum, J. Freitag, C. Risi, and S. Kipfstuhl (2016), Isotopic exchange on the diurnal scale between near-surface snow and lower atmospheric water vapor at Kohnen station, East Antarctica, *The Cryosphere* 10 (4), Publisher: Copernicus GmbH, 1647–1663, DOI: 10.5194/tc-10-1647-2016.

Rohling, E. J., M. Medina-Elizalde, J. G. Shepherd, M. Siddall, and J. D. Stanford (2012), Sea Surface and High-Latitude Temperature Sensitivity to Radiative Forcing of Climate over Several Glacial Cycles, *Journal of Climate* 25 (5), Publisher: American Meteorological Society, 1635–1656, DOI: 10.1175/2011JCLI4078.1.

Sarnthein, M., U. Pflaumann, P. Wang, and H. Wong (1994), Preliminary Report on SONNE-95 Cruise 'Monitor Monsoon' to the South China Sea, *Geol.-Paläont. Inst. Univ. Kiel* 68, 1–229.

Savrda, C. E. (2007), Trace Fossils and Marine Benthic Oxygenation, *Trace Fossils*, 149–158, DOI: 10.1016/B978-044452949-7/50135-2, URL: https://linkinghub.elsevier.com/retrieve/pii/B9780444529497501352.

Savrda, C. E. and D. J. Bottjer (1991), Oxygen-related biofacies in marine strata: an overview and update, *Geological Society, London, Special Publications* 58 (1), Publisher: Geological Society of London, Section: Ancient Shelf Anoxia, 201–219, DOI: 10.1144/GSL.SP.1991.058.01.14.

Schaller, C. F., J. Freitag, S. Kipfstuhl, T. Laepple, H. C. Steen-Larsen, and O. Eisen (2016), A representative density profile of the North Greenland snowpack, *The Cryosphere* 10 (5), 1991–2002, DOI: 10.5194/tc-10-1991-2016.

Schauer, A. J., S. W. Schoenemann, and E. J. Steig (2016), Routine high-precision analysis of triple water-isotope ratios using cavity ring-down spectroscopy, *Rapid Communications in Mass Spectrometry* 30 (18), 2059–2069, DOI: 10.1002/rcm.7682.

Schiffelbein, P. (1985), Calculation of error measures for deconvolved deep-sea stratigraphic records, *Marine Geology* 65 (3), 333–342, DOI: 10.1016/0025-3227(85)90063-5.

Schiffelbein, P. and S. Hills (1984), Direct assessment of stable isotope variability in planktonic foraminifera populations, *Palaeogeography, Palaeoclimatology, Palaeoecology* 48 (2), 197–213, DOI: 10.1016/0031-0182(84)90044-0.

Schlosser, E., N. v. Lipzig, and H. Oerter (2002), Temporal variability of accumulation at Neumayer station, Antarctica, from stake array measurements and a regional atmospheric model, *Journal of Glaciology* 48 (160), 87–94, DOI: 10.3189/172756502781831692.

Schuenemann, K. C., J. J. Cassano, and J. Finnis (2009), Synoptic Forcing of Precipitation over Greenland: Climatology for 1961–99, *Journal of Hydrometeorology* 10 (1), Publisher: American Meteorological Society, Section: Journal of Hydrometeorology, 60–78, DOI: 10.1175/2008JHM1014.1.

Sime, L. C., P. O. Hopcroft, and R. H. Rhodes (2019), Impact of abrupt sea ice loss on Greenland water isotopes during the last glacial period, *Proceedings of the National Academy of Sciences* 116 (10), Publisher: Proceedings of the National Academy of Sciences, 4099–4104, DOI: 10.1073/pnas.1807261116.

Sime, L. C., N. Lang, E. R. Thomas, A. K. Benton, and R. Mulvaney (2011), On high-resolution sampling of short ice cores: Dating and temperature information recovery from Antarctic Peninsula virtual cores, *Journal of Geophysical Research: Atmospheres* 116 (D20), DOI: 10.1029/2011JD015894.

Sime, L. C., G. J. Marshall, R. Mulvaney, and E. R. Thomas (2009), Interpreting temperature information from ice cores along the Antarctic Peninsula: ERA40 analysis, *Geophysical Research Letters* 36 (18), DOI: 10.1029/2009GL038982.

Sjolte, J., G. Hoffmann, S. J. Johnsen, B. M. Vinther, V. Masson-Delmotte, and C. Sturm (2011), Modeling the water isotopes in Greenland precipitation 1959–2001 with the meso-scale model REMO-iso, *Journal of Geophysical Research: Atmospheres* 116 (D18), DOI: 10.1029/2010JD015287.

Sokratov, S. A. and V. N. Golubev (2009), Snow isotopic content change by sublimation, *Journal of Glaciology* 55 (193), 823–828, DOI: 10.3189/002214309790152456.

Steen-Larsen, H. C., V. Masson-Delmotte, M. Hirabayashi, R. Winkler, K. Satow, F. Prié, N. Bayou, E. Brun, K. M. Cuffey, D. Dahl-Jensen, M. Dumont, M. Guillevic, S. Kipfstuhl, A. Landais, T. Popp, C. Risi, K. Steffen, B. Stenni, and A. E. Sveinbjörnsdóttir (2014), What

controls the isotopic composition of Greenland surface snow? *Climate of the Past* 10 (1), 377–392, DOI: 10.5194/cp-10-377-2014.

Steen-Larsen, H. C. (2020a), Snow surface accumulation measured using Bamboo stake measurents, EastGRIP camp Greenland, May 2016, data set in review, DOI: 10.1594/PANGAEA.921855, URL: https://doi.pangaea.de/10.1594/PANGAEA.921855.

Steen-Larsen, H. C. (2020b), Snow surface accumulation measured using SSA stake measurents, EastGRIP camp Greenland, May 2018, data set in review, DOI: 10.1594/PANGAEA.921853, URL: https://doi.pangaea.de/10.1594/PANGAEA.921853.

Steffen, K. and J. Box (2001), Surface climatology of the Greenland Ice Sheet: Greenland Climate Network 1995–1999, *Journal of Geophysical Research: Atmospheres* 106 (D24), 33951–33964, DOI: 10.1029/2001JD900161.

Steig, E. J., V. Gkinis, A. J. Schauer, S. W. Schoenemann, K. Samek, J. Hoffnagle, K. J. Dennis, and S. M. Tan (2014), Calibrated high-precision ^{17}O-excess measurements using cavity ring-down spectroscopy with laser-current-tuned cavity resonance, *Atmospheric Measurement Techniques* 7 (8), Publisher: Copernicus GmbH, 2421–2435, DOI: 10.5194/amt-7-2421-2014.

Steig, E. J., P. M. Grootes, and M. Stuiver (1994), Seasonal Precipitation Timing and Ice Core Records, *Science* 266 (5192), 1885–1886, DOI: 10.1126/science.266.5192.1885.

Stenni, B., V. Masson-Delmotte, E. Selmo, H. Oerter, H. Meyer, R. Röthlisberger, J. Jouzel, O. Cattani, S. Falourd, H. Fischer, G. Hoffmann, P. Iacumin, S. Johnsen, B. Minster, and R. Udisti (2010), The deuterium excess records of EPICA Dome C and Dronning Maud Land ice cores (East Antarctica), *Quaternary Science Reviews* 29 (1-2), 146–159, DOI: 10.1016/j.quascirev.2009.10.009.

Stenni, B., C. Scarchilli, V. Masson-Delmotte, E. Schlosser, V. Ciardini, G. Dreossi, P. Grigioni, M. Bonazza, A. Cagnati, D. Karlicek, C. Risi, R. Udisti, and M. Valt (2016), Three-year monitoring of stable isotopes of precipitation at Concordia Station, East Antarctica, *The Cryosphere* 10 (5), Publisher: Copernicus GmbH, 2415–2428, DOI: 10.5194/tc-10-2415-2016.

Stevens, C. M., V. Verjans, J. M. D. Lundin, E. C. Kahle, A. N. Horlings, B. I. Horlings, and E. D. Waddington (2020), The Community Firn Model (CFM) v1.0, *Geoscientific Model Development* 13 (9), Publisher: Copernicus GmbH, 4355–4377, DOI: 10.5194/gmd-13-4355-2020.

Sturm, M., G. E. Liston, C. S. Benson, and J. Holmgren (2001), Characteristics and Growth of a Snowdrift in Arctic Alaska, U.S.A. *Arctic, Antarctic, and Alpine Research* 33 (3), 319–329, DOI: 10.1080/15230430.2001.12003436.

Tan, S., J. Zhang, H. Li, L. Sun, Z. Wu, M. G. Wiesner, H. Zheng, and J. Chen (2020), Deep Ocean Particle Flux in the Northern South

China Sea: Variability on Intra-Seasonal to Seasonal Timescales, *Frontiers in Earth Science* 8, DOI: 10.3389/feart.2020.00074.

Thirumalai, K., J. W. Partin, C. S. Jackson, and T. M. Quinn (2013), Statistical constraints on El Niño Southern Oscillation reconstructions using individual foraminifera: A sensitivity analysis, *Paleoceanography* 28 (3), 401–412, DOI: 10.1002/palo.20037.

Tonkin, T., N. Midgley, S. Cook, and D. Graham (2016), Ice-cored moraine degradation mapped and quantified using an unmanned aerial vehicle: A case study from a polythermal glacier in Svalbard, *Geomorphology* 258, 1–10, DOI: https://doi.org/10.1016/j.geomorph.2015.12.019.

Touzeau, A., A. Landais, S. Morin, L. Arnaud, and G. Picard (2018), Numerical experiments on vapor diffusion in polar snow and firn and its impact on isotopes using the multi-layer energy balance model Crocus in SURFEX v8.0, *Geoscientific Model Development* 11 (6), Publisher: Copernicus GmbH, 2393–2418, DOI: 10.5194/gmd-11-2393-2018.

Town, M. S., S. G. Warren, V. P. Walden, and E. D. Waddington (2008), Effect of atmospheric water vapor on modification of stable isotopes in near-surface snow on ice sheets, *Journal of Geophysical Research* 113 (D24), D24303, DOI: 10.1029/2008JD009852.

Trauth, M. H. (1998), TURBO: a dynamic-probabilistic simulation to study the effects of bioturbation on paleoceanographic time series, *Computers & Geosciences* 24 (5), 433–441, DOI: 10.1016/S0098-3004(98)00019-3.

Trauth, M. H. (2013), TURBO2, *Computers & Geosciences* 61 (C), 1–10.

Trauth, M. H., M. Sarnthein, and M. Arnold (1997), Bioturbational mixing depth and carbon flux at the seafloor, *Paleoceanography* 12 (3), Citation Key Alias: TrauthBioturbationalmixingdepth1997a, 517–526, DOI: 10.1029/97PA00722.

Urey, H. C. (1948), Oxygen Isotopes in Nature and in the Laboratory.

Vallelonga, P., K. Christianson, R. B. Alley, S. Anandakrishnan, J. E. M. Christian, D. Dahl-Jensen, V. Gkinis, C. Holme, R. W. Jacobel, N. B. Karlsson, B. A. Keisling, S. Kipfstuhl, H. A. Kjær, M. E. L. Kristensen, A. Muto, L. E. Peters, T. Popp, K. L. Riverman, A. M. Svensson, C. Tibuleac, B. M. Vinther, Y. Weng, and M. Winstrup (2014), Initial results from geophysical surveys and shallow coring of the Northeast Greenland Ice Stream (NEGIS), *The Cryosphere* 8 (4), 1275–1287.

van de Wal, R., W. Greuell, M. van den Broeke, C. Reijmer, and J. Oerlemans (2005), Surface mass-balance observations and automatic weather station data along a transect near Kangerlussuaq, West Greenland, *Annals of Glaciology* 42, 311–316, DOI: 10.3189/172756405781812529.

van der Veen, C. J., Y. Ahn, B. M. Csatho, E. Mosley-Thompson, and W. B. Krabill (2009), Surface roughness over the northern half

of the Greenland Ice Sheet from airborne laser altimetry, *Journal of Geophysical Research: Earth Surface* 114 (F1), DOI: 10.1029/2008JF001067.

van der Veen, C. J. and J. F. Bolzan (1999), Interannual variability in net accumulation on the Greenland Ice Sheet: Observations and implications for mass balance measurements, *Journal of Geophysical Research: Atmospheres* 104 (D2), 2009–2014, DOI: 10.1029/1998JD200082.

van der Wel, L. G., H. A. Been, R. S. W. van de Wal, C. J. P. P. Smeets, and H. A. J. Meijer (2015), Constraints on the δ2H diffusion rate in firn from field measurements at Summit, Greenland, *The Cryosphere* 9 (3), 1089–1103, DOI: 10.5194/tc-9-1089-2015.

van Geldern, R. and J. A. Barth (2012), Optimization of instrument setup and post-run corrections for oxygen and hydrogen stable isotope measurements of water by isotope ratio infrared spectroscopy (IRIS), *Limnology and Oceanography: Methods* 10, 1024–1036, DOI: 10.4319/lom.2012.10.1024.

van Sebille, E., P. Scussolini, J. V. Durgadoo, F. J. C. Peeters, A. Biastoch, W. Weijer, C. Turney, C. B. Paris, and R. Zahn (2015), Ocean currents generate large footprints in marine palaeoclimate proxies, *Nature Communications* 6, 6521, DOI: 10.1038/ncomms7521.

Veitinger, J., B. Sovilla, and R. S. Purves (2014), Influence of snow depth distribution on surface roughness in alpine terrain: a multi-scale approach, *The Cryosphere* 8 (2), 547–569, DOI: 10.5194/tc-8-547-2014.

Wacker, L., G. Bonani, M. Friedrich, I. Hajdas, B. Kromer, N. Nemec, M. Ruff, M. Suter, H.-A. Synal, and C. Vockenhuber (2010), MICADAS: Routine and High-Precision Radiocarbon Dating, *Radiocarbon* 52 (2), 252–262, DOI: https://doi.org/10.1017/S0033822200045288.

Wacker, L., J. Lippold, M. Molnár, and H. Schulz (2013), Towards radiocarbon dating of single foraminifera with a gas ion source, *Nuclear Instruments and Methods in Physics Research Section B: Beam Interactions with Materials and Atoms*, Proceedings of the Twelfth International Conference on Accelerator Mass Spectrometry, Wellington, New Zealand, 20-25 March 2011 294, 307–310, DOI: 10.1016/j.nimb.2012.08.038.

Waddington, E. D., E. J. Steig, and T. A. Neumann (2002), Using characteristic times to assess whether stable isotopes in polar snow can be reversibly deposited, *Annals of Glaciology* 35, 118–124, DOI: 10.3189/172756402781817004.

Wahl, S., H. C. Steen-Larsen, A. G. Hughes, L. J. Dietrich, A. M. Zuhr, M. Behrens, A.-K. Faber, and M. Hörhold (2022), Atmosphere-Snow Exchange Explains Surface Snow Isotope Variability, *submitted to Geophysical Research Letters*.

Wahl, S., H. C. Steen-Larsen, J. Reuder, and M. Hörhold (2021), Quantifying the Stable Water Isotopologue Exchange Between the Snow Surface and Lower Atmosphere by Direct Flux Measurements, *Journal of Geophysical Research: Atmospheres* 126 (13), e2020JD034400, DOI: 10.1029/2020JD034400.

Wang, N., B.-Q. Huang, and H. Li (2016), Deep-water carbonate dissolution in the northern South China Sea during Marine Isotope Stage 3, *Journal of Palaeogeography* 5 (1), 100–107, DOI: 10.1016/j.jop.2015.11.004.

Weinhart, A. H., J. Freitag, M. Hörhold, S. Kipfstuhl, and O. Eisen (2020), Representative surface snow density on the East Antarctic Plateau, *The Cryosphere* 14 (11), Publisher: Copernicus GmbH, 3663–3685, DOI: 10.5194/tc-14-3663-2020.

Weller, R., F. Traufetter, H. Fischer, H. Oerter, C. Piel, and H. Miller (2004), Postdepositional losses of methane sulfonate, nitrate, and chloride at the European Project for Ice Coring in Antarctica deep-drilling site in Dronning Maud Land, Antarctica, *Journal of Geophysical Research: Atmospheres* 109 (D7), DOI: 10.1029/2003JD004189.

Werner, M., U. Mikolajewicz, M. Heimann, and G. Hoffmann (2000), Borehole versus isotope temperatures on Greenland: Seasonality does matter, *Geophysical Research Letters* 27 (5), 723–726, DOI: 10.1029/1999GL006075.

Werner, M., P. M. Langebroek, T. Carlsen, M. Herold, and G. Lohmann (2011), Stable water isotopes in the ECHAM5 general circulation model: Toward high-resolution isotope modeling on a global scale, *Journal of Geophysical Research: Atmospheres* 116 (D15), D15109, DOI: 10.1029/2011JD015681.

Westoby, M. J., J. Brasington, N. F. Glasser, M. J. Hambrey, and J. M. Reznolds (2012), 'Structure-from-Motion' photogrammetry: A low-cost, effective tool for geoscience applications, *Geomorphology* 179, 300–314, DOI: http://dx.doi.org/10.1016/j.geomorph.2012.08.021.

Wetzel, A. (1991), Ecologic interpretation of deep-sea trace fossil communities, *Palaeogeography, Palaeoclimatology, Palaeoecology* 85 (1), 47–69, DOI: 10.1016/0031-0182(91)90025-M.

Wetzel, A. (2002), Modern Nereites in the South China Sea–Ecological Association with Redox Conditions in the Sediment, *Palaios* 17, 507–515, DOI: 10.1669/0883-1351(2002)017<0507:MNITSC>2.0.CO;2.

Wetzel, A. (2008), Recent Bioturbation In The Deep South China Sea: A Uniformitarian Ichnologic Approach, *PALAIOS* 23 (9), 601–615, DOI: 10.2110/palo.2007.p07-096r.

Wheatcroft, R. A. (1992), Experimental tests for particle size-dependent bioturbation in the deep ocean, *Limnology and Oceanography* 37 (1), 90–104, DOI: 10.4319/lo.1992.37.1.0090.

Whillans, I. M. and P. M. Grootes (1985), Isotopic diffusion in cold snow and firn, *Journal of Geophysical Research: Atmospheres* 90 (D2), 3910–3918, DOI: 10.1029/JD090iD02p03910.

Wolff, E. W., E. Cook, P. R. F. Barnes, and R. Mulvaney (2005), Signal variability in replicate ice cores, *Journal of Glaciology* 51 (174), Publisher: Cambridge University Press, 462–468, DOI: 10.3189/172756505781829197.

Wörmer, L., M. Elvert, J. Fuchser, J. S. Lipp, P. L. Buttigieg, M. Zabel, and K.-U. Hinrichs (2014), Ultra-high-resolution paleoenvironmental records via direct laser-based analysis of lipid biomarkers in sediment core samples, *Proceedings of the National Academy of Sciences* 111 (44), 15669–15674, DOI: 10.1073/pnas.1405237111.

Wörmer, L., J. Wendt, S. Alfken, J.-X. Wang, M. Elvert, V. B. Heuer, and K.-U. Hinrichs (2019), Towards multiproxy, ultra-high resolution molecular stratigraphy: Enabling laser-induced mass spectrometry imaging of diverse molecular biomarkers in sediments, *Organic Geochemistry* 127, 136–145, DOI: 10.1016/j.orggeochem.2018.11.009.

Xie, S.-P., Q. Xie, D. Wang, and W. T. Liu (2003), Summer upwelling in the South China Sea and its role in regional climate variations, *Journal of Geophysical Research: Oceans* 108 (C8), DOI: 10.1029/2003JC001867.

Young, R. N. and J. B. Southard (1978), Erosion of fine-grained marine sediments: Sea-floor and laboratory experiments, *GSA Bulletin* 89 (5), 663–672, DOI: 10.1130/0016-7606(1978)89<663:EOFMSS>2.0.CO;2.

Zuhr, A. M., A. M. Dolman, S. L. Ho, J. Groeneveld, L. Loewemark, H. Grotheer, C.-C. Su, and T. Laepple (2022a), Age-heterogeneity in marine sediments revealed by three-dimensional high-resolution radiocarbon measurements, *Frontiers in Earth Science - Marine Geoscience* 2022, DOI: 10.3389/feart.2022.871902.

Zuhr, A. M., T. Münch, H. C. Steen-Larsen, M. Hörhold, and T. Laepple (2021a), Local-scale deposition of surface snow on the Greenland ice sheet, *The Cryosphere* 15 (10), 4873–4900, DOI: 10.5194/tc-15-4873-2021.

Zuhr, A. M., S. Wahl, H. C. Steen-Larsen, M. Hörhold, H. Meyer, and T. Laepple (2022b), A snapshot on the buildup of the stable water isotopic signal in the upper snowpack at EastGRIP, Greenland Ice Sheet, *submitted to Journal of Geophysical Research: Earth Surface*.

Zuhr, A., T. Münch, H. C. Steen-Larsen, M. Hörhold, and T. Laepple (2021b), Day-to-day changes in the snow surface height derived from digital elevation models at the EGRIP camp site in 2018, data set, DOI: 10.1594/PANGAEA.936099, URL: https://doi.org/10.1594/PANGAEA.936099.

Zuhr, A., T. Münch, H. C. Steen-Larsen, M. Hörhold, and T. Laepple (2020), Snow height data generated with a Structure-from-Motion

photogrammetry approach at the EGRIP camp site in 2018, data set, DOI: 10.1594/PANGAEA.923418, URL: https://doi.org/10.1594/PANGAEA.923418.

Zuhr, A., T. Münch, H. C. Steen-Larsen, M. Hörhold, and T. Laepple (2021c), Snow surface accumulation measured using manual stick measurents, EastGRIP camp Greenland, May 2018, data set, DOI: 10.1594/PANGAEA.931124, URL: https://doi.pangaea.de/10.1594/PANGAEA.931124.

A

THE ROLE OF SUBLIMATION AS A DRIVER OF CLIMATE SIGNALS IN THE WATER ISOTOPE CONTENT OF SURFACE SNOW: LABORATORY AND FIELD EXPERIMENTAL RESULTS

Abigail G. Hughes[1], Sonja Wahl[2], Tyler R. Jones[1], Alexandra Zuhr[3,4], Maria Hörhold[5], James W. C. White[1], and Hans Christian Steen-Larsen[2]

[1] Institute of Arctic and Alpine Research, University of Colorado Boulder, Boulder, Colorado, USA

[2] Geophysical Institute, University of Bergen and Bjerknes Centre for Climate Research, Bergen, Norway

[3] Alfred-Wegener-Institut Helmholtz-Zentrum für Polar- und Meeresforschung, Research Unit Potsdam, Telegrafenberg A45, 14473 Potsdam, Germany

[4] Institute of Geosciences, University of Potsdam, Karl-Liebknecht-Str. 24–25, 14476 Potsdam-Golm, Germany

[5] Alfred-Wegener-Institut Helmholtz-Zentrum für Polar- und Meeresforschung, Research Unit Bremerhaven, 27568 Bremerhaven, Germany

This chapter is published in:
The Cryosphere, 15(10), 4949–4974, DOI: 10.5194/tc-15-4949-2021, 2021.

Abstract. Ice core water isotope records from Greenland and Antarctica are a valuable proxy for palaeoclimate reconstruction, yet the processes influencing the climate signal stored in the isotopic composition of the snow are being challenged and revisited. Apart from precipitation input, post-depositional processes such as wind-driven redistribution and vapour–snow exchange processes at and below the surface are hypothesized to contribute to the isotope climate signal subsequently stored in the ice. Recent field studies have shown that surface snow isotopes vary between precipitation events and covary with vapour isotopes, which demonstrates that vapour–snow exchange is an important driving mechanism. Here we investigate how vapour–snow exchange processes influence the isotopic composition of the snowpack. Controlled laboratory experiments under forced sublimation show an increase in snow isotopic composition of up to 8 ‰ $\delta^{18}O$ in the uppermost layer due to sublimation, with an attenuated signal down to 3 cm snow depth over the course of 4–6 d. This enrichment is accompanied by a decrease in the second-order parameter d-excess, indicating kinetic fractionation processes. Our observa-

tions confirm that sublimation alone can lead to a strong enrichment of stable water isotopes in surface snow and subsequent enrichment in the layers below. To compare laboratory experiments with realistic polar conditions, we completed four 2–3 d field experiments at the East Greenland Ice Core Project site (northeast Greenland) in summer 2019. High-resolution temporal sampling of both natural and isolated snow was conducted under clear-sky conditions and demonstrated that the snow isotopic composition changes on hourly timescales. A change of snow isotope content associated with sublimation is currently not implemented in isotope-enabled climate models and is not taken into account when interpreting ice core isotopic records. However, our results demonstrate that post-depositional processes such as sublimation contribute to the climate signal recorded in the water isotopes in surface snow, in both laboratory and field settings. This suggests that the ice core water isotope signal may effectively integrate across multiple parameters, and the ice core climate record should be interpreted as such, particularly in regions of low accumulation.

A.1 INTRODUCTION

Water isotope records in polar ice cores have been used as a proxy to reconstruct local temperature and evaporation source conditions dating back hundreds of thousands of years. The isotope– palaeothermometer relationship used to interpret ice core water isotope records is based on the assumption that the observed stable water isotope signal is primarily composed of the input signals from individual precipitation events (Johnsen et al., 2001; Werner et al., 2011; Sime et al., 2019). However, this approach does not take into account the effects of post-depositional surface exchange processes such as vapour exchange and wind-driven redistribution. Recent field studies have shown that the isotopic composition of surface snow varies in parallel with atmospheric water vapour without occurrence of newly precipitated snow (Steen-Larsen et al., 2014) and can change on subdiurnal timescales (Ritter et al., 2016; Casado et al., 2018), suggesting a coupling between the atmospheric water vapour and surface snow through isotope exchange.

The primary water isotope signal (i. e., $\delta^{18}O$, δD) in polar precipitation closely reflects the temperature gradient experienced by an air mass from source to deposition and ultimately the temperature of condensation in the cloud (Dansgaard, 1964; Jouzel and Merlivat, 1984; Jouzel et al., 1997). Therefore, seasonal differences in the isotopic composition of the precipitation have historically been assumed to be the primary contributor to observed annual cycles in the ice core. In addition, the second-order parameter deuterium excess (d-excess = $\delta D - 8 \cdot \delta^{18}O$) results from kinetic fractionation due to molecular differences between the movement of oxygen and hydrogen in the

hydrologic cycle. Traditionally, it is thought that the ice core d-excess signal is driven by the evaporation conditions at the moisture source to an ice core site (Merlivat and Jouzel, 1979).

There are several processes known to influence the climate signal recorded in ice core water isotopes. First, precipitation may not take place continuously throughout the year, and precipitation intermittency and seasonal bias influence the isotope record (Werner et al., 2000; Casado et al., 2018; Münch et al., 2017; Münch and Laepple, 2018; Zuhr et al., 2021a). Second, surface processes such as snow-drift erosion and redistribution may hamper the consecutive deposition and burial of snow layers through time, leading to a lack of a continuous time record. For example, wind-drifted snow can form large persistent surface features/dunes with variations in the snow density and height, altering the isotope signal spatially and vertically. This issue has been approached by stacking multiple cores or snow pit profiles in order to resolve the climate signal (Casado et al., 2018; Münch et al., 2017; Münch and Laepple, 2018; Zuhr et al., 2021a). Third, after deposition the snow and firn undergo vapour diffusion. Unconsolidated snow grains have open pathways between pore spaces, allowing for vapour transport and mixing. Diffusion attenuates the seasonal signal and acts as a smoothing function, and is well-constrained (Whillans and Grootes, 1985; Cuffey and Steig, 1998; Jones et al., 2017a; Johnsen et al., 2000). It has been shown that diffusion may smooth across noise and gaps from intermittent precipitation events, leading to the observed isotope records that imply continuous seasonal temperature changes (Laepple et al., 2016, 2018). However, a remaining missing link between the accumulated signal and the ice core record is a well-defined understanding of snow–air exchange. Continuous isotope exchange between the snow surface and water vapour is known to influence the recorded climate signal, yet the effects are still not fully resolved.

While it was previously assumed that sublimation of snow and ice occurs layer by layer and does not cause isotopic fractionation of remaining ice (Dansgaard, 1964), recent studies have shown this is not the case and that snow is subjected to isotopic fractionation due to sublimation (Ekaykin et al., 2009; Sokratov and Golubev, 2009; Ebner et al., 2017; Madsen et al., 2019). In the accumulation zone of ice sheets, the typical region for ice core drill sites, the snow surface and lower atmosphere are coupled through the continuous humidity exchange in the form of sublimation and deposition of water molecules and isotopologues (Wahl et al., 2021). This interaction continuously imprints on the snow surface $\delta^{18}O$ and δD isotopic composition and suggests an interpretation of snow isotopes as an integrated climate record, rather than a precipitation signal only (Steen-Larsen et al., 2014). As sublimation is a non-equilibrium process comparable to

evaporation, it likewise influences the surface snow d-excess, questioning the interpretation of d-excess as a source region signal.

In this study, we investigated how the isotope signal of surface snow is altered over multiple days via post-depositional exchange between the snow and the near-surface atmospheric water vapour. We utilized multiple types of experiments including both controlled laboratory experiments and in situ field observations. First, we performed a simple laboratory experiment to observe the effects of sublimation under dry air in a controlled environment. Next, we performed two field experiments in northeast Greenland to (1) analyse the change of snow of known isotopic composition under characteristic polar conditions and (2) document the isotope signal evolution of undisturbed snow as it naturally exists at the ice sheet surface. For all experiments, continuous atmospheric vapour measurements were made above the snow surface to complement the snow sampling and allow us to observe ongoing snow–vapour isotope exchange. Thus, these laboratory and field experiments are the first to measure both $\delta^{18}O$ and δD at fine vertical and temporal resolution for multiple depths across several multi-day experimental periods under differing environmental conditions, with simultaneous continuous measurements of atmospheric vapour $\delta^{18}O$ and δD. In the case of the laboratory experiments presented, the vapour isotopic composition can directly be interpreted as the isotopic composition of the flux, since the experimental set-up fulfils the closure assumption and therefore allows a direct comparison of flux and snow isotopic composition. With these data we demonstrate the importance of post-depositional processes on the snow surface water isotope signal, and we provide better constraints on transfer functions between the atmospheric conditions including water vapour isotopic composition and the climate signal recorded in the surface snow, with implications for interpretation of ice core records.

A.2 METHODS

We investigated through a combination of laboratory and field experiments (Table A1) the influence of phase changes (i. e., sublimation and vapour deposition) on the snow surface isotopic composition. Laboratory experiments were run in a controlled environment, which allowed us to isolate the effects of idealized sublimation conditions. The sublimation rate was varied between different experiment runs through adjusting temperature and the flow rate of dry air. Complementary field experiments provided greater insight as to how laboratory findings are consistent with field observations occurring at the surface of the ice sheet. The field experiments were run under close-to-ideal conditions, which limited the duration of the experiments to

intervals of time with clear-sky conditions. In return, the sampling resolution was increased for the field experiments.

Throughout this work, water isotope measurements are reported in standard delta notation given in per mil (‰) (Craig, 1961b):

$$\delta_i = \left(\frac{R_i}{R_{VSMOW}} - 1 \right) \tag{A1}$$

where i refers to δD or $\delta^{18}O$, and R is the ratio of heavy to light isotopes, such that $R_{18_O} = [^1H_2{}^{18}O]/[^1H_2{}^{16}O]$ and and $R_D = [^2H^1H^{16}O]/[^1H_2{}^{16}O]$, where ^2H is referred to as D. Samples were referenced to Vienna Standard Mean Ocean Water (VSMOW).

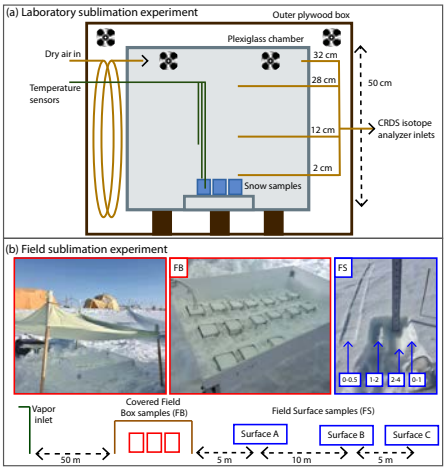

Figure A1: (a) Diagram of laboratory experiment setup. A plexiglass chamber was placed within an outer plywood box in a freezer, and dry air regulated by a mass flow controller was pumped into the inner box above four to six homogeneous snow samples, placed on a small shelf to allow airflow. Fans inside the box maintained air circulation. Three temperature sensors were placed at different heights, and continuous CRDS measurements of the vapour were made at four inlet heights (2, 12, 28, 32 cm above the snow surface). (b) Schematic diagram of the field sampling setup at EastGRIP. From left to right: atmospheric vapour at 10 cm above the snow surface was continuously measured by a CRDS. Homogenous box samples (FB; red) were partially buried and covered, and temperature sensors were placed in the atmosphere, snow surface, and below the surface. Three surface sampling locations (FS A, B, C; blue) were spaced 5–10 m apart, with samples taken at every time interval at each location. A photo example of one sample is shown, in which the left-most sample is the 0–0.5 cm sample, while the intervals for 0–1, 1–2, and 2–4 cm can be seen in the small pit.

A.2.1 *Laboratory experimental methods (L experiments)*

Table A1: Overview of all experiments conducted. Eight laboratory experiments were completed, with L1–L5 completed at the University of Colorado Boulder and L6–L8 completed at the University of Copenhagen. Four field experiments (F1–F4) were completed at the East Greenland Ice Core Project field site. Field experiments included associated field box samples (FB2–FB4) and field surface samples (FS1–FS4). For L experiments, the controlled settings of the individual experiment runs are given, whereas for the field experiments, the environmental conditions are listed. The mean sublimation rate for field (F–FB/FS) experiments was calculated for all observations in which the latent heat flux (LHF) was positive (i.e., directed away from the surface). The median peak sublimation rate in June and July 2019 was 250 g m^{-2} d^{-1}, and maximum observed peak sublimation rates were 600–700 g m^{-2} d^{-1}.

Experiment type	Experiment name	Mean flow rate (litres per minute)	Mean temperature (°C)	Mean sublimation rate (LHF > 0) (g m^{-2} d^{-1})	Peak sublimation rate (LHF > 0) (g m^{-2} d^{-1})	Starting snow $\delta^{18}O$ (‰)	Duration
Laboratory	L1*	2	-12	428.4	-	-20	5 d
	L2	3	-12	428.4	-	-20	5 d
	L3	3	-12	508.4	-	-20	5 d
	L4	4	-12	568.8	-	-20	5 d
	L5*	5	-12	692.3	-	-20	5 d
	L6*	5	-9	779.9	-	-28	6 d
	L7	5	-8	965.0	-	-28	4 d
	L8	5	-5	1329.3	-	-28	5 d
Field box	F2–FB2	-	-7.5	157.5	386.1	-26.1	41 h
	F3–FB3	-	-10.5	218.5	712.9	-25.2	39 h
	F4–FB4	-	-12.7	130.3	279.7	-25.1	51 h
Field surface	F1–FS1	-	-7.6	171.6	619.6	-	57 h
	F2–FS2	-	-7.5	157.5	386.1	-	41 h
	F3–FS3	-	-10.5	218.5	712.9	-	39 h
	F4–FS4	-	-12.7	130.3	279.7	-	51 h

* Stars denote the subset of laboratory experiments selected for further discussion.

For the laboratory experiments (L1–L8), dry air was circulated over boxes containing isotopically homogeneous snow samples that were kept at fixed temperatures (Fig. A1a). An experimental chamber was designed that consisted of an inner plexiglass box, which sat inside an outer plywood box (2.7 cm thick) used for temperature regulation. The entire setup was placed in a large freezer, with the inner temperature moderated by a PID-controlled (Omega CN7800; 50 W) cable heater wrapped around the inside of the plywood box. Dry air was produced with a generator (Puregas CDA-10) and run through Drierite desiccant, resulting in humidity <100 ppm (i.e., <5 % RH). The amount of dry air circulated in the box was regulated by a HORIBA SEC-4400 mass flow controller, and two continuously running computer fans at the top of the chamber maintained mixed air. In order to maintain positive pressure in the box, flow rates less than 2 L min^{-1} could not be used. Four to six small plastic boxes (5.7x5.7x7.6 cm) were filled with snow that was well-mixed and sifted so that the snow grain size (1–2 mm) and isotope value were homogenous, and the initial mass of each sample was measured. The samples were placed at the bottom of the inner box, on a shelf with underlying airflow to prevent a temperature gradient within the samples. Every 24 h, one sample was removed, and the mass of that sample was measured. The boxes could be opened on one side, and a metal spatula was used to collect snow samples with 5 mm resolution to obtain a vertical isotope profile. Snow samples were transferred to 20 mL HDPE scintillation vials for storage and kept frozen until analysis, at which time they were melted and immediately transferred to 2 mL vials. Liquid samples were then analysed using a Picarro L2130-*i* cavity ring-down spectrometer (CRDS), in conjunction with a CTC Analytics HTC PAL autosampler injection system and Picarro V1102-*i* vaporisation module. Each sample was measured with six injections, and the reported value is based on the average of the last three injections to remove memory effects (Schauer et al., 2016). Every analysis run of 40 samples also included three known water isotope standards bracketing the sample isotope values for calibration (e.g., as done in Jones et al., 2017b). The resulting discrete measurements have uncertainties of 0.1 ‰ $\delta^{18}O$ and 1 ‰ δD.

For the duration of all experiments, several additional parameters were monitored. A Picarro L2130-*i* CRDS was continuously measuring (~1 Hz) vapour (humidity, $\delta^{18}O$, δD) from four heights above the snow surface (2, 12, 28, 36 cm), cycling between each level every hour. The second-order parameter d-excess (d-excess = $\delta D - 8 \cdot \delta^{18}O$) was also calculated from those measurements. Three Pico Technologies PT-104 data logger temperature sensors were placed in the box to record continuously: one 10 cm above the snow surface, one on the surface of the snow, and one ~4 cm below the snow surface.

Two sets of experiments were conducted with varying sublimation rates controlled by adjusting temperature and dry air flow rate (Table A1). For five experiment runs, the temperature was held steady at −12 °C while the dry air flow rate was changed between a constant flow rate of 2, 3, 4, and 5 L min^{-1} (L1–L5, respectively). These experiments used snow from Boulder, Colorado, with a starting value of approximately -20 ‰ $\delta^{18}O$, and they were carried out at the Institute of Arctic and Alpine Research at the University of Colorado Boulder. Three additional experiment runs had the temperature of the inner box held constant at -9, -8, or -5 °C (L6–L8, respectively), and the flow rate of dry air above the snow samples was held steady at 5 L min^{-1}. These experiments used snow from the East Greenland Ice Core Project field site with a starting $\delta^{18}O$ value of approximately -28 ‰ and were completed at the section for Physics of Ice, Climate and Earth at the University of Copenhagen. In total, eight experiments were completed.

A.2.2 *Field experimental methods (F experiments)*

Field experiments were conducted at the East Greenland Ice Core Project (EastGRIP) field camp in July 2019. EastGRIP is located at 75.6268° N, 35.9915° W in the accumulation zone of the Greenland Ice Sheet. In July 2019, the meteorological conditions at the site were characterized by low temperatures (mean −9.0 °C, measured at 2 m above the snow surface) and high relative humidities (mean 91 % RH with respect to ice), leading to an average specific humidity of 2.3 g kg^{-1}. Positive temperatures (>0 °C) were very rare, and we observed a positive change in snow height of about 2 cm during July.

The goal of in situ field experiments was to characterize interactions between the snow surface and near-surface atmospheric vapour on short timescales and to monitor the evolution of the isotopic signal in the snow. To do so, we selected four 2–3 d experimental periods (field experiments, F1–F4) during which changes in water isotopes in the snow surface and atmospheric vapour were measured simultaneously through three sample types (Fig. A1b): (1) discrete box samples (field box, FB2–FB4), (2) discrete surface samples (field surface, FS1–FS4), and (3) continuous vapour measurements at 10 cm above the snow surface. Each experiment was conducted during a period of good weather, such that precipitation or windblown snow would not bias results. This required air temperatures below freezing, sustained wind speeds below 5–6 m s^{-1}, and no precipitation.

A.2.2.1 *Discrete box samples (FB experiments)*

At the beginning of each period, 14–16 boxes (5.7 x 5.7 x 7.6 cm) were filled with well-mixed surface snow. Sampling boxes were partially buried in the snow surface, with the top of the sample box 1–2 cm

above the surrounding snow surface to minimize any risk of contamination from windblown snow. Samples were also protected from direct overhead sunlight using a light-coloured thin cloth covering. Although this deviates from natural conditions in which the snow surface is exposed and not covered, this modification was necessary to prevent solar heating of the sample boxes which may have led to melt of the snow samples. A Pico Technologies PT-104 data logger was used to measure temperature during the experimental period, with four sensors placed in an additional snow-filled box. The logger continuously recorded temperatures of the ambient air, snow surface, 3 cm below surface, and 6 cm below surface.

One box was collected every 3 h; each box was equipped with one removable side so that a vertical profile of the snow was accessible. Snow samples were taken at intervals 0–0.5, 0.5–1, 1–1.5, 1.5–2.5, and 2.5–4.5 cm from the surface using a spatula. The snow samples were transferred to a 20 mL HDPE scintillation vial for storage. Discrete samples are referred to as field box (FB) samples, with each experiment designated FB2, FB3, and FB4 (Table A1).

A.2.2.2 *Discrete surface samples (FS experiments)*

In addition to the isolated boxes, every 3 h we collected samples from a clean, undisturbed surface snow area at the same time as the boxes were sampled. Because wind effects can lead to variability in snow surface density and isotopic value, surface samples were collected from three locations, designated sites A, B, and C. The distance from A to B was 10 m and from B to C was 5 m (Fig. A1). At each surface location, samples were collected from 0–0.5, 0–1, 1–2, and 2–4 cm below the surface (Fig. A1b). The snow samples were transferred to a 20 mL HDPE scintillation vial for storage. Discrete surface samples are referred to as field surface (FS) samples, with each experiment designated FS1, FS2, FS3, and FS4 (Table A1).

All snow samples (both field box (FB) and field surface (FS)) were kept frozen after collection and were measured at the Stable Isotope Lab at the University of Colorado Boulder. Samples were analysed using a Picarro L2130-*i*, in conjunction with a CTC Analytics HTC PAL autosampler injection system and Picarro V1102-*i* vaporisation module. The same measurement protocol was used as described in Sect. 2.1.

A.2.2.3 *Continuous vapour measurements*

Continuous atmospheric water vapour isotope measurements were made at 10 cm above the snow surface, ~50 m away from the FS sampling site so as not to be contaminated by snow sampling activity. The measurements were made with a Picarro L2130-*i* CRDS, which was kept in a temperature-controlled tent and measured humidity,

$\delta^{18}O$, and δD. Using a diaphragm pump (KNF model DC-B 12V UNMP850), air was pumped through a ~12 m long heated copper tube to the analyser (similar to the setup described in Madsen et al., 2019).

Four types of calibrations were performed on the water vapour isotope measurements of the CRDS, similar to the calibration protocol described in Steen-Larsen et al. (2013): (1) humidity calibration, (2) humidity-isotope response calibration, (3) VSMOW-VSLAP scale calibration, and (4) drift calibration. All calibrations are applied to water vapour isotope measurements in both laboratory and field experiments. Details of the calibration setup specific to laboratory and field experiments are described in Appendix B.

Latent heat flux (LHF) was also continuously measured during the field campaign using a Campbell Scientific IRGASON eddy-covariance (EC) system. The two-in-one EC system measured humidity and three-dimensional wind at a sampling frequency of 20 Hz in the same sample volume at 2.15 m above the snow surface. LHF values were computed for 30 min intervals using Campbell Scientific's software EasyFlux^{TM} adjusted for sublimation conditions and accounting for wind rotation and frequency corrections. Latent heat flux is related to sublimation: LHF = sublimation rate $\cdot$ λ, where λ is the latent heat of sublimation at 0 °C, 2834 kJ kg^{-1}; a positive LHF indicates sublimation, and negative LHF indicates vapour deposition.

A.3 RESULTS

A.3.1 *Laboratory experiments*

A.3.1.1 *Sublimation rate*

The mean sublimation rate for each laboratory experiment is calculated based on mass loss with time and surface area, reported in Table A1. Sublimation rate does not significantly change with time and is shown for each experiment in Fig. A8. The mass of each box was measured at the onset of the experiment and immediately before each sampling. Since we only push dry air into the chamber, the experiment relates only to sublimation processes. We find that the LHF associated with sublimation varies from approximately 15 W m^{-2} (Experiment L1 at 2 L min^{-1} and −12 °C) to 44 W m^{-2} (Experiment L8 at 5 L min^{-1} and −3 °C).

Latent heat flux values in laboratory experiments are comparable to the peak daytime sublimation fluxes observed during the field campaign, albeit the average LHF during the sublimation period in the field was substantially smaller than observed during the laboratory experiments (Table A1). The mean daytime positive LHF was ~5 W m^{-2}, and the maximum LHF observed was ~23 W m^{-2}. Therefore,

laboratory experiments can be considered representative of processes occurring during peak daytime conditions in the field.

A.3.1.2 *Snow measurements*

Eight laboratory experiments (L1–L8) were completed, with temperature, dry air flow rate, and sublimation rate documented in Table A1. In all experiments, the surface snow experiences substantial isotopic changes, with $\delta^{18}O$ increasing by up to 8 ‰ and d-excess decreasing by over 25 ‰. $\delta^{18}O$ and d-excess signals for all experiments are shown in Fig. A10 (Appendix of the publication), with a subset of experiments shown in Fig. A2. Changes in the isotope signal are observed to propagate several centimetres into the snowpack due to diffusion over 4–6 d, driven by the induced sublimate-related isotope change at the surface. The rate of change is calculated for the mean isotope value for each day of sampling, ranging from 0.25–0.70 ‰ d^{-1} for $\delta^{18}O$ and 0.66–2.64 ‰ d^{-1} for d-excess (Fig. A11a and b). There is a strong relationship between mass loss and isotope values, with an average R^2=0.90 for daily mean box $\delta^{18}O$ vs. mass loss for experiments L1–L8. The relationship between sublimation rate and $\delta^{18}O$ rate of change has R^2=0.13, and sublimation rate vs. d-excess rate of change has R^2=0.54 (Fig. A11c (Appendix of the publication)).

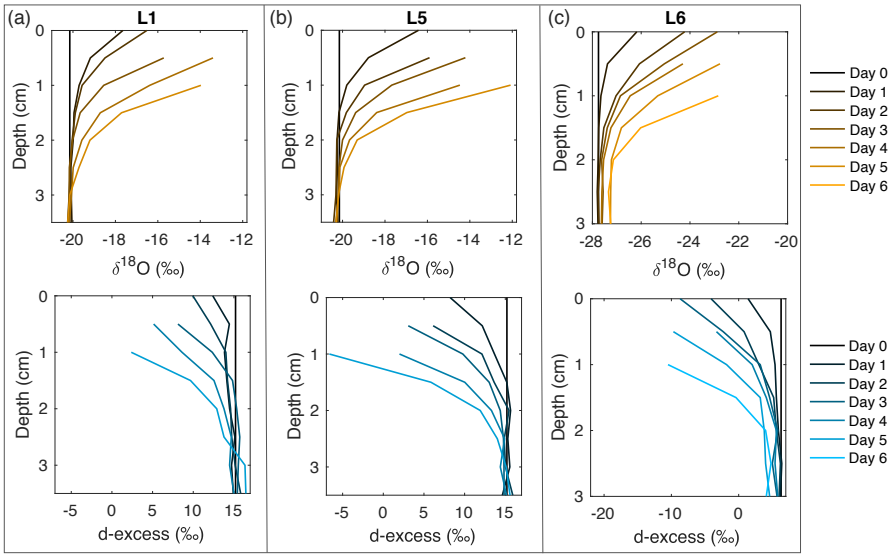

Figure A2: Snow $\delta^{18}O$ (top) and d-excess (bottom) vertical profiles from three of the laboratory experiments: (a) L1 (−12 °C, 2 L min^{-1}), (b) L5 (−12 °C, 5 L min^{-1}) and (c) L6 (−9 °C, 5 L min^{-1}). Day 0 (black) represents the initial homogeneous snow sample, with colours progressively moving towards orange ($\delta^{18}O$) and blue (d-excess) with each day of sampling. As each experiment progresses from Day 0 to Day 6, sublimation drives an increase in $\delta^{18}O$ and decrease in d-excess, with the greatest change at the snow surface. Similar figures for all laboratory experiments (L1–L8) can be found in Fig. A10 (Appendix of the publication).

Because $\delta^{18}O$ reflects equilibrium fractionation and d-excess is influenced by kinetic fractionation, a comparison of these variables provides insight into the extent of fractionation effects occurring during sublimation. The slope of d-excess vs. $\delta^{18}O$ is calculated for samples within each box (Fig. A3a), and the slope with time over the duration of each experiment is shown in Fig. A3b. The slope ranges from -0.91 ‰ to -3.57 ‰ d-excess/‰ $\delta^{18}O$ and decreases over the course of all experiments. In general, there is a decrease in slope associated with an increase in sublimation rate, as indicated by the colour scale reflecting sublimation rate in Fig. A3b and as shown in Fig. A9 (Appendix of the publication).

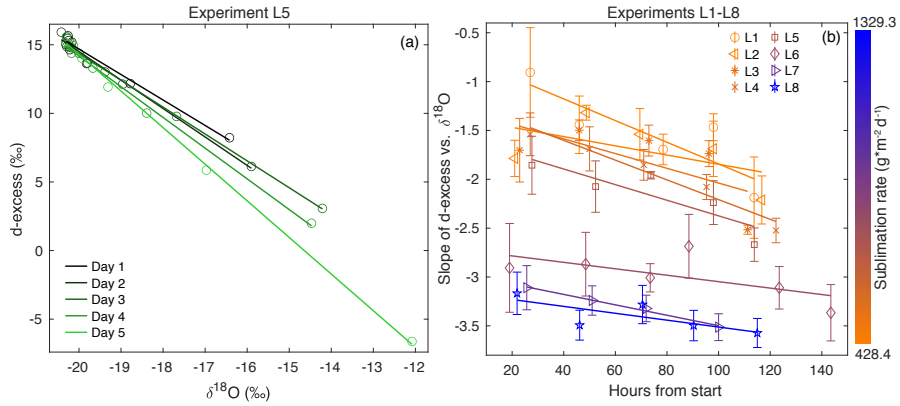

Figure A3: (a) d-excess vs. $\delta^{18}O$ is shown for the vertical snow profile at each day of sampling in Experiment L5, with a linear regression calculated for each day. This gives a slope of d-excess vs. $\delta^{18}O$, which evolves with time. (b) The slope of d-excess vs. $\delta^{18}O$ with time is shown for each experiment L1–L8, demonstrating an inverse relationship between sublimation rate and slope of d-excess vs. $\delta^{18}O$. Error bars indicate 95 % confidence intervals for each slope.

A.3.1.3 *Vapour measurements*

During all laboratory experiments, a Picarro L2130-*i* CRDS was used to continuously measure vapour in the chamber at 2, 12, 28, and 36 cm, cycling through each height for 1 h measurement periods. We exclude the first 20 min of each measurement period to remove memory effects from valve changes. Figure A4 shows an example of temperature and vapour data for experiment L5, including the 28 and 32 cm levels, which represent sublimated vapour which is more well-mixed than that immediately above the snow surface. Dry air pumped into the top of the box is mixed using a set of fans creating turbulence above the snow surface. The vertical differences in humidity and isotopic composition of the air in the box (i.e., differences between 28 and 32 cm as seen in Fig. A4) likely indicate that the ventilation is not strong enough to maintain a fully homogeneous air mass in the box, allowing for a slight vertical gradient.

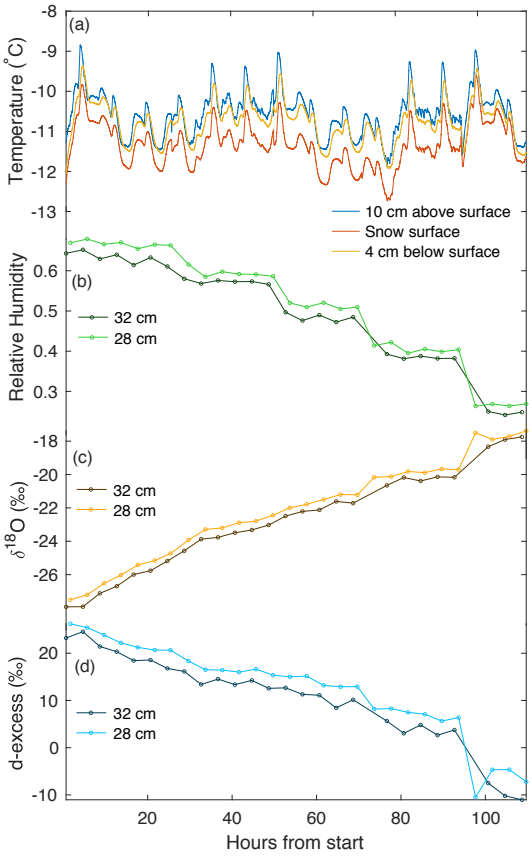

Figure A4: An example of continuous temperature and vapour measurements from experiment L5. (a) Three temperature sensors continuously measure at different heights with respect to the snow surface (10 cm above, on the surface, and ~4 cm below the surface). A CRDS measured (b) humidity, (c) $\delta^{18}O$, and (d) d-excess in vapour, continuously cycling at four heights. Panels (b–d) show vapour measurements at 28 and 32 cm above the snow surface. We document the average of each measurement period, with the first 20 min excluded to remove memory effects.

Over the course of each 4–6 d experimental period, we observe several trends in vapour measurements consistent across all laboratory experiments. Humidity decreases with time, due to a reduction in the sublimating surface area each time a snow sample box is removed. Vapour $\delta^{18}O$ increases with time, consistent with the increase in $\delta^{18}O$ observed in the snow surface. Similarly, d-excess decreases with time in both vapour measurements and the snow surface.

A.3.2 *Field experiments*

Four experiments (F1, F2, F3, F4) were carried out during the 2019 EastGRIP field season, with surface samples (FS1, FS2, FS3, FS4) collected for all experiments and box samples (FB2, FB3, FB4) collected for three experiments. Each of the four experiments lasted 40–60 h

and is supported by continuous measurements of near-surface (10 cm) atmospheric vapour ($\delta^{18}O$, δD, d-excess, humidity), temperature (snow and atmosphere), and LHF. Within each experiment, surface snow and box samples are collected every 3 h. The duration and average environmental conditions of each experiment are reported in Table A1. A compilation of results for measurements of FS, FB, and atmospheric vapour is shown in Fig. A5 and discussed in the next section. All FS and FB samples are shown in Figs. A12 and A13, respectively, with additional vapour measurements shown in Fig. A14 (Appendix of the publication).

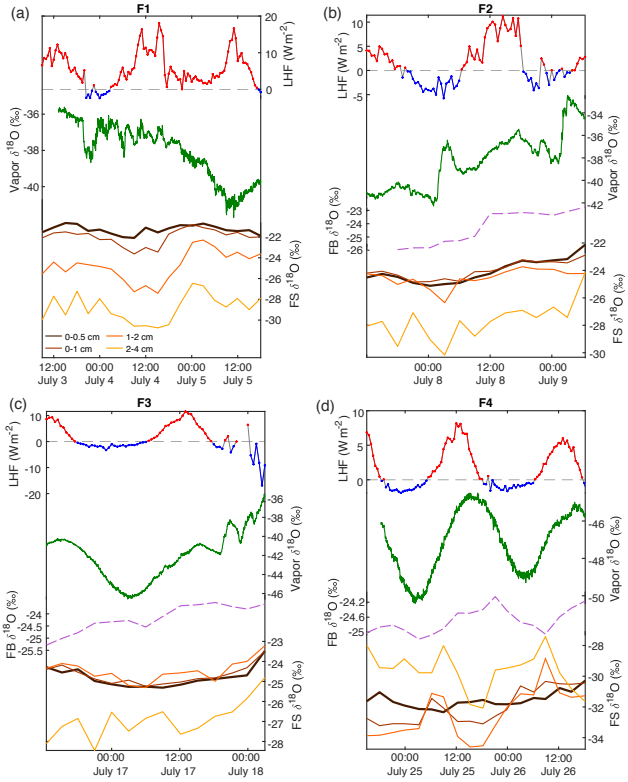

Figure A5: A compilation of data from the 2019 field season shows atmospheric measurements and surface snow samples; from top: latent heat flux (red, positive values; blue, negative values; dashed gray line at 0), $\delta^{18}O$ (green) of atmospheric vapour (2 min average) measured at 10 cm, $\delta^{18}O$ of the top sample (0–0.5 cm) of the FB box sample (pink dashed), and $\delta^{18}O$ of FS snow surface samples. Each snow surface sampling interval shown represents the average of three surface sampling locations (A, B, C) for four different depth intervals: 0–0.5 cm (black), 0–1 cm (red), 1–2 cm (orange), and 2–4 cm (yellow). $\delta^{18}O$ of FS samples tends to reflect $\delta^{18}O$ in atmospheric vapour, with the relationship strongest in the upper surface samples (Table A3). Additional data including temperature and vapour humidity are shown in Fig. A14 (Appendix of the publication).

A.3.2.1 *Variability in $\delta^{18}O$ and d-excess of surface snow*

In order to account for horizontal and vertical spatial variability as a result of redistribution of snow in sastrugi and snow dunes, we averaged isotope values across the three surface locations (A, B, C) for each time of sampling and for each depth interval (i.e., one averaged value each for 0–0.5, 0–1, 1–2, and 2–4 cm at every time sampled). In the following figures and tables we focus on the location-averaged values for each sampling time and depth, referred to as FS1, FS2, FS3, and FS4 for each FS surface experiment. Isotope values for all surface locations (A, B, C) are shown together with the averages in Fig. A12. Location-averaged surface snow measurements at all depths across FS1, FS2, FS3, and FS4 range from approximately -30.3 ‰ to -20.7 ‰ $\delta^{18}O$ and 4.6 ‰ to 14.3 ‰ d-excess. In all experiments, we consistently observe changes in surface snow isotopic composition on an hourly timescale (Fig. A5). The maximum change in average $\delta^{18}O$ of the top surface sample (0–0.5 cm) during a single experiment occurred during FS2, which experienced an enrichment of 3 ‰ $\delta^{18}O$ and decrease of 4.37 ‰ in d-excess. This evolution is substantially smaller than the isotopic change observed in vapour measurements, which has ranges of 5 ‰ – 12 ‰ $\delta^{18}O$ over individual experiment periods and ranges for d-excess of 15 ‰ – 24 ‰. The maximum change in $\delta^{18}O$ and d-excess observed within the top surface sample (0.0–5 cm) during each experiment is reported in Table A2.

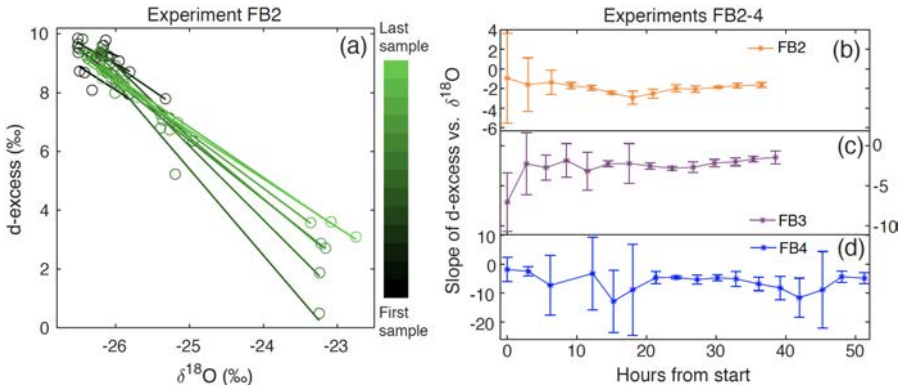

Figure A6: (a) d-excess vs. $\delta^{18}O$ is shown for the vertical snow profile at each time of sampling in Experiment FB2, with a linear regression calculated for each day. This gives a slope of d-excess vs. $\delta^{18}O$, which evolves with time. The sampling time is indicated by the colour scale from black (first sample taken) to light green (last sample taken). The slope of d-excess vs. $\delta^{18}O$ with time is shown for experiments (b) FB2, (c) FB3, and (d) FB4. Error bars indicate the 95 % confidence interval for each slope.

Table A2: The maximum range of isotope measurements is shown for the mean value of the top (0–0.5 cm) sample for all FS experiments.

Experiment	Range $\delta^{18}O$ (‰)	Range d-excess (‰)
FS1	1.44	4
FS2	3	4.37
FS3	1.84	4.12
FS4	2.06	2.62
Mean	2.09	3.78

A.3.2.2 *Relationship between vapour and surface snow*

Over the course of all experiments, the minimum atmospheric vapour $\delta^{18}O$ value observed is -50 ‰, while the maximum observed value is -33 ‰ (a range of 17 ‰). Within each 40–60 h long experiment, the minimum range of variability observed is about 5 ‰ (F4), and the maximum is about 12 ‰ (F3). Vapour $\delta^{18}O$ co-varies with humidity and temperature (Fig. A14), with the lowest $\delta^{18}O$ measurements observed during cold, dry conditions. A clear diurnal cycle is observed in vapour measurements for experiments F3 and F4, while experiments F1 and F2 are more variable. The change in atmospheric $\delta^{18}O$ associated with the diurnal cycle is much smaller than that observed during synoptic weather changes, similar to the pattern previously observed at the northwest Greenland site NEEM (Steen-Larsen et al., 2014). For example, we observe a strong diurnal cycle in F4 and the first half of F3, both of which have an amplitude of approximately 5 ‰ – 6 ‰ $\delta^{18}O$; the change between experiments with different synoptic-scale atmospheric conditions is much greater (i.e., a 17 ‰ $\delta^{18}O$ range is observed between the maximum value during F2 and the minimum value during F4).

Over clear-sky experimental periods with no precipitation, we observe the $\delta^{18}O$ value of surface snow increasing and decreasing on an hourly timescale, corresponding to changes in vapour $\delta^{18}O$ (Fig. A5). To compare the evolution of the isotope signal in vapour and snow measurements, the vapour $\delta^{18}O$ is downsampled to 3 h resolution to match snow sampling resolution. A statistically significant ($p \leqslant 0.05$) relationship is observed between $\delta^{18}O$ of 0–0.5 cm snow surface samples and atmospheric vapour measurements for experiments FS2, FS3, and FS4, but not FS1 (Fig. A15, Table A3). The lack of a significant correlation in FS1 may be a result of some synoptic-scale weather difference, as it is the only experiment period in which there is a sustained decrease in vapour $\delta^{18}O$, and a diurnal cycle in temperature, LHF, and vapour $\delta^{18}O$ is least distinguishable.

Table A3: The *R* value, *P* value, and root-mean-square error (RMSE) are documented for the relationship between the top (0–0.5 cm) FS sample $\delta^{18}O$ and interpolated vapour $\delta^{18}O$. Significance is determined by $p < 0.05$. $\delta^{18}O$ of vapour vs. surface samples is shown in Fig. A15.

Experiment	Slope	*R* value	*P* value	Significance	RMSE
FS1	0.84	0.22	0.374	No	1.62
FS2	2.16	0.73	0.002	Yes	1.67
FS3	4.73	0.82	0	Yes	1.6
FS4	1.56	0.49	0.043	Yes	1.39

A.4 DISCUSSION

In the laboratory experiments, the snow was sublimating under dry air, resulting in a higher LHF than was observed in a typical field setting. For this reason, laboratory experiments are considered an extreme example of natural processes and can be used to identify and understand the physical processes associated with sublimation which would occur on a slower timescale in nature. Laboratory results show a strong signal of enrichment in the snow surface $\delta^{18}O$, as light isotopes preferentially sublimate from the surface due to fractionation. In addition we observe a strong decrease in the snow surface d-excess. Decreasing d-excess driven by kinetic fractionation is also observed when a body of water evaporates into a sub-saturated atmosphere (Benson and White, 1994; Merlivat and Jouzel, 1979). As a similar effect is observed during sublimation in laboratory experiments, we draw the analogy that this is due to kinetic fractionation. This aligns with previous experimental and modelling studies (Ritter et al., 2016; Ebner et al., 2017) and confirms our hypothesis that the upper several centimetres of the snow surface are rapidly (i.e., on a sub-daily timescale) influenced by equilibrium and kinetic fractionation during sublimation. This contradicts the traditional theory of sublimation, which states that sublimation occurs layer by layer and does not alter the snow isotopic composition, on which ice core palaeoclimate water isotope research has been resting (Dansgaard et al., 1973).

In order to interpret these results in the context of natural processes, we consider the results of the field experiments. Previous studies have shown that significant isotopic changes of surface snow are observed (using daily sampling resolution) over periods of time without precipitation, and this is associated with snow metamorphism (Steen-Larsen et al., 2014; Casado et al., 2018). We expand on these findings with higher-resolution field sampling, showing that snow surface $\delta^{18}O$ and d-excess change on an hourly basis, which was hypothesized by Madsen et al., 2019; this demonstrates that similar pro-

cesses to the lab experiments are occurring in a natural environment, albeit less extreme.

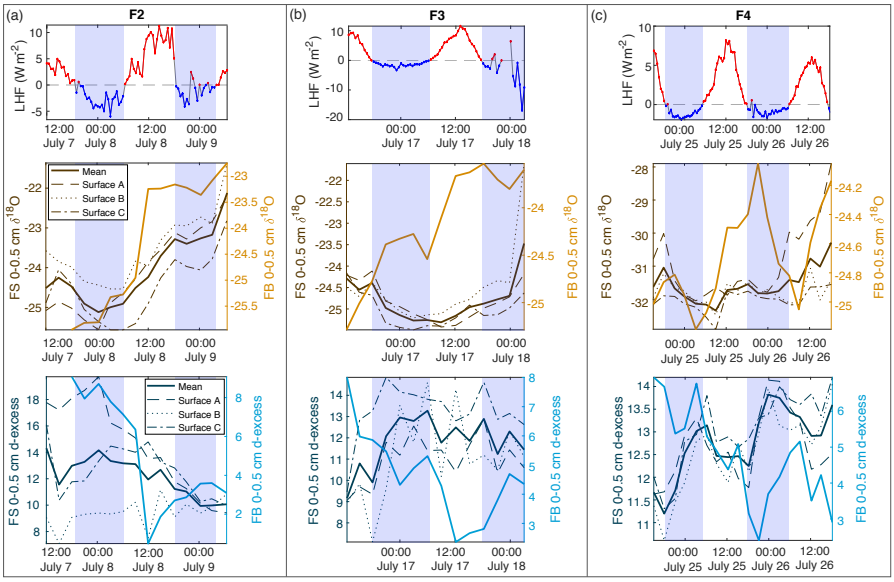

Figure A7: Comparison of latent heat flux (LHF) and 0–0.5 cm samples for mean FS surface samples and FB box samples for (a) F2, (b) F3, and (c) F4. Positive LHF values are indicated in red, and negative LHF values are marked blue with associated shading in all subplots (LHF, δ^{18}O, and d-excess). FS surface snow 0–0.5 cm values are shown in brown (δ^{18}O) and dark blue (d-excess), with each location (A, B, C) designated by dashed lines and the mean of all locations as the bold solid line. FB box snow 0–0.5 cm values are shown in light orange (δ^{18}O) and light blue (d-excess) bold lines.

To interpret the driving factors in snow isotope changes, we consider differences between the FB box and FS surface samples. The FB samples were covered to shield from direct sunlight and windblown snow and therefore were less likely to experience vapour deposition or frost. Figure A7 shows a comparison of the top 0–0.5 cm sample for all FB and FS experiments with LHF. Over the course of the field experiments, we observe several 6–12 h periods of increasing δ^{18}O in 0–0.5 cm FB and FS samples, primarily during periods of positive LHF and decreasing d-excess; this is indicative of sublimation as suggested by laboratory experiments and model results. We also observe several 6–12 h periods in which the FS δ^{18}O decreases, despite experiments taking place during time periods with no precipitation and minimal wind-drifted snow. Periods of decreasing FS δ^{18}O occur primarily during night-time hours with negative or low LHF measurements (Fig. A7; negative LHF indicated by shading) and increasing d-excess. There is no significant decrease in δ^{18}O in FB2 and FB3 associated with these periods, while there is a simultaneous decrease in δ^{18}O in FB4 and FS4. Additionally, the 0–0.5 cm d-excess decreases substantially in all FB experiments, similar to the signal that was ob-

served due to kinetic fractionation during sublimation in laboratory experiments. In general, the box samples experience less decrease in $\delta^{18}O$ than associated FS samples due to minimized vapour deposition during periods of negative LHF and greater total decrease in d-excess due to increased total sublimation across the entire experimental period. This demonstrates that vapour deposition of preferentially isotopically heavy water molecules in the form of frost significantly contributes to the surface snow signal on a rapid timescale (Casado et al., 2018).

There are still several factors in the field experiments which could complicate interpretation of the results. While it is clear in the laboratory experiments that any changes in the snow composition are a direct result of sublimation, we cannot isolate individual processes occurring in field experiments. For example, atmospheric vapour $\delta^{18}O$ measurements often vary in phase with LHF, but during some periods (most notably the latter half of F1 and F3) vapour $\delta^{18}O$ deviates from the LHF trend. At this stage it is unclear whether LHF, vapour $\delta^{18}O$, or another factor is influencing the snow surface, or whether the snow surface composition is driving vapour $\delta^{18}O$. Additionally, the isotopic composition of deeper snow layers could influence the surface snow due to diffusion. We note a general trend observed in Experiments FS1, FS2, and FS3 in which the deepest surface sample (2–4 cm) has the lowest values for both $\delta^{18}O$ and d-excess. However, throughout the duration of FS4, the upper samples (0–0.5, 0–1, and 1–2 cm) have a lower $\delta^{18}O$ value than the 2–4 cm sample, likely due to a precipitation event preceding FS4 which may have deposited surface snow with anomalously low $\delta^{18}O$. If there are significant differences between the composition of adjacent snow layers, the surface snow could be influenced by a combination of interstitial diffusion and atmospheric driving forces (i.e., LHF and vapour $\delta^{18}O$). This may also explain some isotope inter-experiment differences between FB and FS results, as FB samples are homogeneous and FS samples have vertical variability in snow isotopic composition.

A key finding from field experiments is that both sublimation and vapour deposition influence the surface snow on an hourly timescale; this is supported by laboratory experiments, demonstrating that sublimation has the ability to influence the mean surface snow isotopic composition in the top 1–2 cm of the snowpack during precipitation-free periods. These changes are occurring faster than the average recurrence of precipitation events and could produce substantial changes in the mean isotopic composition of the upper several centimetres of the snowpack over a long precipitation-free period. This suggests that effects from sublimation and vapour deposition may be superimposed on the precipitation signal, resulting in a snowpack record indicative of multiple parameters including atmospheric conditions, water vapour isotopic composition, condensation

temperature (i.e., $\delta^{18}O$), and precipitation source region conditions (i.e., d-excess). The extent to which this occurs is dependent on the accumulation rate at the ice core site, as these processes primarily influence the top few centimetres of the snow column. A site such as SE-Dome (southeast Greenland), which receives 102 cm yr^{-1} of ice equivalent precipitation (Furukawa et al., 2017) (i.e., several metres of snowfall), will be less affected than a drier location with significantly less annual accumulation, such as Antarctic sites like WAIS Divide (24 cm annual accumulation) (Fudge et al., 2016) or South Pole (7.4 cm annual accumulation) (Mosley-Thompson et al., 1999).

To assess the relevance of our results on longer timescales, we make use of a simple mass balance calculation and an observed mean LHF in July of 3.1 W m^{-2}, indicating a net removal of snow from the surface due to sublimation. By assuming equilibrium fractionation during sublimation (Wahl et al., 2021), we can calculate the isotopic composition of the humidity flux and the associated removal of isotopologues. When considering reasonable values of a 5,cm layer of snow, a snow density of 300 kg m^{-3}, an initial isotopic composition of -20 ‰ $\delta^{18}O$, and a surface temperature of -9 °C for the month of July, the snow would be enriched by ~4 ‰ $\delta^{18}O$ due to the net humidity flux, which is substantial. For comparison, the seasonal amplitude (i.e., summer peak to winter trough) at the Renland Ice Cap, for example, is about 8 ‰ in $\delta^{18}O$ (Hughes et al., 2020). We acknowledge that this is a highly simplified mass balance calculation without taking into account the vapour isotopic composition or precipitation inputs. However, since vapour exchange is a continuous process, it will continuously affect the layer of snow that is in contact with the atmosphere and will therefore imprint on the snow isotopic composition with a general net daily sublimation signal during months with a net sublimation flux.

Which months show a net sublimation flux is dependent on the geographical location and general climatology of the area. Especially in the context of palaeoclimatological interpretation of ice cores, this cannot be assumed to be constant in time. If the vapour–snow exchange imprints on the seasonal snow isotopic composition as indicated in the result of the mass balance calculation, one would need to take changes in sublimation seasonality into account when making assumptions about vapour-exchange effects on palaeo timescales, as has been previously demonstrated for precipitation seasonality (Werner et al., 2000).

On shorter timescales in our laboratory experiments we observe changes of up to 8 ‰ $\delta^{18}O$ and 20 ‰ d-excess over time periods of several days, and in FS field experiments we find an average change of 2.09 ‰ $\delta^{18}O$ and 3.78 ‰ d-excess on very short (sub-diurnal) timescales. This observation, in combination with our mass balance calculation of 4 ‰ change in $\delta^{18}O$ over the month of July, suggests

that under typical natural conditions, changes in the surface isotope value occurring on a short timescale may have an impact on the mean seasonally recorded isotope signal. Previous studies have addressed the effect of seasonally biased accumulation rate on diffusion and the recorded $\delta^{18}O$ isotope signal (Persson et al., 2011; Casado et al., 2020; Hughes et al., 2020) and the effect of physical modifications and snow redistribution of the snow surface on the accumulation intermittency (Zuhr et al., 2021a), but the effect of sublimation-driven changes in surface snow isotopic composition between precipitation events has not been quantified previously. Whether the magnitude of the mean isotope change due to sublimation and snow–vapour exchange outweighs the effects of snow redistribution, accumulation bias, and diffusion has yet to be determined. This could be further explored through future experiments which account for additional variables or are completed at a larger scale. For example, the effect of snow specific surface area (SSA) could be determined by making simultaneous SSA and isotope measurements. Additionally, to remove the effect of wind redistribution and snow dunes on snow isotope spatial variability, a large pit could be filled with homogeneous snow for continuous sampling. In this case, the snow would have a known starting isotopic composition, similar to the FB experiments completed here but be subject to more natural conditions as in the FS experiments. Finally, as weather conditions would allow, it would be beneficial to have multiple experimental periods greater than 48 h.

In order to fully understand the implications of sublimation and vapour deposition on the ice core record, it is necessary to quantify the effects of these processes over the course of a full year. While not in the scope of this paper, this problem can first be approached through mass and isotope flux measurements throughout the summer field season (Wahl et al., 2021). Subsequent modelling of these processes throughout the annual climate cycle will provide insight as to what magnitude snow–vapour exchange influences surface snow on longer timescales (i.e., months to years), and how it may be recorded in the ice core isotope record. This could inform us to what extent changes in frequency of precipitation events, accumulation rate, and LHF could influence the isotope signal recorded in ice cores on decadal to millennial scales. Our findings suggest that these variables contribute to a combined isotope signal, in which $\delta^{18}O$ and d-excess in ice core records likely incorporate individual precipitation events (i.e., condensation temperature and moisture source region conditions, respectively), surface redistribution (i.e., wind drift and erosion), and a post-depositional alteration signal reflecting atmospheric conditions at the ice core site. Snow isotope models such as CROCUSiso (Touzeau et al., 2018), the Community Firn Model (Stevens et al., 2020), and isotope-enabled climate models would therefore be updated through the incorporation of isotope

fractionation during sublimation, snow–vapour isotope exchange, and snow metamorphosis.

A.5 CONCLUSIONS

In this study, we have combined controlled laboratory experiments with field measurements in an effort to constrain the effects of sublimation on surface snow isotopic composition. Experiments in a controlled laboratory setting demonstrate isotopic enrichment due to fractionation occurring during sublimation. In experimental results, $\delta^{18}O$ increases as light isotopes preferentially sublimate due to fractionation, and d-excess decreases due to kinetic fractionation. These changes occur rapidly, substantially changing the isotopic composition of the top 2–3 cm of snow over a 4–6 d period. Field experiments included continuous measurements of atmospheric vapour and latent heat flux during periods of high-resolution surface snow sampling, during which we observed significant changes in the top 1–2 m of snow surface isotopes on a sub-diurnal timescale. We observed periods of increasing and decreasing $\delta^{18}O$, indicating that both sublimation and vapour deposition influence the surface snow on an hourly basis. This supports our hypothesis that rapid change occurs in a natural setting and propagates into the snowpack, moderately altering the initial precipitation isotope signal.

Post-depositional effects have implications for the interpretation of ice core data, which traditionally is assumed to only record isotopic variability from precipitation. Our results complement previous studies demonstrating spatial and temporal variability in snow surface isotopes, further strengthening the idea that the ice core record not only integrates the climate signal of condensation temperature (i.e., $\delta^{18}O$ and δD) and moisture source conditions (i.e., d-excess) during precipitation, but also may integrate the atmospheric conditions between precipitation events (in both $\delta^{18}O$ and d-excess). These factors should in the future be included in isotope-enabled climate models, which may include estimates of synoptic-scale patterns across annual cycles that would influence latent heat flux, vapour composition, and the resulting influence on surface snow isotopes. This will improve future interpretations of ice core data and may be the missing link in the transfer function between climate and an uninterrupted isotope record, strengthening our interpretation of ice core water isotopes as a proxy for a continuous integrated climate record.

B

ATMOSPHERE-SNOW EXCHANGE EXPLAINS SURFACE SNOW ISOTOPE VARIABILITY

Sonja Wahl[1], Hans Christian Steen-Larsen[1], Abigail G. Hughes[2], Laura Dietrich[1], Alexandra Zuhr[3], Melanie Behrens[4], Anne-Katrine Faber[1], and Maria Hörhold[4]

[1] University of Bergen and Bjerknes Centre for Climate Research, Bergen, Norway

[1] Institute of Arctic and Alpine Research, University of Colorado Boulder, Boulder, CO 80309-0450 USA

[3] Alfred-Wegener-Institut Helmholtz Zentrum für Polar- und Meeresforschung, Research Unit Potsdam, Potsdam, Germany and University of Potsdam, Institute of Geosciences, Potsdam, Germany

[4] Alfred-Wegener-Institut Helmholtz Zentrum für Polar- und Meeresforschung, Research Unit Bremerhaven, Bremerhaven, Germany

This chapter is submitted to:
Geophysical Research Letters,
and published as DOI: 10.1029/2022GL099529, 2022.

ACKNOWLEDGMENTS

After all this time in the ECUS/SPACE group and at AWI, I am more than grateful for the many experiences, challenges, and my personal and scientific growth during the last years. It is now time to say thank you.

I am deeply grateful to Thomas Laepple. Thom, thank you for your guidance in my scientific growth with the right supervision at the right time, for sending me into the field without me knowing what to expect and for the freedom you gave me in many ways but at the same time being a demanding supervisor. Thank you for never doubting my scientific abilities and your alltime support and the trust in me.

Special thanks also go to Ling for her (remote) support and supervision, especially during the preparation of the manuscript but also for hosting me for three weeks at the Institute of Oceanography in Taiwan, and finally for serving as a reviewer for my thesis. I further thank Anaïs Orsi for serving as a reviewer as well.

My journey to stable water isotopes in snow began in the Stable Isotope Facility at AWI Potsdam. Special thanks go to Mikaela for all her help and support with questions and the day-to-day lab work and Hanno for allowing me to measure more than 3,500 snow samples and all the fruitful discussions on stable water isotopes. I also want to thank the entire lab crew for an enjoyable lab time. Thanks go to Sina Sporr, Leonie Hahn and Zoe La France for supporting the measurements of more than 3,500 snow samples. This thesis would not have been possible without you.

I am grateful for the opportunity to participate in two field seasons of the East Greenland Ice Core Project, and for the entire community I have met during my time on the ice. I would also like to thank all those who assisted me with data collection in the field. Special thanks go to Hans Christian, Sonja, and Maria for taking me to the field, as well as for many fruitful discussions and support, especially during the preparation of the last manuscript.

I am grateful for the opportunity to work at the *Laboratoire des Sciences du Climat et de l'Environnement* in France during my PhD. I would like to thank the whole GLACCIOS team who welcomed me warmly and made my stay very pleasant. Special thanks go to Amaëlle Landais for giving me insights into ^{17}O measurements, providing me an interesting data set and supervising me.

Further on, thanks go to all members of the ECUS/SPACE working group! Thank you to Andrew, Torben, Thomas, Maria, Igor, Raphaël, Mathieu, Hanna, Laura, Fyntan, Lena and Jannis for the discussions,

interactions and support during the last years. I would especially like to thank Thomas for his long patience during my writing beginnings and his detailed explanations of isotopic principles. Special thanks also go to Andrew for proofreading part of this thesis, for assistance in R, especially with ggplot issues, and for sharing his experience on radiocarbon analysis with me. Although not directly involved in ECUS/SPACE, thanks also go to Jeroen for assistance in interpreting the radiocarbon data and to the students for collecting hundreds of foraminifera. Again, without your work, this PhD would not have been possible.

I am grateful for the financial support by POLMAR which allowed me to attend several conference. I also benefited from the excellent course programme which helped me to develop my scientific careers as well as my personal skills besides my PhD. I further thank the DAAD for financial support for the four-months research stay at the *Laboratoire des Sciences du Climat et de l'Environnement* in France.

Additionally, I am deeply grateful for my friends, who supported me when the motivation for my PhD was low, who listened to me when I was excited about my data even though they did not understand what I was talking about and who was just there during all the lockdowns during the last two years. Thanks go to Tabea, Tobi, Peter, Michi and Jonas, without whom I would have never dared to think about starting a PhD; Sabrina and Kathi for their remote support and many hours on the phone; and especially Tabea for proofreading parts of this work and countless "Bavaria-Blue-Lieblingsbrötchen"-evenings.

Finally, I am grateful to my family, who has always supported me during the long journey of my studies and this PhD. It means a lot to me that you never doubted my ability to pursue a PhD.

EIDESSTATTLICHE ERKLÄRUNG

Hiermit versichere ich, Alexandra M. Zuhr, dass ich die vorliegende Dissertation mit dem Titel: *Proxy signal formation in palaeoclimate archives: A characterisation of climate signal deposition and modification in marine sediments and polar ice* selbständig verfasst und keine anderen als die angegebenen Quellen und Hilfsmittel verwendet habe. Alle Ausführungen, die anderen Schriften wörtlich oder inhaltlich entnommen wurden, sind als solche kenntlich gemacht.

Ich habe diese kumulative Dissertation am Alfred-Wegener-Institut Helmholtz-Zentrum für Polar- und Meeresforschung in Potsdam erarbeitet und in englischer Sprache angefertigt.

Diese Dissertation wird erstmalig und ausschließlich an der Universität Potsdam eingereicht. Die dem Promotionsverfahren zugrundeliegende Promotionsordnung vom 18.09.2013 ist mir bekannt.

Potsdam, Mai 2022

Alexandra M. Zuhr